Controlled Synthesis and Properties of Layered Double Hydroxides

Chengle Joyce Wang

A thesis submitted in part fulfilment of the requirements for the degree of Doctor of Philosophy at the University of Oxford

St Edmund Hall

Oxford

April 2012

The work described in this thesis was carried out in the Inorganic Chemistry Laboratory, South Parks Road, Oxford and the Chemistry Research Laboratory, Mansfield Road, Oxford from October 2008 to March 2012 under the supervision of Professor Dermot O'Hare. All the work described is my own unless stated to the contrary, and has not been submitted for any degree at this or any other university.

Chengle Joyce Wang
April 2012

Abstract

Controlled Synthesis and Properties of Layered Double Hydroxides

Chengle Joyce Wang St Edmund Hall

D.Phil. Thesis Trinity Term 2012

The aims of this thesis are concerned with the synthesis of layered double hydroxide nanoparticles with controlled morphology and particle size distribution and an investigation of their physical properties. An introduction of layer double hydroxide chemistry, especially existing synthetic approaches, is reviewed in **Chapter 1**. Structural investigations, characterisation techniques, the properties and the applications of LDHs are discussed consecutively.

The first successful synthesis of lithium aluminium nanorods using the hydrothermal treatment of a gibbsite precursor with a rod-like morphology is described in **Chapter 2**. The rod morphology is depicted using electron microscopy and confirmed by comparing refined X-ray diffraction patterns to a standard sample.

Chapter 3 describes the application of reverse microemulsion method to prepare Co-Al and Ni-Al LDH nanoplatelets. The LDH particle sizes can be effectively controlled, and the structures of the nanoplatelets are investigated. The magnetic properties of the LDH nanoplatelets are dependent on the size of the nanoplatelets.

A novel single component microemulsion system for the synthesis of LDHs is developed in **Chapter 4**. Mg-Al LDH nanoplatelets were successfully synthesised with precise particle size control. The factors affecting the formation of the microemulsions and the mechanism of the synthesis are discussed.

Chapter 5 focuses on the applications of the novel single component microemulsion methods to prepare a range of LDHs with different metal combinations including Co-Al, Ni-Al, Zn-Al, Li-Al, Ca-Al, and Ni-Fe. This method proves very effective at controlling the particle sizes. The magnetic properties of the LDHs containing paramagnetic transition metal centres have been studied in detail.

In **Chapter 6**, the DIFFaX program has been used to simulate the XRD patterns of layered structures. The factors influencing the XRD patterns in these materials have been systematically investigated including the effects of particle size, stacking faults, and disorder. The XRD patterns of materials described in previous chapters are simulated using the latest DIFFaX+ code in order to estimate the particle sizes and stacking sequences.

The characterising techniques and the experimental details are listed in **Chapter 7**.

Acknowledgements

It is finally come to the end of my DPhil course. My feelings are so tangled and beyond words when the memory of last four years flash in my mind. I could never make it without the help from every one of you. I truly appreciate and want to say thank you for everything you've done for me.

Foremost, I would like to thank Dermot for letting me join this group and guiding me all the way though my DPhil course. I really appreciate the freedom you gave me on research, allowing me to do whatever I am interested, and providing detailed and patient instructions whenever I needed. This attitude towards research will influence me all my life. Thank you also for supporting me for all the funding applications and caring me about my life here. I even enjoyed chatting with you, about activities outside academic field or views on life and various things. I sincerely appreciate all that you have done for me and feel lucky to have you as my supervisor for the last four years.

I could not find a way to express my eternal gratitude to my parents, Rongxue Wang and Rufeng Yue. You have been supporting me from the moment I decided to come to UK both emotionally and financially, no matter how much you have to sacrifice. I think you would be much more relieved and have accomplished your own dreams if you didn't spend all your savings for me. I hope I could pay you back by making you the happiest people in the world and supporting you whenever and whatever just like what you did for me.

I would also like to dedicate this thesis to my dearest husband, Han. I am sure I could never make it without you. You gave me fully support without a word of complain, when suffering the pain of being apart a few weeks after we got married. You tolerated my bad temper, depression and paranoid complain, which is not often known to others. You always have a way to cheer me up and make me happy. I truly appreciate and look forward to the new life we will start.

Thanks to the DOH group, every one of you has provided me so much fun in my life here. Hasna, thanks for the cakes and being an intimate friend. Charles, thanks for all the knowledge you've shared, all the help you gave me in lab and all the fun we had. Anchalee, thank you for the Thai cooking lesson and all the help you provide for travelling in Thailand. Saul, thank you so much for the help in lab and putting up with me when I bothered you with the cute animals after Charles left. Many thanks to Gareth, since I've been constantly bothering you for ICP, proof reading, being my referee and random questions. Enormous thanks to Ian, Henry, Hannah and Sam for helping me with the long and boring proof reading. Thanks to Andy, Chadwick, Coops, Tom, Shuangde, Qiang, JC, Andrew, Emily and Paul. Thanks for all the favours you did for me, and all the fun you shared with me. I will cherish your accompany for all my life. Thanks to all the DOH group members, Part IIs and visiting students. It was you who made my life colourful and joyful.

Many thanks to the crews in ICL, CRL and Harwell campus, especially to Phil for teaching me use the SQUID and caring me about my football play, as well as giving me the chance to demonstrate the first year practical course. Thanks to Robert Jacobs for teaching and helping me with the AFM and IR. I would like to thank Prof. Philip for being my college adviser and helping me with all the reference letters. Thanks to Edward Dixon for teaching and helping me with the TGA, and Andrew Allan for helping me use the TEM and SEM. I would also like to thank Yimin and Jamie from Department of Materials for giving me a lot help on TEM, and Kerstin from Begbroke science park for helping me with the DLS. Thanks to Matteo who helped me a lot with the DIFFaX+ over emails without even know me. Many thanks to Stephen from London Metropolitan University for performing CHN analyses.

Outside the academic field, I would like to thank Mr and Mrs Hall for treating me like a family. I enjoyed all the trips to your place and treasure the friendship with you for a life time. I appreciate the accompanies of all the dearest friends here, and will remember you all my life, with no particular order, Huijuan Wu, Haiyue Yu, Duode Li, Boshen Wu and so on. Thanks to Trevor and Ming for giving me the chance to work in Chinese Study Library.

I'd like to thank Henry Leicester Trust, GB-China Educational Trust and St Edmund Hall for funding. The financial assists were great help for me.

Sincerely thanks to all of you and I would never forget you in my life.

Contents

Abbreviations

[A]	Concentration of A, in mol L^{-1}
AAAC	Alkylammonium alkylcarbamate
ACD	Advanced Chemistry Development
AFM	Atomic force microscopy
AOT	Bis(2-ethylhexyl) sulfosuccinate
BTAn	4-butylaniline
CMC	Critical micelle concentration
CNS	Carbon nanospheres
CTAB	Cetyltrimethylammonium bromide
CTAC	Cetyltrimethylammonium chloride
D	Distribution Coefficient
DDS	Dodecyl sulphate
DBS	Dodecyl benzenesulfonate
DMA	Dynamic mechanical analysis
DDAm	Dodecylamine
DMTDAm	N,N-dimethyltetradecylamine
DOAm	Dioctylamine
DVB	Divinylbenzene
EA	Elemental analysis
ED	Electron diffraction
EDX	Energy-dispersive X-ray
EM	Electron microscopy
FI-IR	Fourier transform infrared spectroscopy
FITC	Fluoresceinisothiocyanate
FWHM	Full width at half maximum
FC	Field cooling
h	Hour
HMT	Hexamethylenetetramine
HOPG	Highly ordered pyrolytic graphite
IE	Ion exchange
ICP	Inductively coupled plasma
ICP-MS	Inductively coupled plasma mass spectrometry
ICP-OES	Inductively coupled plasma optical emission spectrometry
IR	Infrared
LDH	Layered double hydroxide
LDHs	Layered double hydroxides
LMWH	Low molecular-weight heparin
M	mol L^{-1}
mins	minutes
M_{sat}	Saturation magnetization
MQT	Macroscopic quantum tunneling
MTX	Methotrexate
NaAOT	Sodium bis(2-ethylhexyl) sulphosuccinate
NCs	Nanocrystals
NPs	Nanoparticles

OAc	Oleic acid
OAm	Oleylamine
OPD	Optical path difference
P	Partition Coefficient
PS	Polystyrene
PXRD	Powder X-ray diffraction
RM	Reverse microemulsion
rpm	Round per minute
s	Seconds
SAED	Selected area electron diffraction
SAXS	Small angle X-ray scattering
SDS	sodium dodecylsulphate
SEM	Scanning electron microscopy
SQUID	Superconducting quantum interference device
t	Time
T	Temperature
T_B	Blocking temperature
T_{irr}	Irreversible temperature
TEM	Transmission electron microscopy
UV-Vis	Ultraviolet-Visible
X	An unspecified anion
XRD	X-ray diffraction
ZFC	zero-field cooling
0D	Zero-dimensional
1D	One-dimensional
2D	Two-dimensional
3D	Three-dimensional
5-FU	5-fluorouracil

Chapter 1 Introduction

1.1. Overview

Layered Double Hydroxides (LDHs) are a family of layered materials which exist naturally as minerals and can also be synthesised in the laboratory. The history of LDHs dates back to the mid-19th century when hydrotalcite was discovered in Sweden. The accurate formula, $Mg_6Al_2(CO_3)(OH)_{16}\cdot 4H_2O$, was first presented by Manasse in 1915.[1] Ever since the publication of a series of papers by Feitknecht,[2] LDHs have been investigated extensively.

The general composition of LDHs is often described as $[M^{z+}_{1-x}M^{3+}_{x}(OH)_2]^{a+}(A^{n-})_{a/n}\cdot mH_2O$, where A^{n-} is a charge-balancing organic or inorganic anion. In the majority of cases, $z = 2$, in which case M^{2+} is usually chosen from Mg^{2+}, Ca^{2+}, Mn^{2+}, Zn^{2+}, Cu^{2+}, Ni^{2+} or Co^{2+}, and M^{3+} is Al^{3+}, Cr^{3+}, Mn^{3+}, Fe^{3+}, Ga^{3+}, Co^{3+}, Ni^{3+}, V^{3+} or Sc^{3+}.[3-6] Li-Al LDHs comprise the only set that contains M^{+} and M^{3+} cations. Recently, some LDH-like compounds containing M^{4+} have been reported, including Ti^{4+}, Zr^{4+} and Sn^{4+}.[7-12] However, in some cases, the tetracations are segregated into amorphous M^{4+} oxide particles.[10, 11]

The structure of LDHs can be considered to comprise positively charged brucite-like layers of mixed metal hydroxides with charge-balancing anions and water molecules in the interlayer space.[3] The layered structure allows these compounds to accommodate species between the layers, which provides extensive applications as absorbents,[13-15] catalysts and catalyst precursors,[16-19] drug carriers,[20-24] anion exchangers, and bioactive nanocomposites.[25-33] They can also act as precursors for the synthesis of transition metal oxides such as spinel.[19, 34-40]

Although LDHs were first observed in naturally occurring minerals, the synthesis of LDHs has been studied extensively. Not only have LDHs with new combinations of metal ions been synthesised, but a great variety of anionic species have been introduced into the interlayer spaces. Besides the most widely used co-precipitation method, new synthetic techniques attempting to control particle size or morphology have been invented.

1.2. Structure of LDHs

The determination of the structure of LDHs involves three aspects: the arrangement of the cations within the brucite-like layers, the anion distribution in the interlayer galleries and the stacking sequence of the layers assembling together. The structure of LDHs was confirmed by Allmann,[41] Brown,[42, 43] and Taylor,[44, 45] who carried out single crystal X-ray diffraction studies on mineral samples in the 1960s. The structural model of LDHs containing divalent and trivalent ions is based on that of brucite, $Mg(OH)_2$ (see crystallographic information in **Table 1-1**), which consists of

Table 1-1: Crystallographic information for brucite, gibbsite and bayerite.

	Formula	Crystal System	Space Group	Z	Lattice Parameters
Brucite	$Mg(OH)_2$	trigonal	$P\ \bar{3}\ m\ 1$	1	a = 3.0467(5) Å; c = 4.3554(9) Å
Gibbsite	$Al(OH)_3$	monoclinic	$P\ 1\ 2/n\ 1$	8	a = 8.6410(7) Å; b = 5.0704(6) Å; c = 9.719(4) Å; β = 85.43(8) °
Bayerite	$Al(OH)_3$	monoclinic	$P\ 1\ 2/a\ 1$	4	a = 5.062(1) Å; b = 8.671(2) Å; c = 4.713(1) Å; β = 90.27(3) °

infinite sheets of edge-sharing octahedra with Mg^{2+} ions in the centre and hydroxide groups at the vertices (**Figure 1-1**). Upon substituting some of the Mg^{2+} ions with trivalent ions, the sheets will possess an overall positive charge. To balance it, anions are introduced into the interlayer galleries. The hydroxide layers normally stack in two polymorphic forms, hexagonal and rhombohedral. However, stacking faults and turbostratic disorders are often found in the structure.

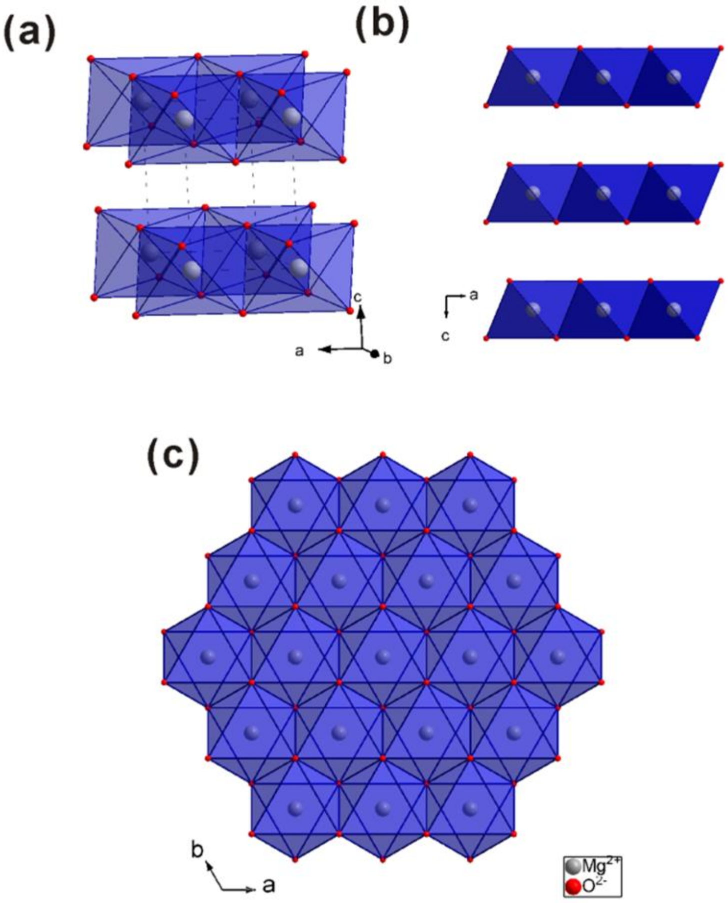

Figure 1-1: (a) 3-Dimensional view, (b) view along the *b*-axis and (c) view along the *c*-axis of brucite.

Unlike the structure of LDHs containing divalent ions, the structures of Li-Al LDHs are constructed from two of the structural modifications of $Al(OH)_3$, gibbsite and bayerite[46, 47] (**Table 1-1**, and **Figure 1-2**). The structures of these two aluminium hydroxides both comprise a close packing of hydroxyl ions in which two-thirds of the octahedral sites in the layers are occupied by Al^{3+} ions. After Li^{+} ions occupy the octahedral vacancies, charge neutrality is restored by the incorporation of exchangeable anions in the interlayer region. The main difference between these two polymorphs is the stacking sequence of the layers. If the hydroxyl ion positions are represented by the upper-case symbols A and B, the stacking sequence in bayerite approximates to ABABAB… (**Figure 1-2** (d)), giving one layer per unit cell. In gibbsite, adjacent layers are stacked one above the other in an eclipsed manner (ABBAABBA…) (**Figure 1-2**

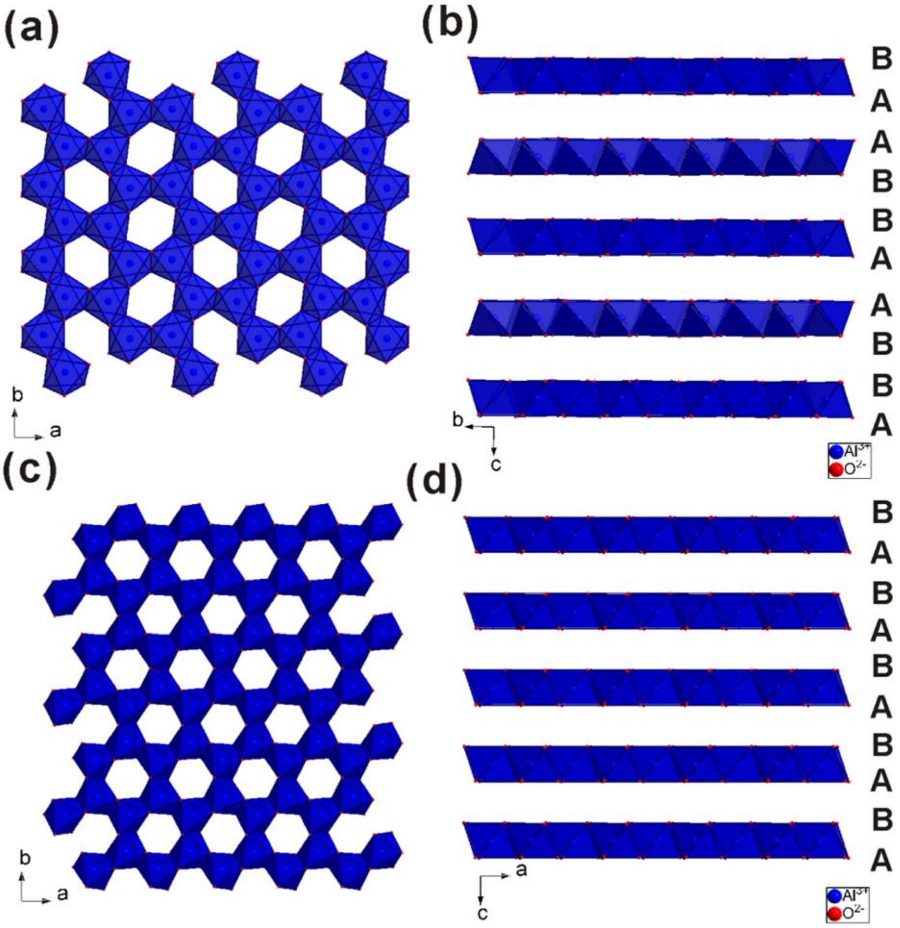

Figure 1-2: View of gibbsite along (a) the *c*-axis and (b) the *a*-axis. View of bayerite along (c) the *c*-axis and (d) the *b*-axis.

(b)) to give two layers per unit cell. It is suggested that the gibbsite-based Li-Al LDHs will adopt a hexagonal symmetry while the bayerite-based Li-Al LDHs will display a rhombohedral structure.[48, 49]

1.2.1. Composition of metal hydroxide layers

In brucite, there are two O-O distances, 2.78 Å and 3.05 Å, which means the MgO_6 octahedra is compressed along the *c*-axis and expanded in the *a*, *b*-plane. The symmetry of the octahedra is lowered from O_h to D_{3d}. The replacement of Mg^{2+} by a smaller trivalent cation, such as Al^{3+} (**Table 1-2**), will cause contraction of the octahedra and deformation of adjacent octahedra. It is believed that the M^{2+}/M^{3} ratio should be kept between 2 and 4 to enable isolation of phase pure LDHs which avoids nearest neighbouring M^{3+} ions.[5, 50-52] In this case, the layer charge $x = M^{3+}/(M^{2+} + M^{3+})$ in the formula $[M^{2+}_{1-x}M^{3+}_{x}(OH)_2]^{x+}(A^{n-})_{x/n} \cdot mH_2O$ should not exceed the range of 0.2 to 0.33. It has been shown by NMR spectroscopy that in Mg-Al LDHs the Al^{3+} ions are fully ordered in a hexagonal arrangement when $x = Al^{3+}/(Al^{3+}+Mg^{2+}) = 0.33$ (**Figure 1-3**), and when $x < 0.33$ the Al^{3+} ions are distributed without Al-O-Al close contact.[53]

Table 1-2: Crystal ionic radii of selected six coordinate metal cations.

M^{+}/M^{2+}	Radius (Å)	M^{3+}	Radius (Å)
Mg^{2+}	0.860	Al^{3+}	0.675
Fe^{2+}	0.920	Co^{3+}	0.750
Co^{2+}	0.885	Fe^{3+}	0.785
Ni^{2+}	0.830	Mn^{3+}	0.785
Cu^{2+}	0.870	Ga^{3+}	0.760
Zn^{2+}	0.880	Rh^{3+}	0.805
Mn^{2+}	0.97	Ru^{3+}	0.820
Pd^{2+}	1.00	Cr^{3+}	0.755
Ti^{2+}	1.00	V^{3+}	0.780
Cd^{2+}	1.14	In^{3+}	0.940
Ca^{2+}	1.09	Y^{3+}	1.04
Li^{+}	0.900	La^{3+}	1.17

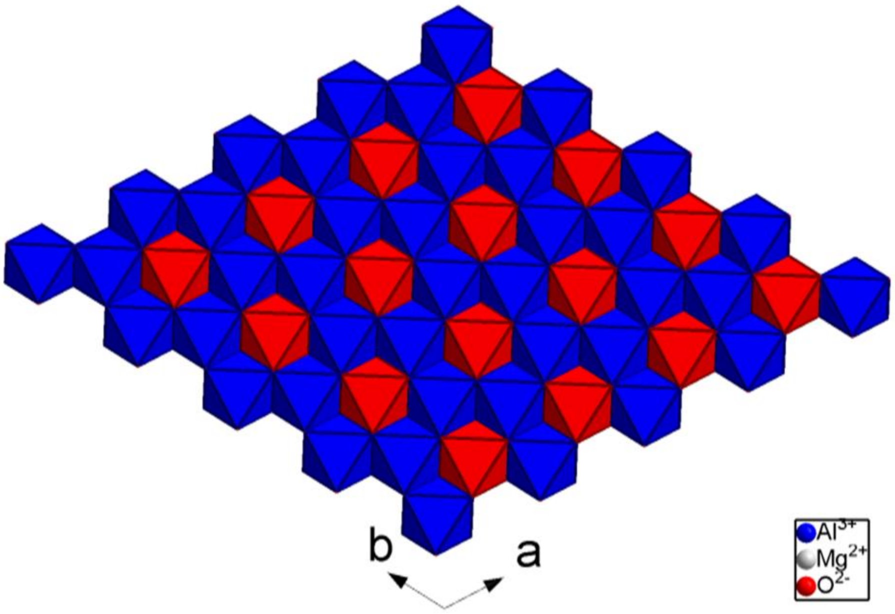

Figure 1-3: View along the *c*-axis of a Mg-Al LDH with Mg^{2+}/Al^{3+} ratio = 2. Red octahedra are Al^{3+} centred, blue are Mg^{2+} centred.

However, M^{3+}-O-M^{3+} linkages have already been found in LDHs when $M^{3+} = Cr^{3+}$.[54]

Instead of substitution of cations, gibbsite/bayerite based LDHs are formed by intercalation of metal cations into the vacancies in $Al(OH)_3$ structures. The Al^{3+} ions occupy two thirds of the octahedral sites in the aluminium hydroxides, where the maximum ratio of M^{z+}/Al^{3+} is 1 : 2. In the first example, $[LiAl_2(OH)_6]X\cdot mH_2O$, the Li^+ ions are located in the hydroxide layers and the anions (*e.g.* Cl^-, Br^-, NO_3^-, etc.) intercalate into the interlayer region (**Figure 1-4**).[55-60] Novel M-Al LDHs ($[MAl_4(OH)_{12}](NO_3)_2\cdot mH_2O$; M = Co^{2+}, Ni^{2+}, Cu^{2+}, Zn^{2+}) or even ternary complexes have also been reported.[59-67] In these cases, the M^{2+} ions only occupy half of the vacancies, resulting in a M^{2+}/Al^{3+} ratio of 1 : 4 (**Figure 1-5**). Recently, bayerite-derived LDHs with a M^{2+}/Al^{3+} ratio of 1 : 3 were reported by Kamath and coworkers.[68]

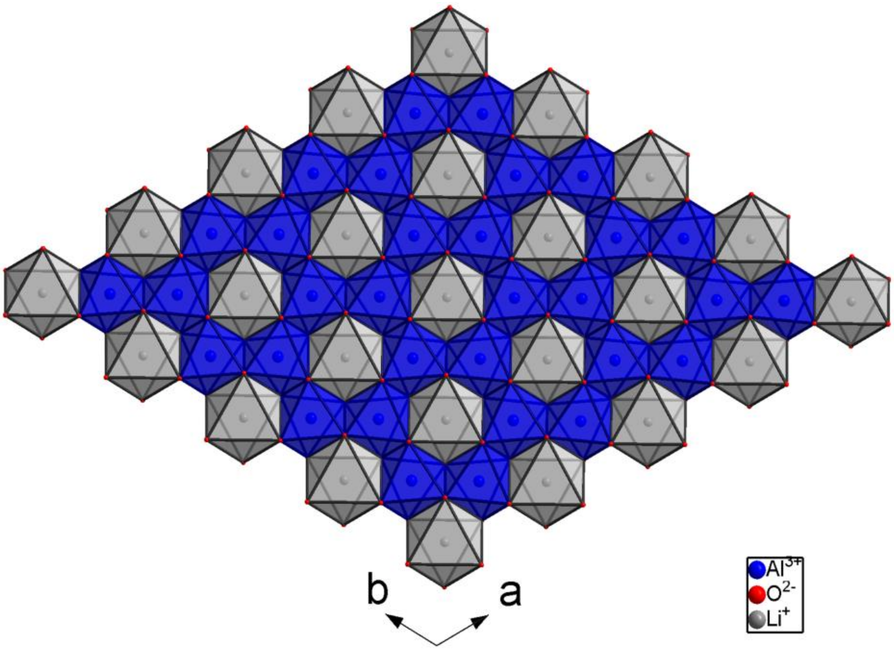

Figure 1-4: View along the *c*-axis of a Li-Al LDH, $[LiAl_2(OH)_6]Cl\cdot mH_2O$. Blue octahedra are Al^{3+} centred, grey are Li^{+} centred.

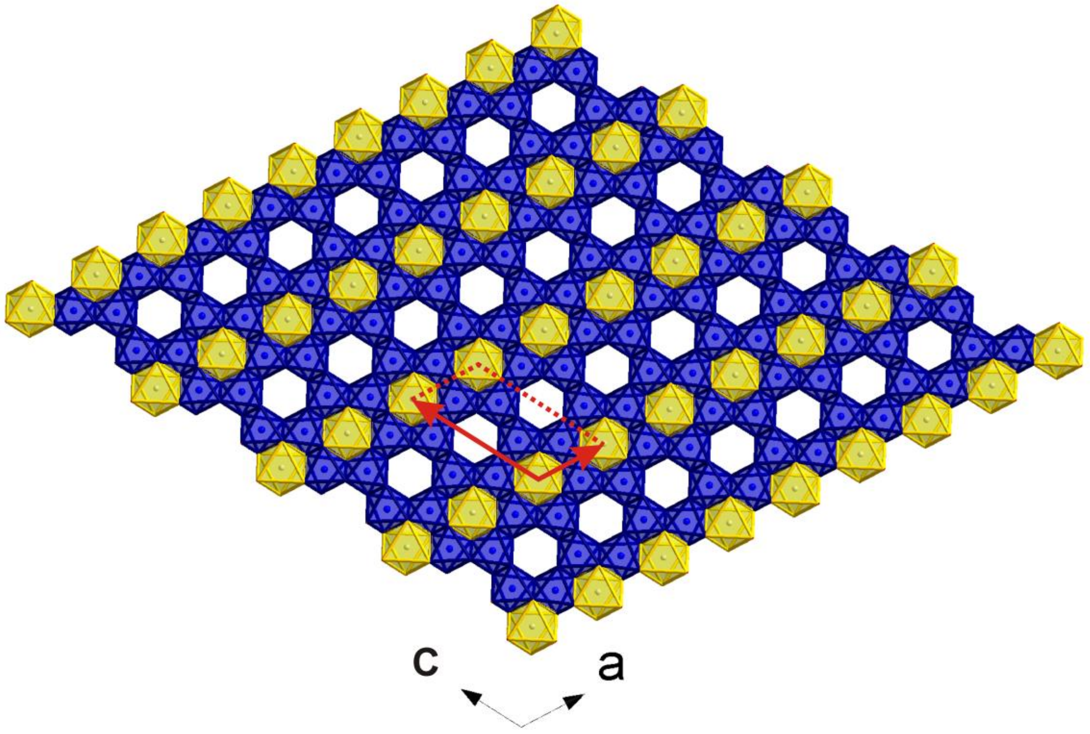

Figure 1-5: View along the *b*-axis of a Zn-Al LDH, $[ZnAl_4(OH)_{12}](NO_3)_2\cdot mH_2O$. Blue octahedra are Al^{3+} centred, yellow are Zn^{2+} centred. The red parallelogram represents the unit cell.

1.2.2. Composition of the interlayer gallery

The interlayer galleries of LDHs contain both water molecules and charge-balancing anions. Although carbonate, sulphate and nitrate are most commonly found in natural minerals, there seems to be no limitation as to the nature of the anions that can be intercalated, providing they do not abstract the metal ions from the hydroxide layer, and they have a sufficient charge density in one cross section, *i.e.*, not much less than 3.0 e/nm^2.[69] The reported anions can range from common inorganic ions, such as halides (X^-), CO_3^{2-}, NO_3^-, OH^-, SO_4^{2-}, HPO_4^{2-}, $H_2PO_4^-$, $P_2O_7^{2-}$, borate and tetraborate, ClO_4^-, MnO_4^-, CrO_4^{2-}, $Cr_2O_7^{2-}$, MoO_4^{2-}, silicate anions, and C_{60} derivatives,[58, 70-76] to organic ions, such as carboxylates, dicarboxylates, benzenecarboxylates, alkylsulfates, alkanesulfonates, chlorocinnamates, *t*-butanoate anion, glycolate, glycerolate, and organic dyes,[77-81] to polymeric and biochemical anions.[30, 82-88]

It is an inevitable outcome of ordered hydroxide layers that the positions and orientations of the interlayer ions should be ordered.[89] The position of anions can obviously be influenced by the distribution of cations and the stacking arrangement of the hydroxide layers due to effect of these parameters on electrostatic effects and hydrogen bonding.[90] It has been suggested that charge compensation for the anions in the interlayer space is achieved by resonance effects: every anion has to satisfy positive excess charges on the faces of the octahedral layers that sandwich it. These octahedral layers, on the other hand, are electronically satisfied from two neighbouring anion-bearing interlayers.[91] Water molecules fill up the interstices, sometimes expanding the interlayer space by hydrating the anions.[92]

Figure 1-6 shows the possible positions for CO_3^{2-} ions in the interlayer space. It

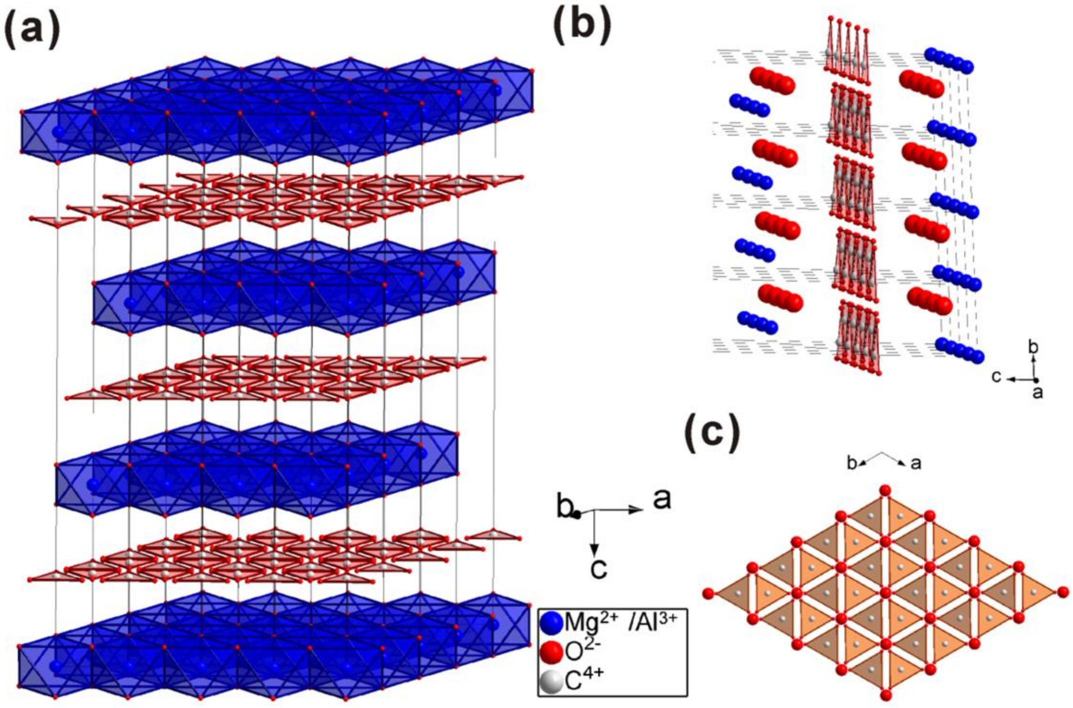

Figure 1-6: Positions of carbonate ions in hydrotalcite. Orange triangles are possible carbonate positions. (a) 3D view (the hydrogen atoms are removed for clarity) and view along (b) the *a*-axis (slightly oblique) and (c) the *c*-axis of the relative positions of carbonates and their closest oxygen and metal ions.

has been proved that CO_3^{2-} ions in the interlayers adopt a position where the C atoms are on the threefold axes of the small $R\bar{3}m$ cells and their planes are parallel to the (001) crystal plane.[93] Other triangular planar anions like NO_3^- adopt similar arrangements.[94] However, tetrahedral anions like SO_4^{2-} have two ways of orientating with the fourfold axis or threefold axis parallel to the (001) crystal plane,[90, 95] the latter being more preferred. **Figure 1-7** shows the possible positions for SO_4^{2-} ions with the threefold axis parallel to the (001) crystal plane in the interlayer space. For large halogen anions, such as Cl^-, Br^-, I^-, the interlayer space is expanded to achieve stability. Organic anions sometimes have several orientations and arrangements, which give different interlayer distances and lattice constants *c*. After extensive investigation on the intercalation of LDHs, a wide variety of anions have been intercalated and the interlayer space can range from 3 Å to over 20 Å.

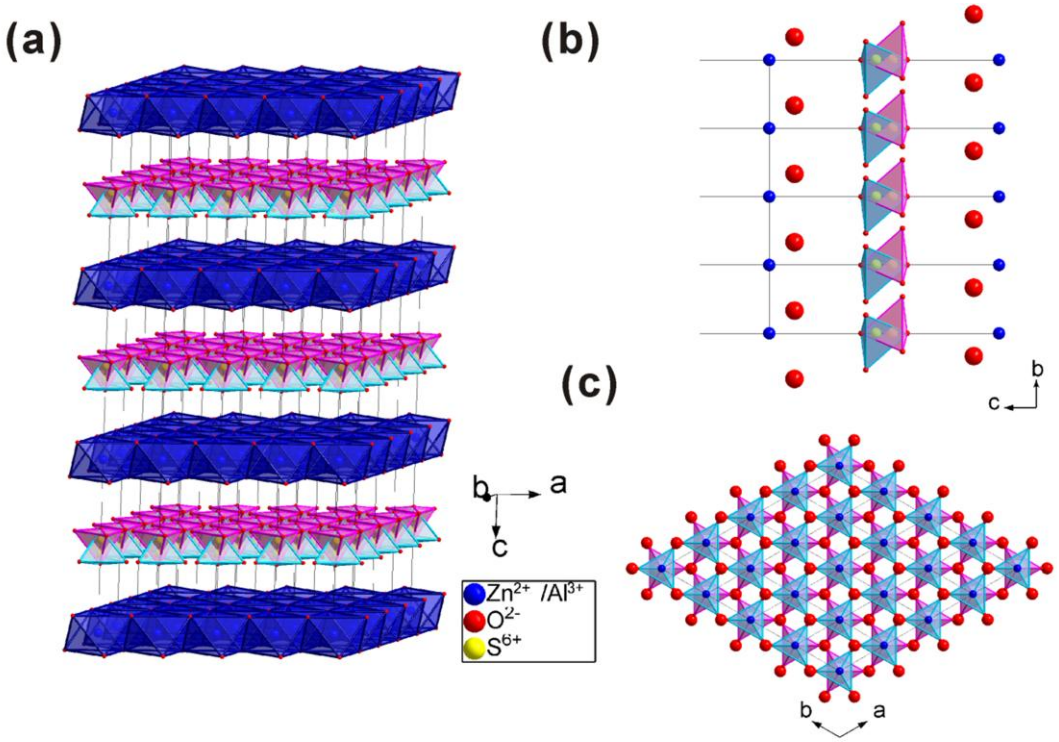

Figure 1-7: Positions of sulphate ions in the Zn-Al LDH, $Zn_{0.625}Al_{0.375}(OH)_2(SO_4)_{0.188}$. Pink and blue tetrahedra are possible positions of sulphate ions. (a) 3D view (the hydrogen atoms are removed for clarity) and view along (b) the *a*-axis and (c) the *c*-axis of the relative position of sulphates and their closest oxygen and metal ions.

1.2.3. Stacking sequences

The brucite-like layers in LDHs may stack to form two polymorphic crystal structures: a rhombohedral sequence (usually indicated as 3R) or a hexagonal sequence (2H). This was first discovered in natural minerals, such as the Mg-Al LDHs: hydrotalcite adopts a rhombohedral stacking sequence, while the related quintinite has a hexagonal sequence. Similarly for the Mg-Fe LDHs (Mg/Fe = 3), pyroaurite has a rhombohedral stacking sequence, while sjögrenite has a hexagonal sequence.[41, 89, 96, 97]

The essential difference between the rhombohedral sequence (3R) and hexagonal sequence (2H) is that the stacking order results in different orientations of the hydroxide layers and therefore different topologies. If upper case symbols A, B and C represent the hydroxyl ion positions, and lower case symbols *m* and *a* represent the positions for metal ions and interlayer cations, the rhombohedral stacking sequence can be expressed as A*m*B *a* B*m*C *a* C*m*A *a* A*m*B…, while the hexagonal stacking sequence is A*m*B *a* B*m*A *a* A*m*B…(**Figure 1-8**).

The two different polytypes can be seen as the hydroxide layers stack one above another with different stacking vectors. The 3R sequence can be simulated by a predefined brucite-like layer (A*m*B) and a stacking vector (2/3, 1/3, 1/3), while the 2H sequence can be simulated by two predefined layers (A*m*B B*m*A) and a stacking vector (0, 0, 1/2). In fact, the crystal structures of LDHs do not contain perfectly stacked hydroxide layers but also contain stacking faults and turbostratic disorder. These can be expressed by the use of more than one stacking vector with predetermined probabilities

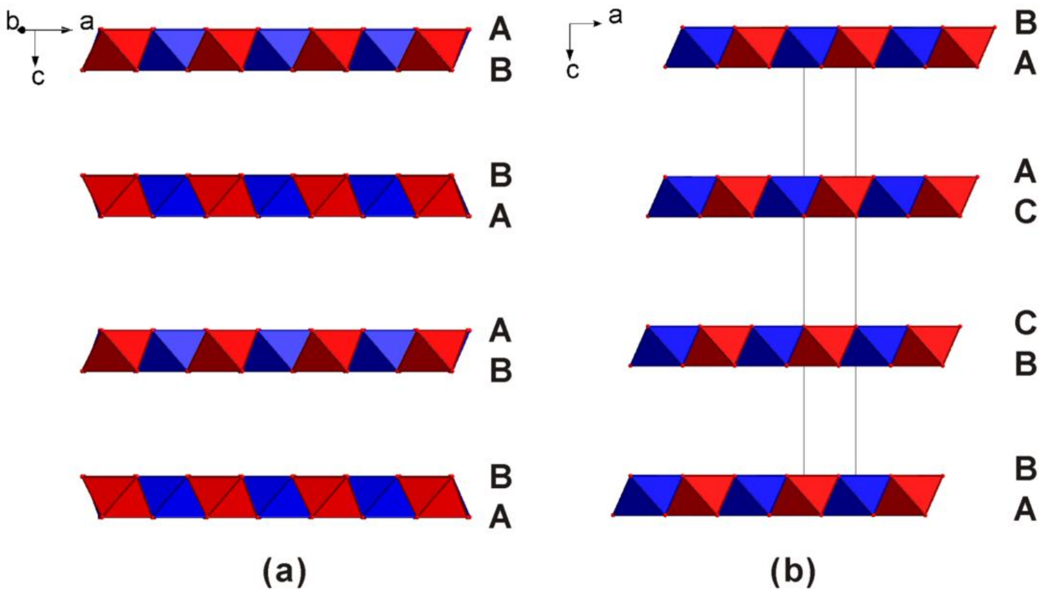

Figure 1-8: Schematic structures of Mg-Al LDHs with (a) a hexagonal sequence (quintinite) and (b) a rhombohedral sequence (hydrotalcite). Red octahedra are Al^{3+} centred, blue are Mg^{2+} centred.

and a stacking vector incorporating a random translation (*x*, *y*, 1/3) or (*x*, *y*, 1/2) (*x*, *y*: random) to introduce turbostratic disorder.

The programme DIFFaX,[98] which is a Fortran based code, has been used to simulate powder X-ray diffraction patterns of LDHs[99-105] and other layered materials.[106-108] The ideal powder XRD pattern would be given by an ideal crystal within which atoms are arranged in a regular repeating pattern over large distances compared to atomic size. However, there are inevitably stacking faults and disorder in real crystals. The simulation of powder XRD patterns using DIFFaX allow varying factors which may have influences on the powder XRD patterns including the number of layers, size of particles, stacking faults and other defects within the crystal. Detailed simulations and discussions about powder XRD patterns using DIFFaX can be found in **Chapter 6**.

1.3. Synthesis of LDHs

LDHs were first discovered as naturally existing minerals, and a wide range of examples have so far been discovered (**Table 1-3**).[109] In the laboratory, a number of synthetic techniques have been successfully employed in the preparation of LDHs. The most common method is co-precipitation, and various refinements of this method have been applied to the synthesis of many LDHs, allowing design and tuning to meet various requirements. Other methods include hydrothermal reaction, the salt-oxide and salt-hydroxide synthesis, sol-gel method, *etc*. More recently, size control and morphology control of these materials have been extensively studied since it has been suggested that particles with uniform sizes or particular morphologies have extremely interesting properties in specific applications.

Table 1-3: Examples of naturally existing LDH minerals.

Name	Chemical composition	Space Group	a (Å)	*c* (Å)
Hydrotalcite	$Mg_6Al_2(CO_3)(OH)_{16}\cdot 4H_2O$	$R\,\bar{3}m$	6.130	46.15
Manasseite	$Mg_6Al_2(CO_3)(OH)_{16}\cdot 4H_2O$	$P\,6_3/mmc$	6.120	15.32
Pyroaurite	$Mg_6Fe_2(CO_3)(OH)_{16}\cdot 4H_2O$	$R\,\bar{3}m$	6.190	46.54
Sjögrenite	$Mg_6Fe_2(CO_3)(OH)_{16}\cdot 4H_2O$	$P\,6_3/mmc$	3.113	15.61
Stichtite	$Mg_6Cr_2(CO_3)(OH)_{16}\cdot 4H_2O$	$R\,\bar{3}m$	6.180	46.38
Barbertonite	$Mg_6Cr_2(CO_3)(OH)_{16}\cdot 4H_2O$	$P\,6_3/mmc$	6.170	15.52
Woodallite	$Mg_6Cr_2(OH)_{16}Cl_2\cdot 4H_2O$	$R\,\bar{3}m$	3.103	24.11
Desautelsite	$Mg_6Mn_2(CO_3)(OH)_{16}\cdot 4H_2O$	$R\,\bar{3}m$	6.230	46.78
Droninoite	$Ni_3FeCl(OH)_8\cdot 2H_2O$	$R\,\bar{3}m$	6.206	46.18
Zaccagnaite	$Zn_4Al_2(OH)_{12}(CO_3)\cdot 3H_2O$	$P\,6_3/mmc$	3.073	15.11
Iowaite	$Mg_4Fe(OH)_8(OCl)\cdot 2-4H_2O$	$R\,\bar{3}m$	3.119	24.52
Hydrocalumite	$Ca_2Al(OH)_6[Cl_{1-x}(OH)_x]\cdot 3H_2O$	$P\,2_1$	9.600	11.40
Kuzelite	$Ca_4Al_{2.4}(OH)_{12.8}(SO_4)\cdot 6H_2O$	$R\,3$	5.760	53.66

1.3.1. Co-precipitation

As stated above, co-precipitation is arguably the most widely used method to prepare LDH materials. It generally involves the mixing of a basic solution and a solution of mixed metal salts, initiating the nucleation process, followed by the crystal growth process. To ensure that two or more cations precipitate simultaneously, it is vital that this is conducted under conditions of supersaturation. This can be ensured by maintaining a pH at a value higher than or equal to that at which the most soluble hydroxide forms. Considering the mixing, there are two different variants:[110] high supersaturation,[111-113] and low supersaturation.[79, 114, 115] Mixing at high supersaturation involves adding the solution of metal salts directly to the basic solution at a slow, constant rate, whereby the pH varies during the process and is referred to as the variable-pH method. Conversely, mixing at low supersaturation, the constant-pH method, involves adding the metal salt and basic solutions separately but simultaneously to a third solution containing a high concentration of the intended interlayer anion under constant pH.

The co-precipitation method has many advantages, such as the ease of scaling up for industrial production and cheap manufacturing costs. A wide variety of anions can be used, for example chloride, nitrate and other organic anions, but not usually sulphate and phosphate due to the prompt formation of insoluble salts.

In the variable-pH method, the metal cations are released under high supersaturation and form nuclei readily, which results in less crystalline products. Due to the continuously changing pH and ion concentration, the M^{2+}/M^{3+} ratio and the interlayer cations are often uncontrollable. An additional side effect is the formation of $M(OH)_2/M(OH)_3$ impurities. A secondary thermal treatment is usually carried out to improve the product crystallinity. Most LDHs can be prepared using this method, including MgAl-CO_3,[3, 114] CoAl-CO_3 and NiAl-CO_3,[116] MgFe-CO_3,[117] and some ternary compounds.[117] Zhao *et al.* reported a refined method whereby separation of the nucleation and aging steps prepares Mg-Al LDH with uniform crystallite size.[116, 118]

In contrast to the variable-pH method, co-precipitation at constant pH offers a relatively stable environment so that the M^{2+}/M^{3+} ratio can be controlled precisely.[107, 108] More crystalline products can be obtained as the rate of crystal growth is higher than the rate of nucleation. The use of an auto-titrator simplifies the synthesis process by monitoring and adjusting the pH automatically. Since metal hydroxides precipitate at different pH, the pH of the basic solution is chosen according to the metal combination. Bravo-Suárez *et al.*[119] reported the pH ranges over which some LDHs may be stable using thermodynamic calculations (**Table 1-4**).[120]

To avoid massive supersaturation around the mixing region, homogeneous

Table 1-4: pH ranges over which selected LDHs may be stable as a suspension in water. (Data is collected from reference 120)

LDHs	pH Range	
	Low Limit	High Limit
$[Zn_{1-x}Cr_x(OH)_2](Cl^-)_{x/n}$	4.5	10.0
$[Ni_{1-x}Al_x(OH)_2](CO_3^{2-})_{x/n}$	5.0	10.0
$[Ni_{1-x}Cr_x(OH)_2](Cl^-)_{x/n}$	5.5	11.5
$[Zn_{1-x}Al_x(OH)_2](Cl^-)_{x/n}$	6.0	10.0
$[Co_{1-x}Fe_x(OH)_2](Cl^-)_{x/n}$	7.5	10.5
$[Mg_{1-x}Al_x(OH)_2](Cl^-)_{x/n}$	8.0	10.5

precipitation has been exploited for LDH synthesis. The slow hydrolysis of urea (**Figure 1-9**) proceeds in two steps, the formation of ammonium cyanate, and subsequent hydrolysis of the cyanate to base (ammonia) and carbonate.[121] The hydrolysis reaction results in a solution with pH of approximately 9. Additionally, the hydrolysis rate and pH may be controlled by adjusting the temperature, and hence can be tailored to suit the conditions required for precipitating different metal hydroxide species. Since the ammonium is released *in situ* the nucleation rate is relatively low, and this method offers optimum conditions to form euhedral and large crystals.[122] First reported in the synthesis of M^{2+}-Al-carbonate LDHs (M = Mg^{2+}, Zn^{2+}, Ni^{2+}) by Costantino *et al.*,[123] this homogenous method has been applied to synthesise a great number of LDHs, such as

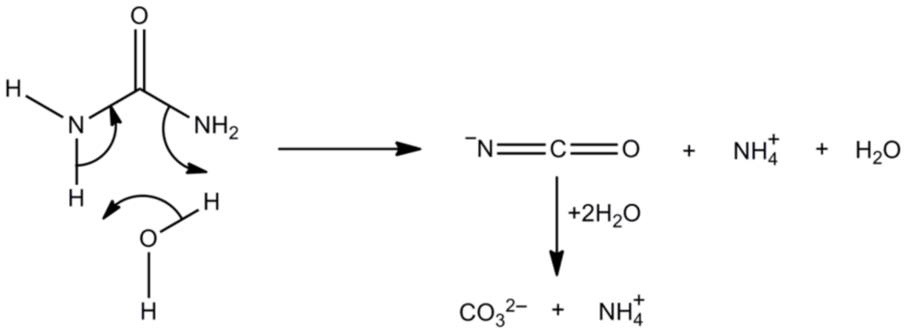

Figure 1-9: The hydrolysis of urea.

Co-Al,[124-127] Ni-Al [128] and Ni-Fe LDHs.[129, 130] The hydrolysis of urea (**Figure 1-9**) generates carbonate, an ion with high affinity for LDHs, with the result that LDHs prepared using this method usually incorporating carbonate. The use of another reagent, hexamethylenetetramine (HMT), provides the possibility of synthesising LDHs intercalated with other ions, since the formaldehyde released from hydrolysis of HMT is neutral and usually not easy to intercalate.[131] The products synthesised by those homogeneous precipitation routes usually adopt a hexagonal platelet morphology with evenly distributed size.

Several modifications to the co-precipitation method have been introduced to optimize the synthesis. One comprises separating the nucleation and aging steps, reported by Zhao *et al.*[118] This method involves a very rapid mixing and nucleation process in a colloid mill, and a separate aging process. Compared to conventional co-precipitation, the as-prepared products fall in a very narrow size distribution range. While the conventional homogeneous precipitation method is not suitable for Cu^{2+} or Cr^{3+} containing LDHs,[123] this separation method has been successfully applied in the synthesis of Cu^{2+} containing LDHs.[132, 133]

Although the majority of precipitation reactions are carried out in aqueous solution, mixed alkoxide/inorganic anion intercalated LDH materials can be obtained by introducing organic solvents into the solution.[134] A further amendment to this method is the use of reverse microemulsions, which can be described as co-precipitation within reverse micelles. The reverse microemulsions usually consist of three components: a surfactant and two immiscible solvents (details are given in **Chapter 3**). Typically, a water/sodium dodecyl sulphate/isooctane system is applied to the synthesis of Mg/Al LDHs.[135-141] Co-precipitations using other alcohols or templates to adjust particle size and morphology have also been developed.[69, 142]

1.3.2. Other conventional synthesis methods

Although co-precipitation is most widely used, various other methods, including ion-exchange,[30, 143-151] hydrothermal,[152] reconstruction method,[153-160] salt-oxides/hydroxides,[48, 49, 58-60, 63, 65, 161-164] oxidation,[165-167] and solid state method,[168] are also used in the synthesis of some LDHs with specific advantages.

The ion-exchange and secondary ion-exchange methods are especially useful for preparing LDHs intercalated with large organic anions, which cannot be directly synthesised by co-precipitation. Typically, in an environment containing a great excess of the target anions, the original anions in the host LDHs are substituted by the target anions through anion exchange. In the same way, the secondary ion-exchange method is used to ensure very large anions or low charge guests can be incorporated into small basal-spaced host materials. For example, using dodecyl sulphate to pre-pillar an LDH, C_{60} can be introduced into the interlayer space.[169]

For guest ions with particularly low affinity for LDHs, a hydrothermal method is suitable. Typically, this is performed using insoluble hydroxides (*e.g.* magnesium and aluminium hydroxides) as inorganic sources to ensure no other competing anions are present.

The reconstruction method was designed for the intercalation of guest ions with low LDH-affinity or those that are unstable in an alkaline environment. In practice, an LDH host containing carbonate or Cl^- is readily synthesised using the co-precipitation method. The host was then calcined to the metal oxides by heating to over 800 °C, followed by rehydration and reconstruction treatment in a solution containing target guest molecules. This method can be used for most LDHs with common metal combinations, and has been frequently used for the intercalation of aromatic molecular anions[159] or voluminous organic species.[160]

Reactions between salts and Al hydroxides are mostly used to synthesise Li-Al LDHs, and were first reported in 1985 by Sissoko.[170] Gibbsite or bayerite (both polymorphs of $Al(OH)_3$) react directly with a 4-fold molar excess of a lithium salt (*e.g.* LiCl, LiBr, $LiNO_3$) to form Li-Al LDHs.[58-60] The use of different polymorphs of $Al(OH)_3$ results in LDHs with differing layer stacking sequences. Mechanistic and kinetic studies of such reactions using *in situ* X-ray diffraction studies have been investigated by Williams and O'Hare.[48, 171, 172] This salt/hydroxide method has been extended to other M-Al LDHs ($[MAl_4(OH)_{12}](NO_3)_2 \cdot mH_2O$; M = Co^{2+}, Ni^{2+}, Cu^{2+}, Zn^{2+}) and ternary compounds.[59-67, 173]

The 'salt-oxide' method was first reported by Boehm *et al.* for the Zn-Cr LDH, which was difficult to obtain using co-precipitation.[78] This method, usually described as a heterogeneous reaction of a divalent metal oxide with a trivalent metal salt solution, has become a common method for the synthesis of a number of LDHs[174] and monometallic hydroxides,[175, 176] especially for those containing Cu^{2+} and Cr^{3+}.[177, 178]

Various LDHs containing transition metal ions can be prepared by oxidising brucite-like M^{2+}-M'^{2+} hydroxide precursors. The oxidation agents can be selected from air, oxygen, perchloric acid, peroxide or Br_2.[165-167] Zeng *et al.* have produced Co^{2+}-Co^{3+}, Mg^{2+}-Co^{2+}-Co^{3+}, and Co^{2+}-Co^{3+}-Al^{3+} LDHs using this method.[179-183] Delmas *et al.* prepared Ni^{2+}-Co^{3+} LDH by oxidising Co^{2+} to Co^{3+} with perchloric acid or peroxide.[40] Rives *et al.* also prepared Mg^{2+}-Mn^{3+} LDH by oxidising Mn^{2+} to Mn^{3+} in the solid state.[184] Also, Co^{2+}-Ni^{3+} and Co^{2+}-Fe^{3+} LDHs were prepared by using bromine to oxidise Ni^{2+} and Fe^{2+} to Ni^{3+} and Fe^{3+}, reported by Ma *et al.*[165-167]

Post-preparative treatments are carried out for LDHs with poor crystallinity. These include hydrothermal,[185, 186] and microwave treatments,[187, 188] where the precipitate is at or often above ambient temperature.

1.3.3. Particle size control

Along with the increasing applications of LDH materials in the fields of pharmacy, medicine, and biology, meeting the demand for LDH nanoparticles with controlled size is becoming a new challenge for scientists. As early as the 1990s, attempts to control particle size by adjusting the synthesis conditions were made by Albiston.[189] After mixing $Al(NO_3)_3$ solution with MgO slurry, the mixture was filtered, washed, and aged at different temperatures and times, resulting in MgAl-NO_3 LDH hexagonal platelets with average diameters of approximately 60 nm, 80 nm, 170 nm, 400 nm, and 770nm. Although the particle sizes were not controlled precisely, a separate-aging method was developed (**Figure 1-10**), by Zhao *et al.* [118] By separating the two steps of crystallisation - nucleation and aging - relatively accurate control of particle size can be achieved. Uniform particles with diameters of 60 - 80 nm were obtained. Xu *et al.* further investigated the influences of aging temperature and time on particle size, extending this method from Mg-Al to Ni-Al, Co-Al, and Fe containing LDHs.[116, 190] Since then, LDH nanomaterials with different particle sizes have been extensively used in biomedical fields such as fluorescent labelling,[27] drug delivery,[26] and targeted cellular uptake.[29]

However, the particle sizes were only adjustable above 100 nm when separating the nucleation and aging steps.[191] For particles smaller than 100 nm, particularly those smaller than 10 nm, the conventional top-down synthesis is not applicable; thus, new

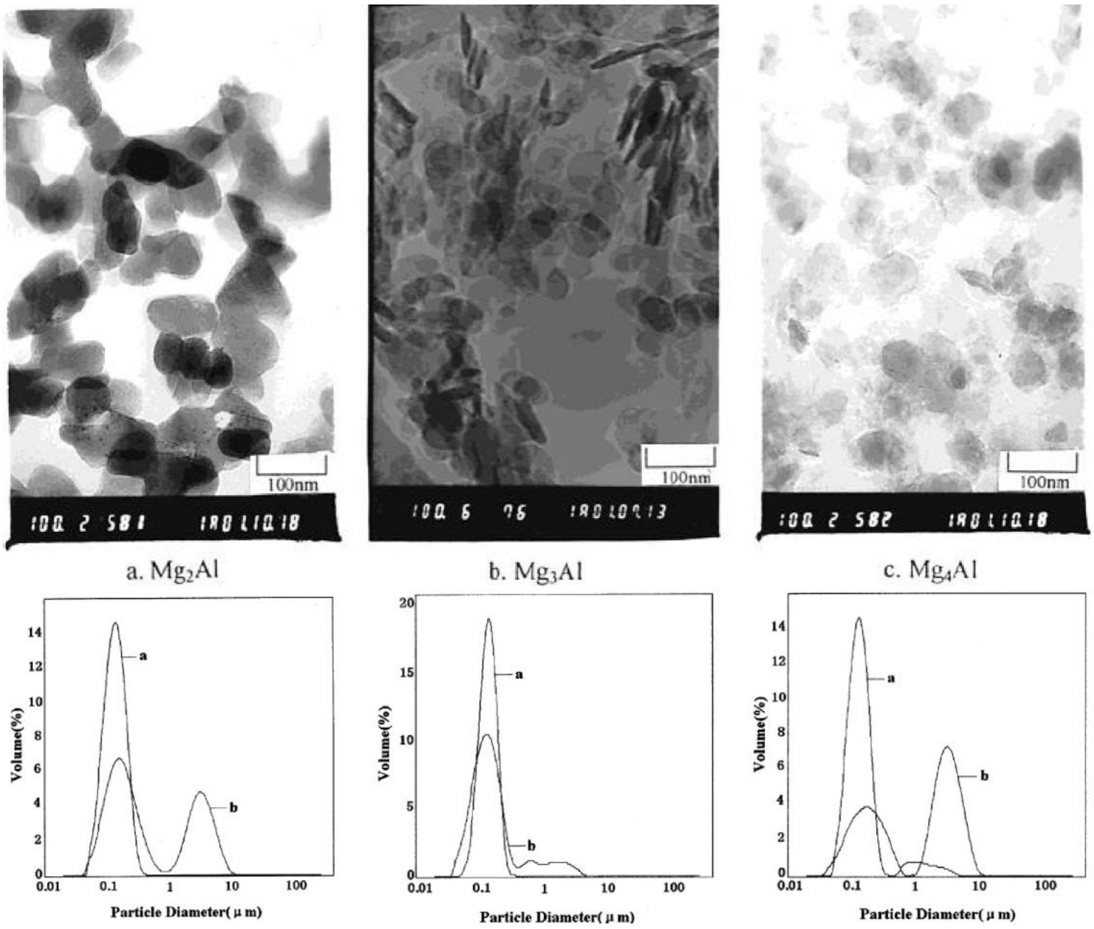

a. Mg_2Al

b. Mg_3Al

c. Mg_4Al

Figure 1-10: TEM micrographs and profiles of the particle diameter distribution for MgAl-CO_3 LDHs with different Mg^{2+}/Al^{3+} ratios. (Images are reprinted with the permission from reference 118. Copyright © 2002 American Chemical Society.)

bottom-up methods were developed, typically using the reverse microemulsion method first reported by Hu *et al.* (**Figure 1-11**).[135, 136] Using isooctane as an organic phase and sodium dodecyl sulphate (DDS) as a surfactant in a system containing only a small amount of aqueous solution, reverse micelles appear like "water pools" encapsulated by surfactant. LDH nanoparticles crystallise within the "water pool" with diameters of 44 - 59 nm and thicknesses of 15 - 130 nm (**Figure 1-12**). The particle sizes were

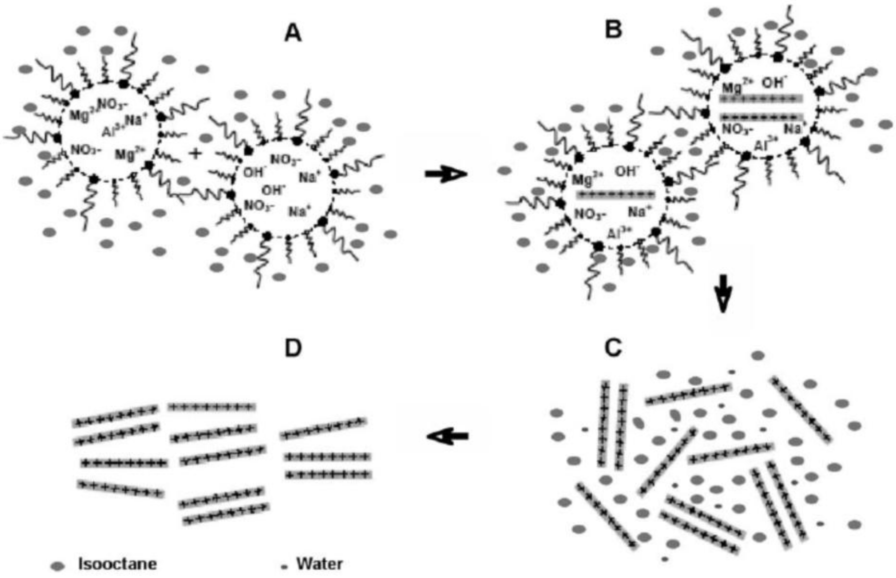

Figure 1-11: Schematic illustration of the synthesis of LDH particles in reverse microemulsions. (Images are reprinted with the permission from reference 135. Copyright © 2007 Royal Society of Chemistry.)

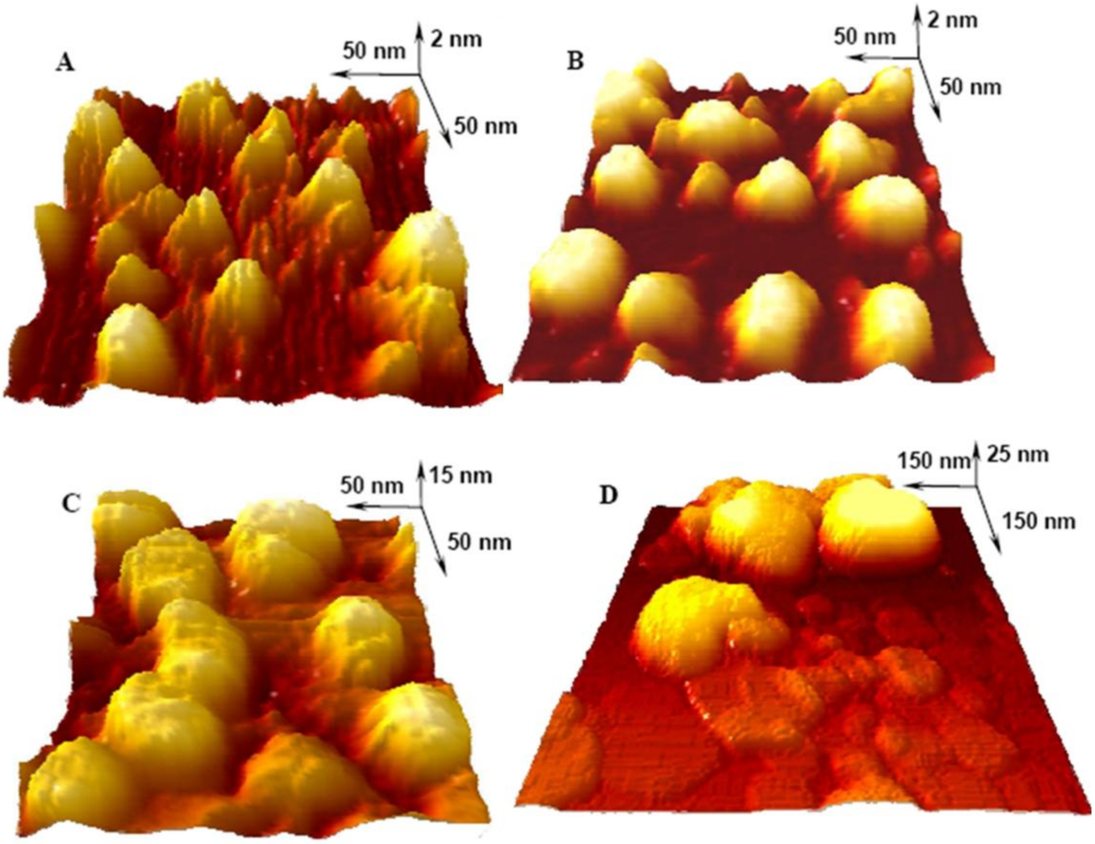

Figure 1-12: 3-dimensional AFM images of illustrative samples of Mg-Al LDH nanoparticles synthesised in reverse microemulsions. (Images are reprinted with the permission from reference 136. Copyright © 2005 American Chemical Society.)

controllable by adjusting the water to surfactant ratio. Although this method has several disadvantages, such as high cost and lack of flexibility, the reverse microemulsion method has been successfully applied to the synthesis of Co-Al, Ni-Al and Fe-containing LDHs.[137-141] To meet the requirements for an industrial process, further optimisation of this method is necessary to overcome those issues.

1.3.4. Morphology control

LDH particles typically show preferential growth perpendicular to the *c*-axis direction and a hexagonal platelet morphology. However, many efforts have been made to synthesise LDHs with unusual nanostructures, such as flowers, rods, and spheres. Under the presence of the surfactant sodium dodecyl sulphate, flower-like LDH spheres are easily obtained.[144, 192-195] Using a facile biopolymer-assisted approach in the presence of sodium alginate biopolymer under hydrothermal conditions, three-dimensional Ni-Al LDH nanostructures have been successfully synthesised with different shapes, including pompom-like, marigold-like, and coral-like.[128] For spherical LDH structures, besides the methods involving soft templates such as surfactants, hard templates involving negatively charged spheres were also introduced to assist assembling spheres composed of LDH nanoshells *via* layer-by-layer assembly. Polystyrene (PS) beads,[36, 196] sulfonated polystyrene-divinylbenzene (DVB) cation-exchange resin beads,[197] carbon nanospheres (CNS),[198] and other inorganic nanospheres[199] have been used. Compared with the soft template approach, the hard template route has the advantage of facile size control[200] and shape direction by functional groups on the template surface.[201] Depending on the assembling direction of the LDH nanosheets, the hollow spheres can be divided into two main groups, as flower-like (edge-on) or raspberry-like (face-on) (**Figure 1-13**).[36]

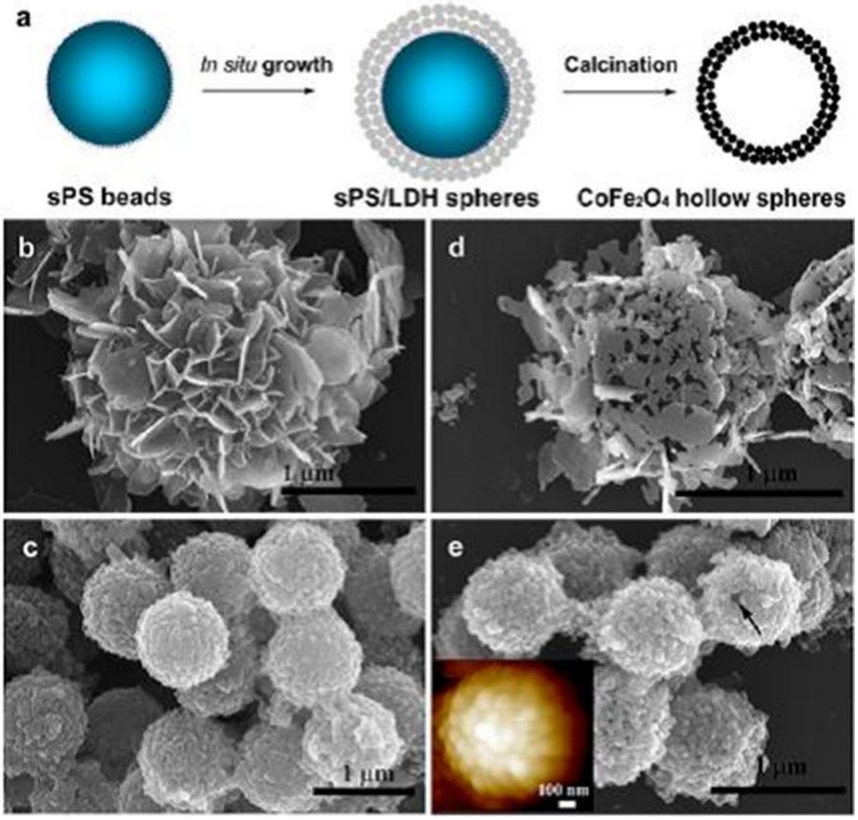

Figure 1-13: (a) Schematic illustration of the $Co^{2+}Fe^{2+}Fe^{3+}$-LDH spherical shell formed on sPS beads and the product after its calcination in air. SEM images of (b) the flower-like sPS/$Co^{2+}Fe^{2+}Fe^{3+}$-LDH spheres, (c) the raspberry-like sPS/$Co^{2+}Fe^{2+}Fe^{3+}$-LDH spheres, (d) $CoFe_2O_4$ porous spheres obtained by calcination of (b), and (e) $CoFe_2O_4$ hollow spheres obtained by calcination of (c). The inset of (e) shows an AFM image. (Images are reprinted with the permission from reference 36. Copyright © 2011 Elsevier.)

Although many efforts have been made, LDH particles with one dimensional nanostructures are rarely seen. There are two main synthesis schemes for LDH nanorods or nanowires. By adjusting the temperature and aging time, Mg-Al,[144] Zn-Al[142] (**Figure 1-14**), and Cu-Co LDH[202] nanorods were successfully synthesised. On the other hand, Mg-Al LDH nanowires,[136, 144] Zn-Al LDH nanorods,[203] Ni-Al LDH nanorods and tubes,[141] and Zn-Co-Fe LDH nanowires[137] have been synthesised using soft assisted templates formed by polymers or surfactants.

Other novel control syntheses have been explored, such as a spray drying method to make LDH microspheres,[204] delamination to obtain LDH nanocomposites,[205] and a microwave method to synthesise LDH nanocones.[206]

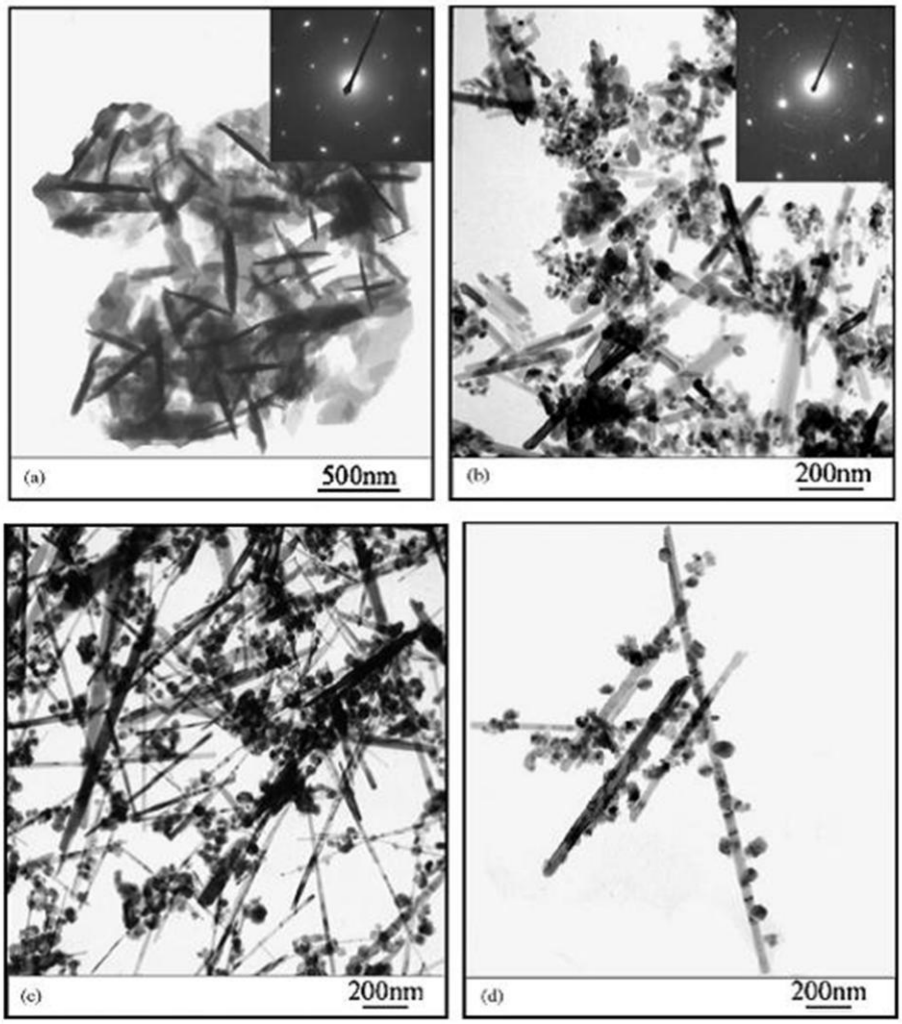

Figure 1-14: TEM images of Zn-Al LDH nanorods. (Images are reprinted with the permission from reference 142. Copyright © 2009 Elsevier.)

1.4. Characterisation of LDHs

1.4.1. Powder X-ray diffraction

Powder X-ray diffraction is the quickest method for the identification of LDH structures. As discussed in **Section 1.2**, LDH materials mostly adopt a rhombohedral or hexagonal lattice system; rhombohedral polytypes can be considered to be based on a triple hexagonal unit cell (**Figure 1-15**). **Equation 1-1** is used to index the XRD patterns of rhombohedral or hexagonal structures.

$$\frac{1}{d^2} = \frac{4}{3}\frac{h^2 + hk + k^2}{a^2} + \frac{l^2}{c^2}$$

Equation 1-1

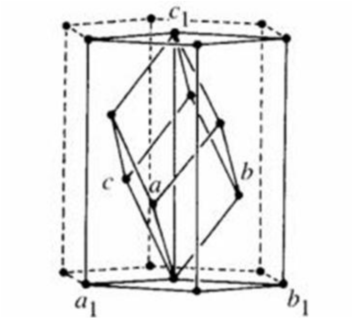

Figure 1-15: Relationship between the primitive rhombohedral cell with axes a, b, c and the triple hexagonal cell with axes a_1, b_1, c_1.

LDH materials all have a series of strong basal reflections which can be indexed as (00l). For a rhombohedral structure, they correspond to (003), (006), (009), … (00$\underline{3n}$) reflections, which can give the cell parameter $c = 3(d_{003}+2d_{006}+3d_{009}+\ldots+nd_{00\underline{3n}})/n$. For a hexagonal structure, they correspond to (002), (004), (006), … (00$\underline{2n}$) reflections, thus give the cell parameter $c = 2(d_{002}+2d_{004}+3d_{006}+\ldots+nd_{00\underline{2n}})/n$. Among the various non-basal reflections (hkl, either h or k is non-zero), the (110) reflection gives a direct measure of $a = b = 2d_{110}$. Other reflections such as (01l), (10l) and (11l) in the intermediate angle can be used to determine the stacking pattern of the layers, and different polytypes can be distinguished by the intensities of the non-basal reflections.[207]

The intensity of the reflections in an XRD pattern is determined by temperature, absorption, polarisation, and the crystal structure. LDHs with a rhombohedral structure (*e.g.* hydrotalcite) can be considered as a unit cell of Mg^{2+}/Al^{3+} (0, 0, 0) and O^{2-} (0, 0, 0.3771) repeating using vectors (*x*+2/3, *y*+1/3, *z*+1/3) and (*x*+1/3, *y*+2/3, *z*+2/3). Since the Mg^{2+} and Al^{3+} ions are randomly distributed within the hydroxide layers, an equivalent scattering factor f_M is used to represent the total scattering from them. Ignoring the interlayer molecules, the structure factor, F_{hkl}, can be calculated using the Miller indices (*h*, *k*, *l*) (**Equation 1-2**).

$$
\begin{aligned}
F_{hkl} &= \sum_{j=1}^{n} f_j e^{2\pi i(hx_j+ky_j+lz_j)} \\
&= f_M\left\{e^{2\pi i[0\cdot h+0\cdot k+0\cdot l]} + e^{2\pi i\left[\frac{2}{3}h+\frac{1}{3}k+\frac{1}{3}l\right]} + e^{2\pi i\left[\frac{1}{3}h+\frac{2}{3}k+\frac{2}{3}l\right]}\right\} \\
&+ f_O\left\{e^{2\pi i[0\cdot h+0\cdot k+0.3771\cdot l]} + e^{2\pi i\left[\frac{2}{3}h+\frac{1}{3}k+\left(0.3771+\frac{1}{3}\right)l\right]} + e^{2\pi i\left[\frac{1}{3}h+\frac{2}{3}k+\left(0.3771+\frac{2}{3}\right)l\right]}\right\} \\
&= \left[f_M + f_O e^{2\pi i\cdot 0.3771\cdot l}\right]\left\{1 + e^{2\pi i\left[\frac{2}{3}h+\frac{1}{3}k+\frac{1}{3}l\right]} + e^{2\pi i\left[\frac{1}{3}h+\frac{2}{3}k+\frac{2}{3}l\right]}\right\}
\end{aligned}
$$

Equation 1-2

When *h* = *k* = 0, **Equation 1-2** can be written as:

$$F_{hkl} = \left[f_M + f_O e^{2\pi i\cdot 0.3771\cdot l}\right]\left[1 + e^{2\pi i\cdot\frac{1}{3}l} + e^{2\pi i\cdot\frac{2}{3}l}\right]$$

Under the conditions that l = 3N + 1 or l = 3N + 2 (N = integer), $\left[1 + e^{2\pi i\cdot\frac{1}{3}l} + e^{2\pi i\cdot\frac{2}{3}l}\right] = 0$. Consequently, $F_{hkl} = 0$, which means the reflections will not appear. When l = 3N, the reflections appear. This explains the reason why only (003), (006), (009), … (00<u>3*n*</u>) reflections are present in the XRD patterns.

Similarly, when *h* = 0 and *k* = 1, **Equation 1-2** can be written as:

$$F_{hkl} = \left[f_M + f_O e^{2\pi i\cdot 0.3771\cdot l}\right]\left[1 + e^{2\pi i(\frac{1}{3}+\frac{1}{3}l)} + e^{2\pi i(\frac{2}{3}+\frac{2}{3}l)}\right]$$

The reflections only appear when *l* = 3N + 2, *i.e.* (012), (015), (018)….reflections.

When *h* = 0 and *k* = 1, **Equation 1-2** can be written as:

$$F_{hkl} = \left[f_M + f_O e^{2\pi i\cdot 0.3771\cdot l}\right]\left[1 + e^{2\pi i(1+\frac{1}{3}l)} + e^{2\pi i(1+\frac{2}{3}l)}\right]$$

The reflections only appear when *l* = 3N, *i.e.* (110), (113), (116)…

The structure of LDH with a hexagonal structure can be considered as a unit cell of Mg^{2+}/Al^{3+} (0, 0, 0) and O^{2-} (1/3, 2/3, 0.06566) repeating using vectors (*x*–*y*, *x*, 1/2+*z*), (*x*–*y*, –*y*, 1–*z*) and (–*y*, –*x*, 1/2–*z*). Similarly, the structure factor, *F*, can be calculated as **Equation 1-3**.

$$F_{hkl} = \sum_{j=1}^{n} f_j e^{2\pi i(hx_j+ky_j+lz_{j)}}$$

$$= f_M\left\{e^{2\pi i[0\cdot h+0\cdot k+0\cdot l]} + e^{2\pi i\left[0\cdot h+0\cdot k+\frac{1}{2}l\right]} + e^{2\pi i[0\cdot h+0\cdot k+0\cdot l]} + e^{2\pi i\left[0\cdot h+0\cdot k+\frac{1}{2}l\right]}\right\}$$

$$+ f_O\left\{e^{2\pi i\left[\frac{1}{3}h+\frac{2}{3}k+0.06566\cdot l\right]} + e^{2\pi i\left[\frac{1}{3}h+\frac{2}{3}k+\left(\frac{1}{2}-0.06566\right)\cdot l\right]} + e^{2\pi i\left[\frac{2}{3}h+\frac{1}{3}k+\left(\frac{1}{2}+0.06566\right)\cdot l\right]}\right.$$

$$\left. + e^{2\pi i\left[\frac{2}{3}h+\frac{1}{3}k+(1-0.06566)\cdot l\right]}\right\}$$

$$= f_M\left[2 + 2e^{\pi i l}\right] + f_O\left[e^{2\pi i\left(\frac{1}{3}h+\frac{2}{3}k\right)} + e^{2\pi i\left(\frac{2}{3}h+\frac{1}{3}k+\frac{1}{2}l\right)}\right]\left[e^{2\pi i\cdot 0.06566\cdot l} + e^{2\pi i\cdot\left(\frac{1}{2}-0.06566\right)\cdot l}\right]$$

Equation 1-3

When *h* = *k* = 0 and *l* = 2N+1 (N = integer), **Equation 1-3** can be calculated as:

$$F_{hkl} = f_M\left[2 + 2e^{\pi i}\right] + f_O\left[1 + e^{\pi i}\right]\left[e^{2\pi i\cdot 0.06566 l} + e^{2\pi i\cdot\left(\frac{1}{2}-0.06566\right)l}\right] = 0$$

As a result, these reflections do not appear, and only the (002), (004), (006), … (00<u>2*n*</u>) reflections can be observed.

Similarly, when h = 1, k = 1 and l = 2N+1, **Equation 1-3** can be written as:

$$F_{hkl} = f_M\left[2 + 2e^{2\pi i\cdot\frac{1}{2}l}\right] + f_O\left[e^{2\pi i} + e^{2\pi i\left(1+\frac{1}{2}l\right)}\right]\left[e^{2\pi i\cdot 0.06566l} + e^{2\pi i\cdot\left(\frac{1}{2}-0.06566\right)l}\right]$$

$$= f_M\left[2 + 2e^{\pi i}\right] + f_O\left[1 + e^{\pi i(2N+3)}\right]\left[e^{2\pi i\cdot 0.06566l} + e^{2\pi i\cdot\left(\frac{1}{2}-0.06566\right)l}\right] = 0$$

As a result, these reflections do not appear, and only (110), (112), (114), … (112*n*) reflections are observed. However, the reflections of (01*l*) all exist as there is no extinction condition.

1.4.2. Infrared spectroscopy

Infrared spectroscopy is a useful and powerful tool for the characterisation of LDH materials, which usually have absorptions from the M-O bonds, the hydroxyl groups, and the interlayer anions. In the hydroxide layers, according to the D_{3d} symmetry, the metal-centred octahedra have several possible vibrations, which fall in the fingerprint region.[208] However, due to the disordered cation distribution and the distortion of the lattices, not all predicted vibrations can be observed. For example, an aged Mg_2-Al LDH with well-distributed cations in the brucite-like sheet structure shows a sharp peak at 445 - 455 cm^{-1}, which is not visible for the freshly prepared material nor for a Mg_3-Al LDH with a less ordered structure.[94, 209] The broad band centred at *ca.* 3400 - 3500 cm^{-1} corresponds to a combination of the stretching vibration of the hydroxide groups in the brucite sheets and the interlayer water molecules (ν_{OH}). The bending vibration of interlayer water (δ_{H2O}) occurs at 1600 - 1650 cm^{-1}, giving a characteristic peak rarely overlapped by others.[210, 211] The absorption in the region 650 - 1000 cm^{-1} can be assigned to the bending vibrations of the hydroxyl groups in the brucite-like layers (δ_{OH}).

IR spectroscopy has great advantages for characterisation of the interlayer anions, since common inorganic anions and organic anions usually have distinctive absorptions. For example, the peaks at 1350 - 1380 cm^{-1} (ν_3), 850 - 880 cm^{-1} (ν_2), and 670 - 690 (ν_4) cm^{-1} are indicative of CO_3^{2-}, while for NO_3^-, the peak for ν_1 is at ~1380 cm^{-1}, ν_2 is at ~830 cm^{-1}, and ν_3 is at 720 - 750 cm^{-1}.[69]

1.4.3. UV-Vis spectroscopy

UV-Vis spectroscopy is used to characterise LDHs containing transition metals by analysing the *d*-*d* transitions of these ions.[212-218] In practise, UV-Vis spectra are usually recorded in diffuse reflectance spectrum mode. In LDH materials, the metal ions are located in the centre of the octahedra and are surrounded by six hydroxyls, similar to the corresponding hexa-aquo complexes. For metal ions having d^2 and d^7configurations, they have three spin-allowed *d*-*d* transitions (υ_1: $^4T_{1g}(F)$ - $^4T_{2g}$, υ_2: $^4T_{1g}(F)$ - $^4A_{2g}$, υ_3: $^4T_{1g}(F)$ - $^4T_{1g}$ (P)) for octahedral symmetry with high spin.[219] As an example, the υ_1 transition of Co^{2+} ions occurs as a broad absorbance around 8000 - 10000 cm^{-1} and the υ_3 transition is an intense absorbance centred at 19000 cm^{-1}. The υ_2 transition is usually weak and appears as a shoulder at around 16000 cm^{-1}.[138] Based on the transition energies in the spectrum, the crystal field strength value (Dq), in addition to the Racah parameters (B_{Oh}) and Dq/B for Co^{2+} ions can be calculated using **Equation 1-4**.

$$\mathrm{E}(\nu_1) = 5\mathrm{Dq} - 7.5\mathrm{B} + (225\mathrm{B}^2 + 100\mathrm{Dq}^2 + 180\mathrm{Dq} \times \mathrm{B})^{\frac{1}{2}}$$

$$\mathrm{E}(\nu_2) = 15\mathrm{Dq} - 7.5\mathrm{B} + (225\mathrm{B}^2 + 100\mathrm{Dq}^2 + 180\mathrm{Dq} \times \mathrm{B})^{\frac{1}{2}}$$

$$\mathrm{E}(\nu_3) = (225\mathrm{B}^2 + 100\mathrm{Dq}^2 + 180\mathrm{Dq} \times \mathrm{B})^{\frac{1}{2}}$$

$$\mathrm{Dq} = [\mathrm{E}(\nu_1) - \mathrm{E}(\nu_2)]/10$$

$$\mathrm{B} = [\,\mathrm{E}(\nu_2) + \mathrm{E}(\nu_3) - 3\mathrm{E}(\nu_1)]/15$$

Equation 1-4

The spectral transitions that occur for d^3 and d^8 ions in octahedral fields are υ_1: ${}^3A_{2g}(F)$ - ${}^3T_{2g}$, υ_2: ${}^3A_{2g}(F)$ - ${}^3T_{1g}$, υ_3: ${}^3A_{2g}(F)$ - ${}^3T_{1g}$ (P). For example, Ni^{2+} ions in an octahedral field have three spin-allowed transitions which generally fall within the range 7000 - 13000 cm^{-1} (υ_1), 11000 - 20000 cm^{-1}(υ_2), and 19000 - 27000 cm^{-1}(υ_3). The corresponding band energies for Ni^{2+} ions are related to the crystal field strength value Dq and the Racah parameters B_{Oh} through **Equation 1-5**.

$$\mathrm{E}(\nu_1) = 10\mathrm{Dq}$$

$$\mathrm{E}(\nu_2) = 15\mathrm{Dq} + 7.5\mathrm{B} - \frac{1}{2}(225\mathrm{B}^2 + 100\mathrm{Dq}^2 - 180\mathrm{Dq} \times \mathrm{B})^{\frac{1}{2}}$$

$$\mathrm{E}(\nu_3) = 15\mathrm{Dq} + 7.5\mathrm{B} + \frac{1}{2}(225\mathrm{B}^2 + 100\mathrm{Dq}^2 - 180\mathrm{Dq} \times \mathrm{B})^{\frac{1}{2}}$$

$$\mathrm{Dq} = \mathrm{E}(\nu_1)/10$$

$$\mathrm{B} = [\,\mathrm{E}(\nu_3) + \mathrm{E}(\nu_2) - 3\mathrm{E}(\nu_1)]/15$$

Equation 1-5

1.4.4. Elemental analysis

Elemental analysis is usually carried out through CHN analysis, ICP-mass spectrometry (ICP-MS) and EDX spectroscopy. These measurements provide the weight percentage of certain elements, and the combined results can give a nominal chemical formula of a LDH complex.

In a usual commercial CHN analysis, a sample is combusted to convert carbon, hydrogen, and nitrogen elements into CO_2, N_2, and H_2O, which are then separated on a column and quantified by thermal conductivity changes in helium carrier gas.

Inductively coupled plasma mass spectrometry (ICP-MS) and inductively coupled plasma optical emission spectrometry (ICP-OES) can be used to determine all the metal elements and some non-metal elements in LDHs. LDH samples need to be dissolved in nitric acid at very low concentration. The solution is pumped with carrier gas and ionized at very high temperature. Then a simultaneous ICP mass spectrometer or an optical spectrometer records the entire analytical spectrum and gives the concentration of elements through calibration with reference standards.

Energy-dispersive X-ray spectroscopy (EDX) is a device normally attached to a scanning electron microscopy (SEM) or a transmission electron microscopy (TEM) instrument. It determines the elements present by analysing the X-rays emitted by the matter in response to being irradiated with charged particles. Besides the elemental percentage, it can also give element distribution mapping.

1.4.5. Electron microscopy

Scanning Electron Microscopy (SEM) and Transmission Electron Microscopy (TEM) are the most common methods to investigate the morphology of nanoparticles since they are able to give a direct view of the macroscopic structure. Both of these techniques involve the use of an electron beam, but for TEM, images are obtained from the electrons transmitted through the ultra-thin specimen, while for SEM, images are mostly formed by collecting the secondary electrons that are ejected from the specimen as a result of the interactions of beam electrons with surface or near surface atoms of the specimen. SEM micrographs can reveal the three-dimensional surface structure of the specimen. TEM images at low magnification are also capable of showing the appearance of the nanoparticles, as different areas of the specimen have different thicknesses which results in different electron absorptions. Significantly higher resolution images are available from TEM; these can demonstrate the inner structure of a particle, such as lattice fringes, atoms, and crystal orientations. TEM can also provide diffraction pattern data of a single crystallite.

A range of information can be obtained from SEM and TEM characterisation of LDH materials, including the morphology, size distribution, and crystal structure of particles. Since LDH materials typically show preferential growth perpendicular to the *c*-axis direction,[114, 121, 220] in TEM and SEM images, they usually display a good dispersion of single or overlapping hexagonal platelets. Rare standing particles perpendicular to the TEM specimen grids provide good sites for close examination of the stacking layers, thus enabling the distance between the layers to be measured. With the use of surfactants, templates, or polymers, the morphology of LDH materials are becoming more and more varied and complicated. A combination of multiple characterisation methods, such as SEM, TEM and atomic force microscopy (AFM) (**Section 1.4.6**), is the most complete way to comprehensively investigate the morphology of LDHs.

1.4.6. Atomic force microscopy

Atomic Force Microscopy (AFM) is a high resolution scanning probe microscopy technique, which records images by “feeling” the sample surface with a sharp probe.[221] Materials with high electron beam sensitivity can be imaged without severe distortion using this technique. For LDH particles, AFM gives not only delicate stereographs but also direct measurements of the sizes in any dimension.

AFM in tapping mode has been successfully applied to characterise some clay materials in air and provided informative results.[135, 136, 222-228] Reports concerning AFM studies on the exfoliation and intercalation of LDH materials have also been published, exploiting its advantage for characterising such delicate materials.[135, 136, 227-230]

1.4.7. Magnetic properties

Although studies of the magnetic properties of LDH materials are still rather limited, the layered transition metal hydroxides, $M_2(OH)_3X$ (M = Co, Cu, Ni, Mn and X = NO_3^-, $CH_3CO_2^-$, Cl^-, $C_{12}H_{25}SO_3^{2-}$), have been extensively studied mainly for three principle reasons. Firstly, the triangular arrangement of the spin carriers is of theoretical importance with regard to magnetic spin frustration.[231] Secondly, they exhibit two-dimensional long-range order within the layers,[232] in addition to magnetic exchange interactions between the layers.[233] The ability of these compounds to accommodate different guest molecules provides the possibility of adjusting the interlayer magnetic exchange, while keeping the intralayer structure unaltered.[234] Thirdly, well separated layers can be considered to comprise multiple replicas of single layer magnets. If the moments are aligned perpendicularly, they can be of great commercial value for high-density magnetic recording materials.[235] Materials with different moment carriers such as Cu (S = 1/2), Ni (S = 1), and Co (S = 3/2), have been investigated with interlayer spaces from *ca.* 5 Å to 30 Å by introducing a range of interlayer molecules, *e.g.* NO_3^-, $CH_3CO_2^-$, isocyanate, *n*-alkyl-carboxylate and *n*-alkyl-sulphate (C = 0 - 12). For Cu compounds, they mostly exhibit an antiferromagnetic ordering between the layers.[236-240] The cobalt compounds (*e.g.* $Co_3(OH)_2$ and $Co_5(OH)_8(C_{12}H_{25}SO_3)_2 \cdot 5H_2O$) are all consistent with ferrimagnetic behaviour,[241-249] while the nickel compounds (*e.g.* $Ni_2(OH)_3(C_{12}H_{25}SO_3) \cdot H_2O$) are ferromagnetically ordered.[234]

The magnetic properties of layered transition metal hydroxides can be explained by a model of two sublattices, one comprising of octahedral metal atoms and another of tetrahedral metal atoms.[247] The mechanism of the exchange between the layers is usually interpreted through dipole-dipole interactions.[242, 243, 247, 250-254]

The magnetic behaviour of layered transition metal hydroxides may shed light on the magnetic responses of LDHs, which have similar structures. The approximately 90 ° M-O-M bridges provide superexchange interactions between the magnetic moment carriers.[255] The interaction between two parallel moments is ferromagnetic, while that between two antiparallel moments is antiferromagnetic. Ferrimagnetic interaction is between two unequal antiparallel moments. In the brucite-like layers of LDH, each cation is connected with six neighbouring cation through the M-O-M bridges. Due to the uncertainty in the distribution of the cations, spin-glass behaviour is expected for LDH materials. This is a frustrated interaction augmented by stochastic positions of the spins. Similar to layered transition metal hydroxides, the interactions between the layers are considered as dipole-dipole interactions.

AC susceptibilities of LDH materials are often measured to study the magnetisation dynamics of the material. When an AC field is applied on the sample, the induced moment is measured, yielding two components, the in-phase component χ' and the out-of-phase component χ''. The frequency-dependent AC susceptibility is used to characterise materials that exhibit spin-glass behaviour,[256-258] superparamagnetism,[259-265] magnetic phase transition[266] and superconductivity,[267, 268] due to the magnetisation of these materials lagging behind the drive field.

The first systematic investigation of the magnetic properties of LDH materials was published in 1991, covering Ni^{2+}-Cr^{3+} LDHs.[269] The susceptibilities of Ni^{2+}-Cr^{3+} LDHs with different Ni/Cr ratios and interlayer anions were simulated using the high-temperature development of Rushbrooke and Woods.[270] The results indicated antiferromagnetic interactions over Ni-O-Cr bridges and ferromagnetic interaction over Ni-O-Ni bridges. When the ratio of Ni/Cr was 1, the compound exhibited ferrimagnetic behaviour, however, when the ratio increased to 3, the behaviour of the compounds became ferromagnetic owing to the decreasing number of antiferromagnetic Ni-Cr interactions. The interlayer interactions were considered antiferromagnetic and were more influenced by the interlayer anion species than the distance, as the interactions were larger in NiCr-CO_3 LDH than in NiCr-Cl LDH, though their interlayer distances were similar. The authors ascribed this phenomenon to the CO_3^{2-} and SO_4^{2-} ions providing more efficient pathways for the interaction between layers.[269] Almansa and co-workers further investigated the behaviour of Ni_xCr-CO_3 compounds and carried out measurements of the AC susceptibility.[271] These compounds displayed spin-glass behaviour, which can be explained by structural disorder and competing magnetic interactions (**Figure 1-16**).

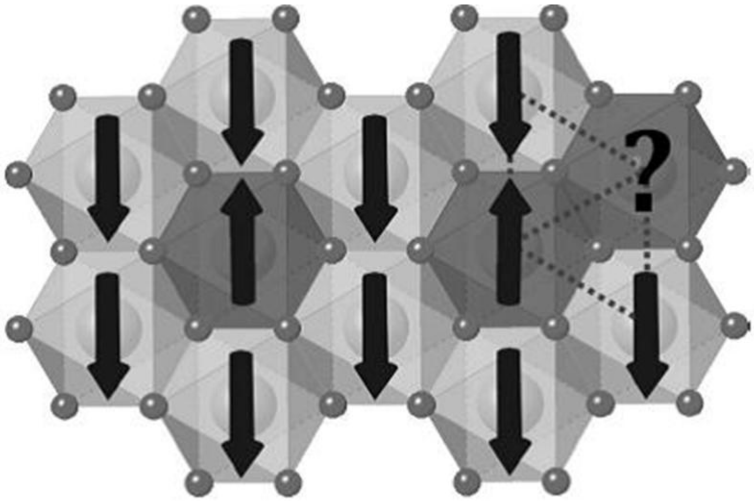

Figure 1-16: Schematic representation of the occurrence of spin frustration in Ni_xCr-CO_3 LDH compounds. (Image is reprinted with the permission from reference 271. Copyright © 2008 WILEY-VCH Verlag GmbH & Co. KGaA, Weinheim.)

LDH compounds containing two magnetic cations, such as Ni-Fe[272, 273] and Co-Fe LDHs,[274] have similar magnetic behaviour to Ni^{2+}-Cr^{3+} LDHs. With the presence of antiferromagnetic Ni^{2+}-O-Fe^{3+} or Co^{2+}-O-Fe^{3+} superexchange bridges and ferromagnetic Ni^{2+}-O-Ni^{2+} or Co^{2+}-O-Co^{2+} bridges, the intralayer interactions show ferrimagnetic behaviour. The interlayer interactions are also considered to comprise dipole-dipole interactions. Coronado *et al.* studied the magnetic properties of hybrid Ni-Fe LDH compounds intercalated with magnetic $[Cr(ox)_3]^{3–}$ or diamagnetic $[Rh(ox)_3]^{3–}$ and found they exhibit similar magnetic behaviour.[275]

For LDHs with diamagnetic Al^{3+} as the M^{3+} ion, the magnetic properties mostly depend on the magnetic property of the M^{2+}-O-M^{2+} interaction, leading to ferromagnetic Ni-Al[275] and Co-Al[274] LDHs and antiferromagnetic Cu-Al LDHs.[276] When M^{3+} is Fe^{3+} and M^{2+} is diamagnetic,[277, 278] since phase pure LDH materials avoid adjacent M^{3+} ions, there should be no detectable Fe^{3+}-O-Fe^{3+} superexchange.

1.5. Applications of LDHs

The applications of LDHs generally stem from two of their structural aspects: the positively charged hydroxide layers and the ability to accommodate guest ions or molecules between the layers. One commercial application of LDH materials is as an antacid using the basicity of the hydroxides to reduce stomach acidity. Other applications include as absorbents,[13-15] catalysts and catalyst precursors,[16-19] drug carriers and anion exchangers,[20-24] as well as bioactive nanocomposites.[25-33]

1.5.1. Anionic hosts

The purposes of using LDHs as anionic hosts generally involve absorbing, exchanging, or releasing anions. There is usually no limitation to the species of anions that can be intercalated, ranging from inorganic ions,[58, 70-76] to organic ions and organic dyes,[77-81, 279-284] to polymeric and biochemical anions.[30, 81-88, 110, 285-304] For absorbance, LDH materials can take up anions through surface adsorption or intercalation. The selective intercalation of anions can be used in pollutant separation and settlement.[305-309] LDH anion exchange ability is widely applied in cellular uptake,[310-312] while anion releasing ability is used for drug delivery and slow release.[20-24]

1.5.2. Catalysts

LDH materials represent a cheap, versatile and environmentally friendly source of catalysts, catalyst precursors, and catalyst supports. A number of examples have demonstrated that uncalcined/calcined LDHs can be used as catalysts for oxidation/reduction reactions,[313-316] hydrogenation/dehydrogenation reactions,[317-319] alkylation/acylation,[320, 321] Knoevagel condensations, Michael additions, Henry reactions and aldol condensations,[322-326] in addition to the steam reforming reaction of methane and carbon monoxide.[327-330]

1.5.3. Biochemical applications

LDHs are now starting to show application in medicine and pharmaceuticals. Pharmaceutically active compounds have been intercalated into LDHs in order to protect their integrity, increase their acid resistance, and deliver controlled release. A variety of anionic medicinal molecules, such as indomethacin,[23] the anticancer drugs methotrexate (MTX) or 5-fluorouracil (5-FU),[331, 332] anti-inflammatory drug such as fenbufen,[333] and ibuprofen,[334] anticoagulant low molecular-weight heparin (LMWH),[22] and the sunscreen agent *p*-aminobenzoic acid (PABA),[20] have been intercalated into LDHs. To avoid being destroyed in the acid environments of the stomach, modified LDH core-shell materials[333] have been developed.

Recently, interest in the biochemical applications of LDHs has focused on the incorporation of biologically active molecules into the LDH, such as genes (DNA or RNA),[28, 30, 32, 335-337] ATP,[338] amino acids,[287, 339] and vitamins.[340] For these applications, the efficiency of cellular uptake is vital. LDH nanoparticles have shown to be effective, bio-compatible delivery systems for these molecules, through cellular uptake tests of fluorescent marked LDHs.[29, 33, 341, 342]

1.6. Aim of this thesis

The aims of this thesis are focused on developing novel methods to enable the synthesis of well-defined functional layered materials with controlled particle size and morphologies. A new topotactic synthesis will be described to enable the formation of one dimensional nanorod materials. The thesis describes the use of reverse microemulsions to direct the synthesis of Mg-Al, Co-Al, Ni-Al, Li-Al, Ca-Al, Zn-Al and Fe-containing LDHs. The stacking disorder in LDH structures and the magnetic properties of LDH nanoplatelets containing transition metals were systematically studied.

1.7. References

1. E. Manasse, *Atti Soc. Toscana Sci. Nat.*, 1915, **24**, 92.
2. W. Feitknecht and M. Gerber, *Helv. Chim. Acta*, 1942, **25**, 131-137.
3. L. Pesic, S. Salipurovic, V. Markovic, D. Vucelic, W. Kagunya and W. Jones, *J. Mater. Chem.*, 1992, **2**, 1069-1073.
4. V. Rives, F. M. Labajos, M. A. Ulibarri and P. Malet, *Inorg. Chem.*, 1993, **32**, 5000-5001.
5. A. I. Khan and D. O'Hare, *J. Mater. Chem.*, 2002, **12**, 3191-3198.
6. P. S. Braterman, Z. P. Xu and F. Yarberry, in *Handbook of layered materials*, Marcel Dekker, New York, Editon edn., 2004, pp. 373-474.
7. S. Velu, V. Ramaswamy and S. Sivasanker, *Chem. Commun.*, 1997, 2107-2108.

8. S. Velu, K. Suzuki, M. Okazaki, T. Osaki, S. Tomura and F. Ohashi, *Chem. Mater.*, 1999, **11**, 2163-2172.
9. N. Das and A. Samal, *Microporous Mesoporous Mater.*, 2004, **72**, 219-225.
10. M. Intissar, J.-C. Jumas, J.-P. Besse and F. Leroux, *Chem. Mater.*, 2003, **15**, 4625-4632.
11. M. Intissar, S. Holler, F. Malherbe, J.-P. Besse and F. Leroux, *J. Phys. Chem. Solids*, 2004, **65**, 453-457.
12. N. V. Tarakina, R. B. Neder, T. A. Denisova, L. G. Maksimova, Y. V. Baklanova, A. P. Tyutyunnik and V. G. Zubkov, *Dalton Trans.*, 2010, **39**, 8168-8176.
13. N. N. Das, J. Konar, M. K. Mohanta and S. C. Srivastava, *J. Colloid Interface Sci.*, 2004, **270**, 1-8.
14. J. Das, B. Patra, N. Baliarsingh and K. Parida, *Appl. Clay Sci.*, 2006, **32**, 252-260.
15. P. C. Pavan, G. d. A. Gomes and J. B. Valim, *Microporous Mesoporous Mater.*, 1998, **21**, 659-665.
16. G. Centi and S. Perathoner, *Microporous Mesoporous Mater.*, 2008, **107**, 3-15.
17. B. Sels, D. D. Vos, M. Buntinx, F. Pierard, A. Kirsch-De Mesmaeker and P. Jacobs, *Nature*, 1999, **400**, 855-857.
18. A. Vaccari, *Catal. Today*, 1998, **41**, 53-71.
19. D. Carriazo, C. Martín and V. Rives, *Eur. J. Inorg. Chem.*, 2006, 4608-4615.
20. L. Perioli, V. Ambrogi, B. Bertini, M. Ricci, M. Nocchetti, L. Latterini and C. Rossi, *Eur. J. Pharm. Biopharm.*, 2006, **62**, 185-193.
21. J. H. Choy, S. J. Choi, J. M. Oh and T. Park, *J. Nanosci. Nanotechno.*, 2007, **7**, 4017-4020.
22. Z. Gu, A. C. Thomas, Z. P. Xu, J. H. Campbell and G. Q. Lu, *Chem. Mater.*, 2008, **20**, 3715-3722.
23. M. Del Arco, E. Cebadera, S. Gutiérrez, C. Martín, M. J. Montero, V. Rives, J. Rocha and M. A. Sevilla, *J. Pharm. Sci.*, 2004, **93**, 1649-1658.
24. J. -H. Yang, Y.-S. Han, M. Park, T. Park, S.-J. Hwang and J.-H. Choy, *Chem. Mater.*, 2007, **19**, 2679-2685.
25. M. Darder, M. López-Blanco, P. Aranda, F. Leroux and E. Ruiz-Hitzky, *Chem. Mater.*, 2005, **17**, 1969-1977.
26. K. Ladewig, M. Niebert, Z. P. Xu, P. P. Gray and G. Q. Lu, *Appl. Clay Sci.*, 2010, **48**, 280-289.
27. A. W. Musumeci, G. M. Mortimer, M. K. Butler, Z. P. Xu, R. F. Minchin and D. J. Martin, *Appl. Clay Sci.*, 2010, **48**, 271-279.
28. J.-H. Choy, S.-Y. Kwak, Y.-J. Jeong and J.-S. Park, *Angew. Chem. Int. Ed.*, 2000, **39**, 4041-4045.
29. J.-M. Oh, S.-J. Choi, G.-E. Lee, J.-E. Kim and J.-H. Choy, *Chem. Asian J.*, 2009, **4**, 67-73.
30. J.-H. Choy, S.-Y. Kwak, J.-S. Park, Y.-J. Jeong and J. Portier, *J. Am. Chem. Soc.*, 1999, **121**, 1399-1400.
31. F. Leroux and J.-P. Besse, *Chem. Mater.*, 2001, **13**, 3507-3515.
32. L. Desigaux, M. B. Belkacem, P. Richard, J. Cellier, P. Léone, L. Cario, F. Leroux, C. Taviot-Guého and B. Pitard, *Nano Lett.*, 2005, **6**, 199-204.
33. Z. P. Xu, M. Niebert, K. Porazik, T. L. Walker, H. M. Cooper, A. P. J. Middelberg, P. P. Gray, P. F. Bartlett and G. Q. Lu, *J. Controlled Release*, 2008, **130**, 86-94.
34. M. del Arco, R. Trujillano and V. Rives, *J. Mater. Chem.*, 1998, **8**, 761-767.
35. J. Fernandez, M. Ulibarri, F. Labajos and V. Rives, *J. Mater. Chem.*, 1998, **8**, 2507-2514.

36. S. Xu, Y. Yang, T. Xu, Y. Kuang, M. Dong, F. Zhang, F. Besenbacher and D. G. Evans, *Chem. Eng. Sci.*, 2011, **66**, 2157-2163.
37. X. F. Zhao, F. Z. Zhang, S. L. Xu, D. G. Evans and X. Duan, *Chem. Mater.*, 2010, **22**, 3933-3942.
38. W. B. Luo and J. R. Dahn, *Chem. Mater.*, 2009, **21**, 56-62.
39. Y. Kobayashi, X. Ke, H. Hata, P. Schiffer and T. E. Mallouk, *Chem. Mater.*, 2008, **20**, 2374-2381.
40. L. Hu, L. Wu, M. Liao, X. Hu and X. Fang, *Adv. Funct. Mater.*, 2012, **22**, 998-1004.
41. R. Allmann, *Acta Crystallogr. Sect. B*, 1968, **24**, 972-977.
42. G. Brown and M. C. Gastuche, *Clay Minerals*, 1967, **7**, 193-201.
43. M. C. Gastuche, G. rown and M. M. Mortland, *Clay Minerals*, 1967, **7**, 177-192.
44. H. F. W. Taylor, *Miner. Mag.*, 1969, **37**, 338.
45. H. F. W. Taylor, *Miner. Mag.*, 1973, **37**, 338.
46. R. Rothbauer, F. Zigan and H. O'Daniel, *Zeitschrift fuer Kristallographie, Kristallgeometrie, Kristallphysik, Kristallchemie*, 1967, **125**, 317-331.
47. H. D. Megaw, *Zeitschrift fuer Kristallographie, Kristallgeometrie, Kristallphysik, Kristallchemie*, 1934, **87**, 185-204.
48. G. R. Williams and D. O'Hare, *J. Phys. Chem. B*, 2006, **110**, 10619-10629.
49. A. Fogg, A. Freij and G. Parkinson, *Chem. Mater.*, 2002, **14**, 232-234.
50. M. Bellotto, B. Rebours, O. Clause, D. Bazin and E. Elkaïm, *J. Phys. Chem.*, 1996, **100**, 8527-8534.
51. M. Vucelic, W. Jones and G. D. Moggridge, *Clays Clay Miner.*, 1997, **45**, 803-813.
52. G. Bourrié, F. Trolard, P. Refait and F. Feder, *Clays Clay Miner.*, 2004, **52**, 382-394.
53. P. J. Sideris, U. G. Nielsen, Z. Gan and C. P. Grey, *Science*, 2008, **321**, 113-117.
54. N. Gutmann and B. Müller, *J. Solid State Chem.*, 1996, **122**, 214-220.
55. *U.S. 4348295 Pat.*, 1982.
56. A. P. Nemurdy, V. P. Isupov, N. P. Kotsupalo and V. V. Boldyrev, *Russ. J. Inorg. Chem.*, 1986, **31**, 651.
57. K. R. Poeppelmeier and S. J. Hwu, *Inorg. Chem.*, 1987, **26**, 3297-3302.
58. A. M. Fogg and D. O'Hare, *Chem. Mater.*, 1999, **11**, 1771-1775.
59. G. R. Williams, T. G. Dunbar, A. J. Beer, A. M. Fogg and D. O'Hare, *J. Mater. Chem.*, 2006, **16**, 1231-1237.
60. G. R. Williams, T. G. Dunbar, A. J. Beer, A. M. Fogg and D. O'Hare, *J. Mater. Chem.*, 2006, **16**, 1222-1230.
61. M. Ogawa and Y. Sugiyama, *J. Ceram. Soc. Jpn.*, 2009, **117**, 179-184.
62. H. C. Greenwell, W. Jones, S. L. Rugen-Hankey, P. J. Holliman and R. L. Thompson, *Green Chemistry*, 2010, **12**, 688-695.
63. A. M. Fogg, G. R. Williams, R. Chester and D. O'Hare, *J. Mater. Chem.*, 2004, **14**, 2369-2371.
64. M. Fleischer, R. G. Burns, L. J. Cabri, C. A. Francis and A. Pabst, *Am. Mineral.*, 1982, **67**, 413-418.
65. S. Britto and P. Kamath, *Inorg. Chem.*, 2009, **48**, 11646-11654.
66. R. Chitrakar, Y. Makita, A. Sonoda and T. Hirotsu, *J. Hazard. Mater.*, 2011, **185**, 1435-1439.
67. G. R. Williams, S. J. Moorhouse, T. J. Prior, A. M. Fogg, N. H. Rees and D. O'Hare, *Dalton Trans.*, 2011, **40**, 6012-6022.
68. S. Britto and P. V. Kamath, *Inorg. Chem.*, 2010, **49**, 11370-11377.

69. G. Hu, D.Phil Thesis, D.Phil Thesis, University of Oxford, 2007.
70. A. M. Fogg, G. R. Williams, R. Chester and D. O'Hare, *J. Mater. Chem.*, 2004, **14**, 2369-2371.
71. A. Ookubo, K. Ooi, F. Tani and H. Hayashi, *Langmuir*, 1994, **10**, 407.
72. M. Badreddine, A. Legrouri, A. Barroug, A. de Roy and J. P. Besse, *Mater. Lett.*, 1999, **38**, 391.
73. S. Miyata, *Clays and Clay Minerals, Proceedings of the Conference*, 1975, **23**, 369-375.
74. F. Malherbe, L. Bigey, C. Forano, A. de Roy and J.-P. Besse, *J. Chem. Soc., Dalton Trans.*, 1999, 3831-3839.
75. J. Twu and P. K. Dutta, *Chem. Mater.*, 1992, **4**, 398-401.
76. W. Ding, G. Gu, W. Zhong, W.-C. Zang and Y. Du, *Chem. Phys. Lett.*, 1996, **262**, 259-262.
77. S. Carlino, *Solid State Ionics*, 1997, **98**, 73.
78. H.-P. Boehm, J. Steinle and C. Vieweger, *Angew. Chem. Int. Ed.*, 1977, **16**, 265-266.
79. M. Meyn, K. Beneke and G. Lagaly, *Inorg. Chem.*, 1990, **29**, 5201-5207.
80. J. L. Guimaraes, R. Marangoni, L. P. Ramos and F. Wypych, *J. Colloid Interface Sci.*, 2000, **227**, 445-451.
81. I. Y. Park, K. Kuroda and C. Kato, *J. Chem. Soc., Dalton Trans.*, 1990, 3071-3074.
82. C. O. Oriakhi, I. V. Farr and M. M. Lerner, *J. Mater. Chem.*, 1996, **6**, 103-107.
83. O. C. Wilson Jr., T. Olorunyolemi, A. Jaworski, L. Borum, D. Young, A. Siriwat, E. Dickens, C. Oriakhi and M. Lerner, *Appl. Clay Sci.*, 1999, **15**, 265-279.
84. P. B. Messersmith and S. I. Stupp, *Chem. Mater.*, 1995, **7**, 454-460.
85. T. Ikeda, H. Amoh and T. Yasunaga, *J. Am. Chem. Soc.*, 1984, **106**, 5772-5775.
86. S. Aisawa, S. Takahashi, W. Ogasawara, Y. Umetsu and E. Narita, *Clay Science*, 2000, **11**, 317-328.
87. A. Fudala, I. Palinko and I. Kiricsi, *Inorg. Chem.*, 1999, **38**, 4653-4658.
88. J.-H. Choy, S.-Y. Kwak, J.-S. Park and Y.-J. Jeong, *J. Mater. Chem.*, 2001, **11**, 1671-1674.
89. V. A. Drits, T. N. Sokolova, G. V. Sokolova and V. I. Cherkashin, *Clays Clay Miner.*, 1987, **35**, 401-417.
90. W. Hofmeister and H. V. Platen, *Cryst. Rev.*, 1992, **3**, 3-26.
91. D. G. Evans and R. C. T. Slade, in *Layered Double Hydroxides*, eds. X. Duan and D. G. Evans, Springer, Editon edn., 2006, vol. 119, pp. 1-88.
92. H. von Platen, W. Hofmeister, E. Urmann, J. Gotzig and U. Assmus, Giulini Chemie GmbH, Internal Research Report, Editon edn., 1990.
93. F. M. Labajos, V. Rives and M. A. Ulibarri, *Spectrosc. Lett.*, 1991, **24**, 499-508.
94. Z. P. Xu and H. C. Zeng, *J. Phys. Chem. B*, 2001, **105**, 1743-1749.
95. G. W. Brindley and S. Kikkawa, *Clays Clay Miner.*, 1980, **28**, 87-91.
96. I. Pausch, H. H. Lohse, K. Schuermann and R. Allmann, *Clays Clay Miner.*, 1986, **34**, 507.
97. R. Allmann, *Chimia*, 1970, **24**, 99-108.
98. M. M. J. Treacy, M. W. Deem and J. M. Newsam, *DIFFaX v1.813*, NEC Research Institute, Princeton, New Jersey, 2010.
99. A. V. Radha, C. Shivakumara and P. V. Kamath, *Clays Clay Miner.*, 2005, **53**, 520-527.
100. G. S. Thomas, A. V. Radha, P. V. Kamath and S. Kannan, *J. Phys. Chem. B*, 2006, **110**, 12365-12371.

101. S. V. Prasanna, P. V. Kamath and C. Shivakumara, *Mater. Res. Bull.*, 2007, **42**, 1028-1039.
102. A. V. Radha, P. V. Kamath and C. Shivakumara, *Acta Crystallogr. Sect. B*, 2007, **63**, 243-250.
103. G. S. Thomas, P. V. Kamath and S. Kannan, *J. Phys. Chem. C*, 2007, **111**, 18980-18984.
104. S. Britto, G. S. Thomas, P. V. Kamath and S. Kannan, *J. Phys. Chem. C*, 2008, **112**, 9510-9515.
105. R. E. Johnsen and P. Norby, *J. Phys. Chem. C*, 2009, **113**, 19061-19066.
106. A. V. Radha, P. Vishnu Kamath and G. N. Subbanna, *Mater. Res. Bull.*, 2003, **38**, 731-740.
107. T. N. Ramesh and P. V. Kamath, *Mater. Res. Bull.*, 2008, **43**, 3227-3233.
108. T. N. Ramesh and P. V. Kamath, *Mater. Res. Bull.*, 2008, **43**, 2827-2832.
109. D. Barthelmy, www.webmineral.com.
110. X. Duan and D. G. Evans, eds., *Layered Double Hydroxides*, Springer, 2006.
111. V. R. L. Constantino and T. J. Pinnavaia, *Inorg. Chem.*, 1995, **34**, 883-892.
112. E. Gardner, K. M. Huntoon and T. J. Pinnavaia, *Adv. Mater.*, 2001, **13**, 1263-1266.
113. W. Meng, F. Li, D. G. Evans and X. Duan, *Mater. Res. Bull.*, 2004, **39**, 1185-1193.
114. S. K. Yun and T. J. Pinnavaia, *Chem. Mater.*, 1995, **7**, 348-354.
115. K. Klemkaite, I. Prosycevas, R. Taraskevicius, A. Khinsky and A. Kareiva, *Central European Journal of Chemistry*, 2011, **9**, 275-282.
116. Z. P. Xu, G. Stevenson, C.-Q. Lu and G. Q. Lu, *J. Phys. Chem. B*, 2006, **110**, 16923-16929.
117. J. Liu, F. Li, D. G. Evans and X. Duan, *Chem. Commun.*, 2003, 542-543.
118. Y. Zhao, F. Li, R. Zhang, D. G. Evans and X. Duan, *Chem. Mater.*, 2002, **14**, 4286-4291.
119. J. J. Bravo-Suárez, E. A. Páez-Mozo and S. T. Oyama, *Quim. Nova*, 2004, **27**, 601-614.
120. A. de Roy, C. Forano, K. El Malki and J. P. Besse, in *Synthesis of microporous materials*, eds. M. L. Occelli and H. E. Robson, Van Nostrand Reinhold, New York, Editon edn., 1992, vol. II, p. 108.
121. M. Ogawa and H. Kaiho, *Langmuir*, 2002, **18**, 4240.
122. H. Cai, A. C. Hillier, K. R. Franklin, C. C. Nunn and M. D. Ward, *Science*, 1994, **66**, 1551.
123. U. Costantino, F. Marmottini, M. Nocchetti and R. Vivani, *Eur. J. Inorg. Chem.*, 1998, **1998**, 1439-1446.
124. Z. Liu, R. Ma, M. Osada, N. Iyi, Y. Ebina, K. Takada and T. Sasaki, *J. Am. Chem. Soc.*, 2006, **128**, 4872-4880.
125. Z. P. Liu, R. Z. Ma, M. Osada, N. Iyi, Y. Ebina, K. Takada and T. Sasaki, *J. Am. Chem. Soc.*, 2006, 4872-4880.
126. Z. Liu, R. Ma, M. Osada, K. Takada and T. Sasaki, *J. Am. Chem. Soc.*, 2005, **127**, 13869-13874.
127. Y. Du and D. O'Hare, *Inorg. Chem.*, 2008, **47**, 3234-3242.
128. H. Wang, G. L. Fan, C. Zheng, X. Xiang and F. Li, *Ind. Eng. Chem. Res.*, 2010, **49**, 2759-2767.
129. Y. F. Han, Z. H. Liu, Z. P. Yang, Z. L. Wang, X. H. Tang, T. Wang, L. H. Fan and K. Ooi, *Chem. Mater.*, 2008, **20**, 360-363.
130. G. Abellan, E. Coronado, C. Marti-Gastaldo, E. Pinilla-Cienfuegos and A. Ribera, *J. Mater. Chem.*, 2010, **20**, 7451-7455.

131. N. Iyi, T. Matsumoto, Y. Kaneko and K. Kitamura, *Chem. Lett.*, 2004, **33**, 1122-1123.
132. Y. Feng, D. Li, C. Li, Z. Wang, D. G. Evans and X. Duan, *Clays Clay Miner.*, 2003, **51**, 566-569.
133. X. R. Jiang, F. Li, D. G. Evans and X. Duan, *Acta Chim. Sinica*, 2004, **62**, 16-21.
134. E. Gardner, K. M. Huntoon and T. J. Pinnavaia, *Adv. Mater.*, 2001, **13**, 1263.
135. G. Hu, N. Wang, D. O'Hare and J. Davis, *J. Mater. Chem.*, 2007, **17**, 2257-2266.
136. G. Hu and D. O'Hare, *J. Am. Chem. Soc.*, 2005, **127**, 17808-17813.
137. H. Wu, Q. Jiao, Y. Zhao, S. Huang, X. Li, H. Liu and M. Zhou, *Mater. Charact.*, 2010, **61**, 227-232.
138. C. L. J. Wang, Y. M. A. Wu, R. M. J. Jacobs, J. H. Warner, G. R. Williams and D. O'Hare, *Chem. Mater.*, 2011, **23**, 171-180.
139. M. E. Pérez-Bernal, R. J. Ruano-Casero, F. Benito and V. Rives, *J. Solid State Chem.*, 2009, **182**, 1593-1601.
140. N. Nassar and M. Husein, *Langmuir*, 2007, **23**, 13093-13103.
141. Y. Zhao, F. F. Xiao and Q. Z. Jiao, *Bull. Mater. Sci.*, 2008, **31**, 831-834.
142. Y. Q. Sun, Y. M. Zhou, Z. Q. Wang and X. Y. Ye, *Appl. Surf. Sci.*, 2009, **255**, 6372-6377.
143. N. Morel-Desrosiers, J. Pisson, Y. Israeli, C. Taviot-Gueho, J.-P. Besse and J.-P. Morel, *J. Mater. Chem.*, 2003, **13**, 2582-2585.
144. Z. P. Xu and P. S. Braterman, *J. Mater. Chem.*, 2003, **13**, 268-273.
145. G. R. Williams, A. J. Norquist and D. O'Hare, *Chem. Mater.*, 2004, **16**, 975-981.
146. J. Wang, M. Wei, G. Rao, D. G. Evans and X. Duan, *J. Solid State Chem.*, 2004, **177**, 366-371.
147. Q. Z. Yang, D. J. Sun, C. G. Zhang, X. J. Wang and W. A. Zhao, *Langmuir*, 2003, **19**, 5570-5574.
148. F. Leroux, P. Aranda, J.-P. Besse and E. Ruiz-Hitzky, *Eur. J. Inorg. Chem.*, 2003, **2003**, 1242-1251.
149. E. Mostafa Moujahid, J.-P. Besse and F. Leroux, *J. Mater. Chem.*, 2002, **12**, 3324-3330.
150. A. I. Khan, L. Lei, A. J. Norquist and D. O'Hare, *Chem. Commun.*, 2001, 2342-2343.
151. M. Wei, S. Shi, J. Wang, Y. Li and X. Duan, *J. Solid State Chem.*, 2004, **177**, 2534-2541.
152. M. Ogawa and S. Asai, *Chem. Mater.*, 2000, **12**, 3253-3255.
153. T. Sato, T. Wakabayashi and M. Shimada, *Industrial & Engineering Chemistry Product Research and Development*, 1986, **25**, 89-92.
154. T. Sato, K. Kato, T. Endo and M. Shimada, *Reactivity of Solids*, 1986, **2**, 253-260.
155. T. Sato, H. Fujita, T. Endo, M. Shimada and A. Tsunashima, *Reactivity of Solids*, 1988, **5**, 219-228.
156. F. Prinetto, D. Tichit, R. Teissier and B. Coq, *Catal. Today*, 2000, **55**, 103-116.
157. F. Kooli, C. Depege, A. Ennaqadi, A. de Roy and J. P. Besse, *Clays Clay Miner.*, 1997, **45**, 92-98.
158. *U.S. Patent Pat.*, 1997.
159. E. Kanezaki, K. Kinugawa and Y. Ishikawa, *Chem. Phys. Lett.*, 1994, **226**, 325-330.
160. K. Chibwe and W. Jones, *J. Chem. Soc., Chem. Commun.*, 1989, 926-927.
161. K. Poeppelmeier and S. Hwu, *Inorg. Chem.*, 1987, **26**, 3297-3302.
162. A. V. Besserguenev, A. M. Fogg, R. J. Francis, S. J. Price, D. O'Hare, V. P. Isupov

and B. P. Tolochko, *Chem. Mater.*, 1997, **9**, 241-247.
163. R. Xu and H. Zeng, *Chem. Mater.*, 2001, **13**, 297-303.
164. Z. P. Xu and G. Q. Lu, *Chem. Mater.*, 2005, **17**, 1055-1062.
165. R. Ma, J. Liang, K. Takada and T. Sasaki, *J. Am. Chem. Soc.*, 2010, **133**, 613-620.
166. R. Z. Ma, Z. P. Liu, K. Takada, N. Iyi, Y. Bando and T. Sasaki, *J. Am. Chem. Soc.*, 2007, **129**, 5257-5263.
167. J. B. Liang, R. Z. Ma, N. B. O. Iyi, Y. Ebina, K. Takada and T. Sasaki, *Chem. Mater.*, 2010, 371-378.
168. C. Vaysse, L. Guerlou-Demourgues, E. Duguet and C. Delmas, *Inorg. Chem.*, 2003, 4559-4567.
169. G. A. Bubniak, W. H. Schreiner, N. Mattoso and F. Wypych, *Langmuir*, 2002, **18**, 5967-5970.
170. I. Sissoko, E. T. Iyagba, R. Sahai and P. Biloen, *J. Solid State Chem.*, 1985, **60**, 283-288.
171. G. R. Williams and D. O'Hare, *Chem. Mater.*, 2005, **17**, 2632-2640.
172. G. R. Williams, A. I. Khan and D. O'Hare, in *Structure Bonding: Layered Double Hydroxides*, Editon edn., 2006 pp. 161-192.
173. W. J. McLaughlin, J. L. White and S. L. Hem, *J. Colloid Interface Sci.*, 1994, **165**, 41.
174. C. I. Markland, D.Phil Thesis, University of Oxford, 2011.
175. H. Hayashi and M. J. Hudson, *J. Mater. Chem.*, 1995, **5**, 781-783.
176. W. Feitknecht, *Helv. Chim. Acta*, 1933, **16**, 427-454.
177. K. El Malki, A. De Roy and J. P. Besse, *European Journal of Solid State Inorganic Chemistry*, 1989, **26**, 339.
178. E. Zhouri and A. El Hajbi, *Annales de Chimie Science des Matériaux*, 1999, **24**, 57-62.
179. Z. P. Xu and H. C. Zeng, *Chem. Mater.*, 2000, **12**, 3459.
180. Z. P. Xu and H. C. Zeng, *Chem. Mater.*, 2000, **12**, 2597.
181. Z. P. Xu and H. C. Zeng, *J. Mater. Chem.*, 1998, **8**, 2499.
182. H. C. Zeng, Z. P. Xu and M. Qian, *Chem. Mater.*, 1998, **10**, 2277.
183. M. Qian and H. C. Zeng, *J. Mater. Chem.*, 1997, **7**, 493.
184. J. M. Fernandez, C. Barriga, M. A. Ulibarri, F. M. Labajos and V. Rives, *J. Mater. Chem.*, 1997, **4**, 1117.
185. F. Cavani, F. Trifiro and A. Vaccari, *Catal. Today*, 1991, **11**, 173.
186. S. P. Newman and W. Jones, *New J. Chem.*, 1998, **22**, 105.
187. S. Kannan and R. V. Jasra, *J. Mater. Chem.*, 2000, **10**, 2311.
188. K. J. Rao, B. Vaidhyanathan, M. Ganguli and P. A. Ramakrishnan, *Chem. Mater.*, 1999, **11**, 882.
189. L. Albiston, K. R. Franklin, E. Lee and J. B. A. F. Smeulders, *J. Mater. Chem.*, 1996, **6**, 871-877.
190. Z. P. Xu, G. S. Stevenson, C.-Q. Lu, G. Q. Lu, P. F. Bartlett and P. P. Gray, *J. Am. Chem. Soc.*, 2005, **128**, 36-37.
191. S. Abelló and J. Pérez-Ramírez, *Adv. Mater.*, 2006, **18**, 2436-2439.
192. D.-y. Wang, A. Leuteritz, U. Wagenknecht and G. Heinrich, *T. Nonferr. Metal Soc.*, 2009, **19**, 1479-1482.
193. T. Vulic, M. Hadnadjev and R. Marinkovic-Neducin, *J. Microsc. - Oxford*, 2008, **232**, 634-638.
194. B. Li and J. He, *J. Phys. Chem. C*, 2008, **112**, 10909-10917.
195. A. Faour, V. Prévot and C. Taviot-Gueho, *J. Phys. Chem. Solids*, 2010, **71**,

487-490.

196. L. Li, R. Ma, N. Iyi, Y. Ebina, K. Takada and T. Sasaki, *Chem. Commun.*, 2006, 3125-3127.
197. Y. Du, G. Hu and D. O'Hare, *J. Mater. Chem.*, 2009, **19**, 1160-1165.
198. P. Gunawan and R. Xu, *Chem. Mater.*, 2009, **21**, 781-783.
199. L. Li, Y. Feng, Y. Li, W. Zhao and J. Shi, *Angew. Chem. Int. Ed.*, 2009, **48**, 5888-5892.
200. R. Mukhopadhyay, O. Al-Hanbali, S. Pillai, A. G. Hemmersam, R. L. Meyer, A. C. Hunter, K. J. Rutt, F. Besenbacher, S. M. Moghimi and P. Kingshott, *J. Am. Chem. Soc.*, 2007, **129**, 13390-13391.
201. W. Wei and Z. Yang, *Adv. Mater.*, 2008, **20**, 2965-2969.
202. H. Liu, Q. Jiao, Y. Zhao, H. Li, C. Sun and X. Li, *J. Alloys Compd.*, 2010, **496**, 317-323.
203. Y. Sun, Y. Zhou, Z. Wang and X. Ye, *Appl. Surf. Sci.*, 2009, **255**, 4497-4502.
204. Y. Wang, F. Zhang, S. Xu, X. Wang, D. G. Evans and X. Duan, *Ind. Eng. Chem. Res.*, 2008, **47**, 5746-5750.
205. L. Qiu and B. Qu, *J. Colloid Interface Sci.*, 2006, **301**, 347-351.
206. X. Liu, R. Ma, Y. Bando and T. Sasaki, *Angew. Chem. Int. Ed.*, 2010, **49**, 8253-8256.
207. T. S. Stanimirova, G. Kirov and E. Dinolova, *J. Mater. Sci. Lett.*, 2001, **20**, 453-455.
208. M. J. Hernandez-Moreno, M. A. Ulibarri, J. L. Rendon and C. J. Serna, *Phys. Chem. Miner.*, 1985, **12**, 34-38.
209. J. T. Kloprogge and R. L. Frost, *J. Solid State Chem.*, 1999, **146**, 506-515.
210. J. T. Kloprogge, L. Hickey and R. L. Frost, *J. Mater. Sci. Lett.*, 2002, **21**, 603-605.
211. J. T. Kloprogge, D. Wharton, L. Hickey and R. L. Frost, *Am. Mineral.*, 2002, **87**, 623-629.
212. J. Evans, M. Pillinger and J. J. Zhang, *J. Chem. Soc., Dalton Trans.*, 1996, **14**, 2963.
213. H. Roussel, V. Briois, E. Elkaim, A. de Roy, J.-P. Besse and J.-P. Jolivet, *Chem. Mater.*, 2001, **13**, 329-337.
214. V. Rives and S. Kannan, *J. Mater. Chem.*, 2000, **10**, 489-495.
215. L. Poul, N. Jouini and F. Fiévet, *Chem. Mater.*, 2000, **12**, 3123-3132.
216. X. L. Duan, D. R. Yuan, X. F. Cheng, X. Q. Wang, Z. M. Wang, D. Xu and M. K. Lv, *Opt. Mater.*, **23**, 327-330.
217. R. Ma, Z. Liu, K. Takada, K. Fukuda, Y. Ebina, Y. Bando and T. Sasaki, *Inorg. Chem.*, 2006, **45**, 3964-3969.
218. N. Das and R. Das, *Appl. Clay Sci.*, 2008, **42**, 90-94.
219. A. B. P. Lever, *Inorganic Electronic Spectroscopy*, Elsevier, New York, 1986.
220. M.-A. Ulibarri, F. M. Labajos, V. Rives, R. Trujillano, W. Kagunya and W. Jones, *Inorg. Chem.*, 1994, **33**, 2592-2599.
221. V. J. Morris, A. R. Kirby and A. P. Gunning, *Atomic Force Microscopy for Biologists*, Imperial College Press, London, 1999.
222. A. Cadene, S. Durand-Vidal, P. Turq and J. Brendle, *J. Colloid Interface Sci.*, 2005, **285**, 719.
223. R. D. Piner, T. T. Xu, f. T. Fisher, Y. Qiao and R. S. Ruoff, *Langmuir*, 2003, **19**, 7995.
224. K. A. Carrado, G. W. Zajac, K. Song and J. R. Brenner, *Langmuir*, 1997, **13**, 2895.
225. D. L. Ho, R. M. Briber and C. J. Glinka, *Chem. Mater.*, 2001, **13**, 1923.

226. M. M. Malwitz, A. Dundigalla, V. Ferreiro, P. D. Butler, M. C. Henk and G. Schmidt, *Phys. Chem. Chem. Phys.*, 2004, **6**, 2977.
227. J. X. He, S. Yamashita, W. Jones and A. Yamagishi, *Langmuir*, 2002, **18**, 1580.
228. J. Lee, S. Rhee and D.-Y. Jung, *Chem. Commun.*, 2003, 2740.
229. L. Li, R. Ma, Y. Ebina, N. Iyi and T. Sasaka, *Chem. Mater.*, 2005, **17**.
230. Q. Wu, A. Olafsen, F. B. Vistad, J. Roots and P. Norby, *J. Mater. Chem.*, 2005, **15**, 4695.
231. K. Binder and A. P. Young, *Reviews of Modern Physics*, 1986, **58**, 801.
232. L. J. de Jongh, *Magnetic Properties of Layered Transition Metal Compounds*, Kluwer Academic Publishers, Dordrecht, 1990.
233. M. Drillon, C. Hornick, V. Laget, P. Rabu, F. M. Romero, S. Rouba, G. Ulrich and R. Ziessel, *Molecular Crystals and Liquid Crystals Science and Technology. Section A. Molecular Crystals and Liquid Crystals*, 1995, **273**, 125-140.
234. M. Kurmoo, P. Day, A. Derory, C. Estournès, R. Poinsot, M. J. Stead and C. J. Kepert, *J. Solid State Chem.*, 1999, **145**, 452-459.
235.Y. Honda, Y. Hirayama, K. Ito and M. Futamoto, *Magnetics, IEEE Transactions on*, 1998, **34**, 1633-1635.
236. P. Rabu, S. Rouba, V. Laget, C. Hornick and M. Drillon, *Chem. Commun.*, 1996, 1107-1108.
237. W. Fujita and K. Awaga, *Inorg. Chem.*, 1996, **35**, 1915-1917.
238. V. Laget, P. Rabu, C. Hornick, F. Romero, R. Ziessel, P. Turek and M. Drillon, *Molecular Crystals and Liquid Crystals Science and Technology. Section A. Molecular Crystals and Liquid Crystals*, 1997, **305**, 291-302.
239. V. Laget, M. Drillon, C. Hornick, P. Rabu, F. Romero, P. Turek and R. Ziessel, *J. Alloys Compd.*, 1997, **262-263**, 423-427.
240. W. Fujita, K. Awaga and T. Yokoyama, *Appl. Clay Sci.*, 1999, **15**, 281-303.
241. X.-M. Zhang, C.-R. Li, X.-H. Zhang, W.-X. Zhang and X.-M. Chen, *Chem. Mater.*, 2008, **20**, 2298-2305.
242. M. B. Salah, S. Vilminot, G. Andre, M. Richard-Plouet, T. Mhiri, S. Takagi and M. Kurmoo, *J. Am. Chem. Soc.*, 2006, **128**, 7972-7981.
243. M. O. H. Shimizu, A.Nakamoto, M. Enomoto, N. Kojima, *Inorg. Chem.*, 2006, **45**, 10240-10247.
244. M. Ben Salah, S. Vilminot, G. Andre, M. Richard-Plouet, T. Mhiri, S. Takagi and M. Kurmoo, *J. Am. Chem. Soc.*, 2006, **128**, 7972-7981.
245. M. Ben Salah, S. Vilminot, G. Andre, F. Bouree-Vigneron, M. Richard-Plouet, T. Mhiri and M. Kurmoo, *Chem. Mater.*, 2005, **17**, 2612-2621.
246. P. M. Forster, M. M. Tafoya and A. K. Cheetham, *J. Phys. Chem. Solids*, 2004, **65**, 11-16.
247. M. Kurmoo, H. Kumagai, S. M. Hughes and C. J. Kepert, *Inorg. Chem.*, 2003, **42**, 6709-6722.
248. M. Kurmoo, *J. Mater. Chem.*, 1999, **9**, 2595-2598.
249. M. Kurmoo, *Chem. Mater.*, 1999, **11**, 3370-3378.
250. K. M. De'Bell, A. B.; Whitehead, J. P., *Reviews of Modern Physics*, 2000, **72**, 225.
251. A. Demessence, G. Rogez and P. Rabu, *Chem. Mater.*, 2006, **18**, 3005-3015.
252. B. S. Mohsen, S. Vilminot, M. Richard-Plouet, G. Andre, T. Mhiri and M. Kurmoo, *Chem. Commun.*, 2004, 2548-2549.
253. M. Drillon, P. Panissod, P. Rabu, J. Souletie, V. Ksenofontov and P. Gulich, *Phys. Rev. B*, 2002, **65**, 104404.
254. A. Rujiwatra, C. J. Kepert, J. B. Claridge, M. J. Rosseinsky, H. Kumagai and M.

Kurmoo, *J. Am. Chem. Soc.*, 2001, **123**, 10584-10594.

255. P. W. Anderson, *Physical Review*, 1950, **79**, 350-356.
256. C. A. M. Mulder, A. J. van Duyneveldt and J. A. Mydosh, *Phys. Rev. B*, 1981, **23**, 1384-1396.
257. T. Jonsson, K. Jonason, P. Jönsson and P. Nordblad, *Phys. Rev. B*, 1999, **59**, 8770-8777.
258. J. A. Mydosh, *J. Magn. Magn. Mater.*, 1996, **157–158**, 606-610.
259. C. Sjogren, C. Johansson, A. Naevestad, P. Sontum, K. BrileySaebo and A. Fahlvik, *Magn. Reson. Imaging*, 1997, **15**, 55-67.
260. C. Seip, E. Carpenter, C. O'Connor, V. John and S. Li, *IEEE T. Magn.*, 1998, **34**, 1111-1113.
261. A. Rondinone, A. Samia and Z. Zhang, *Appl. Phys. Lett.*, 2000, **76**, 3624-3626.
262. A. Rondinone, A. Samia and Z. Zhang, *J. Phys. Chem. B*, 1999, 6876-6880.
263. M. D. Mukadam, S. M. Yusuf, R. Sasikala and S. K. Kulshreshtha, *J. Appl. Phys.*, 2006, **99**.
264. M. Mikhaylova, D. K. Kim, N. Bobrysheva, M. Osmolowsky, V. Semenov, T. Tsakalakos and M. Muhammed, *Langmuir*, 2004, **20**, 2472-2477.
265. D. Brinzei, L. Catala, C. Mathonière, W. Wernsdorfer, A. Gloter, O. Stephan and T. Mallah, *J. Am. Chem. Soc.*, 2007, **129**, 3778-3779.
266. A. G. Berndt, X. Chen, H. P. Kunkel and G. Williams, *Phys. Rev. B*, 1995, **52**, 10160-10169.
267. R. Singh, R. Lal, U. C. Upreti, D. K. Suri, A. V. Narlikar, V. P. S. Awana, J. Albino Aguiar and M. Shahabuddin, *Phys. Rev. B*, 1997, **55**, 1216-1222.
268. R. W. Rollins, H. Kupfer and W. Gey, *J. Appl. Phys.*, 1974, **45**, 5392-5398.
269. M. Bujoli-Dœuff, L. Force, V. Gadet, M. Verdaguer, K. El Malki, A. de Roy, J. P. Besse and J. P. Renard, *Mater. Res. Bull.*, 1991, **26**, 577-587.
270. G. S. Rushbrooke and P. J. Wood, *Mol. Phys.*, 1958, **1**, 257-283.
271. J. J. Almansa, E. Coronado, C. Martí-Gastaldo and A. Ribera, *Eur. J. Inorg. Chem.*, 2008, **2008**, 5642-5648.
272. T. Raja and J. Santhanalakshmi, *J. Mater. Sci. Lett.*, 1996, **15**, 718-720.
273. E. Coronado, J. R. Galán-Mascarós, C. Martí-Gastaldo, A. Ribera, E. a. Palacios, M. Castro and R. n. Burriel, *Inorg. Chem.*, 2008, **47**, 9103-9110.
274. M. Intissar, R. Segni, C. Payen, J.-P. Besse and F. Leroux, *J. Solid State Chem.*, 2002, **167**, 508-516.
275. E. Coronado, J. Galan-Mascaros, C. Marti-Gastaldo, A. Ribera, E. Palacios, M. Castro and R. Burriel, *Inorg. Chem.*, 2008, **47**, 9103-9110.
276. R. Trujillano, M. J. Holgado, F. Pigazo and V. Rives, *Physica B: Condensed Matter*, 2006, **373**, 267-273.
277. S. Morlat-Thérias, C. Mousty, P. Palvadeau, P. Molinié, P. Léone, J. Rouxel, C. Taviot-Guého, A. Ennaqui, A. de Roy and J. P. Besse, *J. Solid State Chem.*, 1999, **144**, 143-151.
278. G. Carja, H. Chiriac and N. Lupu, *J. Magn. Magn. Mater.*, 2007, **311**, 26-30.
279. S. Carlino, *Solid State Ionics*, 1997, **98**, 73-84.
280. M.-M. Hong, J.-M. Oh and J.-H. Choy, *J. Nanosci. Nanotechno.*, 2008, **8**, 5018-5021.
281. S. Cooper and P. K. Dutta, *J. Phys. Chem.*, 1990, **94**, 114-118.
282. C. Markland, G. R. Williams and D. O'Hare, *J. Mater. Chem.*, 2011, **21**, 17896-17903.
283. M. Jakupca and P. K. Dutta, *Chem. Mater.*, 1995, **7**, 989-994.

284. P. K. Dutta and D. S. Robins, *Langmuir*, 1994, **10**, 1851-1856.
285. C. Del Hoyo, *Appl. Clay Sci.*, 2007, **36**, 103-121.
286. M. Baek, I.-S. Kim, J. Yu, H.-E. Chung, J.-H. Choy and S.-J. Choi, *J. Nanosci. Nanotechno.*, 2011, **11**, 1803-1806.
287. S. Aisawa, S. Takahashi, W. Ogasawara, Y. Umetsu and E. Narita, *J. Solid State Chem.*, 2001, **162**, 52-62.
288. S. Aisawa, S. Sasaki, S. Takahashi, H. Hirahara, H. Nakayama and E. Narita, *J. Phys. Chem. Solids*, 2006, **67**, 920-925.
289. S. Aisawa, H. Hirahara, K. Ishiyama, W. Ogasawara, Y. Umetsu and E. Narita, *J. Solid State Chem.*, 2003, **174**, 342-348.
290. M. S. Gasser, *Colloids Surf., B: Biointerfaces*, 2009, **73**, 103-109.
291. V. Ambrogi, G. Fardella, G. Grandolini and L. Perioli, *Int. J. Pharm.*, 2001, **220**, 23-32.
292. T. Kuwahara, H. Tagaya and K. Chiba, *Microporous Mater.*, 1995, **4**, 247-250.
293. S. Mandal, D. Tichit, D. A. Lerner and N. Marcotte, *Langmuir*, 2009, **25**, 10980-10986.
294. Z. Sun, L. Jin, W. Shi, M. Wei, D. G. Evans and X. Duan, *Langmuir*, 2011, **27**, 7113-7120.
295. O. C. Wilson, T. Olorunyolemi, A. Jaworski, L. Borum, D. Young, A. Siriwat, E. Dickens, C. Oriakhi and M. Lerner, *Appl. Clay Sci.*, 1999, **15**, 265-279.
296. T. Kwon, G. A. Tsigdinos and T. J. Pinnavaia, *J. Am. Chem. Soc.*, 1988, **110**, 3653-3654.
297. C. Misra and A. J. Perrotta, *Clays Clay Miner.*, 1992, **40**, 145-150.
298. E. L. Salinas and Y. Ono, *Bull. Chem. Soc. Jpn.*, 1992, **65**, 2465-2470.
299. E. Káfuňková, C. Taviot-Guého, P. Bezdička, M. Klementová, P. Kovář, P. Kubát, J. Mosinger, M. Pospíšil and K. Lang, *Chem. Mater.*, 2010, **22**, 2481-2490.
300. A. Clearfield, M. Kieke, J. Kwan, J. L. Colon and R. C. Wang, *Journal of Inclusion Phenomena and Macrocyclic Chemistry*, 1991, **11**, 361-378.
301. J. Inacio, C. Taviot-Guého, C. Forano and J. P. Besse, *Applied Clay Science*, 2001, **18**, 255-264.
302. L. P. Cardoso, R. Celis, J. Cornejo and J. B. Valim, *J. Agric. Food. Chem.*, 2006, **54**, 5968-5975.
303. J. Cornejo, R. Celis, I. Pavlovic and M. A. Ulibarri, *Clay Minerals*, 2008, **43**, 155-175.
304. E. Touloupakis, A. Margelou and D. F. Ghanotakis, *Pest Management Science*, 2011, **67**, 837-841.
305. A. Ragavan, A. I. Khan and D. O'Hare, *J. Mater. Chem.*, 2006, **16**, 602-608.
306. L. Lei, A. Khan and D. O'Hare, *J. Solid State Chem.*, 2005, **178**, 3648-3654.
307. F. Millange, R. I. Walton, L. Lei and D. O'Hare, *Chem. Mater.*, 2000, **12**, 1990-1994.
308. J. Inacio, C. Taviot-Gueho, C. Forano and J. P. Besse, *Applied Clay Science*, 2001, **18**, 255-264.
309. P. C. Pavan, E. L. Crepaldi and J. B. Valim, *J. Colloid Interface Sci.*, 2000, **229**, 346-352.
310. S.-J. Choi, G. E. Choi, J.-M. Oh, Y.-J. Oh, M.-C. Park and J.-H. Choy, *J. Mater. Chem.*, 2010, **20**, 9463-9469.
311. A. C. S. Alcantara, P. Aranda, M. Darder and E. Ruiz-Hitzky, *J. Mater. Chem.*, 2010, **20**, 9495-9504.
312. L. Perioli, V. Ambrogi, L. di Nauta, M. Nocchetti and C. Rossi, *Appl. Clay Sci.*,

2011, **51**, 407-413.

313. K. Bahranowski, R. Dula, M. Gasior, M. Labanowska, A. Michalik, L. A. Vartikian and E. M. Serwicka, *Appl. Clay Sci.*, 2001, **18**, 93-101.
314. H. B. Friedrich, F. Khan, N. Singh and M. Van Staden, *Synlett*, 2001, 869-871.
315. K. Kaneda, S. Ueno and T. Imanaka, *J. Mol. Catal. A: Chem.*, 1995, **102**, 135-138.
316. J. M. Fraile, J. I. Garcia, D. Marco, J. A. Mayoral, E. Sanchez, A. Monzon and E. Romeo, *Stud. Surf. Sci. Catal.*, 2000, **130B**, 1673-1678.
317. V. Rives, F. M. Labajos, R. Trujillano, E. Romeo, C. Royo and A. Monzon, *Appl. Clay Sci.*, 1998, **13**, 363.
318. A. Monzon, E. Romeo, C. Royo, R. Trujillano, F. M. Labajos and V. Rives, *Appl. Catal. A: Gen.*, 1999, **185**, 3.
319. F. Malherbe, C. Forano, B. Sharma, M. P. Atkins and J. P. Besse, *Appl. Clay Sci.*, 1998, **13**, 381-399.
320. V. R. Choudhary, S. K. Jana and A. B. Mandale, *Catal. Lett.*, 2001, **74**, 95-98.
321. V. R. Choudhary, S. K. Jana and V. S. Narkhede, *Appl. Catal. A*, 2002, **235**, 207-215.
322. S. Velu and C. S. Swamy, *Appl. Catal. A*, 1996, **145**, 225-230.
323. S. Velu and C. S. Swamy, *Appl. Catal. A*, 1996, **145**, 141-153.
324. B. M. Choudary, B. Bharathi, C. V. Reddy, M. L. Kantam and K. V. Raghavan, *Chem. Commun.*, 2001, 1736-1737.
325. M. L. Kantam, A. Ravindra, C. V. Reddy, B. Sreedhar and B. M. Choudary, *Adv. Synth. Catal.*, 2006, **348**, 569-578.
326. S. Abelló, S. Dhir, G. Colet and J. Pérez-Ramírez, *Appl. Catal. A*, 2007, **325**, 121-129.
327. J. Ashok, M. Subrahmanyam and A. Venugopal, *Int. J. Hydrogen Energy*, 2008, **33**, 2704-2713.
328. Z. P. Xu, J. Zhang, M. O. Adebajo, H. Zhang and C. Zhou, *Appl. Clay Sci.*, 2011, **53**, 139-150.
329. S.-i. Fujita, Y. Kanamori, A. M. Satriyo and N. Takezawa, *Catal. Today,* 1998, **45**, 241-244.
330. G. G. C. Arizaga, K. G. Satyanarayana and F. Wypych, *Solid State Ionics*, 2007, **178**, 1143-1162.
331. J.-M. Oh, M. Park, S.-T. Kim, J.-Y. Jung, Y.-G. Kang and J.-H. Choy, *J. Phys. Chem. Solids*, **67**, 1024-1027.
332. S.-J. Choi, J.-M. Oh and J.-H. Choy, *J. Nanosci. Nanotechno.*, 2010, **10**, 2913-2916.
333. B. Li, J. He, D. G. Evans and X. Duan, *Appl. Clay Sci.*, 2004, **27**, 199-207.
334. V. Ambrogi, G. Fardella, G. Grandolini and L. Perioli, *Int. J. Pharm.*, 2001, **220**, 23-32.
335. Y. Wong, K. Markham, Z. P. Xu, M. Chen, G. Q. Lu, P. F. Bartlett and H. M. Cooper, *Biomaterials*, 2010, **31**, 8770-8779.
336. K. Ladewig, M. Niebert, Z. P. Xu, P. P. Gray and G. Q. M. Lu, *Biomaterials*, 2010, **31**, 1821-1829.
337. J.-H. Choy, M. Park and J.-M. Oh, in *NanoBioTechnology: bioinspired devices and materials of the future,* eds. O. Shoseyov and I. Levy, Humana Press, Totowa, New Jersey, Editon edn., 2007, vol. 14, p. 349.
338. J.-H. Choy, S.-Y. Kwak, J.-S. Park and Y.-J. Jeong, *J. Mater. Chem.*, 2001, **11**, 1671-1674.
339. H. Nakayama, N. Wada and M. Tsuhako, *Int. J. Pharm.*, 2004, **269**, 469-478.

340. S.-H. Hwang, Y.-S. Han and J.-H. Choy, *Bull. Korean Chem. Soc.*, 2001, **22**, 1019-1022.
341. J.-M. Oh, C.-B. Park and J.-H. Choy, *J. Nanosci. Nanotechno.*, 2011, **11**, 1632-1635.
342. S.-J. Choi and J.-H. Choy, *Nanomedicine*, 2011, **6**, 803-814.

Chapter 2

Topotactic synthesis of layered double hydroxide nanorods

2.1. Introduction

Layered double hydroxides (LDHs) are a family of layered materials with the composition $[M^{z+}_{1-x}M^{3+}_{x}(OH)_2]^{a+}(X^{n-})_{a/n}\cdot mH_2O$. In the majority of cases $z = 2$, and the M^{2+} and M^{3+} cations can be chosen from a wide variety of metals.[1-4] Li-Al LDHs, where $z = 1$, are the only known examples that contain M^{+} and M^{3+} cations. Typified by $[LiAl_2(OH)_6]Cl\cdot xH_2O$ (LiAl-Cl), the structure of LiAl-Cl LDH usually consists of eclipsed hexagonal $[LiAl_2(OH)_6]^{+}$ layers stacked along the *c*-axis with anions located at the edges of the unit cell, equidistant from the layers. Li^{+} ions are ordered, being found in one third of the octahedral sites in the $Al(OH)_3$ layers.[5, 6] LiAl-X LDHs can be synthesised using two general methods. Direct intercalation involving the treatment of gibbsite or bayerite (both polymorphs of $Al(OH)_3$) with a 4-fold molar excess of the appropriate lithium salt (*e.g.* LiCl, LiBr, $LiNO_3$).[7-9] The use of different polymorphs of $Al(OH)_3$ results in LDHs with differing layer stacking sequences. As discussed in **Chapter 1**, while the reaction of LiX with gibbsite produces $LiAl_2$-X with hexagonal symmetry (a two-layer ABBA stacking sequence, denoted *h*-$LiAl_2$-X), use of the bayerite or nordstrandite polymorphs of $Al(OH)_3$ produces an essentially rhombohedral form of the LDH (a three-layer ABBCCA stacking sequence, *r*-$LiAl_2$-X).[10] The direct cation and anion intercalation synthesis method has been extended to other MAl-X

LDHs ($[MAl_4(OH)_{12}](NO_3)_2\ mH_2O$; M = Co^{2+}, Ni^{2+}, Cu^{2+}, Zn^{2+}) and even ternary complexes.[8-16] An alternative method involves the hydrothermal treatment of an hydrated alumina gel with LiOH to form $LiAl_2$-OH LDH.[17] Li-Al LDHs have been extensively investigated due to their special structure and wide applications in absorbents[18, 19] and photochemistry.[20]

The synthesis and properties of nanomaterials are currently one of the most intensively studied fields in inorganic chemistry, due to the observation that nanoparticles may exhibit distinctively different physical properties and reactivity from those of bulk materials, or even materials at micrometre scale. The synthetic techniques for one-dimensional nanostructures, typically nanowires and nanorods, can be divided into four groups: spontaneous growth, template-based growth, electrospinning and lithography.[21] LDH particles typically show preferential growth perpendicular to the *c* direction and microscale hexagonal platelet morphology. Although many efforts have been made to synthesise LDHs with controlled size or unique nanostructure, LDH particles with one dimension nanostructure are rarely seen. A mixture of bar-like particles and curved sheets of Mg-Al LDHs were obtained by Xu *et al.*[22] by refluxing MgAl-Cl LDHs prepared using surfactants. The explanation they provided was that surfactants adsorbed preferentially onto the *a*, *b*-plane, creating a hydrophobic surface and minimising contact between the LDH and the aqueous phase, and hence leading to growth along *c*-axis. Similar post-exchange hydrothermal treatments also resulted in Zn-Al LDH,[23] and Cu-Co LDH nanorods,[24] and rod-like MgAl-FITC (fluoresceinisothiocyanate) LDHs, which exhibit quick nuclear targeting in cellular uptake studies.[25] Apart from spontaneous growth, template-assisted growth was also applied to LDH synthesis. Sun *et al.* invested collagen templated syntheses of Zn-Al

LDHs, which co-precipitate in the presence of collagen and polymers.[26] The mechanism was described by Al^{3+} ions being attracted to the negatively charged collagen, with precipitation first occurring at the inorganic-organic interface followed by the incorporation of Zn^{2+} ions. If the collagen template is considered as an outward template, reverse microemulsion systems could be inward templates which encapsulate the aqueous phase, with reverse micelles as microreactors. A quaternary microemulsion, cetyltrimethylammonium bromide (CTAB)/water/*n*-hexane/*n*-hexanol, has been applied to synthesise Ni-Al LDH nanorods[27] and Zn-Co-Fe ternary hydroxide nanowires.[28]

In this chapter, we report the first successful topotactic synthesis of rod-like LDH particles with a hexagonal prismatic morphology, through the simultaneous intercalation of Li^+ cations and $X^−$ anions (X = $Cl^−$, $Br^−$, $NO_3^−$) into rod-like γ-$Al(OH_3)$, (**rod-Gibbsite**).

2.2. Results and discussion

2.2.1. Synthesis

The synthesis of a rod-like form of gibbsite (**rod-Gibbsite**) has been reported previously using a templated directed approach by Liu *et al.*[29] Treatment of the **rod-gibbsite** sample with saturated solutions of LiX (X = Cl, Br) under N_2 for 30 mins followed by hydrothermal treatment in a Teflon lined stainless autoclave for 15 hours at 120 ℃ produced phase pure materials, referred as **LiAl-Cl-rod**, and **LiAl-Br-rod**. The XRD data of these products could be indexed to hexagonal lithium aluminium hydroxide chloride, $[LiAl_2(OH)_6]Cl\cdot xH_2O$ (LiAl-Cl LDH, JCPDS PDF 01-87-1765) and hexagonal lithium aluminium hydroxide bromide, $[LiAl_2(OH)_6]Br\cdot xH_2O$ (LiAl-Br LDH, JCPDS PDF 01-87-1766) respectively.[5] A conventional LiAl-Cl LDH sample

(**LiAl-Cl-std**) was synthesised using the conventional method described by A. V. Besserguenev.[5] Detailed experimental procedures are listed in **Chapter 7**.

2.2.2. Powder X-ray diffraction

Figure 2-1 shows the diffraction pattern of the gibbsite nanorods precursor (**rod-Gibbsite**), which can be indexed to the monoclinic gibbsite phase (JCPDS PDF 00-33-0018).

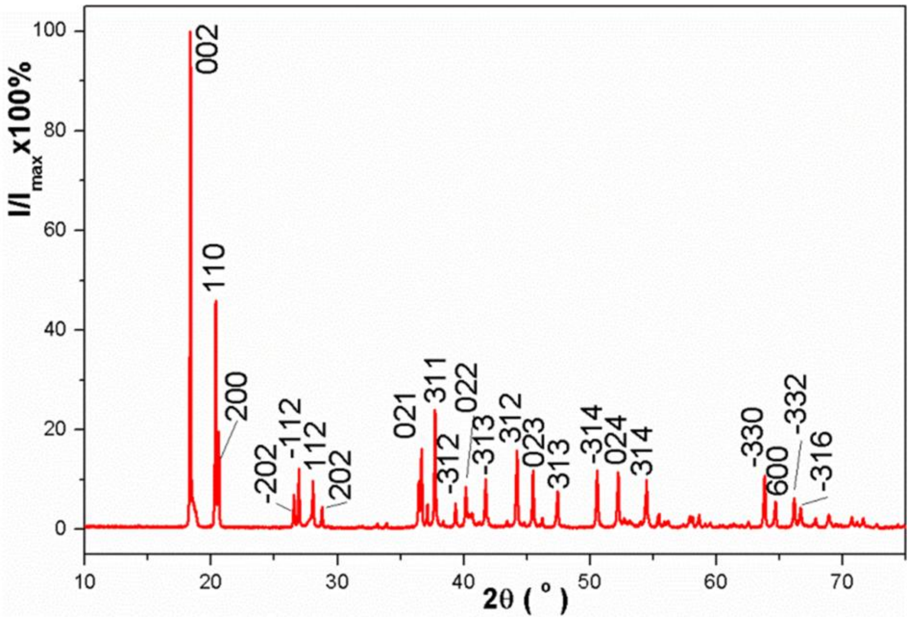

Figure 2-1: XRD pattern of gibbsite nanorods precursor (**rod-Gibbsite**).

The XRD data for both **LiAl-Cl-rod** and **LiAl-Br-rod** were measured supported on a silicon wafer (type P, 75 mm, Agar) in plate Bragg-Brantano geometry.[30] Initial inspection of the relative intensities of the Bragg reflections in the XRD for both **LiAl-Cl-rod** and **LiAl-Br-rod** materials (**Figure 2-2**) suggests that the crystallites adopt an unusual preferential orientation. For example, the XRD data for the **LiAl-Cl-rod** sample supported on a silicon wafer showed significantly enhanced intensity associated with the (100), and (300) Bragg reflections at 2θ *ca.* 20 °and 64 °respectively compared to the XRD pattern for **LiAl-Cl-std** (**Figure 2-3** (b)). This suggests that hydrothermal treatment had not resulted in the dissolution of the $Al(OH)_3$ and the reconstruction of the LDHs on the more commonly observed platelet morphology.

We also prepared a LiAl-NO_3 sample by hydrothermal treatment of the rod-like gibbsite sample with saturated $LiNO_3$ solution. However, the XRD pattern of the

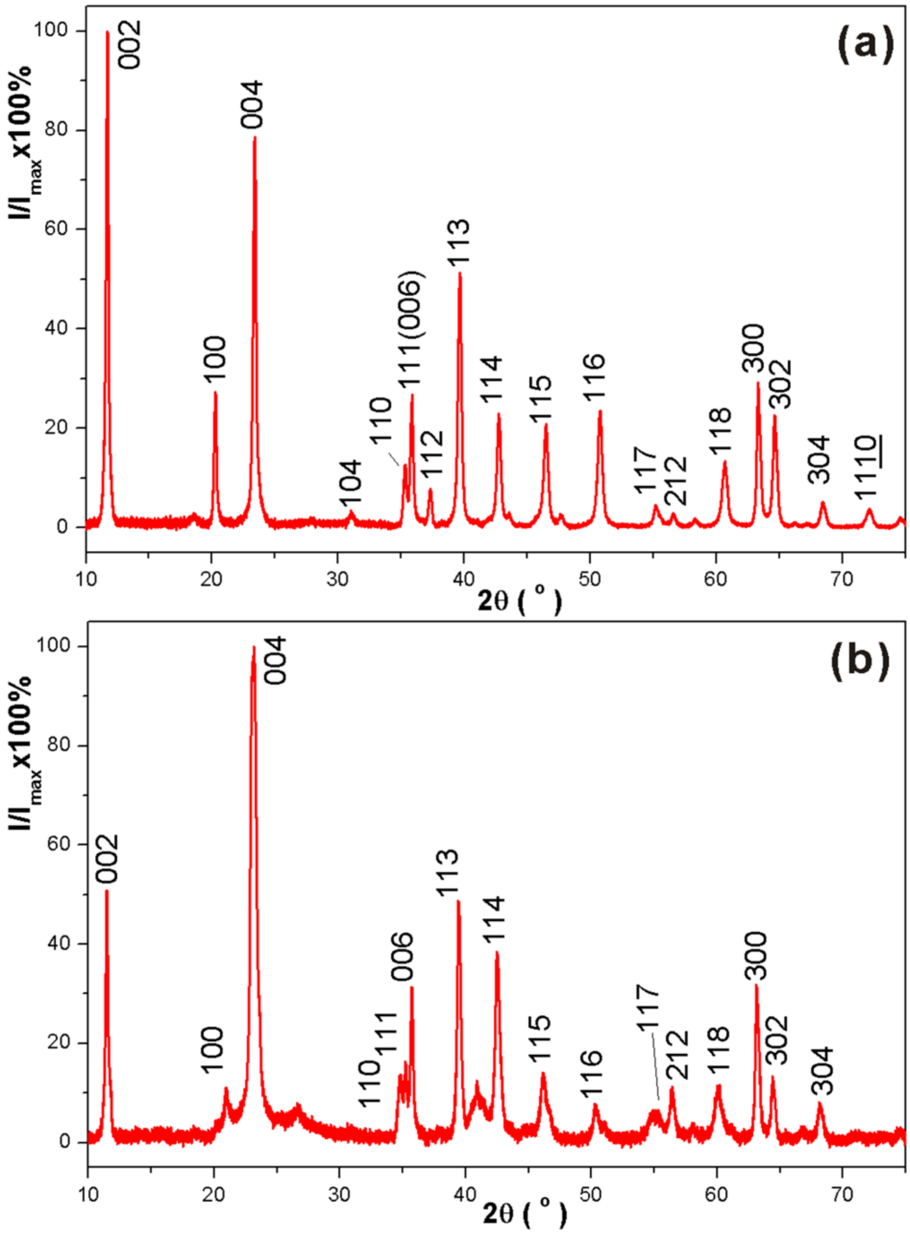

Figure 2-2: XRD patterns of (a) **LiAl-Cl-rod**, and (b) **LiAl-Br-rod**.

LiAl-NO_3 LDH showed the product contained a large amount of gibbsite precursor, which means the intercalation had not reached completion.

In order to quantitatively determine the degree of preferred orientation and the orientation of the alignment vector, we performed Rietveld refinement on the XRD data for both **LiAl-X-rod** (X = Cl, Br) LDHs, and compared the results to those obtained from the analysis of the XRD data from the conventional sample, **LiAl-Cl-std**. The fitted parameters are given in **Table 2-1** (Detailed information in **Appendix I**). The Dollase and March formulation[31, 32] for preferred orientation (R_0) within GSAS[33] was used, as it is applicable for both needle and plate shaped crystals. The conventional LDH sample, **LiAl-Cl-std** is typically composed of agglomerated platelet particles,[34] Rietveld refinement of the XRD data (**Figure 2-3**) resulted in a value of $R_0 = 1.1$, which indicates no preferred orientation. Rietveld refinement of the XRD data resulted in a value of $R_0 = 3.6$ for **LiAl-Cl-rod** and 1.7 for **LiAl-Br-rod,** which is consistent with a rod-like sample adopting an orientation in which the cylinder axis is perpendicular to the diffraction plane.

Table 2-1: Comparison of the crystallographic data for **LiAl-X-rod** (X = Cl, Br) and **LiAl-Cl-std** samples.

	LiAl-Cl-rod	**LiAl-Cl-std**	**LiAl-Br-rod**
Empirical formula	$LiAl_2(OH)_6Cl$	$LiAl_2(OH)_6Cl \cdot H_2O$	$LiAl_2(OH)_6Br$
Crystal system	hexagonal	hexagonal	hexagonal
Space group	$P\ 6_3/mcm$	$P\ 6_3/m$	$P\ 6_3/mcm$
a (Å)	5.0877(8)	5.0578(9)	5.0992(8)
c (Å)	15.3169(4)	15.2992(8)	15.2092(4)
Lamellar separation (Å)	7.6584(7)	7.6496(4)	7.6046(2)
Dollase and March Preferential Orientation, R_0	3.5894(7)	1.1078(6)	1.6864(1)
χ^2	1.376	5.933	4.283
R_{wp}, %	20.49	10.88	3.32
R_p, %	15.54	7.65	2.07

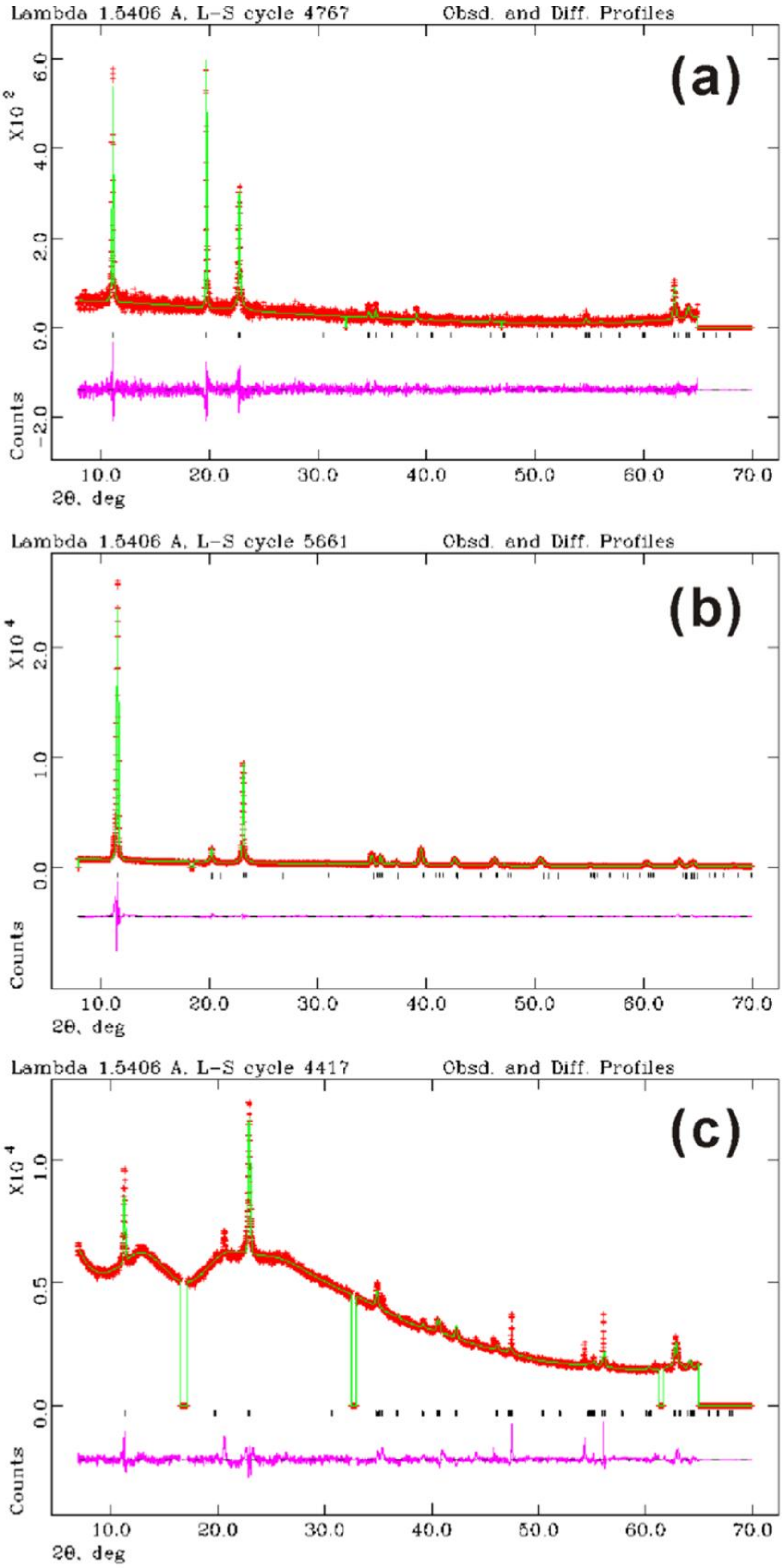

Figure 2-3: Refined XRD pattern of (a) **LiAl-Cl-rod**, (b) **LiAl-Cl-std**, and (c) **LiAl-Br-rod**.

2.2.3. FT-IR spectroscopy

Figure 2-4 shows the FT-IR spectra of **LiAl-Cl-rod** and **LiAl-Br-rod**. The spectra of **LiAl-Cl-rod** and **LiAl-Br-rod** are similar. Both spectra contain a broad absorption at *ca.* 3400 cm^{-1}, which corresponds to a combination of the stretching vibrations of the hydroxide groups in the brucite sheets and of the interlayer water molecules (ν_{OH}). Absorptions centred at *ca.* 1636 and 950 cm^{-1} can be assigned to be the bending vibrations of the interlayer water molecules and the hydroxide groups in the brucite-like layers (δ_{OH}). The absorptions caused by the metal oxygen bonds appear at 700 cm^{-1} in the fingerprint region. In the spectrum of **LiAl-Br-rod**, the absorption at *ca.* 1367 cm^{-1} indicates that small amount of carbonate may coexist in the interlayer gallery.

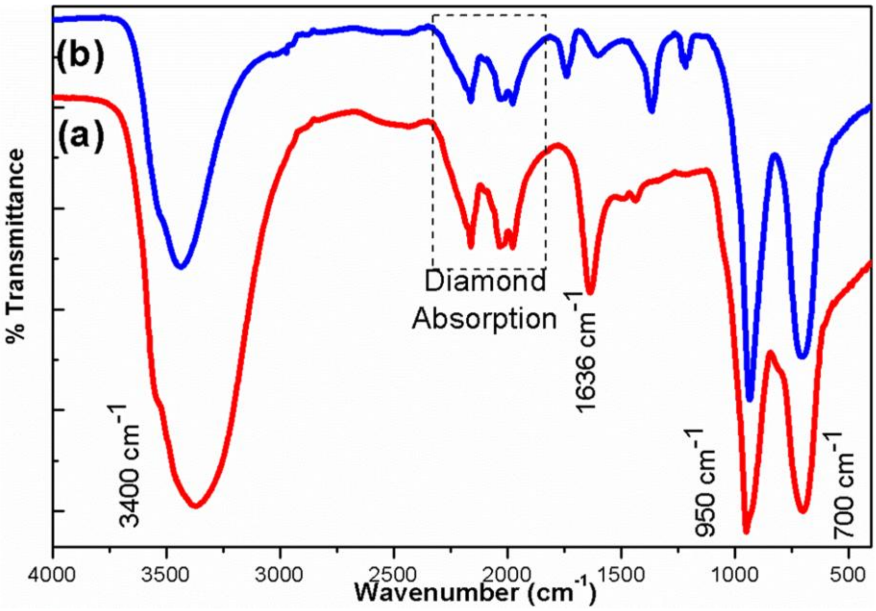

Figure 2-4: FT-IR spectra of (a) **LiAl-Cl-rod** and (b) **LiAl-Br-rod**.

2.2.4. Elemental analysis

The CHN elemental analysis data (**Table 2-2**) verify the composition of the samples. **LiAl-Br-rod** contains a small amount of C. This indicates carbonate ions coexist in the interlayer space with Br^- ions, which is in agreement with the IR spectrum.

Table 2-2: Summary of elemental analysis data for **rod-Gibbsite**, **LiAl-Cl-rod**, **LiAl-Br-rod** and **LiAl-cyclamate**.

Sample	Observed (*calc.*) (%)			Calc. Formula
	C	H	N	
rod-Gibbsite	-	3.73 (3.85)	-	$Al(OH)_3$
LiAl-Cl-rod	-	3.32 (3.02)	-	$[LiAl_2(OH)_6]Cl$
LiAl-Br-rod	0.35 (0)	2.67 (2.47)	-	$[LiAl_2(OH)_6]Br$
LiAl-cyclamate	20.07 (21.11)	5.70 (5.28)	4.57 (4.11)	$[LiAl_2(OH)_6](C_6H_{12}NSO_3)$

2.2.5. Electron microscopy

The as-prepared **rod-Gibbsite**, **LiAl-Cl-rod** and **LiAl-Br-rod** were studied by TEM, HR-TEM and SEM. The low-magnification SEM and TEM images of the **rod-Gibbsite** (**Figure 2-5** (a) & (b)), **LiAl-Cl-rod** LDH (**Figure 2-6** (a) & (b)) and

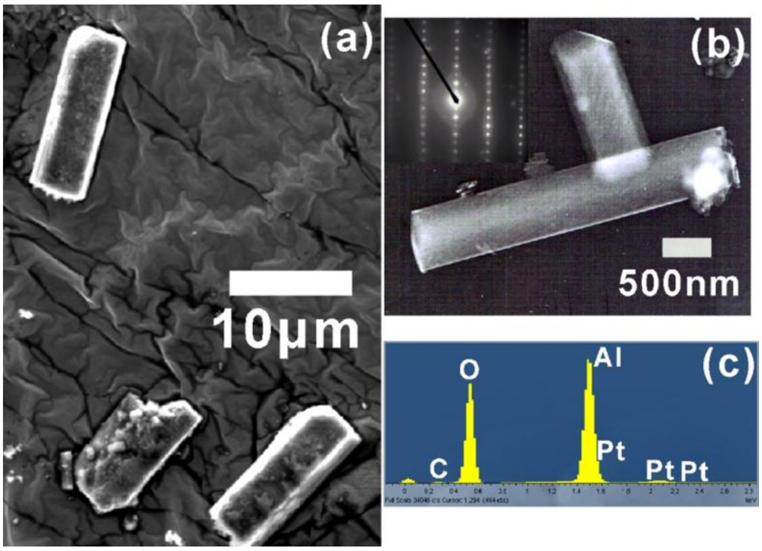

Figure 2-5: (a) SEM image, (b) TEM image and (c) EDX spectrum of **rod-Gibbsite**. (Inset (b): a corresponding SAED pattern.)

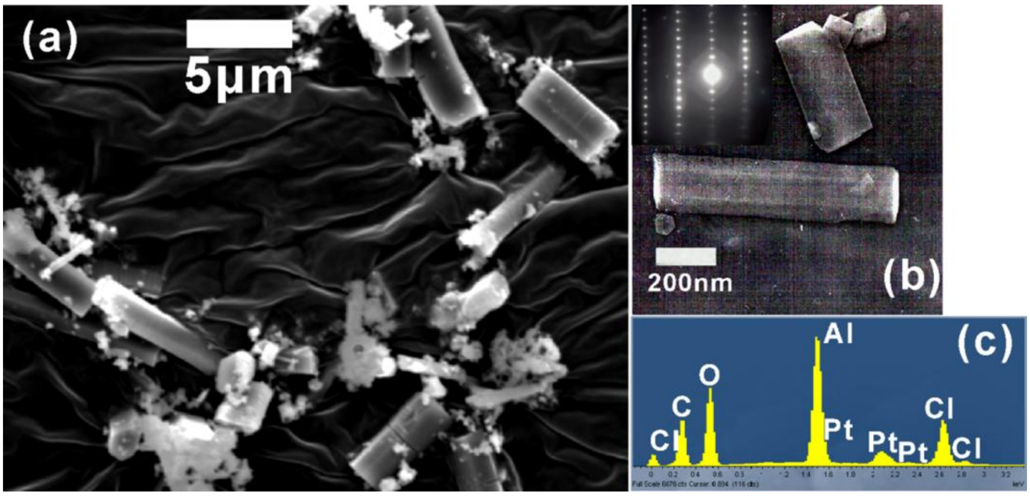

Figure 2-6: (a) SEM image, (b) TEM image, and (c) EDX spectrum of **LiAl-Cl-rod**. (Inset (b): a corresponding SAED pattern.)

LiAl-Br-rod LDH (**Figure 2-7** (a)) clearly demonstrate the hexagonal prismatic morphology of all three samples. The SAED patterns show that the samples are single crystals. In the high resolution TEM image of the **LiAl-Cl-rod** LDH (**Figure 2-8**), lattice fringes can clearly be seen, demonstrating that the brucite-layers in LDHs do indeed stack along the *c*-axis to form a one-dimensional nanostructure. The line profile

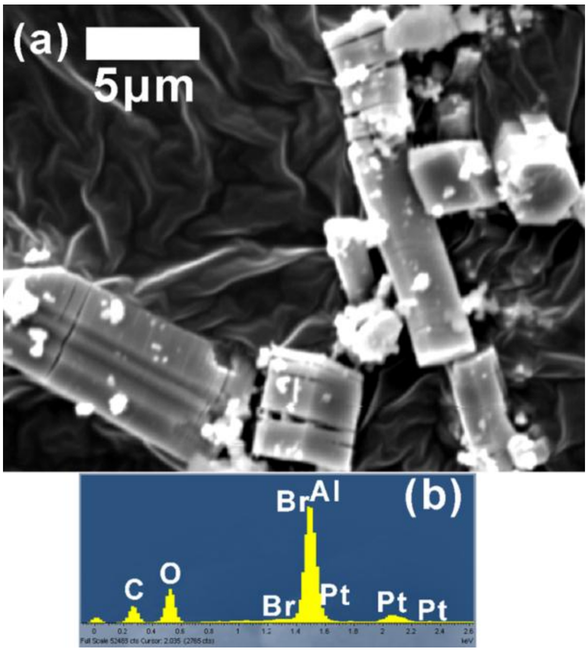

Figure 2-7: (a) SEM image and (b) EDX spectrum of **LiAl-Br-rod**.

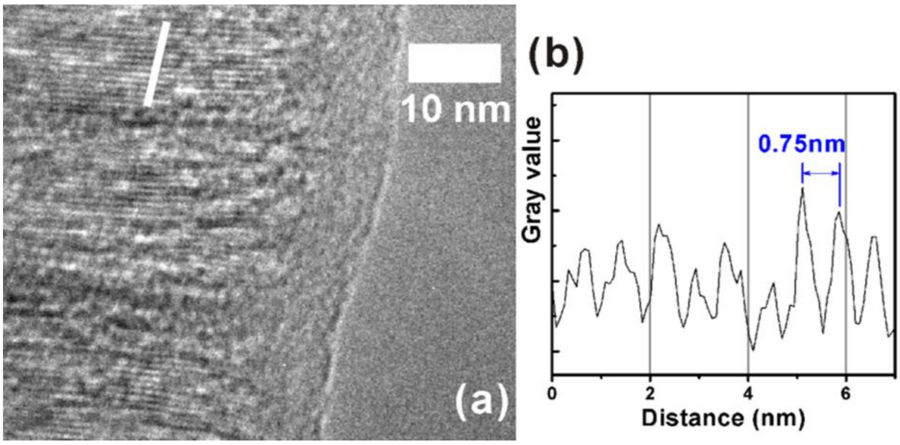

Figure 2-8: (a) High resolution TEM image of **LiAl-Cl-rod** and (b) line profile perpendicular to the *c*-axis along with the white line in (a).

along the lamellar layers (**Figure 2-8** (b)) illustrates an interlamellar separation, *d*, of *approx.* 0.75 nm, which agrees well with the interlayer separation calculated from the XRD data.

The intercalation of halide ions into gibbsite can be further confirmed by Energy-dispersive X-ray Spectroscopy (EDX) (**Figure 2-5** (c) & **Figure 2-6** (c) & **Figure 2-7** (b)). In **rod-Gibbsite**, oxygen and aluminium are the only elements present, whereas in the LDH compounds, chloride or bromide are present too (any carbon detected originates from the conductive adhesive carbon tabs, whilst platinum may be detected from the thin platinum layer deposited over the samples that increases conductivity).

2.3. Intercalation of cyclamate into LiAl-Cl-rod

It is found that the **LiAl-X-rod** (X = Cl, Br) behave as conventional LDHs and so can engage in further anion exchange chemistry. For example, treatment of **LiAl-Cl-rod** with sodium cyclamate gives **LiAl-cyclamate**, which is chemically similar to the material reported by Markland *et al.*[35] with an interlayer separation of 20.86 Å (**Figure**

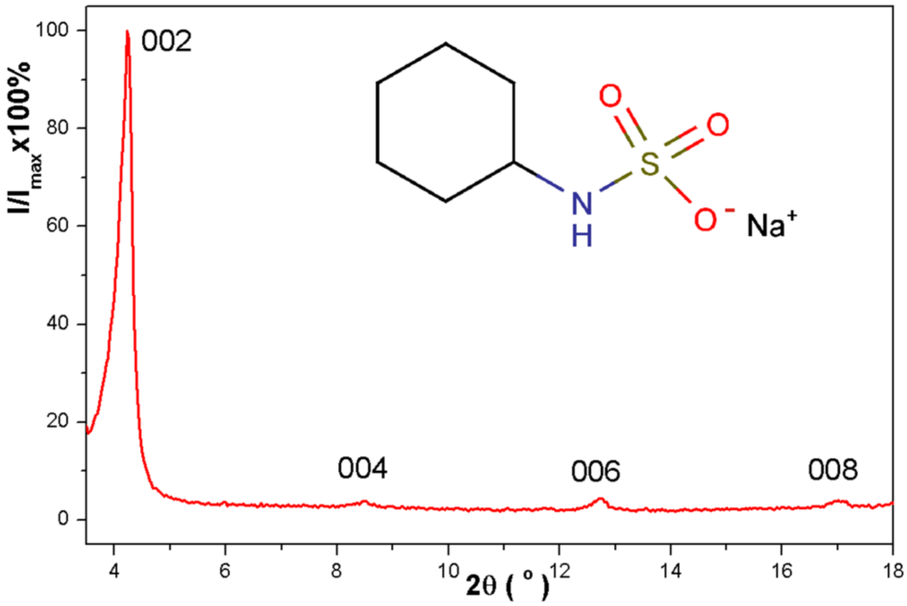

Figure 2-9: XRD pattern of **LiAl-cyclamate**. (Inset: structure of sodium cyclamate.)

2-9). There is therefore potential to widen application of this method to the synthesis of a range of rod-like LDHs intercalation compounds.

Figure 2-10 shows the FT-IR spectra of **LiAl-cyclamate** (a) and pure sodium cyclamate (b). **LiAl-cyclamate** has similar characteristic absorptions to other Li-Al LDHs. However, due to the intercalation of cyclamate between the layers, the spectrum of **LiAl-cyclamate** also contains the characteristic absorptions of cyclamate. Compare the spectra of **LiAl-cyclamate** with that of pure sodium cyclamate, the absorption of stretching vibrations of N-H bonds (ν_{NH}) at *ca.* 3275 cm^{-1} appears as a shoulder overlapped by the broad absorption of O-H stretching vibration. The two absorptions at *ca.* 2930 and 2855 cm^{-1} are due to the stretching vibrations of C-H bonds in the cycloaliphatic ring, while the absorption at *ca.* 1433 cm^{-1} is assigned to the bending vibrations of the C-H bonds in the cycloaliphatic ring. The absorptions close to the fingerprint region are complicated, but we can still separate the asymmetrical and symmetrical bending vibrations of the S=O bonds at 1168 cm^{-1} ($\delta_{asyS=O}$) and 1037 cm^{-1}

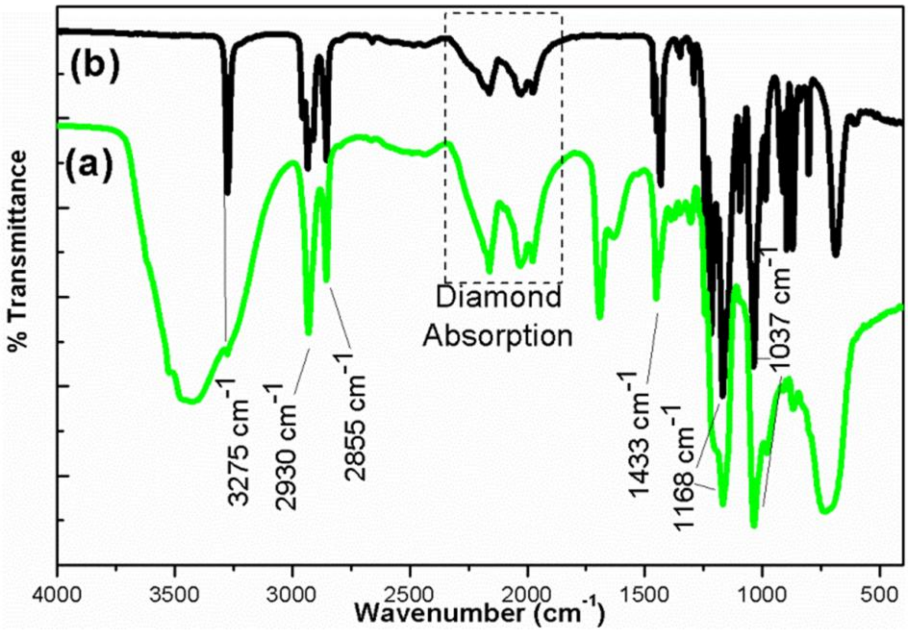

Figure 2-10: FT-IR spectra of (a) **LiAl-cyclamate** and (b) pure sodium cyclamate.

($\delta_{symS=O}$), respectively. The IR spectra verified the incorporation of cyclamate into **LiAl-Cl-rod** LDH.

The CHN elemental analysis (**Table 2-2**) further verifies that the cyclamate is intercalated.

An SEM image (**Figure 2-11**) shows that the **LiAl-cyclamate** sample retain its

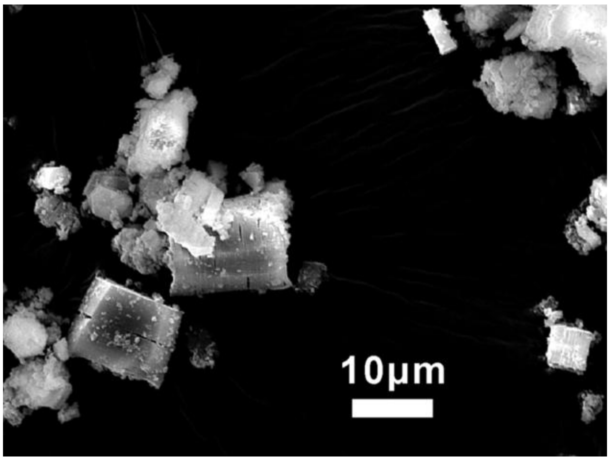

Figure 2-11: SEM image of **LiAl-cyclamate**.

rod-like morphology, although the rods become shorter and more fragments can be seen, which suggests the intercalation of larger ions makes the rod more fragile and prone to break apart.

2.4. Discussion

The mechanism of intercalation of lithium salts into Gibbsite has been extensively investigated by O'Hare and co-workers[5, 36-38] using time-resolved *in situ* X-ray diffraction. The reaction is believed to be a direct process involving a nucleation-growth mechanism whereby instantaneous nucleation is followed by two-dimensional diffusion controlled growth.[36]

Instantaneous nucleation refers to a situation in which all the potential nucleation sites (*i.e.* the edges of the layers) are saturated at the start of the reaction. The rate-limiting step is then likely to be expansion of the interlayer spaces to accommodate the first guest species to intercalate. Once a pair of layers has been prised apart, the guests are free to diffuse into the interlayer region (hence 2D diffusion). Once the Li-Cl ion pair is accommodated between the layers, it is likely that it will be facile for the Li^+ cations to occupy the voids in the layers. This process allows the host to maintain its original morphology during the intercalation reaction. **Figure 2-12** is a schematic illustration of this process for a rod-like morphology host. The intercalation of the halide anions causes an increase in the interlayer separation from *ca*. 0.48 nm to *ca*. 0.75 nm, with the net effect is that these rods increase in length by over 50 % during this process. An extension of this method to other M-Al LDH nanorods, such as M = Co, Ni, Cu, Zn, can be expected providing the intercalation does not cause destruction of the morphology of the host.

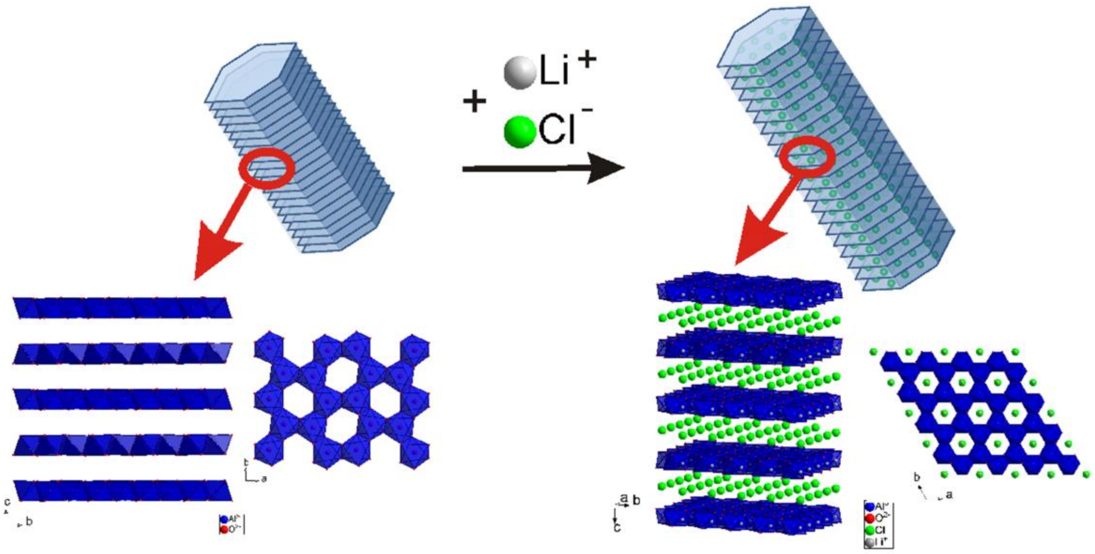

Figure 2-12: Schematic representation of the formation of **LiAl-Cl-rod** LDH nanorods.

Previous kinetics experiments have revealed that intercalation of lithium salts into gibbsite is reversible. Typically, intercalation reactions can be driven to completion using 4 - 20 M lithium halide solutions at 60 °C.[5] Here, however, we find that intercalation into the **rod-Gibbsite**, requires more highly concentrated solutions and higher temperatures in order to reach completion. For the synthesis of LiAl-NO_3 LDH nanorods, even a saturated solution of $LiNO_3$ was not sufficient to drive the reaction to completion. The origin for this kinetic behaviour is still unclear, however, as the reaction was thought to be nucleated at crystal defects on either basal plane surfaces or edge planes of the host crystallite, it could be that the rod-like gibbsite crystallites are more rigid or provide fewer nucleation sites for intercalation.

2.5. Conclusion

In conclusion, nanorods of LiAl-X have been synthesised by the topotactic intercalation of LiX (X = Cl, Br) into a rod-like polymorph of gibbsite, while the intercalation of $LiNO_3$ does not fully intercalate by this method. XRD and TEM reveal that the longest rod-axis corresponds to the layer stacking axis of the LDH. **LiAl-X-rod** (X = Cl, Br) can further undergo anion exchange intercalation, as demonstrated by the intercalation of cyclamate into **LiAl-Cl-rod**.

2.6. References

1. L. Pesic, S. Salipurovic, V. Markovic, D. Vucelic, W. Kagunya and W. Jones, *J. Mater. Chem.*, 1992, **2**, 1069-1073.
2. V. Rives, F. M. Labajos, M. A. Ulibarri and P. Malet, *Inorg. Chem.*, 1993, **32**, 5000-5001.
3. A. I. Khan and D. O'Hare, *J. Mater. Chem.*, 2002, **12**, 3191-3198.
4. P. S. Braterman, Z. P. Xu and F. Yarberry, in *Handbook of layered materials*, Marcel Dekker, New York, Editon edn., 2004, pp. 373-474.
5. A. V. Besserguenev, A. M. Fogg, R. J. Francis, S. J. Price, D. O'Hare, V. P. Isupov and B. P. Tolochko, *Chem. Mater.*, 1997, **9**, 241-247.
6. A. Fogg, A. Freij and G. Parkinson, *Chem. Mater.*, 2002, **14**, 232-234.
7. A. M. Fogg and D. O'Hare, *Chem. Mater.*, 1999, **11**, 1771-1775.
8. G. R. Williams, T. G. Dunbar, A. J. Beer, A. M. Fogg and D. O'Hare, *J. Mater. Chem.*, 2006, **16**, 1231-1237.
9. G. R. Williams, T. G. Dunbar, A. J. Beer, A. M. Fogg and D. O'Hare, *J. Mater. Chem.*, 2006, **16**, 1222-1230.
10. S. Britto and P. Kamath, *Inorg. Chem.*, 2009, **48**, 11646-11654.
11. M. Ogawa and Y. Sugiyama, *J. Ceram. Soc. Jpn.*, 2009, **117**, 179-184.
12. H. C. Greenwell, W. Jones, S. L. Rugen-Hankey, P. J. Holliman and R. L. Thompson, *Green Chemistry*, 2010, **12**, 688-695.
13. A. M. Fogg, G. R. Williams, R. Chester and D. O'Hare, *J. Mater. Chem.*, 2004, **14**, 2369-2371.
14. M. Fleischer, R. G. Burns, L. J. Cabri, C. A. Francis and A. Pabst, *Am. Mineral.*, 1982, **67**, 413-418.
15. R. Chitrakar, Y. Makita, A. Sonoda and T. Hirotsu, *J. Hazard. Mater.*, 2011, **185**, 1435-1439.
16. G. R. Williams, S. J. Moorhouse, T. J. Prior, A. M. Fogg, N. H. Rees and D. O'Hare, *Dalton Trans.*, 2011, **40**, 6012-6022.
17. M. Nayak, T. R. N. Kutty, V. Jayaraman and G. Periaswamy, *J. Mater. Chem.*, 1997, **7**, 2131-2137.
18. M. Jakupca and P. K. Dutta, *Chem. Mater.*, 1995, **7**, 989-994.
19. P. K. Dutta and D. S. Robins, *Langmuir*, 1994, **10**, 1851-1856.
20. S. Cooper and P. K. Dutta, *J. Phys. Chem.*, 1990, **94**, 114-118.
21. G. Cao and Y. Wang, *Nanostructures and nanomaterials: synthesis, properties, and applications*, World Scientific, 2010.
22. Z. P. Xu and P. S. Braterman, *J. Mater. Chem.*, 2003, **13**, 268-273.
23. Y. Q. Sun, Y. M. Zhou, Z. Q. Wang and X. Y. Ye, *Appl. Surf. Sci.*, 2009, **255**, 6372-6377.
24. H. Liu, Q. Jiao, Y. Zhao, H. Li, C. Sun and X. Li, *J. Alloys Compd.*, 2010, **496**, 317-323.

25. Z. P. Xu, M. Niebert, K. Porazik, T. L. Walker, H. M. Cooper, A. P. J. Middelberg, P. P. Gray, P. F. Bartlett and G. Q. Lu, *J. Controlled Release*, 2008, **130**, 86-94.
26. Y. Sun, Y. Zhou, Z. Wang and X. Ye, *Appl. Surf. Sci.*, 2009, **255**, 4497-4502.
27. Y. Zhao, F. F. Xiao and Q. Z. Jiao, *Bull. Mater. Sci.*, 2008, **31**, 831-834.
28. H. Wu, Q. Jiao, Y. Zhao, S. Huang, X. Li, H. Liu and M. Zhou, *Mater. Charact.*, 2010, **61**, 227-232.
29. Y. Liu, D. Ma, R. A. Blackley, W. Z. Zhou, X. W. Han and X. H. Bao, *J. Phys. Chem. C*, 2008, **112**, 4124-4128.
30. M. Murakami, A. Segmuller and K.-N. Tu, *Treatise on materials science and technology*, Academic Press, 1988.
31. W. A. Dollase, *J. Appl. Crystallogr.*, 1986, **19**, 267-272.
32. A. March, *Z. Kristallogr.*, 1932, **81**, 285-297.
33. A. C. Larson and R. B. Von Dreele, *General Structure Analysis System (GSAS)*, Los Alamos National Laboratory Report LAUR 86-748, 2004.
34. A. M. Fogg, D.Phil Thesis, University of Oxford, 1998.
35. C. Markland, G. R. Williams and D. O'Hare, *J. Mater. Chem.*, 2011, **21**, 17896-17903.
36. G. R. Williams and D. O'Hare, *J. Phys. Chem. B*, 2006, **110**, 10619-10629.
37. G. R. Williams and D. O'Hare, *Chem. Mater.*, 2005, **17**, 2632-2640.
38. G. R. Williams, A. I. Khan and D. O'Hare, in *Structure Bonding: Layered Double Hydroxides*, Editon edn., 2006 pp. 161-192.

Chapter 3

Reverse micelle directed nucleation and growth of Co and Ni containing LDHs

3.1. Introduction

Layered double hydroxides (LDHs) are a family of layered materials with the composition $[M^{z+}_{1-x}M^{3+}_{x}(OH)_2]^{a+}(X^{n-})_{a/n}\cdot mH_2O$. In the majority of cases $z = 2$, and the M^{2+} and M^{3+} cations can be chosen from a wide variety of metals,[1-4] while X^{n-} is a charge-balancing organic or inorganic anion. The structure of LDHs can be considered to comprise positively charged brucite-like layers of mixed metal hydroxides with charge-balancing anions and water molecules in the interlayer space.[1, 3, 4]

Although many synthetic methods have been reported, the co-precipitation method, which involves the steady mixing of a solution of metal cations and a basic solution under vigorous stirring, is the most widely used.[5-7] Recently, to avoid the rapid precipitation of the more insoluble metal hydroxide in the mixing region, another method has been exploited, the so-called “homogeneous precipitation” method. This is a process whereby one of the reagents in the formation of a highly insoluble material is gradually generated *in situ*, by the slow hydrolysis of urea or hexamethylenetetramine (HMT), thus avoiding massive supersaturation while mixing reagents. This method reduces the number of nuclei, therefore generating larger, better crystalline product particles. This method was first successfully applied to the synthesis of Mg-Al LDH,[8-13] and has been extended to Co-Al, Zn-Al, Fe-Al LDH and other ternary compounds.[14-19]

Although the synthesis of LDHs has been studied thoroughly, in monophasic systems, the particle size and the particle size distribution of the LDHs usually cannot be controlled with the desired precision. Albiston *et al.* used a so-called salt-oxide method to prepare Mg-Al LDH particles with sizes of 60 - 770 nm. However, in this method, the LDH particles produced were intensely agglomerated.[20] Zhao *et al.* prepared Mg-Al LDH particles with uniform crystallite size by separating the nucleation and aging steps.[21] In this method, the metal salt solution and the base solution were mixed simultaneously in a colloidal mill rotating at 3000 rpm for 2 minutes. The slurry was then removed and aged at 100 ℃ for 13 hours. Xu *et al.* further investigated the influence of the aging time, temperature and concentration.[22] More recently, Hu *et al.* reported the use of a reverse micelle/microemulsion method to synthesise controlled size Mg-Al LDH nanoplatelets: this “bottom up” approach provides an excellent method for controlling LDH nucleation and growth.[23]

Reverse micelle/microemulsion systems are ternary systems containing water (aqueous solutions of salts for synthetic purposes), oil, and surfactants. In the microemulsion system, the hydrocarbon chains of the surfactant tend to self-associate to minimize contact with the water molecules. For a system containing a small amount of water with $\omega < 12 - 15$ (ω is the molar ratio of water to surfactant), micelles appear with the hydrophilic heads of the surfactant molecules aggregating inside and the hydrophobic chains sticking out into the oil phase. The size of the “water pools” encapsulated by the surfactant molecules can be adjusted by varying the molar ratio of water to surfactant. This method has been successfully extended to Fe hydroxides,[24] Ni-Al LDH,[25, 26] and Zn-Co-Fe LDH.[27]

The magnetic properties of layered metal hydroxides such as $[M_2(OH)_3]X$ (M = Co^{2+}, Cu^{2+}; X = anionic guest) have been extensively studied and are prototype models for the competition between in-plane magnetic superexchange interactions and long-range inter-plane dipolar interactions.[28-33] Modulation of these interactions can be achieved by varying the interlayer separation through the intercalation of anion surfactants of varying length, or other organic molecules.[34-38] In contrast the magnetic properties of LDHs containing transition metals have been much less developed.[39-41] Recently, Coronado and co-workers have carried out an extensive study of the composition dependence of the magnetic properties of $[Ni_{3-x}Cr_x(OH)_6(CO_3)_{x/2}.yH_2O]$ (x = 0.69 - 0. 93).[42]

In this chapter, uniformly dispersed magnetic LDH crystallites were prepared in the size regime in which the magnetic properties are dependent on the size of the platelets. Dispersible superparamagnetic[43] layered hydroxide nanoplatelets would be of significant interest as properties such as macroscopic quantum tunnelling (MQT)[44, 45] are of essential importance to the technological application of magnetic nanoparticles in high-density data storage[46] and as magnetic carriers for site-specific drug delivery.[47]

3.1.1. Reverse microemulsion

The term ‘microemulsion’ was first coined by Hoar *et al.* in 1943,[48] and referred a water/surfactant/oil ternary system. A reverse microemulsion is a transparent system in which the oil is the continuous phase with dispersed reverse micelles.

Normally, surfactants are molecules with a polar hydrophilic head and a hydrophobic hydrocarbon chain. According to the composition of their heads, they can be classified as anionic (*e.g.* sodium dodecylsulphate, SDS), cationic (*e.g.* cetyltrimethylammonium chloride, CTAC, or cetyltrimethylammonium bromide, CTAB) and neutral. According to their tail numbers, there are single-tailed and double-tailed surfactants (*e.g.* sodium bis(2-ethylhexyl) sulphosuccinate, NaAOT).[49] Single-tailed surfactants with large heads possess a cone shape, while double-tailed surfactants usually have a champagne cork shape with the branched chains. When the surfactant reaches its critical micelle concentration (CMC), micelles appear with the hydrophilic heads of the surfactant molecules aggregating inside and the hydrophobic chains sticking out into the oil phase. By adjusting the amount of oil and water, the shape and dimension of the aggregates changes to interconnected water channels, or cylinders, or other complicated microstructures.[49] The spontaneous curvature for reverse micelles corresponds to the energetically favourable packing configuration of the surfactant molecules at the interface, which basically depends on the molecular geometry of the surfactant.[50, 51] It has been proved that in the range of $\omega < 12 - 15$ (ω is the molar ratio of water to surfactant), the radii of the micelles are roughly proportional to ω, though they can be affected by many other parameters such as temperature, pressure and solubility of oil phase.[52-55] The "water pools" encapsulated by surfactants are not permanent but exchanging dynamically. The mobility of the micelles can be characterised by measuring surface tension, conductivity, light scattering, self-diffusion, and the molality of dissolved compounds.[56, 57]

Although the oil phase performs as a solvent, the structure and properties of the oil phase have an effect on the formation of micelles, such as inducing the curvature.[50, 58] On repeating the synthesis reported by Hu *et al.*,[23] the solvent, isooctane, was replaced by other organic solvents (**Table 3-1**). The results indicated that not all alkanes are able to form microemulsion, however the reasons are still unclear.

Table 3-1: Summary of various common organic solvents that form microemulsions.

Organic Solvents	Formation of microemulsion
Isooctane	Yes
Pentane	Yes
Hexane	Yes
Heptane	Yes
Cyclohexane	No
Cyclohexene	Yes
Dichloromethane	Yes
1, 2-Dichloroethane	Yes
Chloroform	Yes
Benzene	Yes
Toluene	No
60-80 ℃ bp. Petroleum Spirit	Yes

3.1.2. Synthesis of nanoparticles in reverse microemulsions

Reverse microemulsion synthesis is an example of kinetically controlled growth, which is to spatially confine the growth so that the growth stops when the limited amount of source materials is consumed or the available space is filled up.[59] Not only inorganic reactions but organic and biological reactions have been carried out in reverse microemulsions.[60-62] The major advantage of synthesising nanoparticles in reverse microemulsions is the adjustable size of the microreactors, which can result in size-controllable nanoparticles.[63]

Assuming micelles are spherical, the radius of the sphere can be expressed as **Equation 3-1** where R, V, and Σ are the radius, the volume and the surface area of the sphere. Assuming all the surfactant molecules are arranged at the interface, the radius of the water pool is approximately equal to the sphere radius, as it is proportional to the molar ratio of water to surfactant, ω, as in **Equation 3-2** where V_{aq} is the volume of water molecule, and σ is the area of the polar head of surfactant molecule. Various experiments such as small-angle X-ray scattering (SAXS) and small angle neutron scattering (SANS) have confirmed the linear variation.[52, 54, 64]

$$\mathrm{R} = \frac{3V}{\Sigma}$$

Equation 3-1

$$R_w = R = \frac{3V_{aq}[H_2O]}{\sigma[S]} = \frac{3V_{aq}}{\sigma}\frac{[H_2O]}{[S]} \propto \omega$$

Equation 3-2

Reverse microemulsion systems have been applied extensively for the synthesis metallic nanoparticles (NPs),[65-72] bimetallic nanoparticles,[73-75] silica,[76] oxides,[66, 77-80] semiconductor,[81, 82] quantum dots,[83] polymer particles[84-86] and other materials. Not only zero-dimensional (0D) nanoparticles but also one-dimensional (1D) nanorods and nanowires[82] and core-shell structures[87-92] could form in these systems with controllable sizes. Effects of stabilizer (emulsifier) type and concentration and the type of continuous phase, reducing agent and additive on the particle formation are summarized and evaluated.[93]

3.2. Results and discussion

3.2.1. Synthesis

In previously reported LDH syntheses in reverse microemulsions, the aqueous solutions and oil phases were prepared separately before being mixed together. However, in this chapter, stable reverse microemulsions without metal ions were prepared before the solid metal salts and urea/HMT were added to the microemulsion (**Figure 3-1**). The total volume of water and the consistency of metal salts and urea in the three systems were kept constant while the amount of surfactant was adjusted. These conditions were employed to ensure that the total volume of spheroidal reverse micelles in the three systems was constant. The use of more surfactant will result in smaller micelles.

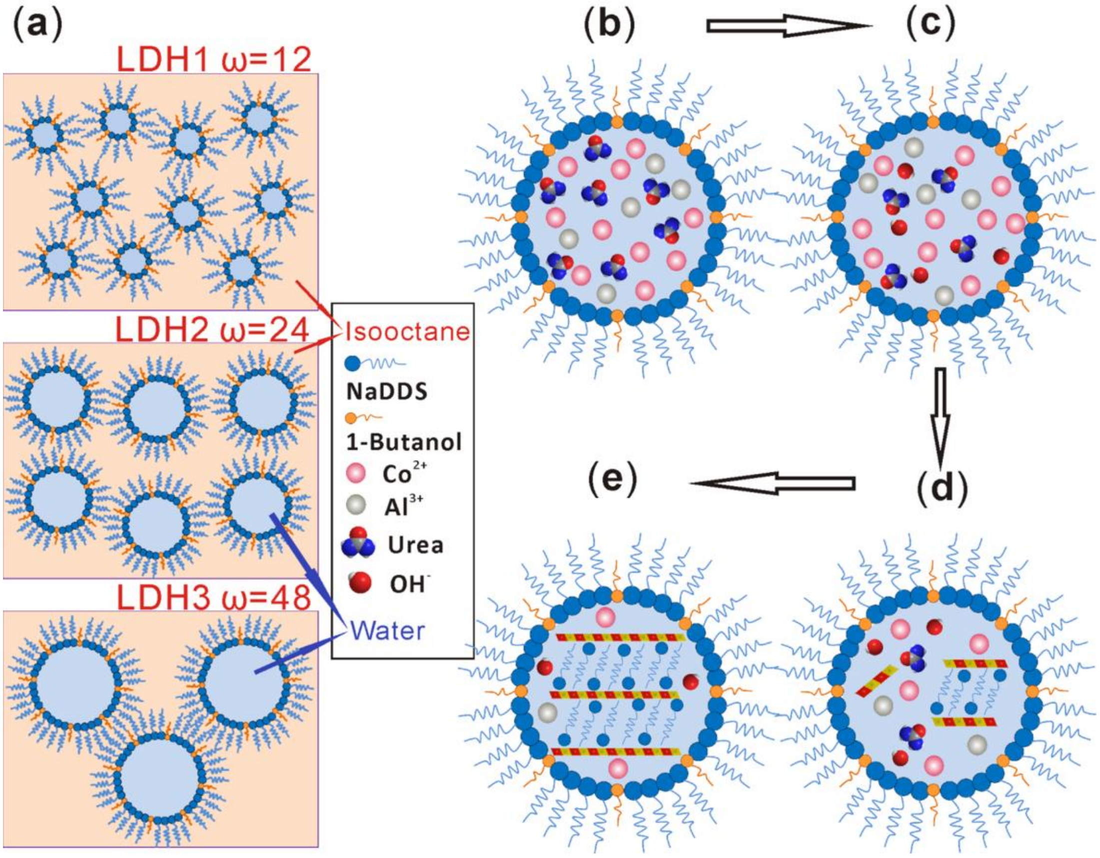

Figure 3-1: Schematic representation of the formation of LDH nanoplatelets in a reverse microemulsion: (a) Three microemulsions with different water to surfactant ratios; (b) the mixture of metal salts and urea inside a micelle; (c) the urea begins to undergo hydrolysis; (d) the LDH phase starts to crystallize; (e) the final product in a "water pool".

Stable and transparent microemulsions were formed by mixing sodium dodecyl sulphate, isooctane and deionized water and then dropwise addition of 1-butanol. The microemulsions gave an initial pH of around 6.7. Metal salts and urea/HMT were then dissolved in the emulsion, and the systems turned to a transparent pink/green colour with a pH of 2.2, which indicated that the hydrolysis of urea/HMT was slow and had not yet created sufficient OH^- ions to form LDH nuclei. Upon refluxing, the microemulsions became cloudy and reached a final pH of around 7. In reverse microemulsion systems, the water-in-oil droplets are assumed to be spherical and the water pool radius linearly correlated with the water content.[23] In practice, although some other parameters such as the solvent, temperature, number and size of droplets, and addition of solutes should be considered, it is still reasonable to assume that the radius of the water pool is largely dependent on water content. A larger ω value leads to the formation of larger water pools, thus larger LDH particles are expected with increasing ω.

Employing microemulsion systems with ω = 12, 24 and 48 allowed the isolation of six different LDH samples, **CoAl-RM*n*** (*n* = 1 - 3) and **NiAl-RM*n*** (*n* = 1 - 3). For comparison, we also prepared a conventional Co-Al LDH sample containing intercalated dodecyl sulphate (DDS) (**CoAl-Bulk**). Detailed experimental procedures are listed in **Chapter 7**.

3.2.2. Elemental analysis

The elemental analysis data (**Table 3-2**) indicates that the Co/Al molar ratio for each of **CoAl-RM*n*** (*n* = 1 - 3) samples is about 1.6, and is 2 for **CoAl-Bulk**. The Ni/Al molar ratio for **NiAl-RM*n*** (*n* = 1 - 3) samples is about 2.4. The data are consistent with a common chemical formulation of $[Co_{1.9}Al_{1.1}(OH)_6](C_{12}H_{25}SO_4)_x(OH)_{1.1-x}\, yH_2O$ (*x ca.* 0.8; *y ca.* 2 - 6) for the Co-Al LDHs, while for the Ni-Al LDHs, the general formulation can only be roughly calculated as $[Ni_{2.1}Al_{0.9}(OH)_6](C_{12}H_{25}SO_4)_x(OH)_{0.9-x}$ (*x ca.* 0.5).

Table 3-2: Summary of elemental analysis data for **CoAl-RM*n*** (n = 1 - 3), **CoAl-Bulk**, and **NiAl-RM*n*** (n = 1 - 3).

Sample	Observed (*calc.*) (%)				Calc. Formula
	Co / Ni	Al	C	H	
CoAl-RM1	19.51	5.86	25.43	6.54	$[Co_{1.8}Al_{1.2}(OH)_6](DDS)(OH)_{0.2} \cdot 2.7H_2O$
	(19.01)	(5.80)	(25.83)	(6.61)	
CoAl-RM2	19.76	5.20	20.97	6.34	$[Co_{1.9}Al_{1.1}(OH)_6](DDS)_{0.8}(OH)_{0.3} \cdot 5.7H_2O$
	(19.86)	(5.26)	(20.45)	(6.74)	
CoAl-RM3	20.73	5.83	20.72	6.23	$[Co_{1.9}Al_{1.1}(OH)_6](DDS)_{0.8}(OH)_{0.3} \cdot 4.2H_2O$
	(20.86)	(5.53)	(21.48)	(6.52)	
CoAl-Bulk	21.00	5.13	21.72	5.90	$[Co_2Al(OH)_6](DDS)_{0.8}(OH)_{0.2} \cdot 4.5H_2O$
	(21.68)	(4.96)	(21.21)	(6.53)	
NiAl-RM1*	35.89	7.00	22.26	5.50	$[Ni_{2.1}Al_{0.9}(OH)_6](DDS)_{0.5}(OH)_{0.4}$
	(31.68)	(6.24)	(18.52)	(4.90)	
NiAl-RM2*	37.16	7.08	24.22	6.53	$[Ni_{2.1}Al_{0.9}(OH)_6](DDS)_{0.5}(OH)_{0.4}$
	(31.68)	(6.24)	(18.52)	(4.90)	
NiAl-RM3*	48.46	10.50	25.65	6.34	$[Ni_2Al(OH)_6](DDS)_{0.4}(OH)_{0.6}$
	(32.36)	(7.44)	(18.89)	(4.61)	

* The data for those samples are less accurate because the surfactant was insoluble when preparing samples for ICP.

3.2.3. Powder X-Ray diffraction

3.2.3.1. XRD data of Co-Al LDHs

Figure 3-2 shows the diffraction patterns for a **CoAl-RM*n*** (n = 1 - 3) and **CoAl-Bulk** samples. All of the four Co-Al LDH samples exhibit a series of (00l) Bragg reflections. These may be indexed as the Bragg reflections (00$\underline{3n}$, n = 1 - 7) for a rhombohedral (3R) sequence giving c-lattice parameters of between 77.38 and 78.22 Å for **CoAl-RM*n*** (n = 1 - 3) (**Table 3-3**). The position of the (110) Bragg reflections gives a direct measure of the a and b lattice parameters ($a = b = 2d_{110}$ = 3.05 - 3.06 Å) for **CoAl-RM*n*** (n = 1 - 3).[23] The measured interlayer spacing of 2.6 nm implies that the intercalated DDS^- ions adopt an interpenetrating anti-parallel arrangement with a 69 ° angle between the DDS chains and the LDH layer (**Figure 3-3**). This packing arrangement was proposed first by Takagi *et al.*[94] and has been generally accepted as the most favourable structure for DDS intercalated LDHs. A summary of the X-ray diffraction data is given in **Table 3-3**. For the **CoAl-RM*n*** (*n* = 1 - 3), samples the Bragg reflections are significantly broader than for the conventional bulk sample prepared by homogeneous precipitation and ion-exchange. As a result of the high background and broad peaks, it was not possible to calculate accurate particle sizes using the Scherrer equation. The results from Scherrer analysis suggest that the **CoAl-RM*n*** (*n* = 1 - 3)

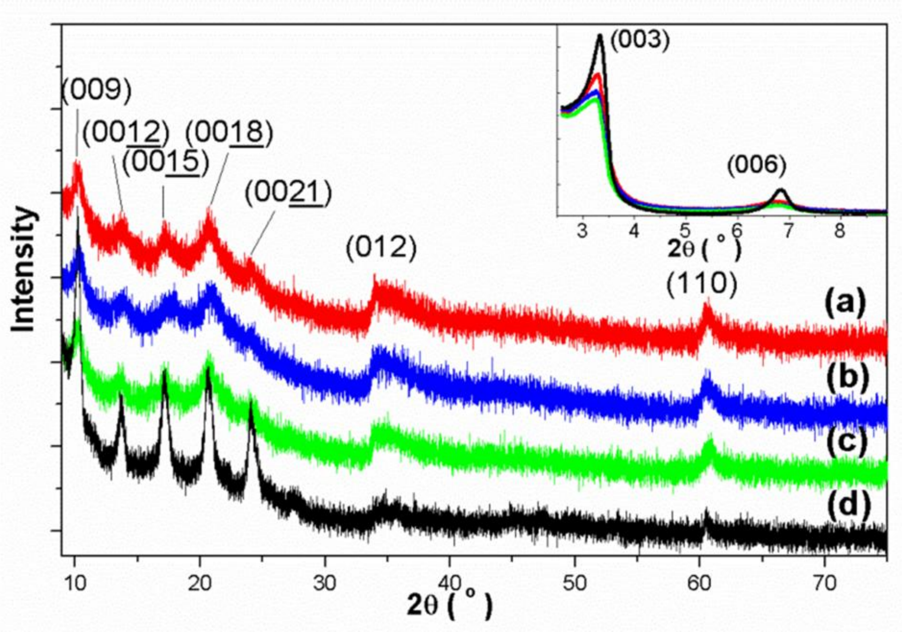

Figure 3-2: XRD patterns of (a) **CoAl-RM1**, (b) **CoAl-RM2**, (c) **CoAl-RM3** and (d) **CoAl Bulk**. (Inset: XRD patterns at low angle.)

Table 3-3: Summary of powder X-ray diffraction data for the LDH samples.

Sample	Bragg reflection (2θ: °)						Lattice parameters (Å)	
	003	006	009	0012	012	110	*a*	*c*
CoAl-RM1	3.28	6.74	10.24	13.69	33.98	60.51	3.060	78.22
CoAl-RM2	3.27	6.80	10.36	13.84	33.98	60.39	3.065	77.38
CoAl-RM3	3.27	6.77	10.22	13.68	33.93	60.36	3.049	78.22
CoAl-Bulk	3.34	6.83	10.23	13.72	34.25	60.56	3.058	78.07
NiAl-RM1	3.25	6.75	10.12	14.17	34.71	61.39	3.020	79.59
NiAl-RM2	3.36	6.64	10.38	13.96	35.15	61.41	3.019	78.48
NiAl-RM3	3.34	6.74	10.17	13.81	34.93	61.49	3.016	78.77

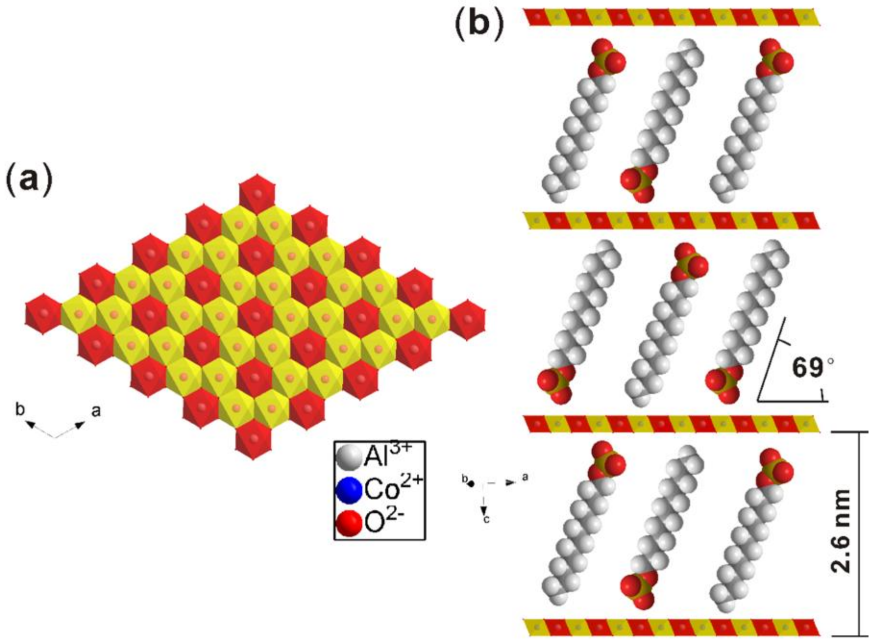

Figure 3-3: Schematic view of the structural model of **CoAl-RM*n*** *(n* = 1 - 3*)* (a) of the *a*, *b*-plane, (b) along the *c*-axis. Red octahedra are Al^{3+} centred, yellow are Co^{2+} centred.

crystallites size is around 100 nm in diameter (*a*, *b*-plane) and 30 - 40 nm in thickness (*c*-axis).

3.2.3.2. XRD data of Ni-Al LDHs

For the **NiAl-RM*n*** (*n* = 1 - 3) samples (**Figure 3-4**), their XRD patterns are similar to those of **CoAl-RM*n*** (*n* = 1 - 3), suggesting similar crystal structures. The calculated lattice parameters are given in **Table 3-3**. The *c* parameter can give a direct measure of the lamellar separation of *ca.* 26.4 Å.

The structures of **NiAl-RM*n*** (*n* = 1 - 3) samples are thought to be analogous to those of **CoAl-RM*n*** (*n* = 1 - 3), by replacing the Co^{2+} ions with Ni^{2+} ions. The calculation of particle sizes using Scherrer equation was not carried out due to lack of resolution.

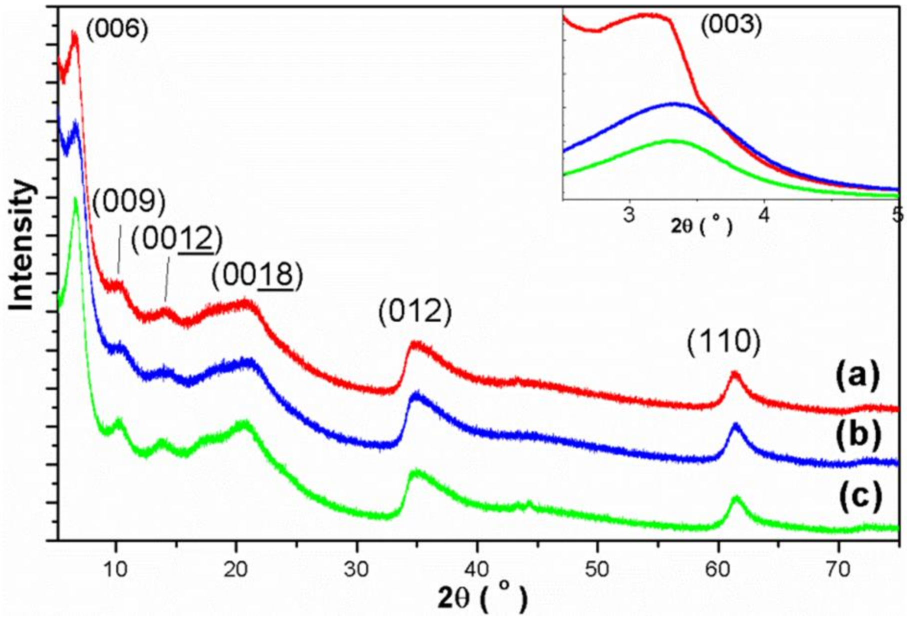

Figure 3-4: XRD patterns of (a) **NiAl-RM1**, (b) **NiAl-RM2**, and (c) **NiAl-RM3**. (Inset: XRD patterns at low angle.)

3.2.4. FT-IR spectroscopy

3.2.4.1. FT-IR spectroscopy of Co-Al LDHs

The IR spectra of **CoAl-RM*n*** (*n* = 1 - 3) and **CoAl-Bulk** samples are given in **Figure 3-5**. All the samples show three absorbances at 2850, 2918 and 2958 cm^{-1}, which are attributed to symmetric and asymmetric stretching vibrations of CH_2 (ν_{CH}) and the asymmetric stretching of CH_3 (ν_{CH}) from the dodecyl chain. The absorbances at *ca.* 1060 and 1196 cm^{-1} are assignable to the symmetric and asymmetric S=O stretching modes of the sulphate groups. In addition, a small absorbance appears at 1467 cm^{-1} together with two very weak signals at 1433 and 1364 cm^{-1} which can be attributed to CH_2 scissoring (δ_{CH}), and CH_3 asymmetric and symmetric bending (δ_{CH}) from the long dodecyl chains. The δ_{CH} absorbances from long $–(CH_2)_n–$ ($n \geq 4$) chains are visible on all the spectra at 720 cm^{-1}, which further verifies the existence of the dodecyl chain. The broad band centred at *ca.* 3450 cm^{-1} corresponds to a combination of the stretching

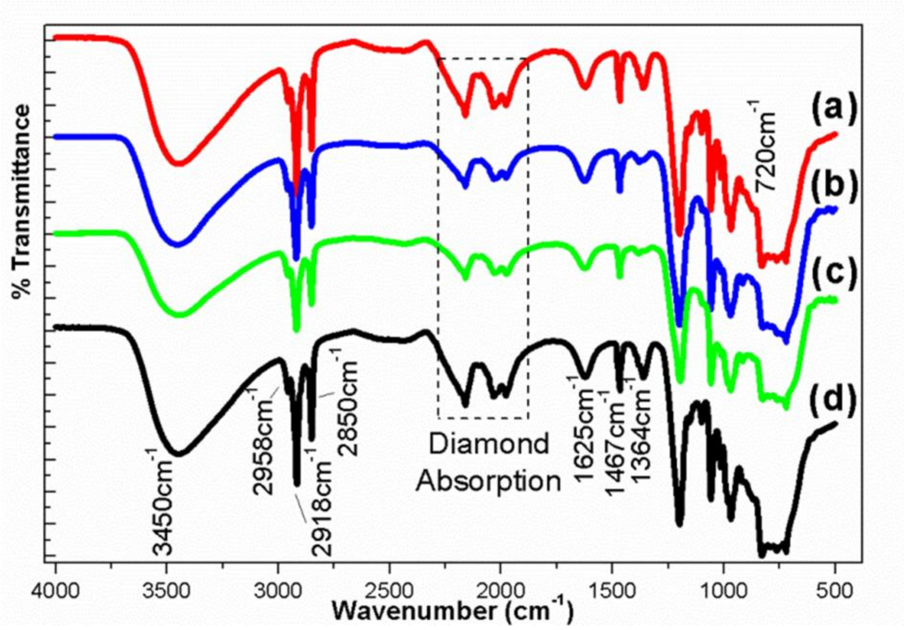

Figure 3-5: FT-IR spectra of (a) **CoAl-RM1**, (b) **CoAl-RM2**, (c) **CoAl-RM3**, and (d) **CoAl-Bulk**.

vibration of the hydroxide groups in the brucite sheets and the interlayer water molecules (ν_{OH}).[95] The absorbance at 1625 and 970 cm^{-1} are assigned to be the bending vibrations of the interlayer water molecules and the hydroxide groups in the brucite-like layers (δ_{OH}), respectively.[96] The IR spectra further confirm the incorporation of intact DDS anions into the LDH matrix.

3.2.4.2. FT-IR spectroscopy of Ni-Al LDHs

The IR spectra of **NiAl-RM*n*** (*n* = 1 - 3) are in **Table 3-6**. The spectra of Ni-Al LDHs and Co-Al LDHs are generally the same with a few slight differences in the fingerprint region. The extra absorption at *ca.* 600 cm^{-1} can be assigned to the vibration of M-O bonds. The IR spectra further confirm the structures of Ni-Al LDHs are based on those of Co-Al LDHs with the Co^{2+} ions in the brucite-like layers substituted by Ni^{2+} ions.

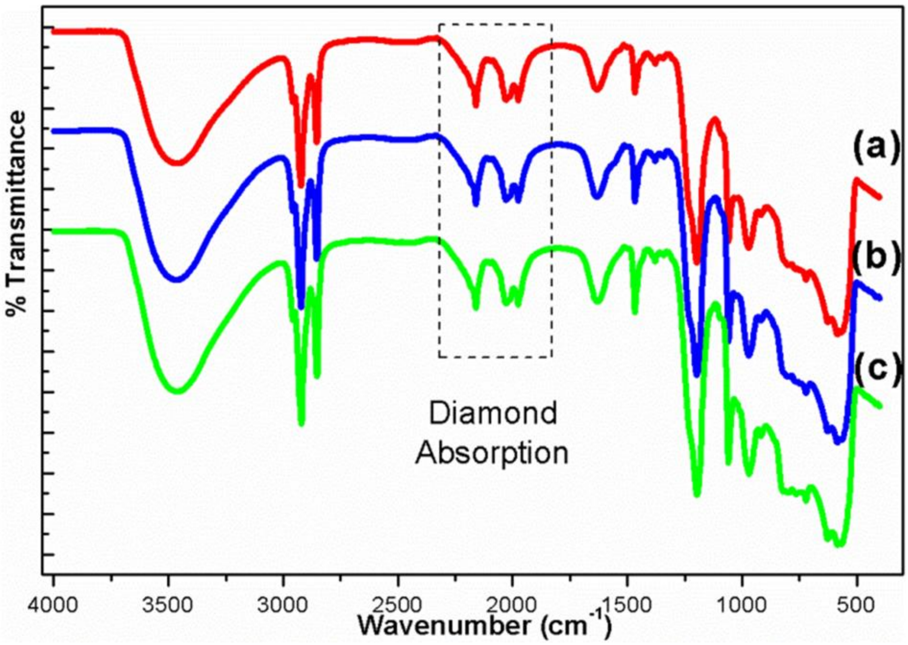

Figure 3-6: FT-IR spectra of (a) **NiAl-RM1**, (b) **NiAl-RM2**, and (c) **NiAl-RM3**.

3.2.5. UV-Vis spectroscopy

3.2.5.1. UV-Vis spectroscopy of Co-Al LDHs

High spin Co^{2+} ion in octahedral symmetry is expected to exhibit three spin-allowed *d-d* transitions (υ_1: $^4T_{1g}$-$^4T_{2g}$, υ_2: $^4T_{1g}$-$^4A_{2g}$, υ_3: $^4T_{1g}$-$^4T_{1g}$ (P)). The UV-Vis spectra of **CoAl-RM*n*** (*n* = 1 - 3) and **CoAl-Bulk** samples are depicted in **Figure 3-7**. All the samples show a broad absorbance around 8000 - 10000 cm^{-1} and an intense absorbance centred at 19000 cm^{-1}, which are assigned to the υ_1 and υ_3 transitions respectively. The υ_2 transitions are weak and appear as a shoulder at around 16000 cm^{-1}. Based on the transition energies observed in the spectra, the crystal field strength values Dq, the Racah parameters B_{Oh} and Dq/B (**Table 3-4**) can be calculated using **Equation 1-2,** and are in good agreement with those given in the literature (Dq = 920 cm^{-1}, and B_{Oh} = 825 cm^{-1}) for $[Co(OH)_6]^{4-}$.[97, 98]

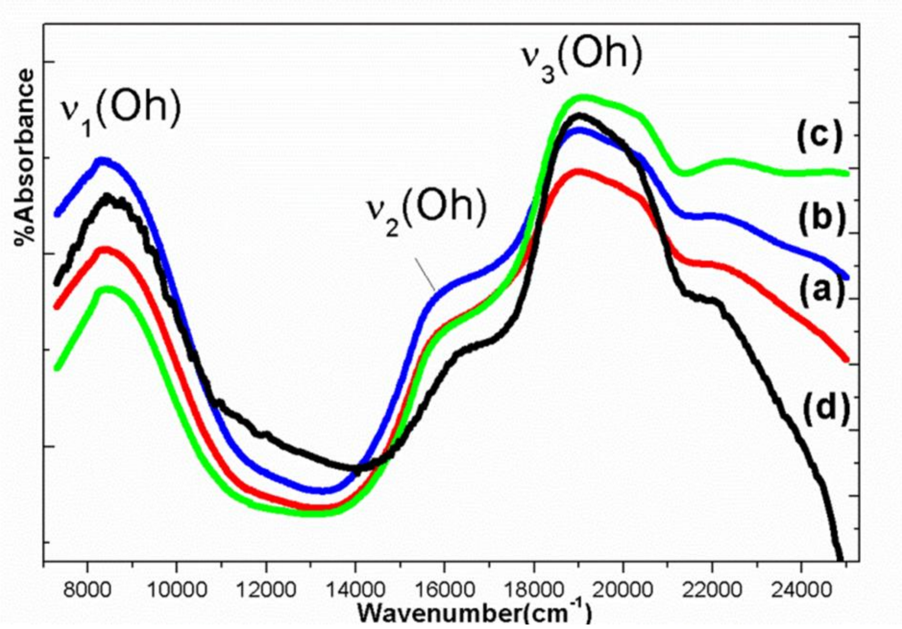

Figure 3-7: Diffuse reflectance UV-Vis spectra of (a) **CoAl-RM1**, (b) **CoAl-RM2**, (c) **CoAl-RM3**, and (d) **CoAl-Bulk**.

3.2.5.2. UV-Vis spectroscopy of Ni-Al LDHs

High spin Ni^{2+} ion in octahedral symmetry is expected to exhibit three spin-allowed *d-d* transitions (υ_1: $^3A_{2g}(F)$-$^3T_{2g}$, υ_2: $^3A_{2g}(F)$-$^3T_{1g}$, υ_3: $^3A_{2g}(F)$-$^3T_{1g}$ (P)),[98] which can be found in the spectra at *ca*. 9300 cm^{-1}, 15900 cm^{-1} and 27200 cm^{-1} respectively (**Figure 3-8**). In addition, two spin-forbidden bands can be seen as two shoulder peaks adjacent to υ_2 and υ_3, which are the transitions to ^1E_g and $^1T_{2g}$. Based on

Table 3-4: Summary of UV-Vis data of **CoAl-RM*n***, **CoAl-Bulk** and **NiAl-RM*n*** (*n* = 1 - 3).

Sample	υ_1	υ_2	υ_3	Dq	B	Dq/B
CoAl-RM1	8418	-	19048	953	783	1.22
CoAl-RM2	8371	-	19011	948	783	1.21
CoAl-RM3	8396	-	19157	951	792	1.20
CoAl-Bulk	8418	-	18975	952	778	1.22
NiAl-RM1	9294	15898	27174	929	1013	0.92
NiAl-RM2	9346	15898	27174	935	1002	0.93
NiAl-RM3	9234	15898	27174	923	1025	0.90

the transition energies observed in the spectra, the crystal field strength values Dq, the Racah parameters B_{Oh} and Dq/B are calculated using **Equation 1-3** and listed in **Table 3-4**. The data for $[Ni(H_2O)]^{2+}$ in literature are similar as Dq = 850 cm^{-1} and B_{Oh} = 907 cm^{-1}.

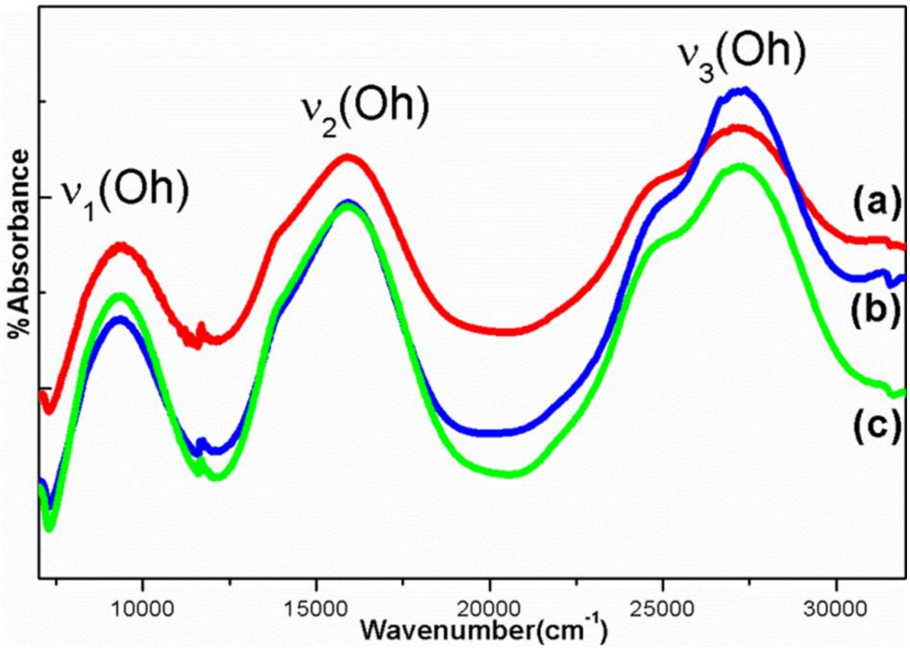

Figure 3-8: Diffuse reflectance UV-Vis spectra of (a) **NiAl-RM1**, (b) **NiAl-RM2**, and (c) **NiAl-RM3**.

3.2.6. Electron microscopy imaging

3.2.6.1. EM images of CoAl-RM*n* (*n* = 1 – 3)

All three **CoAl-RM*n*** (*n* = 1 - 3) samples were studied by high resolution transmission electron microscopy (**Figure 3-9**). From the low-magnification images given in **Figure 3-9**, the well-dispersed LDH platelets can be seen to present disc-like structures of around 100 - 200 nm in width, whereas some platelets are overlapped to generate aggregates of about 500 nm in width. Because the platelets are very thin, one platelet can often be seen through another. At the edge of the large aggregates, some

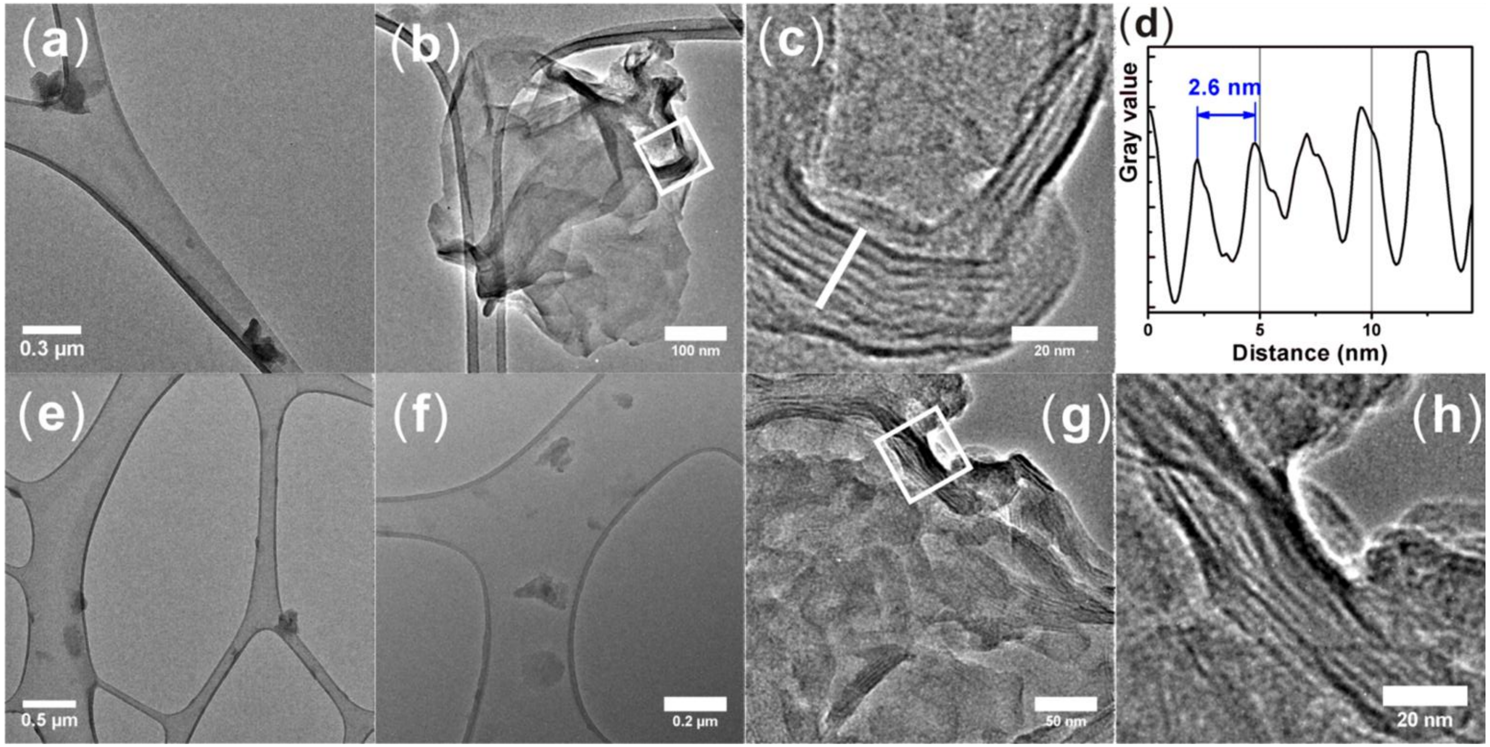

Figure 3-9: (a) Low magnification TEM image of dispersed **CoAl-RM1** single platelets. (b) Low magnification TEM image of an aggregate of **CoAl-RM2** platelets. (c) Higher magnification TEM image of the edge-on area indicated with the white box in (b). (d) Line profile perpendicular to the *c*-axis along with the white line in (c). (e) Low magnification TEM image of dispersed **CoAl-RM2** single platelets. (f) Low magnification TEM image of dispersed **CoAl-RM3** single platelets. (g) TEM image of an aggregate of **CoAl-RM3** platelets. (h) Higher magnification TEM image of the edge-on area indicated with the white box in (g).

platelets tend to curl. From the high-resolution images of the edge-on area, it is clear that the platelets of **CoAl-RM1** consist of 6 - 10 layers, while the **CoAl-RM3** particles are thicker (about 15 layers). A line profile along the lamellar layers is shown in **Figure 3-9** (d), which gives an interlamellar separation, *d*, of about 2.6 nm. This value agrees well with the interlayer separation calculated from XRD data.

3.2.6.2. EM images of CoAl-Bulk

The **CoAl-Bulk** sample was studied by both TEM and SEM. **Figure 3-10** shows that the particles of **CoAl-Bulk** are about 2 - 3 μm wide and 0.5 - 1 μm thick.

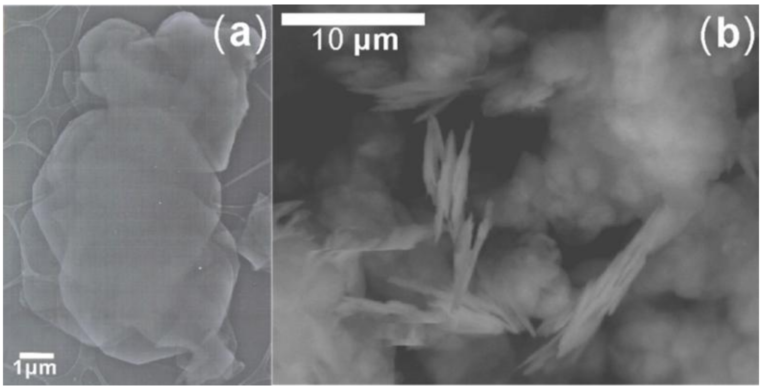

Figure 3-10: (a)TEM and (b)SEM images of **CoAl-Bulk**.

3.2.6.3. EM images of NiAl-RM*n* (*n* = 1 - 3)

The Ni-Al LDHs were studied using low magnification TEM (**Figure 3-11**). For all the samples, both large aggregates and dispersed single particles can be seen. The large aggregates are composed of thin and curly LDH sheets, while the single particles are round or oval platelets with uniform particle sizes. Due to the limitation of this technology, the thickness of the particles cannot be determined using TEM. However, the width of the single particles can be measured manually in order to determine the particle size distribution. The mean diameters, of the three samples are 28.7 nm for

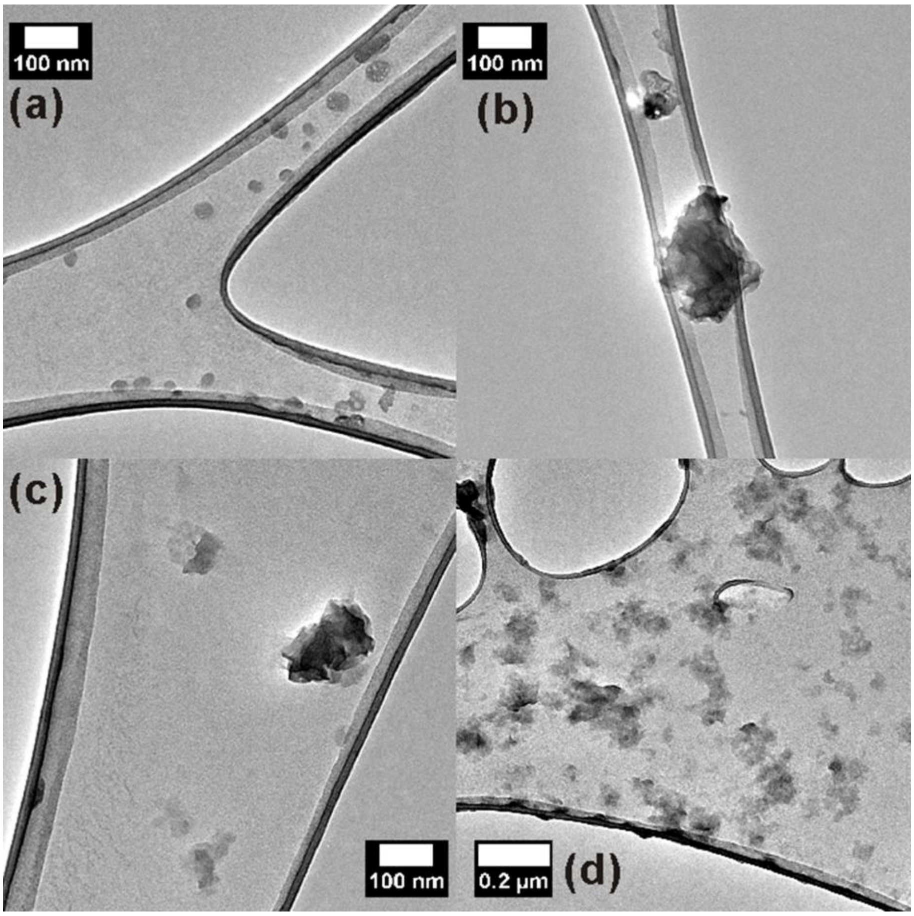

Figure 3-11: Low magnification TEM images of (a) & (b) **NiAl-RM1**, (c) **NiAl-RM2** and (d) **NiAl-RM3**.

NiAl-RM1, 37.3 nm for **NiAl-RM2**, and 46.8 nm for **NiAl-RM3**, which are proportional to the ratio of water to surfactant (ω).

3.2.7. AFM imaging and particle size analyses

3.2.7.1. AFM images and particle size analyses of CoAl-RM*n* (*n* = 1 - 3)

AFM in tapping mode has been successfully applied to characterize a number of clay materials, including in studies on the exfoliation and restacking of LDH materials. In this chapter, AFM was used to investigate the particle size and particle size distribution of the nanoplatelets.

In **Figure 3-12** (a), the overall image of a 1.5 × 1.5 μm area of **CoAl-RM1** on a highly ordered pyrolytic graphite (HOPG) substrate is shown. Well-dispersed single particles with width of about 60 nm and thickness of 13 nm are observed (**Figure 3-12** (c) & (d)). Cross-sectional analysis of a number of single particles gives an average diameter of 59.0 ± 3.8 nm and average thickness of 12.9 ± 1.5 nm. Although the out of plane (thickness) measurements are well calibrated, the in plane lateral dimensions given here are the maximum limits of the particles size as the true dimension is convoluted with the AFM tip geometry. The diameter distribution is similar to the range

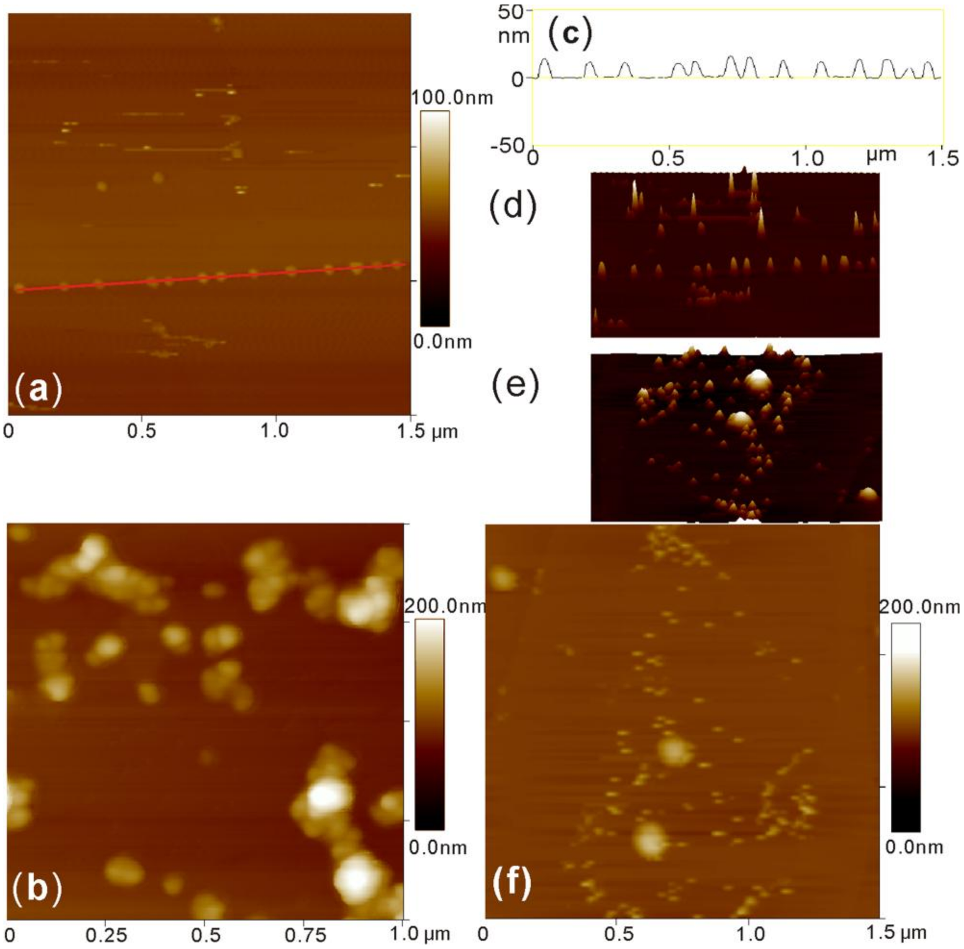

Figure 3-12: (a) AFM image of a 1.5×1.5 μm area of **CoAl-RM1**. (b) AFM image of a 1.0×1.0 μm area of **CoAl-RM2**. (c) Cross-sectional analysis along the red line in (a). (d) 3-dimensional AFM image of **CoAl-RM1**. (e) 3-dimensional AFM image of **CoAl-RM3**. (f) AFM image of a 1.5×1.5 μm area of **CoAl-RM3**.

measured by the Scherrer equation and TEM.

Figure 3-12 (b) gives an AFM image of a 1 × 1 μm area of **CoAl-RM2**. Along with dispersed single particles, larger aggregates can also be observed as seen previously in the TEM images. **Figure 3-12** (f) illustrates the image of a 1.5 × 1.5 μm area of **CoAl-RM3**. Single particles surrounded by a lot of excessive surfactant are clearly visible. Particle profile analyses gives the width and thickness values of 76.9 ± 4.0 nm and 28.4 ± 1.7 nm for **CoAl-RM2**, and 156.9 ± 11.4 nm and 42.6 ± 4.0 nm for **CoAl-RM3**. XRD data analysis has confirmed that the thickness of a CoAl-DDS LDH monolayer is 26.45 Å. So for **CoAl-RM*n*** (*n* = 1 - 3), the platelets consist of 5, 11 and 16 layers respectively, which is consistent with the observations from TEM. The particle sizes are approximately linearly correlated with the ratio of water to surfactant (ω), which further verifies that the particle growth can be controlled, and that a larger ω leads to the formation of larger particles.

Dynamic light scattering measurements were recorded in suspensions of the LDH particles in ethanol or methanol to confirm the distribution of the nanoparticles and the tendency to grow with ω. The data (depicted in **Figure 3-13**) gives a particle size distribution of about 60 - 90 nm for **CoAl-RM1**, 70 - 100 nm for **CoAl-RM2** and 120 - 200 nm for **CoAl-RM3**. Due to aggregation, we typically observe another peak corresponding to aggregates with size greater than 500 nm. The dynamic light scattering experiment probes the hydrodynamic radius of suspended particles, which for anisotropic plate-like particles is a complex function of both the platelet diameter and thickness.[99, 100] However, the DLS data does support the observation that the particle size increases with the ratio of water to surfactant.

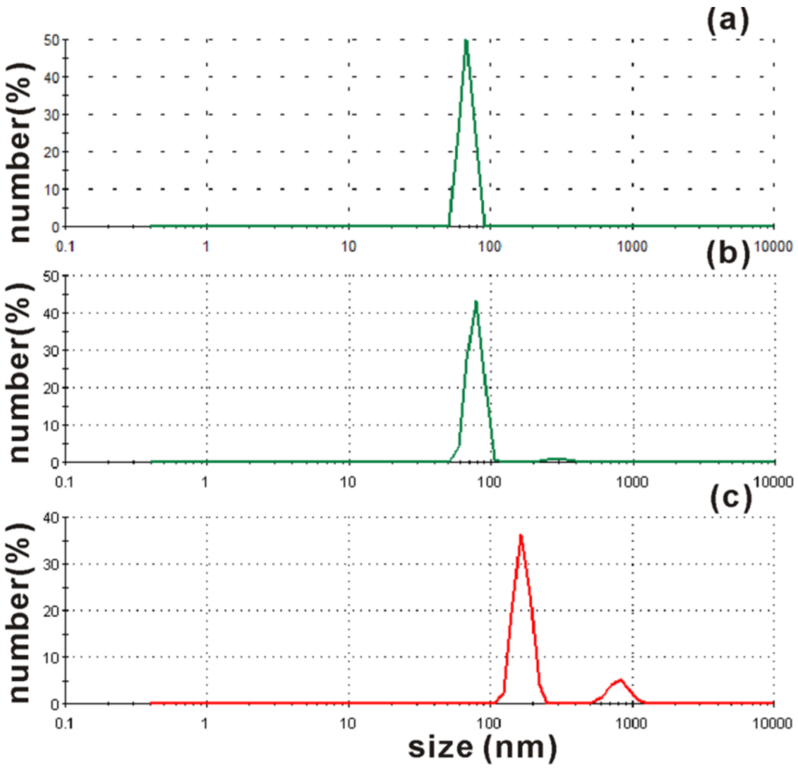

Figure 3-13: Dynamic light scattering data for (a) **CoAl-RM1**, (b) **CoAl-RM2**, (c) **CoAl-RM3**. (*x* axes are logarithmic.)

3.2.8. Magnetic properties

3.2.8.1. Magnetic properties of Co-Al LDHs

The molar magnetic susceptibilities of **CoAl-RM*n*** (*n* = 1 - 3) and **CoAl-Bulk** have been measured between 2 K and 300 K. **Figure 3-14** show plots of $\chi_M T$ and χ_M^{-1} *vs.* T for **CoAl-RM*n*** (*n* = 1 - 3) and **CoAl-Bulk**. Between 50 and 300 K, the materials obey the Curie-Weiss law (**Equation 3-3**, including a small temperature independent paramagnetic term) with C = 6.28 emu K mol^{-1} (μ_{eff} = 5.28 μ_B per Co), 5.86 emu K mol^{-1} (μ_{eff} = 5.06 μ_B per Co) and 6.19 emu K mol^{-1} (μ_{eff} = 5.20 μ_B per Co) for **CoAl-RM*n*** (*n* = 1 - 3) respectively (**Table 3-5**). These values are also very close to the observed moment of the conventional bulk sample. The magnetic moments are larger than the expected spin-only value for octahedral Co^{2+}, d^7 (μ_{eff} = 3.87 μ_B, S = 3/2) indicating that a significant orbital contribution is involved. However, the values are in line with other octahedral Co^{2+} containing compounds with oxide or hydroxide ligand fields. The values of the Weiss constant (θ) is 6.3 K, 5.6 K, and 6.7 K for **CoAl-RM*n*** (*n* = 1 - 3) respectively, suggesting short range ferromagnetic interactions.

$$\chi_M = \frac{C}{T-\theta} + \chi_{TIP}$$

Equation 3-3

Below 50 K, the values of $\chi_M T$ exhibit a rapid increase to a maximum at 7 K, which is ascribed to the onset of ferromagnetic ordering of the Co^{2+} spins. The mechanism for spin-spin interactions in layered metal hydroxides containing magnetic ions has been extensively studied. In these highly anisotropic materials, it is thought that conventional M-O-M superexchange operates within the plane of the layers and the development of a 3D ordered state is possible *via* long range dipole-dipole interactions.[34] This mechanism has been verified for a number of compounds including the $Cu_2(OH)_3(n\text{-}C_mH_{2m+1}COO)$ series,[101, 102] the $Cu_2(OH)_3(C_nH_{2n+1}SO_4)$ series,[103] $Ni_2(OH)_3(C_{12}H_{25}SO_3)$[104] and $Co_5(OH)_8(C_{12}H_{25}SO_3)_2$.[35] We also observe a bifurcation in the zero-field cooling (ZFC) and field cooling (FC) magnetic susceptibility below an irreversibility temperature T_{irr} (**Figure 3-15**). At low temperatures the FC magnetization continues increasing, while the ZFC magnetization shows a broad maximum at *ca.* 2.3 K. However, there was no bifurcation in the zero-field cooling (ZFC) and field cooling (FC) magnetic susceptibility of the **CoAl-Bulk** sample, which may due to large size of the particles.

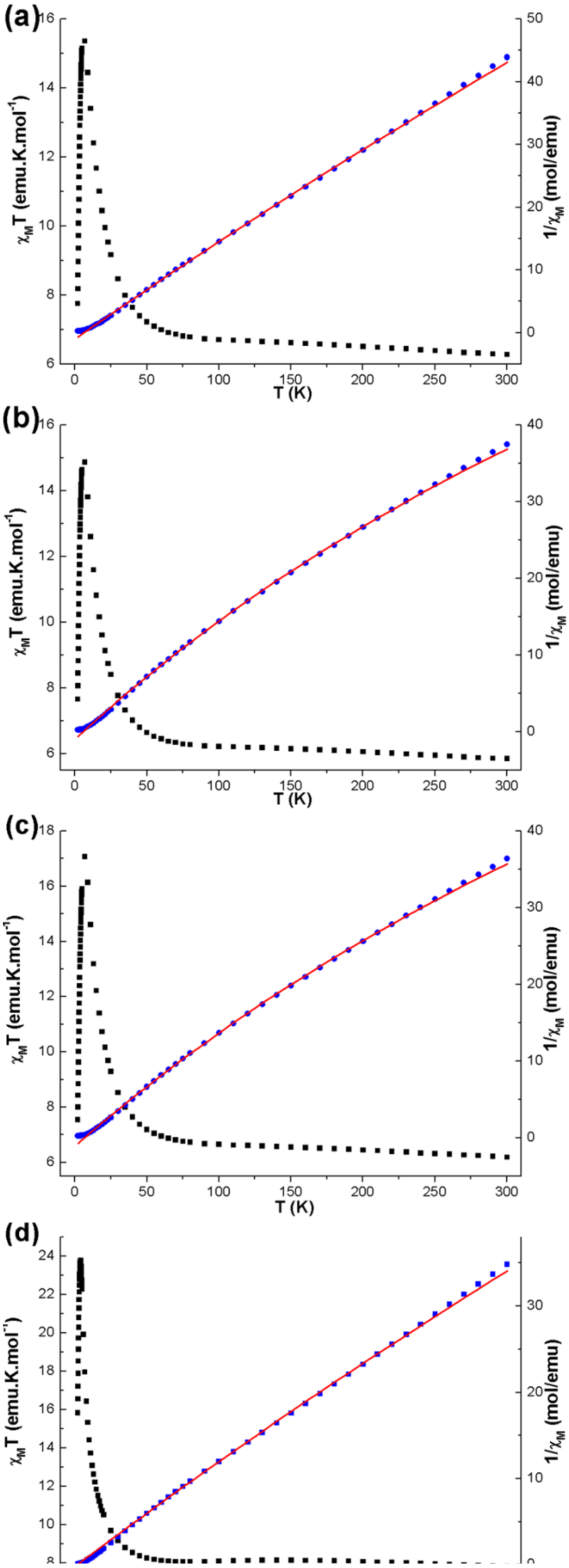

Figure 3-14: Plots of χ_MT (black squares) and χ_M^{-1} (blue circles) *vs.* T between 2 to 300 K for (a) **CoAl-RM1**, (b) **CoAl-RM2**, (c) **CoAl-RM3**, and (d) CoAl-Bulk. The solid lines are best fit to **Equation 3-3**.

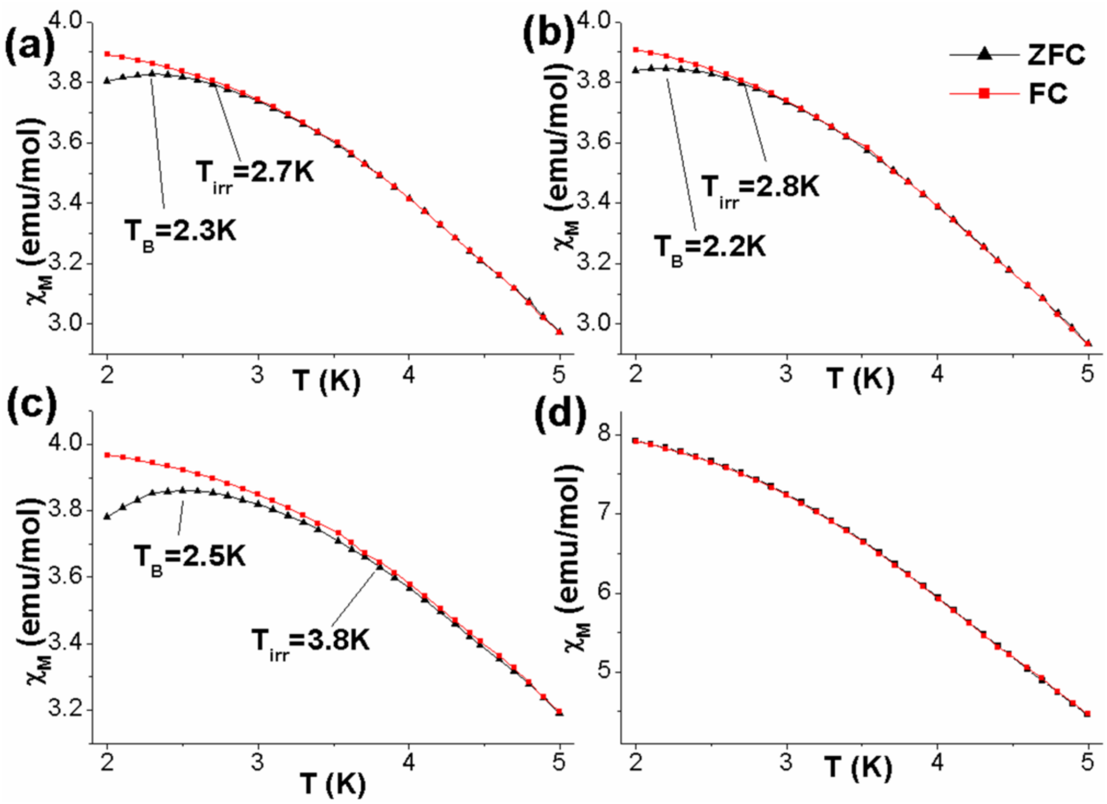

Figure 3-15: Low temperature ZFC (black triangles) and FC (red squares) molar magnetisation showing the bifurcation point (T_{irr}) and blocking temperature (T_B) for (a) **CoAl-RM1**, (b) **CoAl-RM2**, (c) **CoAl-RM3**, and (d) **CoAl-Bulk**.

The onset of spontaneous magnetization was confirmed by the occurrence of nonzero signals in the in-phase (χ') and out of phase (χ'') AC magnetic susceptibility (**Figure 3-16**). The critical temperature (T_c) is *ca*. 5.5K for all the samples. However, the nature of the magnetic interactions in these materials is not straightforward. We observe that the temperature at which both the in-phase (χ') and out-of-phase (χ'') reaches a maximum increases with increasing frequency, implying a slow relaxation process (**Figure 3-16**). The maximum value of χ' also decreases by *ca*. one-third when using frequencies between 1 - 10^3 Hz. When sizes of magnetically ordered particles are reduced to the nanometre length scale they may become single domain particles. At finite temperature and in the absence of any magnetic field the ferromagnetically aligned magnetic moments within these single-domain particles fluctuate between their

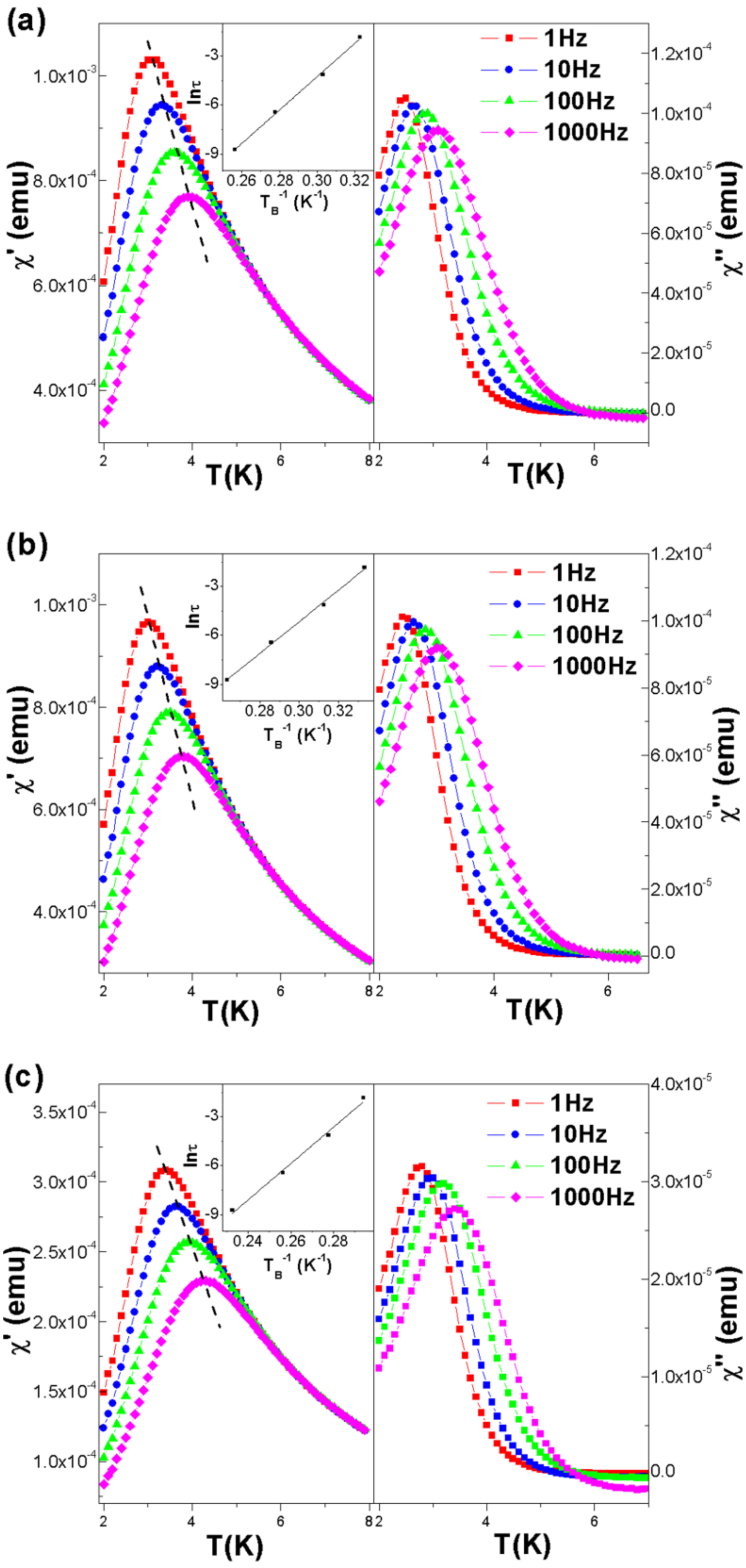

Figure 3-16: Frequency dependence of in-phase (χ’) and out-of-phase (χ’’) susceptibilities under an oscillating field of 5 Oe (a) **CoAl-RM1**, (b) **CoAl-RM2** and (c) **CoAl-RM3**. (Inset: Frequency dependence of the blocking temperature T_B. The lines are the least squares fit to the Arrhénius law (**Equation 3-4**).)

two energetically degenerate states on a time scale, assuming a simple Arrhénius law (**Equation 3-4**, where τ is the relaxation time, τ_0 is a constant and E_a is the total magnetocrystalline anisotropy energy of the particle.).

$$\tau(\mathrm{T}) = \tau_0 \exp(\frac{E_a}{k_B T})$$

Equation 3-4

The blocking temperature (T_B) is the temperature at which χ' and χ'' reach a maximum. It corresponds to the temperature at which $\tau = \tau_m$, the measurement time or frequency^{-1} of the measurement. A fit of ln(τ) *vs.* T_B^{-1} to **Equation 3-4** for **CoAl-RM*n*** (*n* = 1 - 3) is shown in **Figure 3-16** inset. The values of τ_0 and E_a/k_B for **CoAl-RM*n*** (*n* = 1 - 3) are tabulated in **Table 3-5**. We observe an increase in E_a/k_B as the volume of the platelets increases. According to the Stoner-Wohlfarth theory for superparamagnetism, the magnetocrystalline anisotropy energy (**Equation 3-5**, where K is the anisotropy constant, V is the volume of the particle, θ is the angle between magnetization and the easy axis). Thus E_a is expected to increase as the volume of the particles increases. Furthermore, the frequency dependence of the maximum in χ' can be parameterized using the frequency-shift parameter, φ, according to **Equation 3-6** introduced by Mydosh. The values of φ are found to be 0.068 0.070 and 0.070 for **CoAl-RM*n*** (*n* = 1 - 3), respectively.[105]

$$E_a = KV sin\theta$$

Equation 3-5

$$\varphi = \frac{\Delta T_B}{T_B \Delta(log f)}$$

Equation 3-6

Table 3-5: Summary of the magnetic data for **CoAl-RM*n*** (*n* = 1 - 3) and **CoAl-Bulk**.

	CoAl-RM1	**CoAl-RM2**	**CoAl-RM3**	**CoAl-Bulk**
χ_MT @ 300K (emu K mol^{-1})	6.28	5.85	6.18	7.81
μ_{eff} (μ_B per Co^{2+})	5.28	5.06	5.20	5.59
C (emu K mol^{-1})	6.28	5.86	6.19	7.96
θ (K)	6.3	5.6	6.7	1.4
TIP (emu mol^{-1})	0.002	0.007	0.007	0.003
T_{irr} (K)	2.7	2.8	3.5	-
T_B (K)	2.3	2.2	2.5	-
M_{sat} (μ_B)^a	2.21	2.23	2.10	-
μ (μ_B)^a	9.39	9.40	9.78	-
τ_0 (s)^b	6.0×10^{-16}	1.4×10^{-15}	8.3×10^{-16}	-
E_a/k_B (K)^b	88.9	99.9	109.2	-
φ	0.068	0.070	0.070	-

T_{irr}: temperature of the divergence of the ZFC and FC magnetic susceptibility
T_b: maximum in χ' or maximum in the ZFC magnetic susceptibility
[a] parameters obtained by fitting of the M *vs.* H/T data to **Equation 3-7**.
[b] parameters obtained by fitting of the AC magnetic susceptibility data to **Equation 3-4**.

In order to further understand the nature of magnetic ordering in these samples, we plotted the magnetization per Co of **CoAl-RM1** as a function of H/T at various temperatures. For T > 5K plots of M *vs.* H/T superimpose on a single curve (**Figure 3-17** (a)). This type of behavior is usually observed in paramagnets and/or noninteracting superparamagnets with uniform cluster-moment distribution above their blocking temperatures. We were unable to fit the data using the Brillouin function for paramagnetic Co^{2+} ions (S = 3/2). However, we get a good fit using the Langevin function, which assumes noninteracting spin clusters with uniform size, temperature and magnetic-field dependences (**Equation 3-7**, where μ is the average magnetic moment of a spin cluster and M_s is the saturation magnetisation.)[106]

$$\mathrm{M} = M_s L(\frac{\mu}{k_B T} H)$$

$$\mathrm{L}(\alpha) = \coth(\alpha) - \frac{1}{\alpha}$$

Equation 3-7

The fitted curve at 15 K gives $\mu = 21.21\ \mu_B$ and $M_s = 2.31\ \mu_B$. In addition, the M *vs.* H curves for T > 5 K (**Figure 3-17** (a)) do not show any hysteresis as expected for a noninteracting superparamagnet. Below the blocking temp (T_B) a superparamagnet should behave more like an ordered spin ensemble and, for example, show hysteresis. As predicted, the M *vs.* H/T curves for T < 5 K do not superimpose on the ones for T > 5 K. The M *vs.* H at 2K (see **Figure 3-17** (b) inset) starts to show a very small coercive field and remnant magnetization which may not be too unexpected as they are just below the blocking temperature. Magnetization for **CoAl-RM*n*** (*n* = 1 - 3) reaches saturation magnetization (M_{sat}) *ca.* 2.1 μ_B which is lower than expected value for ferromagnetically aligned Co^{2+} ($M_{sat} = gS\mu_B$; g = 2, S = 3/2), however this is not an uncommon value of the low temperature saturation magnetization for Co^{2+} compounds. For example, a value at $M_{sat} = 2.87\ \mu_B$ per Co^{2+} was found for $Co_2(OH)_3(NO_3)$ which contains exclusively octahedral Co^{2+}.[29]

In conclusion, the **CoAl-RM*n*** (*n* = 1 – 3) nanoplatelets show magnetic behavior which is different to a chemically equivalent bulk sample made by conventional methods of homogeneous precipitation and ion-exchange. Several aspects of the magnetic responses are also dependent on the size of the nanoplatelets. However, it is very difficult to make a definite statement as to the true nature of the low temperature magnetic interactions in these nanomaterials are they also structurally disordered and so aspects of spin glass,[107-109] or cluster spin glass,[110] may play a role in addition to superparamagnet[111-113] behavior.

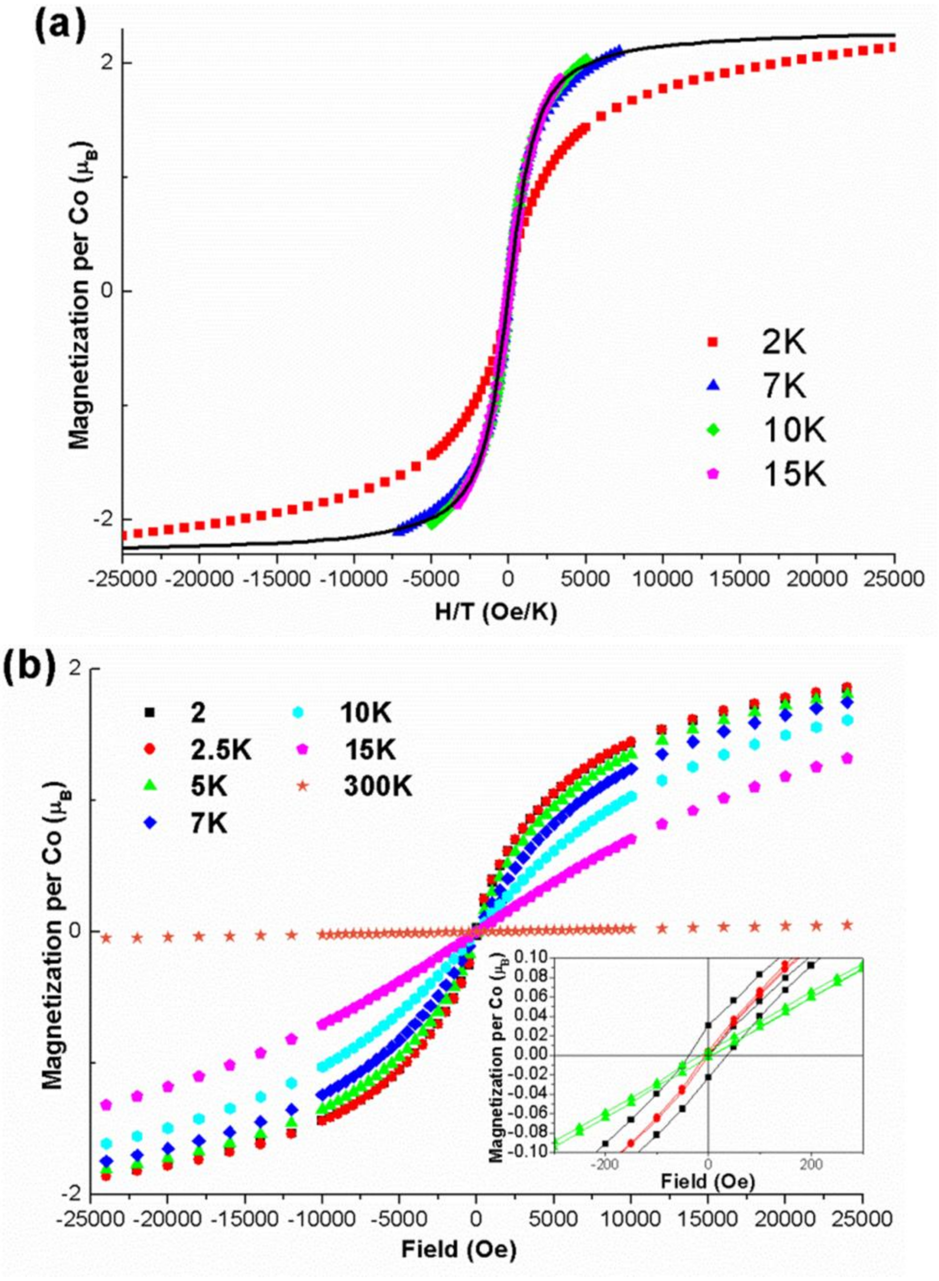

Figure 3-17: (a) M *vs*. H/T curves at 2 K (red squares), 7 K (blue triangles), 10 K (green diamonds), and 15 K (purple hexagons) for **CoAl-RM1**. The solid line is best fitted to the data using Langevin function (**Equation 3-7**). (b) M *vs*. H at 2 K (black squares), 2.5 K (red circles), 5 K (green triangles), 7 K (blue diamonds), 10 K (cyan hexagons), and 15 K (purple pentagons), and 300 K (orange stars) for **CoAl-RM1**. (Inset: curves at low field.)

3.2.8.2. Magnetic properties of Ni-Al LDHs

The magnetic properties of NiAl-NO_3 LDHs have been studied by Coronado *et al.*[114] Combining the earlier research on the magnetic properties of layered nickel hydroxides[104] and nickel clusters,[115] the magnetic behaviour of Ni-Al LDHs with long dodecyl chain in the lamellar space were studied.

The molar magnetic susceptibilities of **NiAl-RM*n*** (*n* = 1 - 3) were measured between 2 K and 300 K. The plots of χ_MT and χ_M^{-1} *vs.* T for **NiAl-RM*n*** (*n* = 1 - 3) are given in **Figure 3-18**. Between 50 - 300 K, the materials obey the Curie-Weiss law (**Equation 3-3**) with C = 2.39 emu K mol^{-1} (μ_{eff} = 3.02 μ_B per Ni), 2.47 emu K mol^{-1} (μ_{eff} = 2.37 μ_B per Ni) and 2.22 emu K mol^{-1} (μ_{eff} = 2.98 μ_B per Ni) for **NiAl-RM*n*** (*n* = 1 - 3) respectively (**Table 3-6**).The values are in good agreement with the expected spin-only value for octahedral Ni^{2+}, d^8 (μ_{eff} = 2.82 μ_B, S = 1). After fitting the data above 50 K to **Equation 3-3**, we can estimate the values of the Weiss constant (θ), which are 19.84 K, 20.78 K, and 20.32 K for **NiAl-RM*n*** (*n* = 1 - 3) respectively, confirming the presence of ferromagnetic interactions. The χ_MT values of **NiAl-RM1** and **NiAl-RM2** samples near room temperature are much higher than that of **NiAl-RM3**. Moreover, the plots of χ_M^{-1} *vs.* T of **NiAl-RM1** and **NiAl-RM2** samples are not linear but bend towards lower values. Both of these phenomena are due to the big temperature independent terms in the Curie-Weiss law.

Below 50 K, the magnetic moments start to increase rapidly, suggesting the onset of cooperative interactions. At low temperature, similar to **CoAl-RM*n*** (*n* = 1 - 3), the zero-field cooling (ZFC) curve and field cooling (FC) curve bifurcate at irreversible temperature. The zero-field cooling (FC) curve continue to increase, while the field cooling curve (ZFC) reach a climax at blocking temperature of *ca.* 2.6 K (**Figure 3-19**).

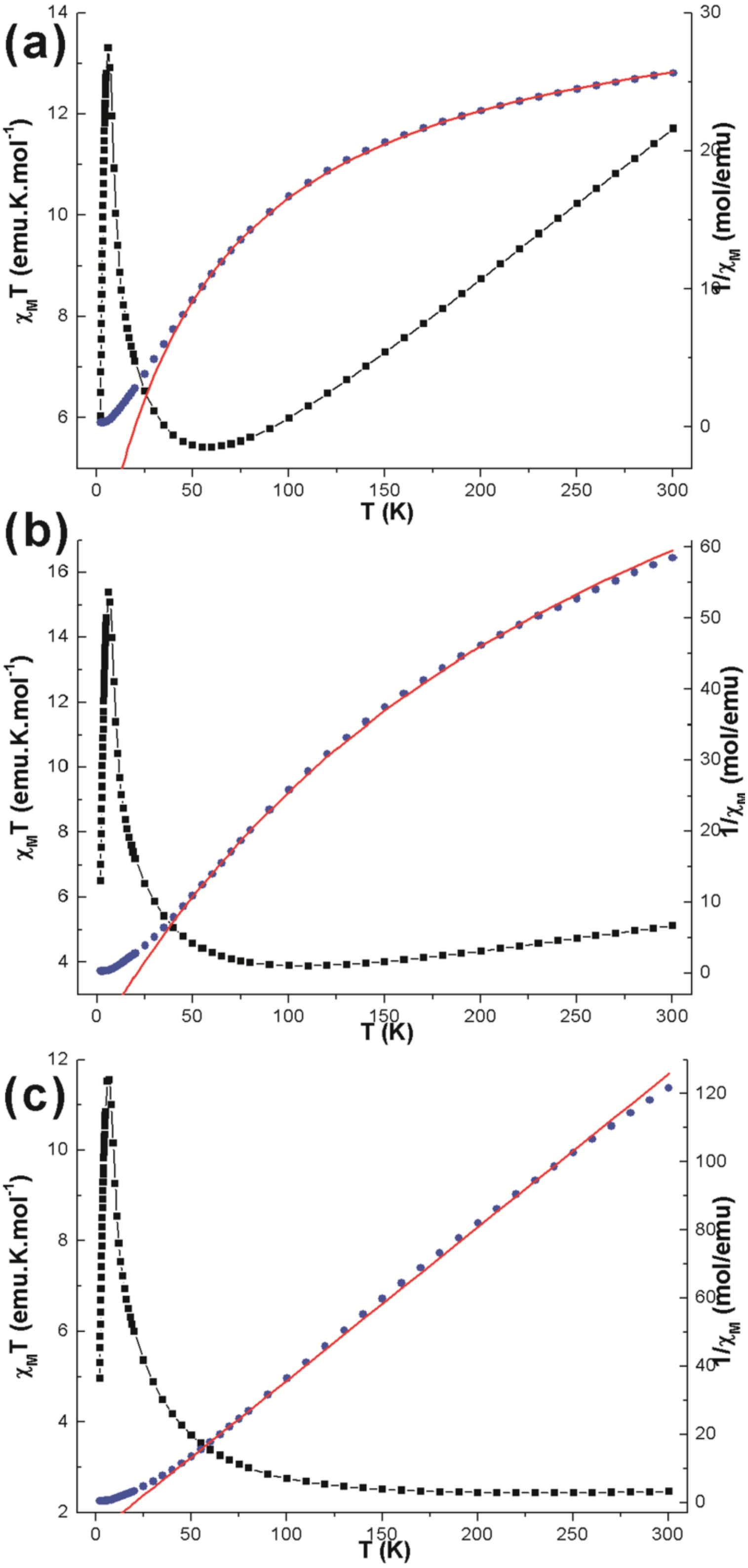

Figure 3-18: Plots of χ_MT (black squares) and χ_M^{-1} (blue circles) *vs.* T between 2 to 300 K for (a) **NiAl-RM1**, (b) **NiAl-RM2**, and (c) **NiAl-RM3**. The solid lines are best fit to **Equation 3-3**.

The AC behaviour of **NiAl-RM*n*** (*n* = 1 - 3) are also similar to those of **CoAl-RM*n*** (*n* = 1 - 3) (**Figure 3-20**). The in-phase (χ’) and out of phase (χ’’) AC magnetic susceptibility becoming nonzero is a signature of the onset spontaneous magnetization. The temperature of maximum in-phase (χ’) and out-of-phase (χ’’) increase with the increasing frequency, which indicates slow relaxation. A fit of ln(τ) *vs.* T_B^{-1} to **Equation 3-4** for **NiAl-RM*n*** (*n* = 1 - 3) is shown in **Figure 3-20** inset. The fitted values of τ_0 and E_a/k_B are tabulated in **Table 3-6**. E_a is increasing as the volume of the particles increases, as expected by **Equation 3-5**. The frequency-shift parameter, φ, according to **Equation 3-6**, are found as 0.055, 0.051 and 0.042 for **NiAl-RM*n*** (*n* = 1 - 3) respectively.

The ZFC and FC data for these samples suggest that below the blocking temperature, *ca.* 2.5 K, the samples behave ferromagnetically, while above that temperature, superparamagnetic properties gradually appear. Therefore, the hysteresis loops (**Figure 3-21**) for all three samples were measured at 2 K, 3 K, 5 K, 10 K and 20 K. For T > 10 K plots of M *vs.* H/T superimpose on a single curve (**Figure 3-21** (b), (d) & (f)), indicating superparamagnetism above blocking temperatures. All the M *vs.* H curves nearly overlap with each other, and reach a saturation magnetization (M_{sat}) *ca.* 1.1 μ_B which is lower than expected value for ferromagnetically aligned Ni^{2+} ($M_{sat} = gS\mu_B$; g = 2, S = 1) but this value is commonly seen for Ni-Al LDHs.[114] The M *vs.* H/T curves at 10 K can be fitted to Langevin function. Below blocking temperature, characteristic phenomena for ferromagnetic materials, coercive field and remnant magnetization, can be found for the M *vs.* H curves at 2 K, while curves at 3 K and 5 K have no coercive field and remnant magnetization.

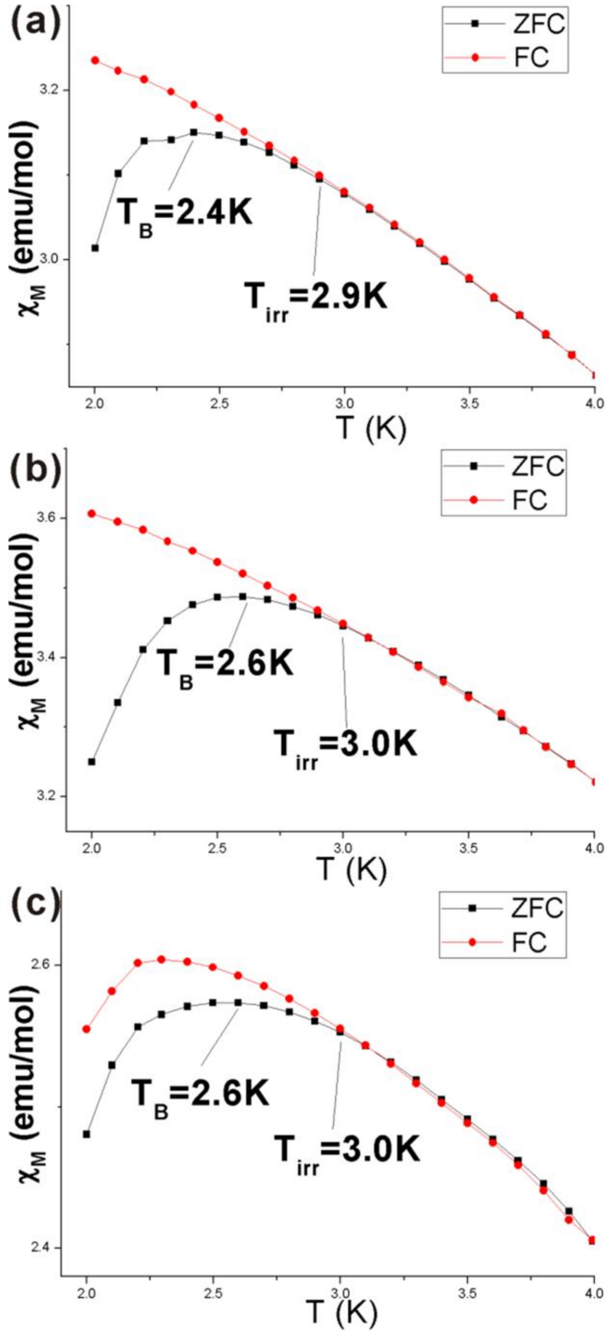

Figure 3-19: Low temperature ZFC (black squares) and FC (red circles) molar magnetisation showing the bifurcation point (T_{irr}) and blocking temperature (T_B) for (a) **NiAl-RM1**, (b) **NiAl-RM2**, and (c) **NiAl-RM3**.

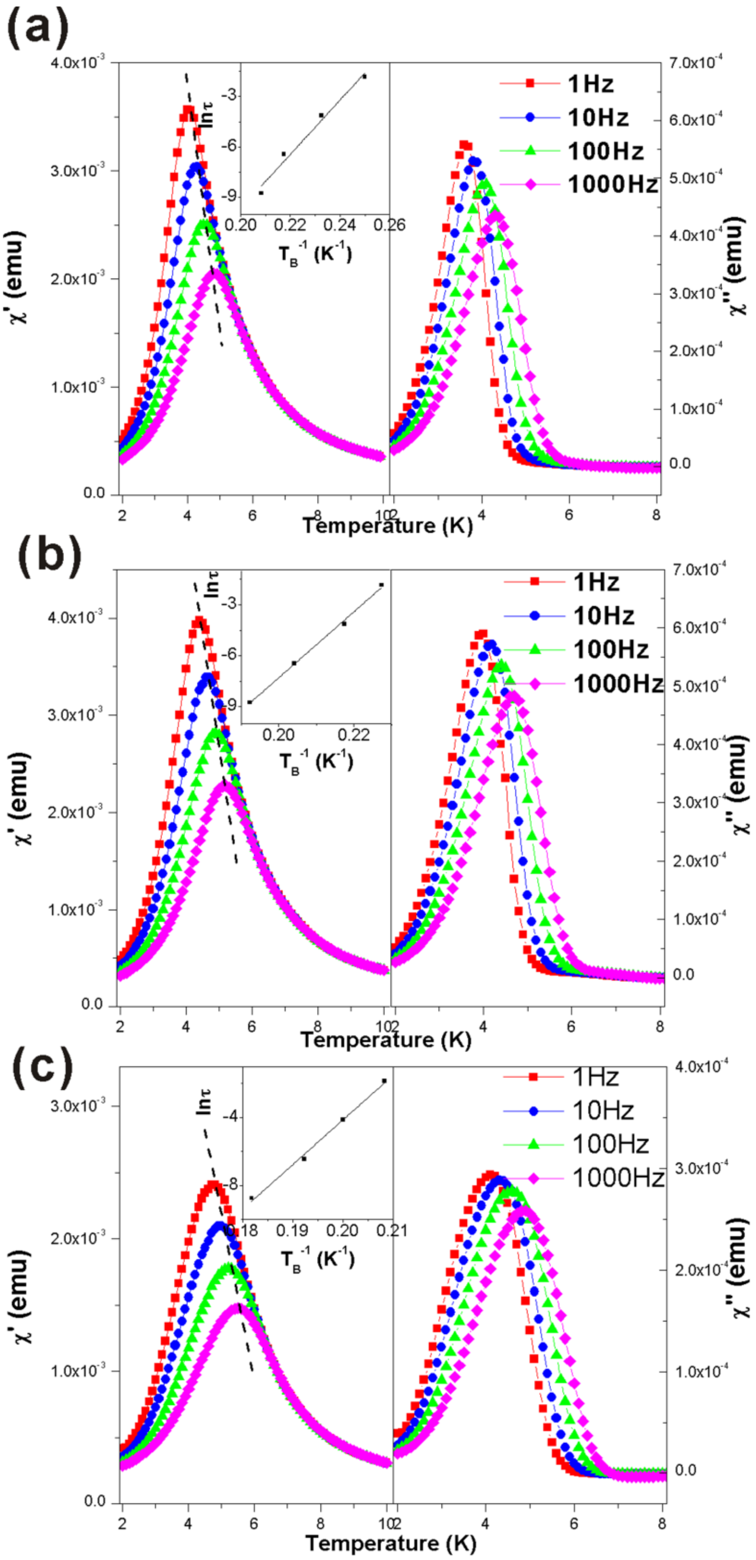

Figure 3-20: Frequency dependence of in-phase (χ') and out-of-phase (χ'') susceptibilities under an oscillating field of 5 Oe (a) **NiAl-RM1**, (b) **NiAl-RM2** and (c) **NiAl-RM3**. (Inset: Frequency dependence of the blocking temperature T_B. The lines are least squares fit to the Arrhénius law (**Equation 3-4**).)

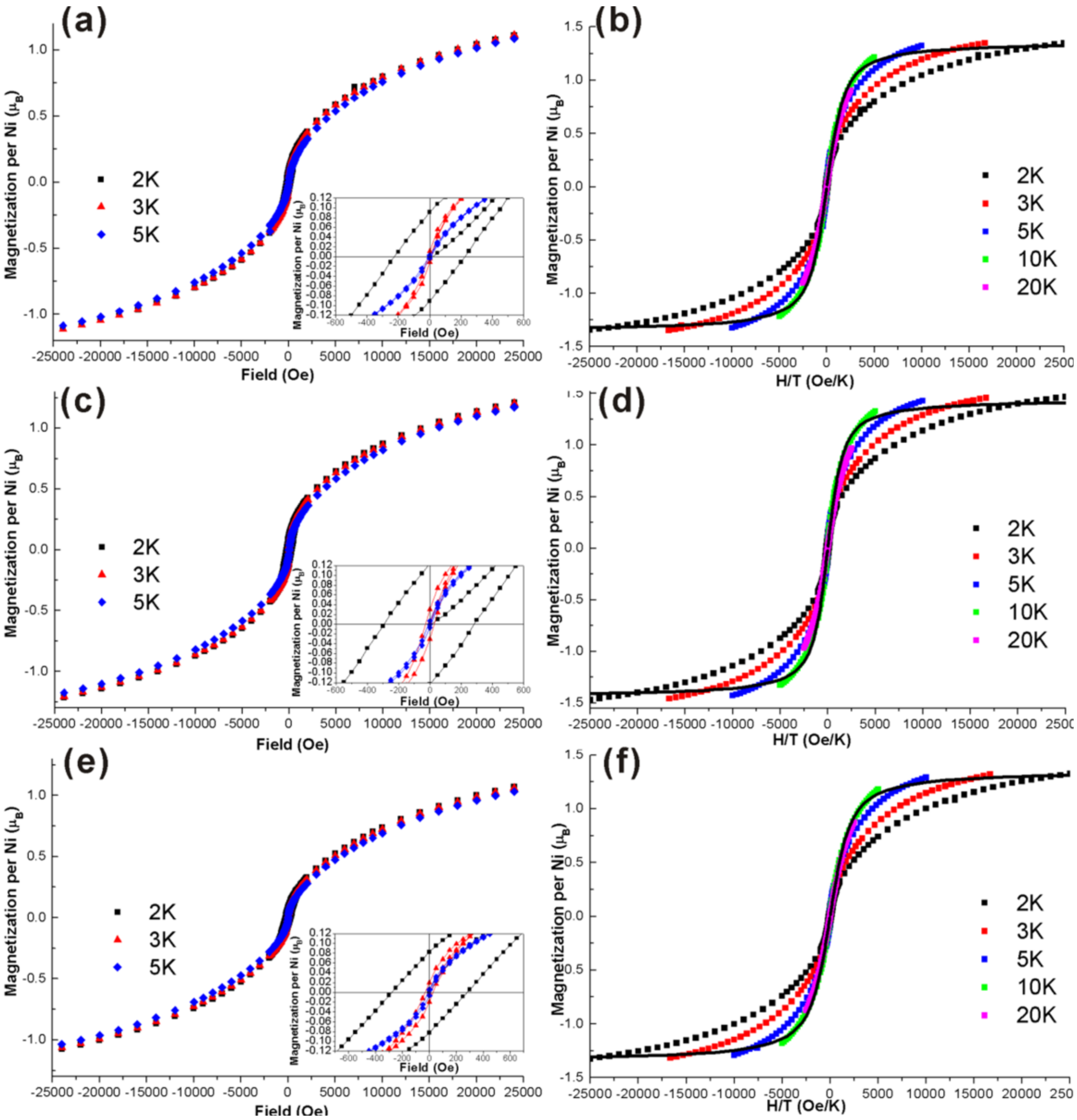

Figure 3-21: M *vs*. H curves at 2 K (black squares), 3 K (red triangles), and 5 K (blue diamonds) for (a) **NiAl-RM1**, (c) **NiAl-RM2**, and (e) **NiAl-RM3**. (The insets are zoom-in images at low field regions.) M *vs*. H/T curves at 2 K (black), 3 K (red), 5 K (blue), 10 K (green) and 20 K (purple) for (b) **NiAl-RM1**, (d) **NiAl-RM2**, and (f) **NiAl-RM3**. The solid lines are best fit using Langevin function (**Equation 3-7**).

Table 3-6: Summary of the magnetic data for **NiAl-RM*n*** (*n* = 1 - 3)

	NiAl-RM1	**NiAl-RM2**	**NiAl-RM3**
$\chi_M T$ @ 300K (emu K mol^{-1})	11.71	5.14	2.47
μ_{eff} (μ_B per Ni^{2+})	3.02	2.37	2.98
C (emu K mol^{-1})	2.39	1.47	2.22
θ (K)	19.84	20.78	20.32
TIP (emu mol^{-1})	0.03	0.08	0
T_{irr} (K)	2.9	3.0	3.0
T_B (K)	2.4	2.6	2.6
M_{sat} (μ_B)[a]	1.36	1.44	1.35
μ (μ_B)[a]	21.44	24.82	18.67
τ_0 (s)[b]	6.3×10^{-19}	9.3×10^{-21}	2.4×10^{-25}
E_a/k_B (K)[b]	161.3	194.2	262.7
φ	0.055	0.051	0.042

T_{irr}: temperature of the divergence of the ZFC and FC magnetic susceptibility
T_b: maximum in χ’ or maximum in the ZFC magnetic susceptibility
[a] parameters obtained by fitting of the M *vs.* H/T data at 10 K to **Equation 3-7**.
[b] parameters obtained by fitting of the AC magnetic susceptibility data to **Equation 3-4**.

3.3. Conclusion

CoAl-RM*n* and **NiAl-RM*n*** (*n* = 1 - 3) LDH samples with different particle sizes have been synthesised through a reverse microemulsion method combined with homogeneous precipitation in the aqueous phase. X-ray crystallography and IR spectra verified that the six samples adopt a layered structure with long dodecyl chains located between the brucite-like layers, leading to an interlamellar distance of *ca.* 26 Å. Within the brucite-like layers, Co/Ni ions and Al ions are in octahedral symmetry surrounded by six oxygen atoms with an average Co/Al molar ratio of about 1.6 and Ni/Al molar ratio of about 2.3. TEM and AFM imaging reveal that the particle size is directly related to the ratio of water to surfactant. The Co-Al LDH nanoplatelets show magnetic behaviour which is different to a chemically equivalent bulk sample. Several aspects for the magnetic responses are dependent on the size of the nanoplatelets.

3.4. References

1. L. Pesic, S. Salipurovic, V. Markovic, D. Vucelic, W. Kagunya and W. Jones, *J. Mater. Chem.*, 1992, **2**, 1069-1073.
2. V. Rives, F. M. Labajos, M. A. Ulibarri and P. Malet, *Inorg. Chem.*, 1993, **32**, 5000-5001.
3. A. I. Khan and D. O'Hare, *J. Mater. Chem.*, 2002, **12**, 3191-3198.
4. P. S. Braterman, Z. P. Xu and F. Yarberry, in *Handbook of layered materials*, Marcel Dekker, New York, Editon edn., 2004, pp. 373-474.
5. S. Miyata, *Clays Clay Miner.*, 1980, **28**, 50.
6. A. Roy, C. Forano and J. P. Besse, in *Layered Double Hydroxides: Present and Future*, Nova Science, New York, Editon edn., 2001.
7. J. He, M. Wei, B. Li, Y. Kang, D. G. Evans and X. Duan, in *Layered Double Hydroxides, Structure and Bonding*, eds. X. Duan and D. G. Evans, Springer, Editon edn., 2001, pp. 89-119.
8. U. Costantino, F. Marmottini, M. Nocchetti and R. Vivani, *Eur. J. Inorg. Chem.*, 1998, **1998**, 1439-1446.
9. M. Adachi-Pagano, C. Forano and J.-P. Besse, *J. Mater. Chem.*, 2003, **13**, 1988-1993.
10. U. Costantino, N. Coletti, M. Nocchetti, G. G. Aloisi, F. Elisei and L. Latterini, *Langmuir*, 2000, **16**, 10351-10358.
11. L. Li, R. Ma, Y. Ebina, N. Iyi and T. Sasaki, *Chem. Mater.*, 2005, **17**, 4386-4391.
12. E. E. Sileo, M. Jobbágy, C. O. Paiva-Santos and A. E. Regazzoni, *J. Phys. Chem. B*, 2005, **109**, 10137-10141.
13. M. M. Rao, B. R. Reddy, M. Jayalakshmi, V. S. Jaya and B. Sridhar, *Mater. Res. Bull.*, 2005, **40**, 347-359.
14. M. Ogawa and H. Kaiho, *Langmuir*, 2002, **18**, 4240-4242.
15. N. Iyi, T. Matsumoto, Y. Kaneko and K. Kitamura, *Chem. Lett.*, 2004, **33**, 1122-1123.
16. Z. Liu, R. Ma, M. Osada, K. Takada and T. Sasaki, *J. Am. Chem. Soc.*, 2005, **127**, 13869-13874.
17. Z. Liu, R. Ma, M. Osada, N. Iyi, Y. Ebina, K. Takada and T. Sasaki, *J. Am. Chem. Soc.*, 2006, **128**, 4872-4880.
18. R. Z. Ma, Z. P. Liu, K. Takada, N. Iyi, Y. Bando and T. Sasaki, *J. Am. Chem. Soc.*, 2007, 5257-5263.
19. Y. Du and D. O’Hare, *Inorg. Chem.*, 2008, **47**, 3234-3242.
20. L. Albiston, K. R. Franklin, E. Lee and J. B. A. F. Smeulders, *J. Mater. Chem.*, 1996, **6**, 871-877.
21. Y. Zhao, F. Li, R. Zhang, D. G. Evans and X. Duan, *Chem. Mater.*, 2002, **14**, 4286-4291.
22. Z. P. Xu, G. Stevenson, C.-Q. Lu and G. Q. Lu, *J. Phys. Chem. B*, 2006, **110**, 16923-16929.
23. G. Hu, N. Wang, D. O'Hare and J. Davis, *J. Mater. Chem.*, 2007, **17**, 2257-2266.
24. N. Nassar and M. Husein, *Langmuir*, 2007, **23**, 13093-13103.
25. M. E. Pérez-Bernal, R. J. Ruano-Casero, F. Benito and V. Rives, *J. Solid State Chem.*, 2009, **182**, 1593-1601.
26. Y. Zhao, F. F. Xiao and Q. Z. Jiao, *Bull. Mater. Sci.*, 2008, **31**, 831-834.
27. H. Wu, Q. Jiao, Y. Zhao, S. Huang, X. Li, H. Liu and M. Zhou, *Mater. Charact.*,

2010, **61**, 227-232.
28. V. Laget, C. Hornick, P. Rabu, M. Drillon and R. Ziessel, *Coord. Chem. Rev.*, 1998, **178–180, Part 2**, 1533-1553.
29. P. Day and A. E. Underhill, *Metal-organic and organic molecular magnets*, Royal Society of Chemistry, 1999.
30. B. S. Mohsen, S. Vilminot, M. Richard-Plouet, G. Andre, T. Mhiri and M. Kurmoo, *Chem. Commun.*, 2004, 2548-2549.
31. M. Ben Salah, S. Vilminot, G. Andre, M. Richard-Plouet, T. Mhiri, S. Takagi and M. Kurmoo, *J. Am. Chem. Soc.*, 2006, **128**, 7972-7981.
32. W. Maalej, S. Vilminot, G. André and M. Kurmoo, *Inorg. Chem.*, 2010, **49**, 3019-3024.
33. B. Subhankar and K. Wolfgang, *J. Phys. D: Appl. Phys.*, 2009, **42**, 013001.
34. M. Drillon and P. Panissod, *J. Magn. Magn. Mater.*, 1998, **188**, 93-99.
35. M. Kurmoo, P. Day, A. Derory, C. Estournès, R. Poinsot, M. J. Stead and C. J. Kepert, *J. Solid State Chem.*, 1999, **145**, 452-459.
36. M. Intissar, R. Segni, C. Payen, J.-P. Besse and F. Leroux, *J. Solid State Chem.*, 2002, **167**, 508-516.
37. M. Kurmoo, H. Kumagai, S. M. Hughes and C. J. Kepert, *Inorg. Chem.*, 2003, **42**, 6709-6722.
38. E. Delahaye, S. Eyele-Mezui, J.-F. Bardeau, C. Leuvrey, L. Mager, P. Rabu and G. Rogez, *J. Mater. Chem.*, 2009, **19**, 6106-6115.
39. V. Laget, C. Hornick, P. Rabu and M. Drillon, *J. Mater. Chem.*, 1999, **9**, 169-174.
40. M. Kurmoo, *Chem. Mater.*, 1999, **11**, 3370-3378.
41. Z.-L. Huang, M. Drillon, N. Masciocchi, A. Sironi, J.-T. Zhao, P. Rabu and P. Panissod, *Chem. Mater.*, 2000, **12**, 2805-2812.
42. J. J. Almansa, E. Coronado, C. Martí-Gastaldo and A. Ribera, *Eur. J. Inorg. Chem.*, 2008, **2008**, 5642-5648.
43. A. Aharoni, *Introduction to the theory of ferromagnetism*, Oxford University Press, 2000.
44. J. Tejada, R. F. Ziolo and X. X. Zhang, *Chem. Mater.*, 1996, **8**, 1784-1792.
45. D. D. Awschalom and D. P. DiVincenzo, *Physics Today*, 1995, **48**, 43-48.
46. M. H. Kryder, *MRS Bull.*, 1996, **21**, 17.
47. U. Häfeli, *Scientific and clinical applications of magnetic carriers*, Plenum Press, 1997.
48. T. P. Hoar and J. H. Schulman, *Nature*, 1943, **152**, 102-103.
49. M.-P. Pileni, *Nat Mater*, 2003, **2**, 145-150.
50. S. J. Chen, D. F. Evans, B. W. Ninham, D. J. Mitchell, F. D. Blum and S. Pickup, *J. Phys. Chem.*, 1986, **90**, 842-847.
51. D. F. Evans, D. J. Mitchell and B. W. Ninham, *J. Phys. Chem.*, 1986, **90**, 2817-2825.
52. M. Zulauf and H. F. Eicke, *J. Phys. Chem.*, 1979, **83**, 480-486.
53. B. H. Robinson, C. Toprakcioglu, J. C. Dore and P. Chieux, *J. Chem. Soc., Faraday Trans. 1*, 1984, **80**.
54. M.-P. Pileni, T. Zemb and C. Petit, *Chem. Phys. Lett.*, 1985, **118**, 414-420.
55. G. Porte, J. Appell and Y. Poggi, *J. Phys. Chem.*, 1980, **84**, 3105-3110.
56. P. D. I. Fletcher, B. H. Robinson and J. Tabony, *J. Chem. Soc., Faraday Trans. 1*, 1986, **82**.
57. P. D. I. Fletcher, A. M. Howe and B. H. Robinson, *J. Chem. Soc., Faraday Trans. 1*, 1987, **83**.

58. I. S. Barnes, S. T. Hyde, B. W. Ninham, P. J. Derian, M. Drifford and T. N. Zemb, *J. Phys. Chem.*, 1988, **92**, 2286-2293.
59. G. Cao and Y. Wang, *Nanostructures and nanomaterials: synthesis, properties, and applications*, World Scientific, 2010.
60. T. Dwars, E. Paetzold and G. Oehme, *Angew. Chem. Int. Ed.*, 2005, **44**, 7174-7199.
61. M. P. Pileni, *Langmuir*, 1997, **13**, 3266-3276.
62. A. K. Ganguli, A. Ganguly and S. Vaidya, *Chem. Soc. Rev.*, 2010, **39**.
63. V. Uskoković and M. Drofenik, *Adv. Colloid Interface Sci.*, 2007, **133**, 23-34.
64. P. Brochette, C. Petit and M. P. Pileni, *J. Phys. Chem.*, 1988, **92**, 3505-3511.
65. C. Stubenrauch, T. Wielpütz, T. Sottmann, C. Roychowdhury and F. J. DiSalvo, *Colloids and Surfaces A: Physicochemical and Engineering Aspects*, 2008, **317**, 328-338.
66. M. Sanchez-Dominguez, M. Boutonnet and C. Solans, *J. Nanopart. Res.*, 2009, **11**, 1823-1829.
67. O. P. Yadav, A. Palmqvist, N. Cruise and K. Holmberg, *Colloids and Surfaces A: Physicochemical and Engineering Aspects*, 2003, **221**, 131-134.
68. M. Boutonnet, J. Kizling, P. Stenius and G. Maire, *Colloids and Surfaces*, 1982, **5**, 209-225.
69. A. Salabat, *Russian Journal of Physical Chemistry A, Focus on Chemistry*, 2010, **84**, 1255-1256.
70. D. E. Zhang, X. M. Ni, H. G. Zheng, Y. Li, X. J. Zhang and Z. P. Yang, *Mater. Lett.*, 2005, **59**, 2011-2014.
71. A. Tavakoli, M. Sohrabi and A. Kargari, *Chemical Papers*, 2007, **61**, 151-170.
72. I. Capek, *Adv. Colloid Interface Sci.*, 2004, **110**, 49-74.
73. D. H. Chen and C. J. Chen, *J. Mater. Chem.*, 2002, **12**, 1557-1562.
74. A. Pal, S. Shah and S. Devi, *Colloids and Surfaces A: Physicochemical and Engineering Aspects*, 2007, **302**, 483-487.
75. I. Srnová-Šloufová, B. Vlčková, Z. Bastl and T. L. Hasslett, *Langmuir*, 2004, **20**, 3407-3415.
76. F. J. Arriagada and K. Osseo-Asare, *J. Colloid Interface Sci.*, 1999, **211**, 210-220.
77. A. Bumajdad, J. Eastoe, M. I. Zaki, R. K. Heenan and L. Pasupulety, *J. Colloid Interface Sci.*, 2007, **312**, 68-75.
78. A. K. Ganguli, T. Ahmad, S. Vaidya and J. Ahmed, *Pure Appl. Chem.*, 2008, **80**, 2451-2477.
79. A. K. Ganguli and T. Ahmad, *J. Nanosci. Nanotechno.*, 2007, **7**, 2029-2035.
80. T. Ahmad, K. V. Ramanujachary, S. E. Lofland and A. K. Ganguli, *J. Chem. Sci.*, 2006, **118**, 513-518.
81. M. Ethayaraja and R. Bandyopadhyaya, *J. Am. Chem. Soc.*, 2006, **128**, 17102-17113.
82. J. H. Zhan, X. G. Yang, D. W. Wang, S. D. Li, Y. Xie, Y. Xia and Y. Qian, *Adv. Mater.*, 2000, **12**, 1348-1351.
83. X. Hu, P. Zrazhevskiy and X. Gao, *Annals of Biomedical Engineering*, 2009, **37**, 1960-1966.
84. A. Hammouda, T. Gulik and M. P. Pileni, *Langmuir*, 1995, **11**, 3656-3659.
85. M. Summers, J. Eastoe and S. Davis, *Langmuir*, 2002, **18**, 5023-5026.
86. J. Eastoe and B. Warne, *Current Opinion in Colloid & Interface Science*, 1996, **1**, 800-805.
87. F. Barroso and C. Tojo, *J. Colloid Interface Sci.*, 2011, **363**, 73-83.
88. M. L. Viger, L. S. Live, O. D. Therrien and D. Boudreau, *Plasmonics*, 2008, **3**,

33-40.

89. R. Jain, D. Shukla and A. Mehra, *Ind. Eng. Chem. Res.*, 2006, **45**, 2249-2254.
90. D. Shukla and A. Mehra, *Langmuir*, 2006, **22**, 9500-9506.
91. B. N. Wanjala, J. Luo, R. Loukrakpam, B. Fang, D. Mott, P. N. Njoki, M. Engelhard, H. R. Naslund, J. K. Wu, L. Wang, O. Malis and C. J. Zhong, *Chem. Mater.*, 2010, **22**, 4282-4294.
92. Y. Sheng, X. Tang and J. Xue, *J. Mater. Chem.*, 2012, **22**.
93. C. I, *Adv. Colloid Interface Sci.*, 2004, **110**, 49-74.
94. T. Kanoh, T. Shichi and K. Takagi, *Chem. Lett.*, 1999, 117-118.
95. W. Kagunya, R. Baddour-Hadjean, F. Kooli and W. Jones, *Chem. Phys.*, 1998, **236**, 225-234.
96. Z. P. Xu and G. Q. Lu, *Chem. Mater.*, 2005, **17**, 1055-1062.
97. F. Leroux, E. M. Moujahid, C. Taviot-Guého and J.-P. Besse, *Solid State Sciences*, 2001, **3**, 81-92.
98. A. B. P. Laver, *Inorganic Electronic Spectroscopy*, Elsevier, New York, 1984.
99. S. J. S. Qazi, G. Karlsson and A. R. Rennie, *J. Colloid Interface Sci.*, 2010, **348**, 80-84.
100. N. A. Mazer, G. B. Benedek and M. C. Carey, *Biochemistry*, 1980, **19**, 601-615.
101. W. Fujita, K. Awaga and T. Yokoyama, *Appl. Clay Sci.*, 1999, **15**, 281-303.
102. W. Fujita and K. Awaga, *Inorg. Chem.*, 1996, **35**, 1915-1917.
103. P. Rabu, S. Rouba, V. Laget, C. Hornick and M. Drillon, *Chem. Commun.*, 1996, 1107-1108.
104. M. Taibi, S. Ammar, N. Jouini, F. Fievet, P. Molinie and M. Drillon, *J. Mater. Chem.*, 2002, **12**.
105. J. A. Mydosh, *Spin Glasses: An Experimental Introduction*, Taylor & Francis, London, 1993.
106. M. D. Mukadam, S. M. Yusuf, R. Sasikala and S. K. Kulshreshtha, *J. Appl. Phys.*, 2006, **99**.
107. R. V. Chamberlin, M. Hardiman, L. A. Turkevich and R. Orbach, *Phys. Rev. B*, 1982, **25**, 6720-6729.
108. H. A. Katori and A. Ito, *J. Phys. Soc. Jpn.*, 1994, **63**, 3122-3128.
109. G. G. Kenning, D. Chu and R. Orbach, *Phys. Rev. Lett.*, 1991, **66**, 2923-2926.
110. R. S. Freitas, L. Ghivelder, F. Damay, F. Dias and L. F. Cohen, *Phys. Rev. B*, 2001, **64**, 144404.
111. J. C. Denardin, A. L. Brandl, M. Knobel, P. Panissod, A. B. Pakhomov, H. Liu and X. X. Zhang, *Phys. Rev. B*, 2002, **65**, 064422.
112. B. J. Hickey, M. A. Howson, S. O. Musa, G. J. Tomka, B. D. Rainford and N. Wiser, *J. Magn. Magn. Mater.*, 1995, **147**, 253-259.
113. M. D. Mukadam, S. M. Yusuf, P. Sharma and S. K. Kulshreshtha, *J. Magn. Magn. Mater.*, 2004, **269**, 317-326.
114. E. Coronado, J. Galan-Mascaros, C. Marti-Gastaldo, A. Ribera, E. Palacios, M. Castro and R. Burriel, *Inorg. Chem.*, 2008, 9103-9110.
115. J. M. Clemente-Juan, E. Coronado, J. R. Galán-Mascarós and C. J. Gómez-García, *Inorg. Chem.*, 1998, **38**, 55-63.

Chapter 4

Synthesis of Mg-Al Layered Double Hydroxide (LDH) nanoparticles in single component microemulsions

4.1. Introduction

Nanoparticles (NPs) are one of the great interests for scientists, since their vast surface energy grants enormous potential in many applications. In the synthesis of NPs, (i) identical size of all particles (also called monosized or with uniform size distribution), (ii) identical shape or morphology, (iii) identical chemical composition and crystal structure, and (iv) individually dispersed or monodispersed, *i.e.* no agglomeration are the four fundamental requirements.[1] To achieve these requirements, scientists have been trying to manipulate the synthesis of nanoparticles by controlling two steps; nucleation and subsequent growth. For nucleation, homogeneous nucleation in three mediums: liquid, gas and solids are most widely used, while heterogeneous nucleation, described as a new phase formed on a surface of another material, are applied to co-evolution deposition and other methods. For controlling subsequent growth, four general methods are applied: (i) using liquid droplets in the gas phase such as aerosol synthesis and spray pyrolysis, (ii) liquid droplets in a liquid, such as micelles and micro emulsion syntheses, (iii) template-based synthesis, and (iv) self-terminating synthesis.[1] Two or more control means can be combined in synthesising nanoparticles (NPs).

Besides zero-dimensional nanoparticles, (*e.g.* nanospheres, nanoplatelets, and nanocubes) one-dimensional structures, (*e.g.* nanowires and nanorods) and two-dimensional structures, (*e.g.* thin films) are also of great interests.

4.1.1. Mg-Al layered double hydroxides (LDHs)

Layered double hydroxides (LDHs) are a family of layered materials with the composition $[M^{z+}{}_{1-x}M^{3+}{}_{x}(OH)_2]^{a+}(X^{n-})_{a/n} \cdot mH_2O$. When z = 2, M^{2+} and M^{3+} may be selected from a wide range of divalent and trivalent metallic ions, while X^{n-} is a charge-balancing anion.[2-5] Li-Al LDHs are the only sets that contain M^{+} and M^{3+} cations. LDHs are also known as hydrotalcite-like materials, since the parent material of this class is the naturally occurring mineral hydrotalcite, which has the formula $Mg_6Al_2(OH)_{16}CO_3 \cdot 4H_2O$.[6] As one of the oldest members of this family, Mg-Al LDHs have been studied extensively. The structure of Mg-Al LDHs can be considered to comprise positively charged brucite-like layers of mixed metal hydroxides with charge-balancing anions and water molecules in the interlayer space.[2] As a typical representative of the whole LDH family, Mg-Al LDHs have extensive applications as absorbents,[7-10] catalysts and catalyst precursors,[11, 12] drug carriers,[13-23] and bioactive nanocomposites.[24-34] Furthermore, the successful synthesis of Mg-AL LDHs at nanometer scale and their high biocompatibility opens the way to many novel applications in medicine and gene delivery technologies.[28-30, 33, 34] The size of nanoparticles plays an important role in their adhesion to, and interaction with, the biological cell. Oh *et al.* found that the cellular uptake rate of LDH nanoparticles are highly dependent on the particle size in the range of 50 - 350 nm.[35]

Traditionally the co-precipitation method, which involves steady mixing of a solution of cations and a basic solution with vigorous stirring, is most widely used to synthesise LDH materials.[36-41] Many methods have been investigated to control the Mg-Al LDH particle size, *e.g.* the salt-oxide method,[39] synthesis by separate nucleation and aging steps,[42] and spray drying,[43] as well as particle shape, *e.g.* hollow spheres.[44, 45] Hu *et al.* reported the use of a reverse micelle/microemulsion method to precisely control the particle size of Mg-Al LDHs.[46, 47] The size of the "water pools" encapsulated by the surfactant molecules can be adjusted by varying the molar ratio of water to surfactant.

However, the complex constituent ratios of reverse microemulsion, in conjunction with the large quantity of organic solvent used, result in poor flexibility and high production costs for large scale manufacture. In this chapter, a new single component reverse microemulsion approach to synthesise LDHs is developed. In this method, oleylamine performs multiple functions, acting as the oil phase, base and surfactant. Using this system, Mg-Al LDH nanoparticles are synthesised with uniform sizes from 30 - 80 nm.

4.1.2. Oleylamine in inorganic synthesis

Oleylamine (OAm), $C_{18}H_{37}N$, which is also called (9Z)-octadecen-1-amine, is a primary amine with a long alkyl chain containing 18 carbons (**Figure 4-1**). Some of its physical and thermal properties are listed in **Table 4-1**. It can be a perfect candidate for

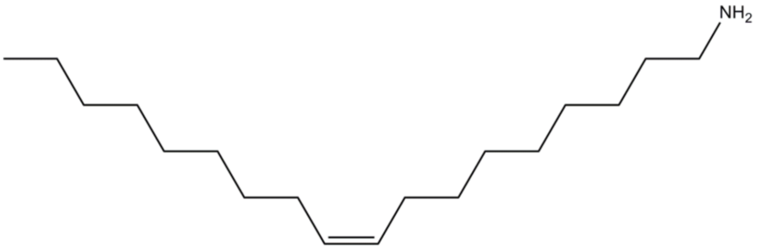

Figure 4-1: Structure of oleylamine

Table 4-1: Physical and thermal properties of oleylamine.

Melting Point	–9.5 ℃	logD [a]	4.68	pH 5 Temp: 25 ℃
Boiling Point	364.4 ±21.0 ℃		4.69	pH 6 Temp: 25 ℃
pKa	10.67 ±0.10		4.78	pH 7 Temp: 25 ℃
Polar Surface Area	26.0 Å^2		5.25	pH 8 Temp: 25 ℃
			6.12	pH 9 Temp: 25 ℃
logP [a]	7.780 ±0.198		7.03	pH 10 Temp: 25 ℃

[a] Partition Coefficient (P) and Distribution Coefficient (D) are calculated using Advanced Chemistry Development (ACD/Labs) Software V11.02 (© 994-2012 ACD/Labs.

inorganic template synthesis because it is a liquid under common synthesis temperatures, can provide a basic environment when combined with water, and its polar head group and long carbon chain provide the possibility of it being a surfactant at the interface of a two phase system.

In practice, oleylamine has been chosen to play important roles in the synthesis of many nanomaterials. Acting as a reducing and capping reagent, oleylamine is one of the most widely used ligands for shape and size controlled synthesis of noble metal nanocrystals (NCs), such as Au nanowires[48-50] and nanorods,[51] Ag nanoparticles,[52-54] Pt nanocubes,[55] monodispersed Pd nanospheres[56, 57] and Pd tetrahedra and multipods.[58] PtFe alloy nanocubes,[59] ultrathin SnSe nanosheets,[60] Au@ZnO nanopyramids,[61] Au/CdS nanocomposites[62] and Pt@Fe_2O_3 nanowires[63] were also obtained using oleylamine due to its strong shape control ability. The protonation of oleylamine provides an alkaline environment, which is suitable to synthesise spinels,[64, 65] oxides[66, 67] and hydroxides.[68] By adjusting the amount of oleylamine in the system, precise shape control on nanoparticle can be achieved. Li *et al.* reported the control of the morphology of $Cu_{2-x}S$ nanoparticles from spherical to tetradecahedral and dodecahedral geometries.[69] Y. Li and co-workers reported a facile process for the controllable synthesis of uniform Mn_3O_4 nanocrystals with different sizes and shapes, which includes dots, rods and wires

(**Figure 4-2**).[66] In some cases, a mixture of oleylamine and its corresponding acid, oleic acid (OAc), was used to design novel nanostructures and peculiar nanomaterials.[53, 56, 58]

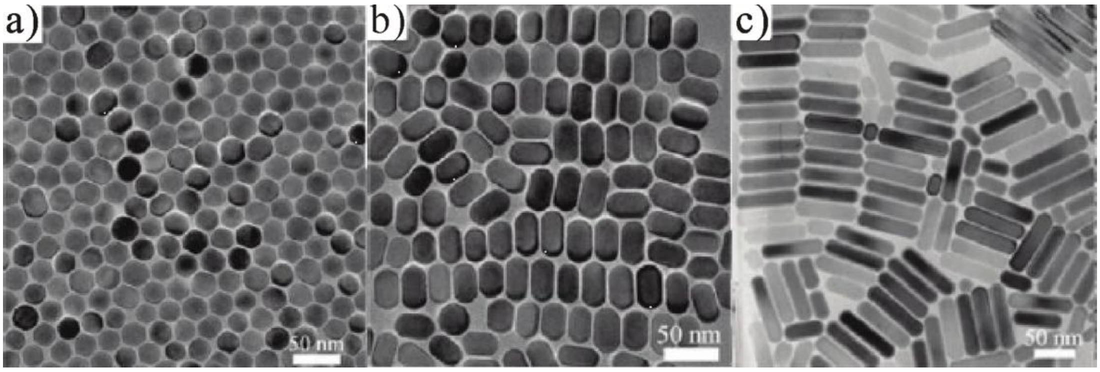

Figure 4-2: TEM images of Mn_3O_4 (a) spheres, (b) short rods, and (c) long rods. (Images are reprinted with the permission from reference 66. Copyright © 2010 American Chemical Society.)

4.2. Results

4.2.1. Synthesis

Oleylamine and 1-butanol were pre-mixed under a purge of N_2, as the amine can react with the CO_2 in the air and form alkylammonium alkylcarbamate (AAAC) pairs according to **Equation 4-1**.[70, 71]

$$2\mathrm{CH_3(CH_2)_nNH_2} + \mathrm{CO_2} \longleftrightarrow \mathrm{CH_3(CH_2)_nNC(O)O} \cdots \mathrm{H_2N(CH_2)_nCH_3}$$

Equation 4-1

After dropwise addition of a solution of mixed metal salts, the mixture was heated at 120 ℃ for 24 hours in a Teflon lined stainless steel autoclave. The total volume of salt solution and oleylamine was maintained at 10 ml, while the volume ratio of oleylamine/solution was controlled as 9 for **MgAl-OAm-1**, 4 for **MgAl-OAm-2** and 1 for **MgAl-OAm-3**. The products were collected by centrifugation. Detailed experimental procedures are listed in **Chapter 7**.

To investigate the mechanism of crystal growth, the synthesis of **MgAl-OAm-1** was carried out in triplicate and stopped after heating for 1, 3, and 5 hours respectively. The samples were collected by centrifugation, washed, dried, and named as **MgAl-OAm-1-1h**, **MgAl-OAm-1-3h**, and **MgAl-OAm-1-5h**.

4.2.2. Elemental analyses

The elemental analysis data (**Table 4-2**) indicates that the Mg/Al molar ratios for the three **MgAl-OAm-*n*** (*n* = 1 - 3) samples are 2.3, 2 and 2.3, respectively. Due to absorbed oleylamine, the carbon contents deviate slightly from the calculated value. The chemical formulations of the samples can be found in **Table 4-2**.

Table 4-2: Summary of elemental analysis data for **MgAl-OAm-*n*** (*n* = 1 - 3).

Sample	Observed (*calc.*) (%)				Calc. Formula
	Mg	Al	C	H	
MgAl-OAm-1	12.91	5.78	3.41	4.76	$[Mg_{2.1}Al_{0.9}(OH)_6]Cl_{0.9}\cdot 9H_2O$ [a,*]
	(13.18)	(6.27)	(3.52)	(6.85)	
MgAl-OAm-2	18.51	10.05	0.77	4.36	$[Mg_2Al_1(OH)_6]Cl\cdot 3H_2O$ [b,*]
	(18.53)	(10.13)	(0.82)	(4.73)	
MgAl-OAm-3	15.04	7.14	2.05	4.69	$[Mg_{2.1}Al_{0.9}(OH)_6]Cl_{0.9}\cdot 7H_2O$ [c,*]
	(14.94)	(7.11)	(1.90)	(6.23)	

[a] containing 4% absorbed oleylamine.

[b] containing 1% absorbed oleylamine.

[c] containing 2% absorbed oleylamine.

[*] all three samples contain trace CO_3^{2-} observed in IR spectra

4.2.3. X-ray powder diffraction

4.2.3.1. XRD data of MgAl-OAm-*n* (*n* = 1 - 3)

Figure 4-3 shows the diffraction patterns of **MgAl-OAm-*n*** (*n* = 1 - 3). All three samples exhibit a series of (00*l*) Bragg reflections for a rhombohedral (3R) sequence giving *c*-lattice parameters of *ca.* 23.2 Å for **MgAl-OAm-*n*** (*n* = 1 - 3). The calculated interlayer separation is *ca.* 7.73 Å, which is similar to the value found for Cl^- ion intercalated LDHs. The positions of the (110) Bragg reflections gives a direct measure of *a* and *b* lattice parameters $a = b = 2d_{110}$ = 3.05 Å for **MgAl-OAm-*n*** (*n* = 1 - 3). Summary of X-ray crystallographic data can be found in **Table 4-3**

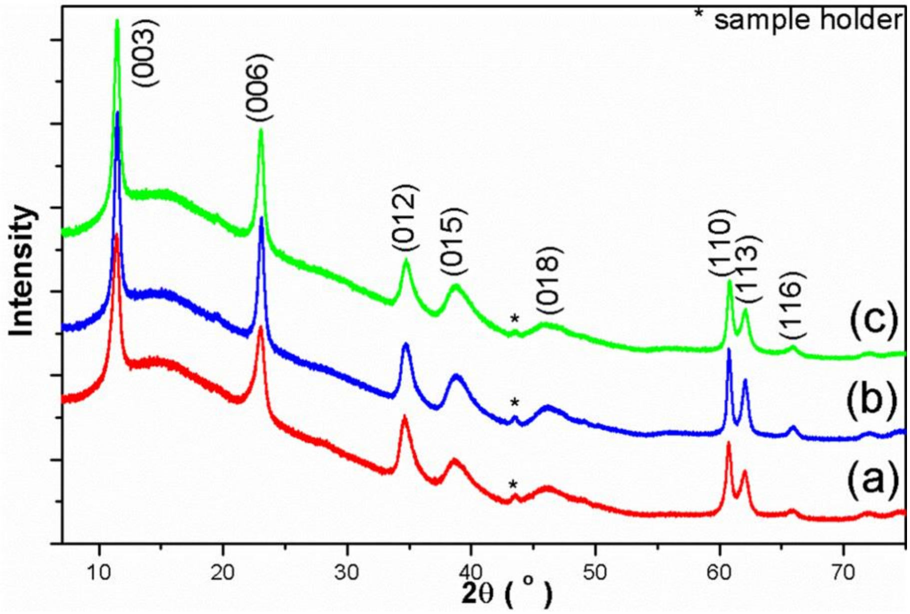

Figure 4-3: XRD patterns of (a) **MgAl-OAm-1**, (b) **MgAl-OAm-2**, and (c) **MgAl-OAm-3**.

Table 4-3: Summary of X-ray crystallographic data for **MgAl-OAm-*n*** (*n* = 1 - 3).

Sample	Bragg reflections (FWHM) (°)					Lattice parameters (Å)	
	003	006	012	015	110	*a*	*c*
MgAl-OAm-1	11.40(0.50)	23.04(0.50)	34.57	38.52	60.69(0.76)	3.05	23.22
MgAl-OAm-2	11.43(0.76)	23.06(0.76)	34.65	38.52	60.77(0.50)	3.05	23.18
MgAl-OAm-3	11.45(0.50)	23.02(0.76)	34.73	38.62	60.78(0.76)	3.05	23.19

4.2.3.2. XRD data of MgAl-OAm-1-*n*h (*n* = 1, 3, and 5)

The powder XRD patterns of **MgAl-OAm-1-1h**, **MgAl-OAm-1-3h**, and **MgAl-OAm-1-5h** are given in **Figure 4-4**. Since the amount of the sample is insufficient to fill the sample holder, Bragg reflections due to the sample holder are observed at *ca.* $2\theta = 43.4°$ and $50.4°$ ((111) and (200) reflections for Ni, JCPDS PDF 00-001-1258). Comparison of the XRD patterns with the pattern of the completed sample **MgAl-OAm-1**, all the diffraction peaks appear after 1 hour of solvothermal treatment, which means the nanoparticles start to crystallise soon after mixing. However, the Bragg reflections in the XRD patterns of **MgAl-OAm-1-1h**, **MgAl-OAm-1-3h**, and **MgAl-OAm-1-5h** are clearly broader than those in the XRD pattern of **MgAl-OAm-1**, implying the samples heated for between 1 - 5 hours are not as crystalline and form smaller particles than are found in the final products.

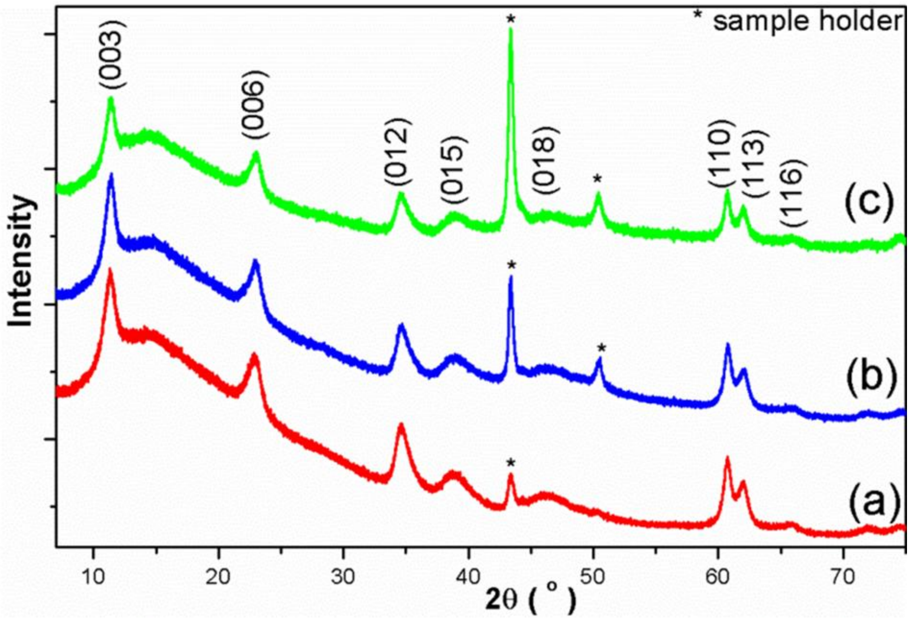

Figure 4-4: XRD patterns of (a) **MgAl-OAm-1-1h**, (b) **MgAl-OAm-1-3h**, and (c) **MgAl-OAm-1-5h**.

4.2.4. FT-IR spectroscopy

The IR spectra of **MgAl-OAm-*n*** (*n* = 1 - 3) are given in **Figure 4-5**. The broad band centred at *ca*. 3400 cm^{-1} corresponds to a combination of the stretching vibration of the hydroxide groups in the brucite sheets and the interlayer water molecules ($\nu_{O\text{-}H}$).[72] The absorbance at 1620 cm^{-1} is assigned to the bending vibrations of the interlayer water molecules ($\delta_{O\text{-}H}$).[73] The strong absorbance at around 1355 cm^{-1} indicates the existence of CO_3^{2-} ($\nu_{C\text{-}O}$), which is due to unavoidable absorption of CO_2 from the air. The absorbances below 1000 cm^{-1} can be ascribed as vibrations of metal oxygen bonds ($\nu_{M\text{-}O}$).

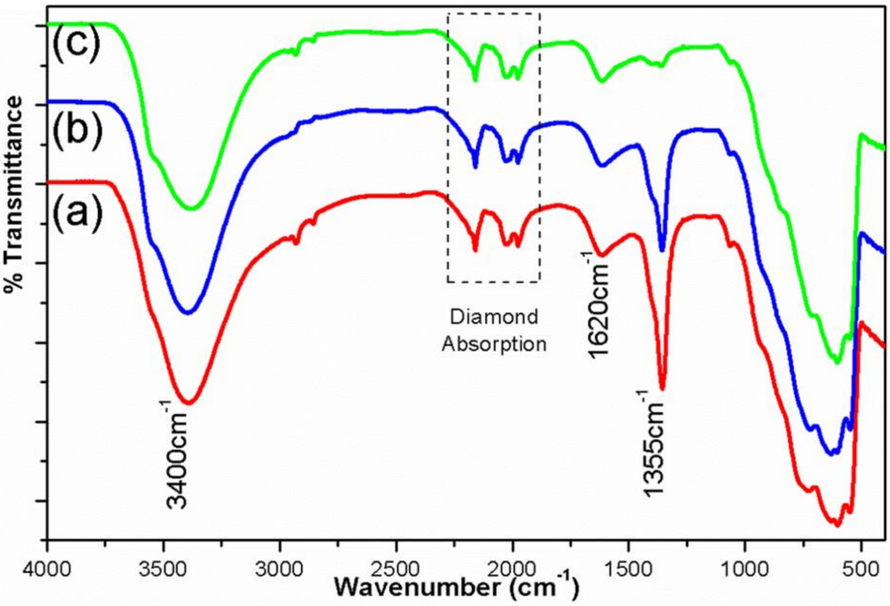

Figure 4-5: IR spectra of (a) **MgAl-OAm-1**, (b) **MgAl-OAm-2**, and (c) **MgAl-OAm-3**.

4.2.5. TEM imaging and particle size analyses

Figure 4-6 shows TEM images of **MgAl-OAm-*n*** (*n* = 1 - 3). All the platelets are very thin, as one platelet can often be imaged through another. Most of the platelets

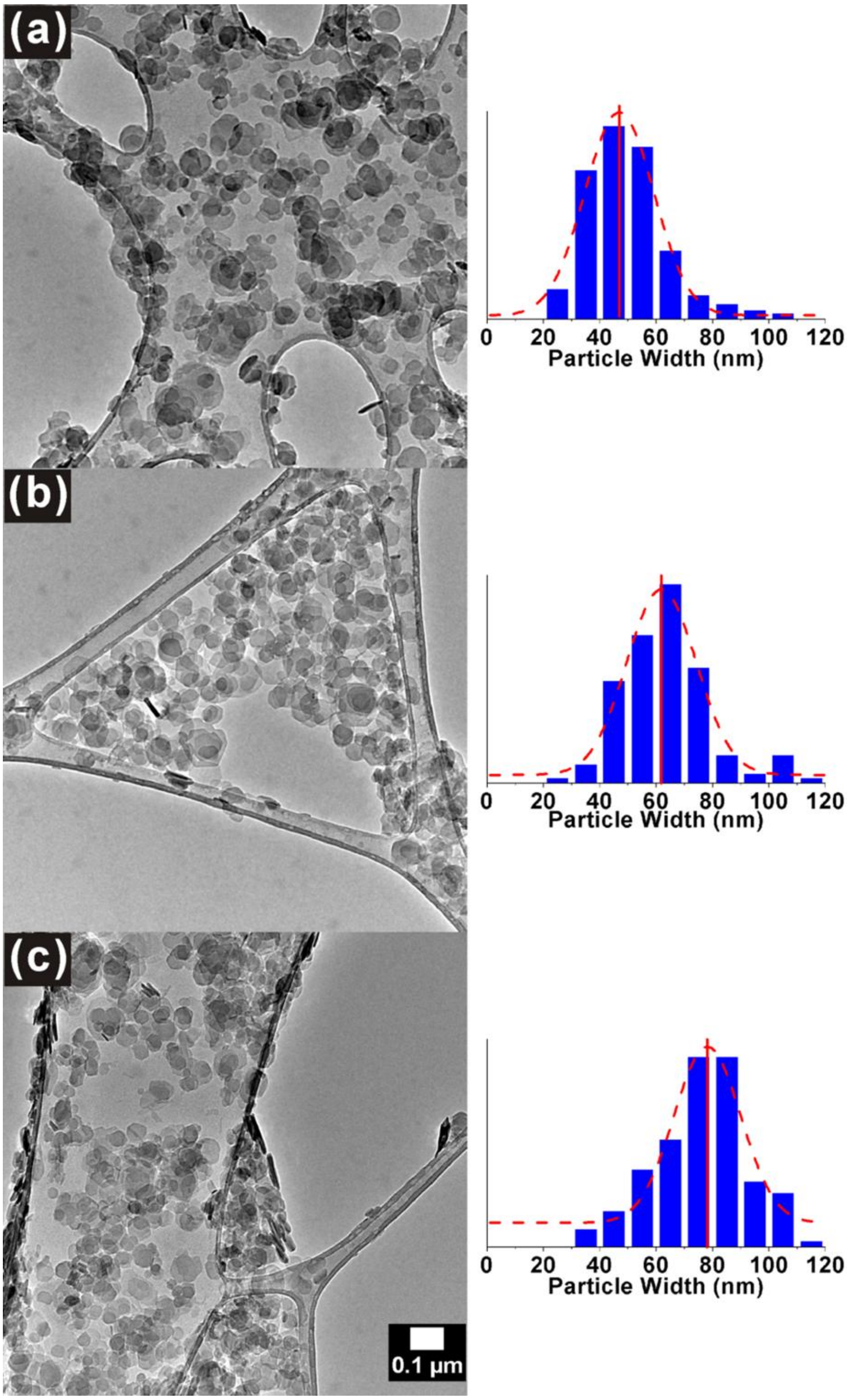

Figure 4-6: TEM images and particle size distributions of (a) **MgAl-OAm-1**, (b) **MgAl-OAm-2**, and (c) **MgAl-OAm-3**. The dashed lines are best fit to Gaussian equation.

adopt a hexagonal shape. Particle size distribution was estimated by measuring in excess of 100 particles. Statistical analysis of the particle size distribution to a normal distribution gives the mean (μ), standard deviation ($\sigma = \sqrt{\frac{1}{N-1}\sum_{i=1}^{N}(x_i-\mu)^2}$) and variance ($\sigma^2$)[74] (**Table 4-4)**. The mean diameters are 49.18, 63.97 and 75.41 nm for **MgAl-OAm-*n*** (*n* = 1 - 3), respectively. Little change in the variance indicates that the distributions of diameters are similar for the three samples.

Table 4-4: Summary of statistical analysis of particle diameters and thicknesses for **MgAl-OAm-*n*** (*n* = 1 - 3).

Sample	Diameter (nm)			Thickness (nm)		
	Mean (μ)	Stdev. (σ)	Var. (σ^2)	Mean (μ)	Stdev. (σ)	Var. (σ^2)
MgAl-OAm-1	49.18	14.95	223.6	10.75	1.791	3.206
MgAl-OAm-2	63.97	17.21	296.1	15.58	3.447	11.89
MgAl-OAm-3	75.41	15.91	253.1	27.03	3.507	12.30

4.2.6. AFM imaging

In **Figure 4-7** (a), the overall image of a 1.5 × 1.5 μm area of **MgAl-OAm-1** on a highly ordered pyrolytic graphite (HOPG) substrate is shown. Well-dispersed single particles with widths of about 40 nm and thicknesses of 10 nm are observed, as well as a few aggregates. Cross-sectional analysis of a number of single particles gives an average thickness of 10.75 nm. The diameter distribution is similar to the range measured by TEM. **Figure 4-7** (b) gives an AFM image of a 2 × 2 μm area of **MgAl-OAm-2**. Dispersed single particles can be observed as seen previously in the TEM images. **Figure 4-7** (c) illustrates the image of a 2 × 2 μm area of **MgAl-OAm-3**. Single particles along with a few aggregates can be seen in the image. Particle profile analyses lead to the calculation of thickness values of 15.58 nm for **MgAl-OAm-2**, and 27.03 nm for **MgAl-OAm-3**. The detailed statistical data is listed in **Table 4-4**.

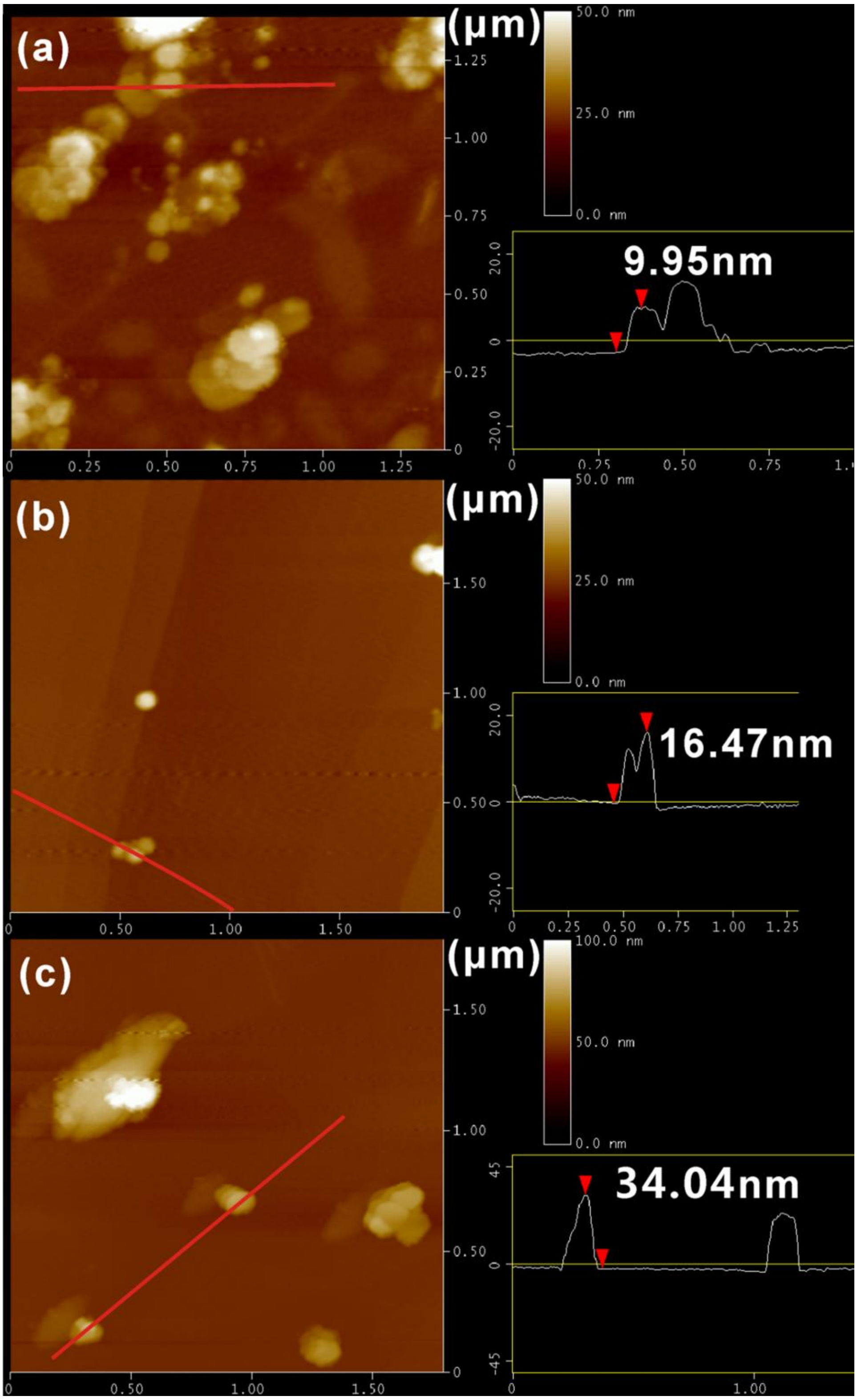

Figure 4-7: AFM images of (a) **MgAl-OAm-1**, (b) **MgAl-OAm-2**, and (c) **MgAl-OAm-3**. The curves are the corresponding cross sectional data along the red lines in the images.

XRD data analysis has confirmed that the thickness of a **MgAl-OAm-*n*** (*n* = 1 - 3) monolayer is 7.73 Å. Therefore, for **MgAl-OAm-*n*** (*n* = 1 - 3), the platelets consist of 14, 20 and 35 layers respectively. The particle sizes are approximately linearly correlated with the volume ratio of oleylamine to water (**Section 4.3.2**), which further suggests that particle growth can be controlled, and that a smaller ratio leads to the formation of larger particles.

4.3. Discussion

4.3.1. Crystal growth

The TEM images of the **MgAl-OAM-1-*n*h** (*n* = 1, 3, and 5) samples reveal insights into the process of particle growth (**Figure 4-8**).

For **MgAl-OAm-1-1h** sample, the solids were separated from the reaction mixture after heating at 120 ℃ for 1 hour. The particles are around 20 nm in diameter without any specific morphology, which indicates that an instantaneous nucleation process takes place under supersaturation conditions. Once nuclei have formed, crystal growth occurs simultaneously. After this initial nucleation, both the concentration and supersaturation of the growth species decreases.[1] This halts the nucleation process, and the reaction proceeds to a subsequent growth step. After 3 hours, the particles grow to nearly full size and start to show a hexagonal platelet morphology, which illustrates that growth proceeds until the concentration of growth species has attained the equilibrium concentration or solubility,[75] or the growth is terminated by spatial confinements. However, thermodynamic control is not the only restriction to this process. The micelles formed by water, oleylamine and 1-butanol kinetically control the particle growth, which is demonstrated by **MgAl-OAm-1-5h**. After reacting for 5 hours, the particles are

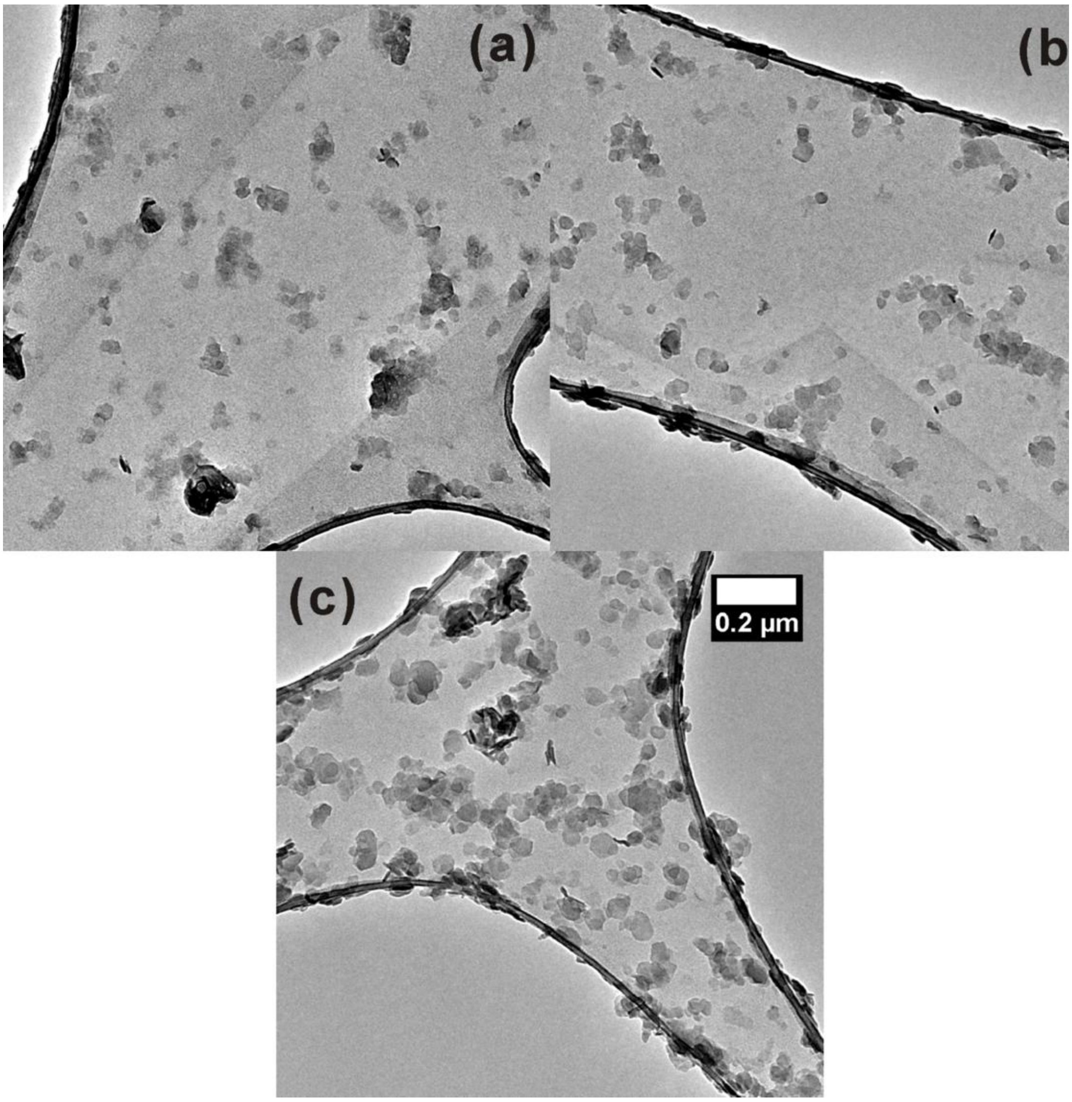

Figure 4-8: TEM images of (a) **MgAl-OAm-1-1h**, (b) **MgAl-OAm-1-3h**, and (c) **MgAl-OAm-1-5h**.

nearly as same as the final product which is monosized hexagonal platelets. In summary, the whole synthesis process involves a typical instantaneous nucleation when the aqueous solution was added into oleylamine and a synergistic effect of micelles and reaction equilibrium controlled the particle size during the crystal growth step.

4.3.2. The role of oleylamine

The single component in the microemulsion, oleylamine, plays three roles in this synthesis. The protonation of amine provides the alkaline environment for the precipitation of the LDH particles. With the protonated amine head and the long alkyl chain, oleylamine also functioned as a surfactant which forms reverse micelles that act as a template for crystal growth. Excess oleylamine rather than a separate oil phase was used because unlike common powder surfactant, oleylamine is a liquid at room temperature. This brings more advantages, such as recyclability and low environmental impact.

The diameters and the thicknesses of the three samples are inversely proportional to the volume ratio of oleylamine to water (**Figure 4-9**). This matches previous reports about reverse microemulsions, as the radius of the water pool is in line with the molar ratio of water to surfactant.[76-78]

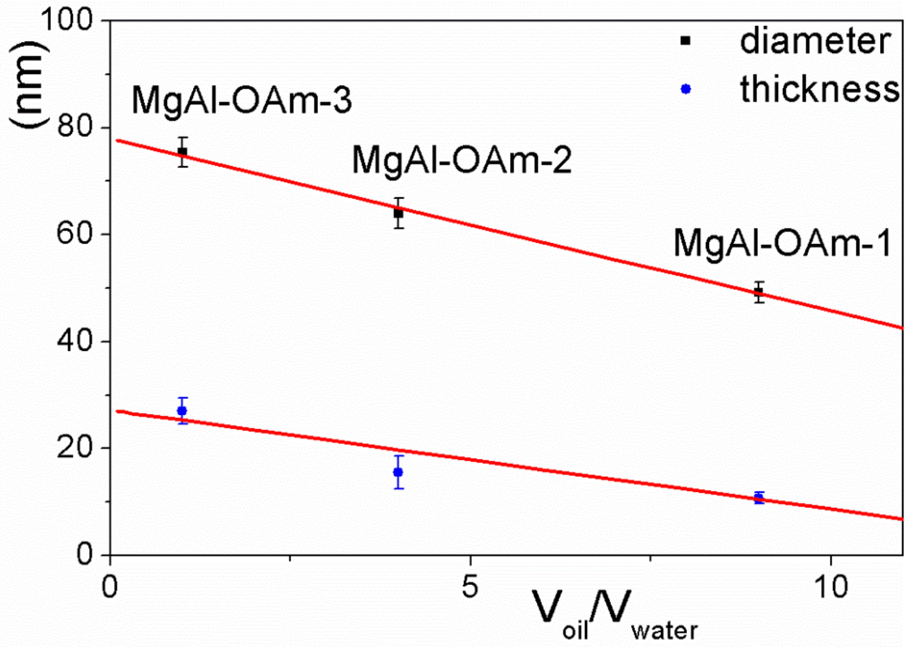

Figure 4-9: The plot of diameters of particles *vs.* volume ratio of oil to water. The error bars are the 95% confidence intervals (*i.e.* the range within which the true treatment effect is likely to lie).[79]

4.4. Conclusion

Monosized Mg-Al LDH nanoplatelets have been successfully synthesised in three different microemulsion systems, in which oleylamine acts as the surfactant, as well as base and oil phase. X-ray diffraction and IR spectra verified that the three samples were intercalated with Cl^- ions between layers, as well as small amount absorbed CO_3^{2-} and oleylamine. The interlamellar separations are about 7.73 Å. TEM and AFM imaging reveals that the particles adopt a hexagonal disc-like structure and the sizes of the samples are well controlled. The diameters of the three samples are proportional to the volume ratio of oleylamine to water.

4.5. References

1. G. Cao and Y. Wang, *Nanostructures and nanomaterials: synthesis, properties, and applications*, World Scientific, 2010.
2. L. Pesic, S. Salipurovic, V. Markovic, D. Vucelic, W. Kagunya and W. Jones, *J. Mater. Chem.*, 1992, **2**, 1069-1073.
3. V. Rives, F. M. Labajos, M. A. Ulibarri and P. Malet, *Inorg. Chem.*, 1993, **32**, 5000-5001.
4. A. I. Khan and D. O'Hare, *J. Mater. Chem.*, 2002, **12**, 3191-3198.
5. P. S. Braterman, Z. P. Xu and F. Yarberry, *Handbook of Layered Materials*, 2004, 373-474.
6. E. Manasse, *Atti Soc. Toscana Sci. Nat.*, 1915, **24**, 92.
7. P. C. Pavan, G. d. A. Gomes and J. B. Valim, *Microporous Mesoporous Mater.*, 1998, **21**, 659-665.
8. J. Das, B. Patra, N. Baliarsingh and K. Parida, *Appl. Clay Sci.*, 2006, **32**, 252-260.
9. N. N. Das, J. Konar, M. K. Mohanta and S. C. Srivastava, *J. Colloid Interface Sci.*, 2004, **270**, 1-8.
10. C. Markland, G. R. Williams and D. O'Hare, *J. Mater. Chem.*, 2011, **21**, 17896-17903.
11. G. Centi and S. Perathoner, *Microporous Mesoporous Mater.*, 2008, **107**, 3-15.
12. D. Carriazo, C. Martín and V. Rives, *Eur. J. Inorg. Chem.*, 2006, **2006**, 4608-4615.
13. J. -H. Yang, Y.-S. Han, M. Park, T. Park, S.-J. Hwang and J.-H. Choy, *Chem. Mater.*, 2007, **19**, 2679-2685.
14. L. Perioli, V. Ambrogi, B. Bertini, M. Ricci, M. Nocchetti, L. Latterini and C. Rossi, *Eur. J. Pharm. Biopharm.*, 2006, **62**, 185-193.
15. Z. Gu, A. C. Thomas, Z. P. Xu, J. H. Campbell and G. Q. Lu, *Chem. Mater.*, 2008, **20**, 3715-3722.
16. M. Del Arco, E. Cebadera, S. Gutiérrez, C. Martín, M. J. Montero, V. Rives, J.

Rocha and M. A. Sevilla, *J. Pharm. Sci.*, 2004, **93**, 1649-1658.

17. J.-M. Oh, M. Park, S.-T. Kim, J.-Y. Jung, Y.-G. Kang and J.-H. Choy, *J. Phys. Chem. Solids*, **67**, 1024-1027.
18. B. Li, J. He, D. G. Evans and X. Duan, *Appl. Clay Sci.*, 2004, **27**, 199-207.
19. S.-H. Hwang, Y.-S. Han and J.-H. Choy, *Bull. Korean Chem. Soc.*, 2001, **22**, 1019-1022.
20. J.-H. Choy, J.-S. Jung, J.-M. Oh, M. Park, J. Jeong, Y.-K. Kang and O.-J. Han, *Biomaterials*, 2004, **25**, 3059-3064.
21. J. H. Choy, S. J. Choi, J. M. Oh and T. Park, *J. Nanosci. Nanotechno.*, 2007, **7**, 4017-4020.
22. S.-J. Choi, J.-M. Oh and J.-H. Choy, *J. Nanosci. Nanotechno.*, 2010, **10**, 2913-2916.
23. V. Ambrogi, G. Fardella, G. Grandolini and L. Perioli, *Int. J. Pharm.*, 2001, **220**, 23-32.
24. A. W. Musumeci, G. M. Mortimer, M. K. Butler, Z. P. Xu, R. F. Minchin and D. J. Martin, *Appl. Clay Sci.*, 2010, **48**, 271-279.
25. F. Leroux and J.-P. Besse, *Chem. Mater.*, 2001, **13**, 3507-3515.
26. M. Darder, M. López-Blanco, P. Aranda, F. Leroux and E. Ruiz-Hitzky, *Chem. Mater.*, 2005, **17**, 1969-1977.
27. J.-H. Choy, S.-Y. Kwak, Y.-J. Jeong and J.-S. Park, *Angew. Chem. Int. Ed.*, 2000, **39**, 4041-4045.
28. J.-H. Choy, S.-Y. Kwak, J.-S. Park, Y.-J. Jeong and J. Portier, *J. Am. Chem. Soc.*, 1999, **121**, 1399-1400.
29. L. Desigaux, M. B. Belkacem, P. Richard, J. Cellier, P. Léone, L. Cario, F. Leroux, C. Taviot-Guého and B. Pitard, *Nano Lett.*, 2005, **6**, 199-204.
30. Y. Wong, K. Markham, Z. P. Xu, M. Chen, G. Q. Lu, P. F. Bartlett and H. M. Cooper, *Biomaterials*, 2010, **31**, 8770-8779.
31. H. Nakayama, N. Wada and M. Tsuhako, *Int. J. Pharm.*, 2004, **269**, 469-478.
32. J. Liu, R. Harrison, J. Z. Zhou, T. T. Liu, C. Yu, G. Q. Lu, S. Z. Qiao and Z. P. Xu, *J. Mater. Chem.*, 2011, **21**, 10641-10644.
33. K. Ladewig, M. Niebert, Z. P. Xu, P. P. Gray and G. Q. M. Lu, *Biomaterials*, 2010, **31**, 1821-1829.
34. J.-H. Choy, S.-Y. Kwak, J.-S. Park and Y.-J. Jeong, *J. Mater. Chem.*, 2001, **11**, 1671-1674.
35. J.-M. Oh, S.-J. Choi, G.-E. Lee, J.-E. Kim and J.-H. Choy, *Chem. Asian J.*, 2009, **4**, 67-73.
36. S. Miyata, *Clays Clay Miner.*, 1980, **28**, 50.
37. A. Roy, C. Forano and J. P. Besse, in *Layered Double Hydroxides: Present and Future*, Nova Science, New York, Editon edn., 2001.
38. J. He, M. Wei, B. Li, Y. Kang, D. G. Evans and X. Duan, in *Layered Double Hydroxides, Structure and Bonding*, eds. X. Duan and D. G. Evans, Springer, Editon edn., 2001, pp. 89-119.
39. L. Albiston, K. R. Franklin, E. Lee and J. B. A. F. Smeulders, *J. Mater. Chem.*, 1996, **6**, 871-877.
40. Z. P. Xu, G. Stevenson, C.-Q. Lu and G. Q. Lu, *J. Phys. Chem. B*, 2006, **110**, 16923-16929.
41. R. Chitrakar, Y. Makita, A. Sonoda and T. Hirotsu, *J. Hazard. Mater.*, 2011, **185**, 1435-1439.
42. Y. Zhao, F. Li, R. Zhang, D. G. Evans and X. Duan, *Chem. Mater.*, 2002, **14**,

4286-4291.

43. Y. Wang, F. Zhang, S. Xu, X. Wang, D. G. Evans and X. Duan, *Ind. Eng. Chem. Res.*, 2008, **47**, 5746-5750.
44. L. Li, R. Ma, N. Iyi, Y. Ebina, K. Takada and T. Sasaki, *Chem. Commun.*, 2006, 3125-3127.
45. E. Gardner, K. M. Huntoon and T. J. Pinnavaia, *Adv. Mater.*, 2001, **13**, 1263-1266.
46. G. Hu, N. Wang, D. O'Hare and J. Davis, *J. Mater. Chem.*, 2007, **17**, 2257-2266.
47. G. Hu and D. O'Hare, *J. Am. Chem. Soc.*, 2005, **127**, 17808-17813.
48. X. Lu, M. S. Yavuz, H.-Y. Tuan, B. A. Korgel and Y. Xia, *J. Am. Chem. Soc.*, 2008, **130**, 8900-8901.
49. Z. Huo, C.-k. Tsung, W. Huang, X. Zhang and P. Yang, *Nano Lett.*, 2008, **8**, 2041-2044.
50. N. Pazos-Pérez, D. Baranov, S. Irsen, M. Hilgendorff, L. M. Liz-Marzán and M. Giersig, *Langmuir*, 2008, **24**, 9855-9860.
51. Z. Li, J. Tao, X. Lu, Y. Zhu and Y. Xia, *Nano Lett.*, 2008, **8**, 3052-3055.
52. L. Polavarapu, K. K. Manga, K. Yu, P. K. Ang, H. D. Cao, J. Balapanuru, K. P. Loh and Q.-H. Xu, *Nanoscale*, 2011, **3**, 2268-2274.
53. S. Çınar, G. Gündüz, B. Mavis and Ü. Çolak, *J. Nanosci. Nanotechno.*, 2011, **11**, 3669-3679.
54. F. Mojahed, S. Dehghanpour, M. Alizadeh and A. Mahmoudi, *Synthesis and Reactivity in Inorganic, Metal-Organic, and Nano-Metal Chemistry*, 2011, **41**, 664-670.
55. C. Wang, H. Daimon, Y. Lee, J. Kim and S. Sun, *J. Am. Chem. Soc.*, 2007, **129**, 6974-6975.
56. V. Mazumder and S. Sun, *J. Am. Chem. Soc.*, 2009, **131**, 4588-4589.
57. Y. Liu, C. Wang, Y. Wei, L. Zhu, D. Li, J. S. Jiang, N. M. Markovic, V. R. Stamenkovic and S. Sun, *Nano Lett.*, 2011, **11**, 1614-1617.
58. B. Hu, K. Ding, T. Wu, X. Zhou, H. Fan, T. Jiang, Q. Wang and B. Han, *Chem. Commun.*, 2010, **46**, 8552-8554.
59. M. Chen, J. Kim, J. P. Liu, H. Fan and S. Sun, *J. Am. Chem. Soc.*, 2006, **128**, 7132-7133.
60. D. D. Vaughn, S.-I. In and R. E. Schaak, *ACS Nano*, 2011, **5**, 8852-8860.
61. N. P. Herring, K. AbouZeid, M. B. Mohamed, J. Pinsk and M. S. El-Shall, *Langmuir*, 2011, **27**, 15146-15154.
62. E. Khon, N. N. Hewa-Kasakarage, I. Nemitz, K. Acharya and M. Zamkov, *Chem. Mater.*, 2010, **22**, 5929-5936.
63. H. Hong, L. Hu, M. Li, J. Zheng, X. Sun, X. Lu, X. Cao, J. Lu and H. Gu, *Chemistry – A European Journal*, 2011, **17**, 8726-8730.
64. S. Q. Tang, S. J. Moon, K. H. Park, S. H. Paek, K.-W. Chung and S. Bae, *J. Nanosci. Nanotechno.*, 2011, **11**, 82-89.
65. K. P. Naidek, F. Bianconi, T. C. R. da Rocha, D. Zanchet, J. A. Bonacin, M. A. Novak, M. das Graças Fialho Vaz and H. Winnischofer, *J. Colloid Interface Sci.*, 2011, **358**, 39-46.
66. P. Li, C. Nan, Z. Wei, J. Lu, Q. Peng and Y. Li, *Chem. Mater.*, 2010, 4232-4236.
67. C.-H. Ho, C.-P. Tsai, C.-C. Chung, C.-Y. Tsai, F.-R. Chen, H.-J. Lin and C.-H. Lai, *Chem. Mater.*, 2011, **23**, 1753-1760.
68. T.-D. Nguyen, C.-T. Dinh and T.-O. Do, *Inorg. Chem.*, 2011, **50**, 1309-1320.
69. W. Li, A. Shavel, R. Guzman, J. Rubio-Garcia, C. Flox, J. Fan, D. Cadavid, M. Ibanez, J. Arbiol, J. R. Morante and A. Cabot, *Chem. Commun.*, 2011.

70. D. M. Rudkevich and H. Xu, *Chem. Commun.*, 2005, 2651-2659.
71. N. Belman, J. N. Israelachvili, Y. Li, C. R. Safinya, J. Bernstein and Y. Golan, *Nano Lett.*, 2009, **9**, 2088-2093.
72. W. Kagunya, R. Baddour-Hadjean, F. Kooli and W. Jones, *Chem. Phys.*, 1998, **236**, 225-234.
73. Z. P. Xu and G. Q. Lu, *Chem. Mater.*, 2005, **17**, 1055-1062.
74. J. Gurland and R. C. Tripathi, *The American Statistician*, 1971, **25**, 30-32.
75. M. Haruta and B. Delmon, *J Chim. Phys.*, 1986, **83**, 859.
76. M. P. Pileni, *J. Phys. Chem.*, 1993, **97**, 6961-6973.
77. M.-P. Pileni, T. Zemb and C. Petit, *Chem. Phys. Lett.*, 1985, **118**, 414-420.
78. M. P. Pileni, *Langmuir*, 1997, **13**, 3266-3276.
79. R. A. Fisher, *Statistical methods and scientific inference*, Oxford, England: Hafner Publishing Co., 1956.

Chapter 5

Synthesis of M-Al and M-Fe (M = Co, Ni, Zn, Li, Ca) Layered Double Hydroxide (LDH) nanoparticles in single component microemulsions

5.1. Introduction

As discussed in the preceding chapter, Mg-Al layered double hydroxide (LDH) nanoparticles have been synthesised using a novel single component microemulsion system formed by oleylamine. In the system, oleylamine played the roles of oil phase, base and surfactant all together. Narrow size distribution of Mg-Al LDH nanoparticles with diameters from 40 nm to 80 nm were obtained through homogeneous nucleation followed by subsequent crystal growth. The particle sizes of the LDHs can be controlled by adjusting the oleylamine-water ratio. Compared to existing syntheses, this method has the advantages of high productivity and flexibility. In this chapter, the method has been extended to LDHs with other metal combinations, *e.g.* Co-Al, Ni-Al, Zn-Al, Li-Al, Ca-Al, Ni-Fe.

Since the solubility of different metal hydroxides varies, a specific pH range is required to provide supersaturation for homogeneous nucleation of certain metal combinations. As discussed in **Chapter 1**, the pH is relevant to the concentration of the metal ions, the solubility of the metal hydroxides and the temperature. Usually, Mg-Al

LDHs precipitate at pH 8 - 10,[1-3] while Ca-Al LDHs form at slightly higher pH (10 - 12).[4-6] Al-containing LDHs generally precipitate at a higher pH than Fe-containing LDHs, for example, Ni-Fe and Co-Fe LDHs were prepared at pH = 7 or even lower.[7-13]

5.1.1. Single component microemulsions

In **Chapter 4**, we designed a single component microemulsion system using oleylamine as both oil phase and surfactant, 1-butanol as assistant surfactant, and aqueous solution as the water phase. Since 1-butanol has limited solubility in water, we could consider the system as oleylamine dispersing in a 1-butanol/water two phase mixture (**Figure 5-1**). Therefore, the ratio of oleylamine concentration in 1-butanol to that in water is described by a Partition Coefficient (P). After distribution in water, oleylamine would be protonated to the oleylaminium cation and hydroxyl anion. The ratio of oleylamine concentration in 1-butanol to the total concentration of neutral and protonated oleylamine is defined by the Distribution Coefficient (D). For common organic chemicals, their logP and logD parameters using octanol as oil phase can be

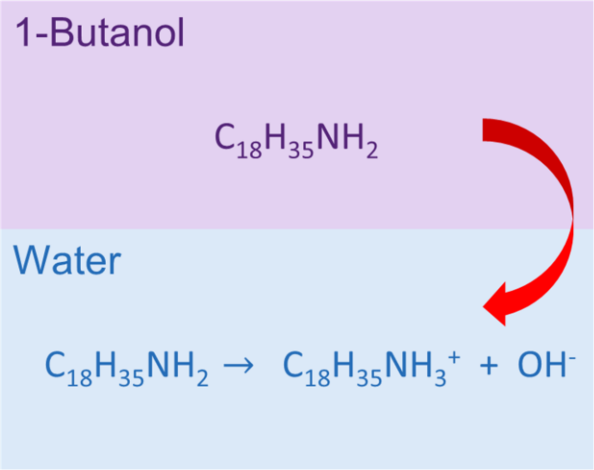

Figure 5-1: Illustration of the oleylamine distribution in a 1-butanol/water two phase mixture.

calculated using Advanced Chemistry Development (ACD/Labs) Software. Suppose both coefficients in 1-butanol/water system are the same as those in octanol/water system, the relationship between logP and logD can be expressed as **Equation 5-1**.[14]

$$\mathrm{P} = \frac{[Oleylamine]_{1-butanol}}{[Oleylamine]_{water}}$$

$$\mathrm{D} = \frac{[Oleylamine]_{1-butanol}}{[Oleylamine]_{water} + [Oleylaminium]_{water}}$$

$$\mathrm{logD} = \mathrm{logP} + \log\frac{1}{1 + 10^{pH-pK_a}} \quad (in\ acids)$$

$$\mathrm{logD} = \mathrm{logP} + \log\frac{1}{1 + 10^{pK_a-pH}} \quad (in\ bases)$$

Equation 5-1

With known logD, logP and pKa, the pH value in the aqueous phase can be calculated. In this system, the pH value is approximately 9.9, which is a suitable pH for Mg-Al LDHs to precipitate.

To provide a suitable environment with the correct pH for the precipitation of other LDHs, a great number of various amines or anilines were investigated. Mainly three factors were taken into account: (i) price, (ii) melting point and boiling point, and (iii) the pH of the system. As amine acts as the oil phase in the system, a low price would lower production costs. Meanwhile, the candidate amine should be liquid at room temperature and have a relatively high boiling point to reduce possible risk of explosion. The pH of the system depends on logP, logD and pKa. Generally, the basicity of a primary amine is the highest followed by secondary and tertiary amines, respectively, due to steric hindrance and solubility factors. Long aryl chains enhance the basicity because of inductive effects, while aromatic rings diminish it due to the mesomeric effect. Considering these three factors, several amines were chosen as candidates for further experiments: dodecylamine (DDAm), dioctylamine (DOAm), 4-butylaniline (BTAn), and N,N-dimethyltetradecylamine (DMTDAm). Their physical properties and prices are listed in **Table 5-1**. The pH given in the table is calculated assuming an ideal distribution system. The differences when substituting octanol with 1-butanol, the influence of changing the ratio of the phases, and the original pH of the salt solutions were not taken into account.

Practically, dodecylamine (DDAm) was ruled out because of its high melting point, as well as 4-butylaniline because of its insufficient carbon chain length to from micelles. Therefore, oleylamine, dioctylamine and N,N-dimethyltetradecylamine were selected to generate various microemulsions to synthesise LDHs, though they are still not able to cover the whole pH range of LDH synthesis. Upon further investigation, other amines

Table 5-1: Summary of physical properties of candidate amines and anilines.

	dodecylamine	dioctylamine	N,N-dimethyltetradecylamine	4-butylaniline
Formula	$CH_3(CH_2)_{11}NH_2$	$NH(CH_3(CH_2)_7)_2$	$(CH_3)_2N(CH_2)_{13}CH_3$	$CH_3(CH_2)_3C_6H_4NH_2$
Price (£)*	26.80 /100 ml	38.30 /100 g	19.70 /100 ml	32.90 /100 g
Melting point (℃)	28.3	13	-	-14
Boiling point (℃)	259	297.5	105	261
pKa	10.67 ± 0.10	11.10 ± 0.19	9.78 ± 0.28	4.91 ± 0.10
logP	5.132 ± 0.183	6.771 ± 0.200	6.742 ± 0.222	3.061 ± 0.196
log D (at 25 ℃)	2.13, pH 7	3.71, pH 7	4.13, pH 7	2.12, pH 4
	2.60, pH 8	3.97, pH 8	4.98, pH 8	2.81, pH 5
	3.46, pH 9	4.71, pH 9	5.90, pH 9	3.03, pH 6
	4.38, pH 10	5.64, pH 10	6.54, pH 10	3.06, pH 7-10
pH	10.2	10.7	9.8	6.6

* from Sigma-Aldrich website.

or anilines may complete the pH range and make this single component microemulsion system generally applicable in LDH synthesis.

5.2. Results and discussion

5.2.1. Synthesis

Oleylamine (OAm), dioctylamine (DOAm) and N,N-dimethyltetradecylamine (DMTDAm) have been used to generate four single component microemulsions. Co-Al, Ni-Al, Zn-Al, Li-Al, Ca-Al, and Ni-Fe LDHs were synthesised in these four microemulsions. Ca-Al LDHs were synthesised in the microemulsions formed by OAm, or DOAm, or a mixture of equal OAm and DOAm, since they usually precipitate at relatively high pH. Co-Al and Ni-Al LDHs were prepared in both OAm and DMTDAm. As the pH values of both microemulsions are suitable for synthesising Co-Al and Ni-Al LDHs, they were able to provide a comparison between the microemulsions formed by OAm and those formed by DMTDAm. Except Zn-Al LDHs, all the other products were synthesised by a solvothermal process at 120 ℃ for 24 hours. Due to the facile formation of ZnO at higher temperature, the syntheses of Zn-Al LDHs were kept at 60 ℃ for 12 hours. For all the samples, the total volume of salt solution and amine was maintained at 10 ml, while the volume ratio of amine/solution was controlled as 9, 4, and 1 for sample 1, 2, and 3, respectively. The products were collected by centrifugation. A summary of synthesis conditions of the products are listed in **Table 5-2**. Detailed experimental procedures can be found in **Chapter 7**.

Table 5-2: Summary of synthetic details using single component microemulsions.

Amine	Metal Combination	Condition (℃, h)	Sample
dioctylamine (DOAm)	Ca-Al	120, 24	CaAl-DOAm-1 CaAl-DOAm-2 CaAl-DOAm-3
DOAm/OAm = 1:1	Ca-Al	120, 24	CaAl-DOAm-OAm-1 CaAl-DOAm-OAm-2 CaAl-DOAm-OAm-3
oleylamine (OAm)	Co-Al	120, 24	CoAl-OAm-1 CoAl-OAm-2 CoAl-OAm-3
	Ni-Al	120, 24	NiAl-OAm-1 NiAl-OAm-2 NiAl-OAm-3
	Ca-Al	120, 24	CaAl-OAm-1 CaAl-OAm-2 CaAl-OAm-3
N,N-dimethyltetradecylamine (DMTDAm)	Co-Al	120, 24	CoAl-DMTDAm-1 CoAl-DMTDAm-2 CoAl-DMTDAm-3
	Ni-Al	120, 24	NiAl-DMTDAm-1 NiAl-DMTDAm-2 NiAl-DMTDAm-3
	Li-Al	120, 24	LiAl-DMTDAm-1 LiAl-DMTDAm-2 LiAl-DMTDAm-3
	Zn-Al	60, 12	ZnAl-DMTDAm-1 ZnAl-DMTDAm-2 ZnAl-DMTDAm-3
	Ni-Fe	120, 24	NiFe-DMTDAm-1 NiFe-DMTDAm-2 NiFe-DMTDAm-3

5.2.2. Powder X-ray diffraction

5.2.2.1. XRD data of Co-Al LDHs

The powder XRD patterns of all the Co-Al LDHs synthesised using oleylamine or N,N-dimethyltetradecylamine are shown in **Figure 5-2**. A series of (00*l*) Bragg reflections for a rhombohedral (3R) sequence can be seen for all six samples. Their

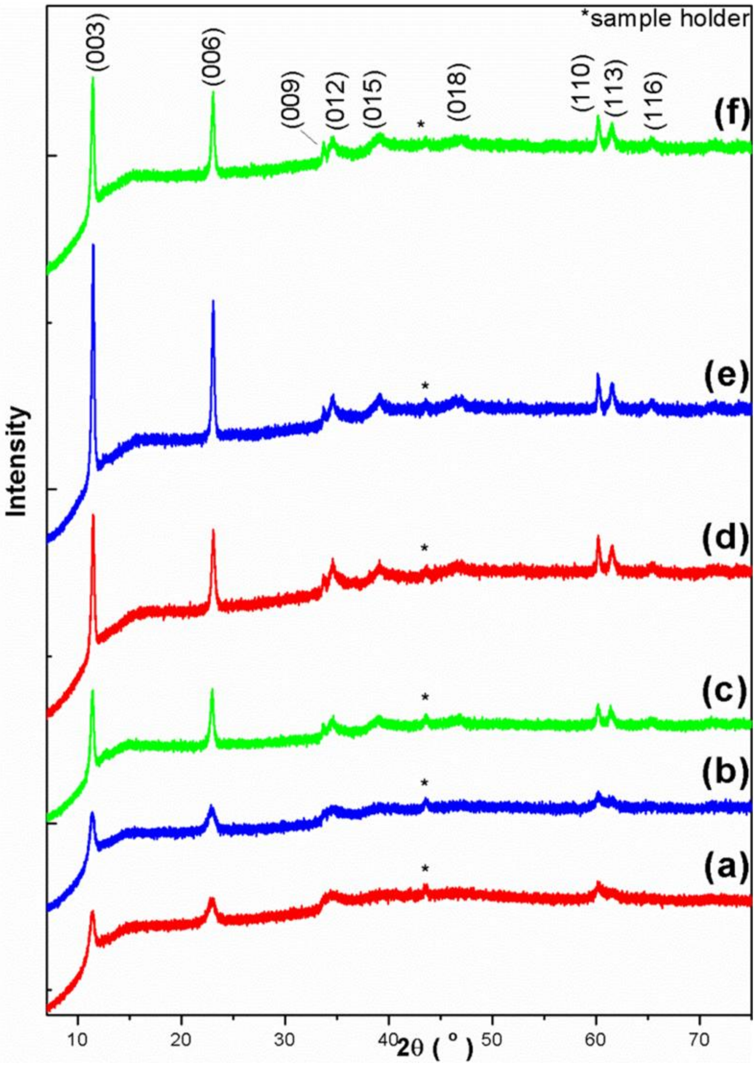

Figure 5-2: Powder XRD patterns of (a) **CoAl-OAm-1**, (b) **CoAl-OAm-2**, (c) **CoAl-OAm-3**, (d) **CoAl-DMTDAm**-1, (e) **CoAl-DMTDAm-2** and (f) **CoAl-DMTDAm-3**.

positions give *c*-lattice parameters of 23.25 Å for **CoAl-OAm-*n*** (*n* = 1 - 3) and *ca.* 23.12 Å for **CoAl-DMTDAm-*n*** (*n* = 1 - 3). The corresponding interlamellar separations range from 7.70 Å to 7.75 Å, which are similar to the values found for LDHs with intercalated Cl^- ions. The position of (110) Bragg reflection gives a direct measure of *a* and *b* lattice parameters $a = b = 2d_{110} = 3.07$ Å for **CoAl-OAm-*n*** and **CoAl-DMTDAm-*n*** (*n* = 1 - 3). The X-ray crystallographic data for Co-Al LDH samples is listed in **Table 5-3**.

It is clear that the reflections in the XRD patterns of the **CoAl-DMTDAm-*n*** (*n* = 1 - 3) (**Figure 5-2** (d - f)) are sharper than those in the XRD patterns of the **CoAl-OAm-*n*** (*n* = 1 - 3) (**Figure 5-2** (a - c)). Under the same measurement conditions, including the slide width and measuring speed, this phenomenon sugests the crystallinity of **CoAl-DMTDAm-*n*** (*n* = 1 - 3) is higher than that of **CoAl-OAm-*n*** (*n* = 1 - 3). In addition, the XRD patterns of **CoAl-OAm-1** and **CoAl-OAm-2** have broader (113) reflections, which appear as a shoulder on the (110) reflections. On the other hand, the XRD data for **CoAl-DMTDAm-*n*** (*n* = 1 - 3) indicates a crystallinity in the order **CoAl-DMTDAm-1** ≈ **CoAl-DMTDAm-3** < **CoAl-DMTDAm-2**. This may be due to the formation of other micelles such as interconnecting cylinders or onion structures when changing the ratio of water to oil phase.

Crystallite sizes were calculated using the Scherrer equation and are listed in **Table 5-3**. Detailed calculations can be found in **Chapter 7**. The thicknesses of **CoAl-OAm-*n***

Table 5-3: Summary of X-ray crystallographic data for Co-Al LDH samples.

Sample	Bragg Reflection 2θ (FWHM) (°)			Lattice parameters (Å)		Crystallite size using Scherrer Equation (nm)	
	003	006	110	*a*	*c*	*a, b*-plane	*c*-axis
CoAl-OAm-1	11.40 (0.562)	23.02 (0.764)	60.25 (-) *	3.07	23.23	-	12.99
CoAl-OAm-2	11.40 (0.550)	22.96 (0.769)	60.25 (-) *	3.07	23.26	-	13.14
CoAl-OAm-3	11.42 (0.340)	22.98 (0.344)	60.21 (0.329)	3.07	23.24	37.95	28.96
CoAl-DMTDAm-1	11.48 (0.301)	23.09 (0.340)	60.22 (0.312)	3.07	23.12	42.17	32.54
CoAl-DMTDAm-2	11.49 (0.259)	23.07 (0.269)	60.19 (0.303)	3.07	23.11	44.92	47.45
CoAl-DMTDAm-3	11.46 (0.299)	23.06 (0.308)	60.21 (0.382)	3.07	23.16	29.48	35.38

* FWHM values were not available due to insufficient resolution

(*n* = 1 - 3) are 12.99, 13.14, and 28.96 nm, respectively. Due to the (110) reflections of **CoAl-OAm-1** and **CoAl-OAm-2** overlapping with the (113) reflections, the FWHM values of these two reflections were not accessible, resulting in unavailable widths of *a*, *b*-plane for these two samples. The crystallite size of the *a*, *b*-plane of **CoAl-OAm-3** can be estimated as 37.95 nm. In addition, the calculation of crystallite sizes of the *a*, *b*-plane and along the *c*-axis were obtained as 42.17 nm and 32.54 nm for **CoAl-DMTDAm-1**, 44.92 nm and 47.45 nm for **CoAl-DMTDAm-2**, and 29.48 nm and 35.38 nm for **CoAl-DMTDAm-3**. Although the values may not accurately reflect the actual sizes, the comparison of the particle sizes between those samples can be roughly deduced. The sizes for these six samples are in the order of **CoAl-OAm-*n*** (*n* = 1 - 3) < **CoAl-DMTDAm-1** ≈ **CoAl-DMTDAm-3** < **CoAl-DMTDAm-2**.

5.2.2.2. XRD data of Ni-Al LDHs

Figure 5-3 shows the powder XRD patterns of all the Ni-Al LDHs synthesised using oleylamine or N,N-dimethyltetradecylamine. Similarly to Co-Al LDHs, (00*l*), (01*l*) and (11*l*) Bragg reflections for a rhombohedral (3R) sequence can be seen for all six samples. Their positions give the *c*-lattice parameters from 23.13 Å to 23.38 Å, while $a = b = 2d_{110} = 3.03$ Å for **NiAl-OAm-*n*** and **NiAl-DMTDAm-*n*** (*n* = 1 - 3). The X-ray crystallographic data for the Ni-Al LDH samples is listed in **Table 5-4**. The corresponding interlamellar separations range from 7.71 Å to 7.80 Å, which is similar to the values for Cl^- ions intercalated in LDHs.

In the XRD patterns of **NiAl-OAm-*n*** (*n* = 1 - 3), the Bragg reflection widths decrease across the sequence, which is consistent with the particle sizes being proportional to the volume of the salt solution used in the synthesis. In addition, in the patterns of **NiAl-OAm-1** and **NiAl-OAm-2**, the (113) reflections are broad and

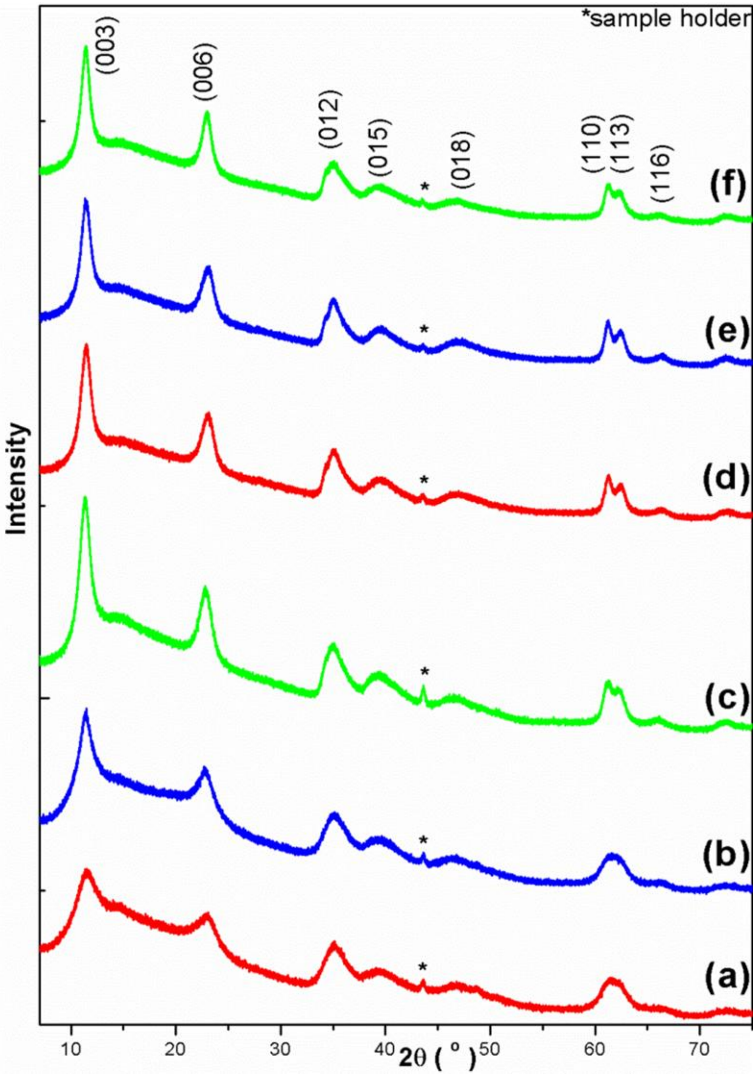

Figure 5-3: Powder XRD patterns of (a) **NiAl-OAm-1**, (b) **NiAl-OAm-2**, (c) **NiAl-OAm-3**, (d) **NiAl-DMTDAm-1**, (e) **NiAl-DMTDAm-2**, and (f) **NiAl-DMTDAm-3**.

overlapped with (001) reflections. However, in the remaining patterns, the (113) reflections can be clearly seen as separated peaks. The patterns of **NiAl-DMTDAm-*n*** (*n* = 1 - 3) do not exhibit obvious coherent tendency but have similar peak intensity and width to the pattern of **NiAl-OAm-3**, which may suggest the crystallite sizes of **NiAl-DMTDAm-*n*** (*n* = 1 - 3) are similar to that of **NiAl-OAm-3** and the ratio of water to oil phase has little influence on particle size in this case. The actual particle sizes can be measured using TEM images and the reasons are discussed **Section 5.2.5.2**. The calculated crystallite sizes of the *a*, *b*-plane and along the *c*-axis using the Scherrer equation agree with the assumption above. The widths of the six samples are from 9.30 nm to 15.54 nm, while the thicknesses fall in the range of 6.11 nm to 12.14 nm (**Table 5-4**).

Table 5-4: Summary of X-ray crystallographic data for Ni-Al LDH samples.

Sample	Bragg Reflection 2θ (FWHM) (°)			Lattice parameters (Å)		Calculation by Scherrer Equation (nm)	
	003	006	110	*a*	*c*	*a, b*-plane	*c*-axis
NiAl-OAm-1	11.43 (1.260)	23.03 (1.386)	61.31 (1.008)	3.02	23.20	9.31	6.11
NiAl-OAm-2	11.35 (0.756)	22.81 (1.008)	61.18 (1.008)	3.03	23.38	9.30	9.49
NiAl-OAm-3	11.34 (0.756)	22.86 (1.008)	61.14 (0.630)	3.03	23.38	15.53	9.49
NiAl-DMTDAm-1	11.45 (0.882)	23.14 (1.008)	61.23 (0.630)	3.03	23.13	15.54	8.67
NiAl-DMTDAm-2	11.42 (0.756)	23.16 (1.008)	61.21 (0.630)	3.03	23.15	15.53	9.49
NiAl-DMTDAm-3	11.40 (0.630)	22.99 (0.756)	61.20 (0.630)	3.03	23.25	15.53	12.14

5.2.2.3. XRD data of Zn-Al LDHs

The powder XRD patterns of the Zn-Al LDHs synthesised using N,N-dimethyltetradecylamine are given in **Figure 5-4**. They can be indexed to zinc aluminium carbonate hydroxide hydrate (JCPDS PDF 00-048-1022). The impurity in **ZnAl-DMTDAm-1** is wurtzite zinc oxide (JCPDS PDF 01-080-0074), which is a common intermediate during co-precipitation synthesis followed by hydrothermal treatment.[15] The lattice parameters are summarised in **Table 5-5**, the *c* parameters range from 22.92 Å to 23.33 Å and $a = b = 2d_{110} = 3.08$ Å for **ZnAl-DMTDAm-*n*** (n = 1 - 3). The corresponding interlamellar separations range from 7.64 Å to 7.78 Å. Since the

Bragg reflection widths for all three samples are similar, the estimated crystallite sizes using the Scherrer equation are 20 nm in the *a*, *b*-plane and 14 nm along the *c*-axis.

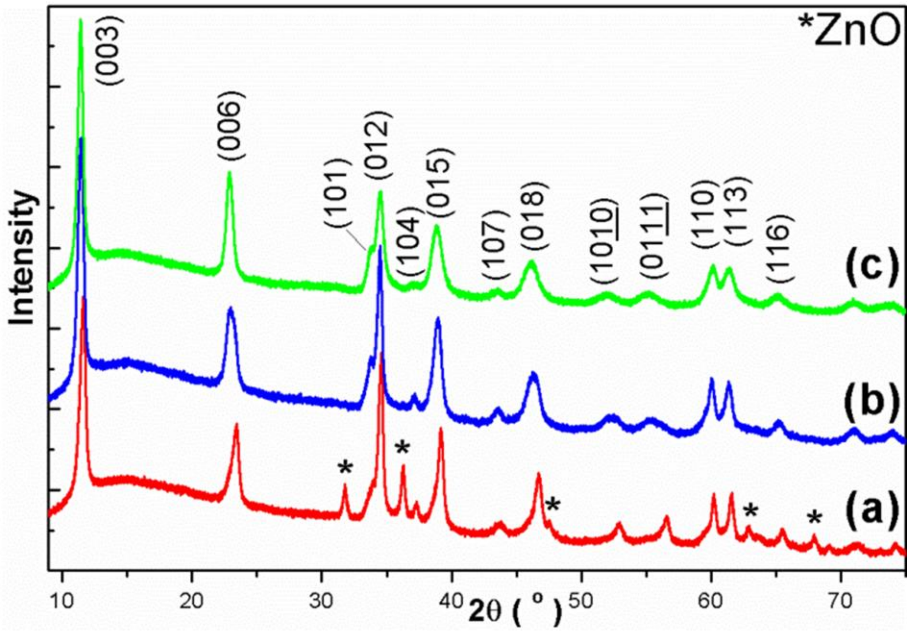

Figure 5-4: Powder XRD patterns of (a) **ZnAl-DMTDAm-1**, (b) **ZnAl-DMTDAm-2**, and (c) **ZnAl-DMTDAm-3**.

Table 5-5: Summary of X-ray crystallographic data for **ZnAl-DMTDAm-*n*** (*n* = 1 - 3) samples.

Sample	Bragg Reflection 2θ (FWHM) (°)			Lattice parameters (Å)		Calculation by Scherrer Equation (nm)	
	003	006	110	*a*	*c*	*a*, *b*-plane	*c*-axis
ZnAl-DMTDAm-1	11.53 (0.756)	23.39 (0.504)	60.12 (0.504)	3.08	22.92	20.16	14.14
ZnAl-DMTDAm-2	11.39 (0.756)	22.95 (0.756)	60.09 (0.756)	3.08	23.27	12.59	10.94
ZnAl-DMTDAm-3	11.37 (0.756)	22.88 (0.504)	60.12 (0.504)	3.08	23.33	20.17	14.13

5.2.2.4. XRD data of Li-Al LDHs

The powder XRD patterns of the Li-Al LDHs synthesised using N,N-dimethyltetradecylamine are given in **Figure 5-5**. The XRDs can be indexed to

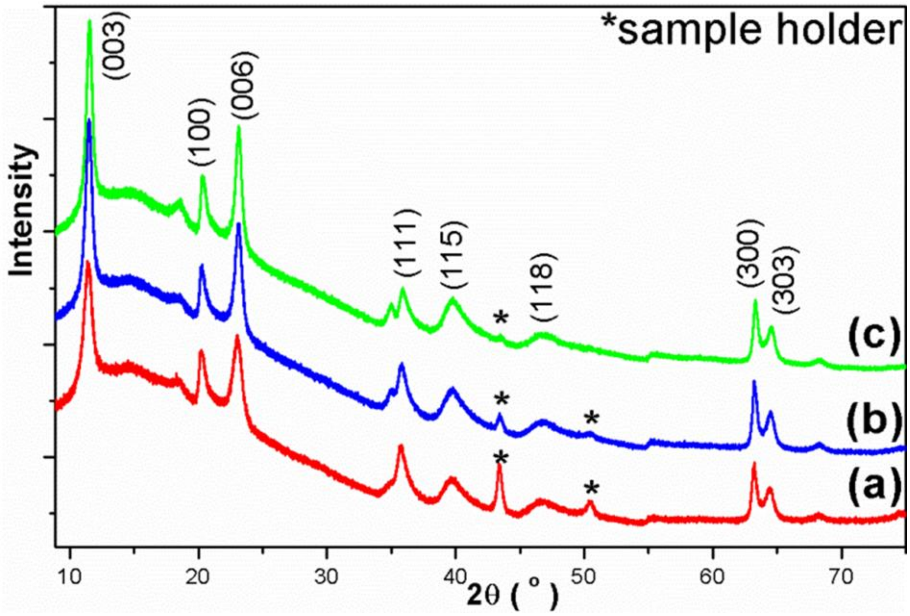

Figure 5-5: Powder XRD patterns of (a) **LiAl-DMTDAm-1**, (b) **LiAl-DMTDAm-2**, and (c) **LiAl-DMTDAm-3**.

Table 5-6: Summary of X-ray crystallographic data for **LiAl-DMTDAm-*n*** (*n* = 1 - 3) samples.

Sample	Bragg Reflection 2θ (FWHM) (°)			Lattice parameters (Å)		Calculation by Scherrer Equation (nm)	
	003	006	110	*a*	*c*	*a*,*b*-plane	*c*-axis
LiAl-DMTDAm-1	11.43 (0.630)	23.06 (0.630)	20.36 (0.756)	5.07	23.19	10.98	13.36
LiAl-DMTDAm-2	11.49 (0.504)	23.12 (0.504)	20.29 (0.504)	5.07	23.09	17.33	17.28
LiAl-DMTDAm-3	11.55 (0.346)	23.13 (0.504)	20.46 (0.504)	5.06	23.03	17.33	22.82

lithium aluminium hydroxide hydrate (JCPDS PDF 00-040-0710) with lattice parameters $a = b = 2\sqrt{3}*d_{100} = 5.06$ Å and $c = 23.1$ Å. The corresponding lamellar distances are from 7.68 Å to 7.73 Å. The Bragg reflection widths are in decreasing sequence, which indicates that the crystallite sizes increase along with the ratio of water to oil phase. The estimated crystallite widths and thicknesses from the Scherrer equation are given in **Table 5-6**. The widths grow from 10.98 nm for **LiAl-DMTDAm-1** to 17.33 nm for **LiAl-DMTDAm-2** and **LiAl-DMTDAm-3**, while the thicknesses increase from 13.36 nm for **LiAl-DMTDAm-1** to 17.28 nm for **LiAl-DMTDAm-2** and 22.82 nm for **LiAl-DMTDAm-3**.

5.2.2.5. XRD data of Ca-Al LDHs

The powder XRD patterns of all the Ca-Al LDHs synthesised using dioctylamine, oleylamine, and DOAm/OAm = 1 : 1 are given in **Figure 5-6**. Not all reverse microemulsion systems synthesise Ca-Al LDHs successfully, only **CaAl-DOAm-OAm-1** (**Figure 5-6** (d)), **CaAl-OAm-1** (**Figure 5-6** (g)), and **CaAl-OAm-2** (**Figure 5-6** (h)) can be indexed to calcium aluminium hydroxide chloride hydrate (JCPDS PDF 00-035-0105). The rest of the samples contain boehmite (aluminium oxide hydroxide, JCPDS PDF 00-021-1307, **Figure 5-6** (a) & (b) & (e)), and gibbsite (aluminum oxide hydrate, JCPDS PDF 00-001-0263, **Figure 5-6** (f) & (i)). The reason for these failures may be due to inappropriate pH for the synthesis of Ca-Al LDHs. The X-ray crystallographic data of **CaAl-OAm-1**, **CaAl-OAm-2**, and **CaAl-DOAm-OAm-1** are given in **Table 5-7**. The lattice parameters can be calculated from those data as $a = b = 2\sqrt{3}*d_{100}$ = 5.75 Å and c = 47.10 Å, while the corresponding lamellar separations are from 15.52 Å to 15.72 Å.

The (006) Bragg reflection in the XRD pattern of **CaAl-DOAm-OAm-1** are sharper than those in the XRD patterns of **CaAl-OAm-1** and **CaAl-OAm-2**, which suggests the thickness of crystallites for **CaAl-DOAm-OAm-1** are larger than **CaAl-OAm-1** and **CaAl-OAm-2**. In addition, the intensity of the (006) reflection in **CaAl-DOAm-OAm-1** is more significant comparing to the intensity of the (110) reflection, while the intensity ratios of these two peaks in the patterns of **CaAl-OAm-1** and **CaAl-OAm-2** are close to 1. This observation may be caused by the preferential orientation of the particles, suggesting the particles of **CaAl-OAm-1** and **CaAl-OAm-2** samples may have a needle or rod morphology.

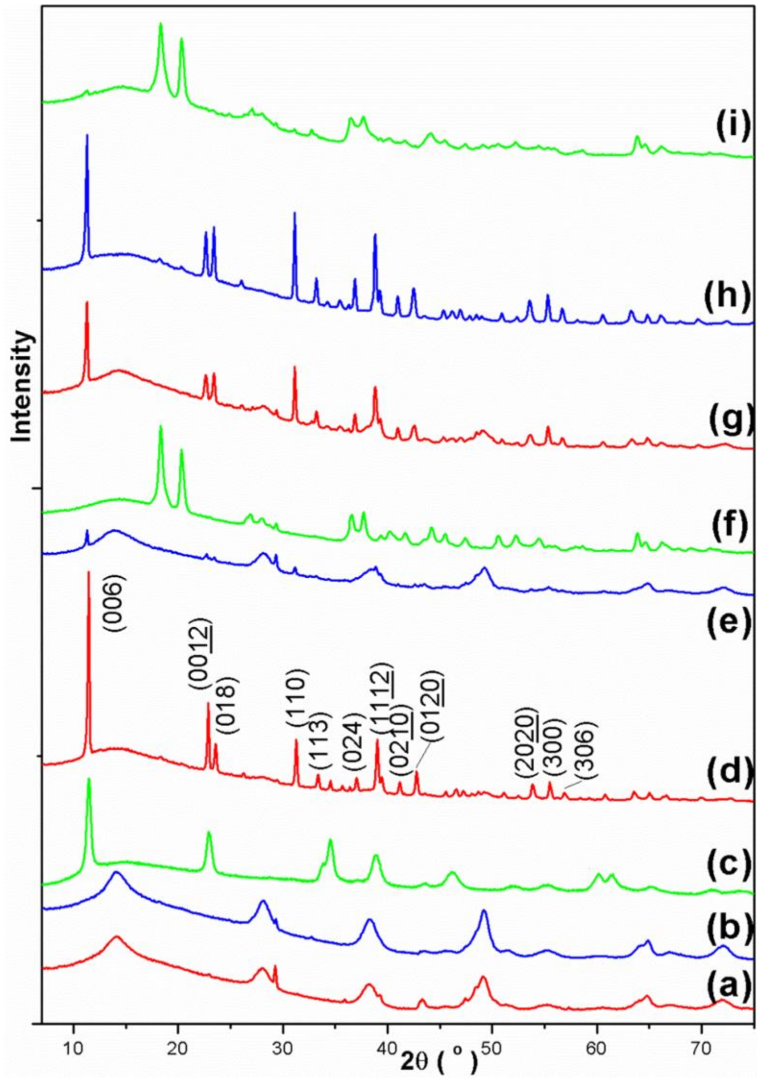

Figure 5-6: Powder XRD patterns of (a) **CaAl-DOAm-1**, (b) **CaAl-DOAm-2**, (c) **CaAl-DOAm-3**, (d) **CaAl-DOAm-OAm-1**, (e) **CaAl-DOAm-OAm-2**, (f) **CaAl-DOAm-OAm-3**, (g) **CaAl-OAm-1**, (h) **CaAl-OAm-2**, and (i) **CaAl-OAm-3**.

Table 5-7: Summary of X-ray crystallographic data for Ca-Al LDH samples.

Sample	Bragg Reflection 2θ (FWHM) (°)			Lattice parameters (Å)		Calculation by Scherrer Equation (nm)	
	006	0012	110	*a*	*c*	*a*,*b*-plane	*c*-axis
CaAl-OAm-1	11.25 (0.791)	22.64 (0.572)	31.12 (0.295)	5.75	47.15	43.07	12.67
CaAl-OAm-2	11.26 (0.338)	22.64 (0.424)	31.11 (0.301)	5.75	47.13	40.98	25.43
CaAl-DOAm-OAm-1	11.43 (0.256)	22.88 (0.328)	31.25 (0.317)	5.73	46.56	36.70	40.90

5.2.2.6. XRD data of Ni-Fe LDHs

The powder XRD patterns of the Ni-Fe LDHs synthesised using N,N-dimethyltetradecylamine are given in **Figure 5-7**. The series of (00*l*), (01*l*) and (11*l*) Bragg reflections indicates a rhombohedral (3R) sequence for all three samples. The peak positions give *c*-lattice parameters from 23.74 Å to 23.83 Å, while $a = b = 2d_{110} = 3.09$ Å for **NiFe-DMTDAm-*n*** ($n = 1 - 3$). The corresponding lamellar distances are from 7.91 Å to 7.94 Å, which are also similar to the values of Cl^- ions intercalated LDHs. The X-ray crystallographic data for Ni-Fe LDH samples are listed in **Table 5-8**. In the patterns of **NiFe-DMTDAm-1**, the (113) reflections are broad and appear as a shoulder peak with (001) reflections. However, in the patterns of **NiFe-DMTDAm-2** and **NiFe-DMTDAm-3**, the (113) reflections are well separated from (110) reflections and can be clearly seen. The peak intensities of the patterns grow along with the ratio of oil phase to water, which implies an increasing crystallite size from **NiFe-DMTDAm-1** to **NiFe-DMTDAm-3**. The thicknesses of the particles calculated using the Scherrer equation are from 10.10 nm for **NiFe-DMTDAm-1**, 12.13 nm for **NiFe-DMTDAm-2** and 13.35 nm for **NiFe-DMTDAm-3**, while the widths are 16.16, 21.84 and 21.83 nm for **NiFe-DMTDAm-*n*** ($n = 1 - 3$), respectively.

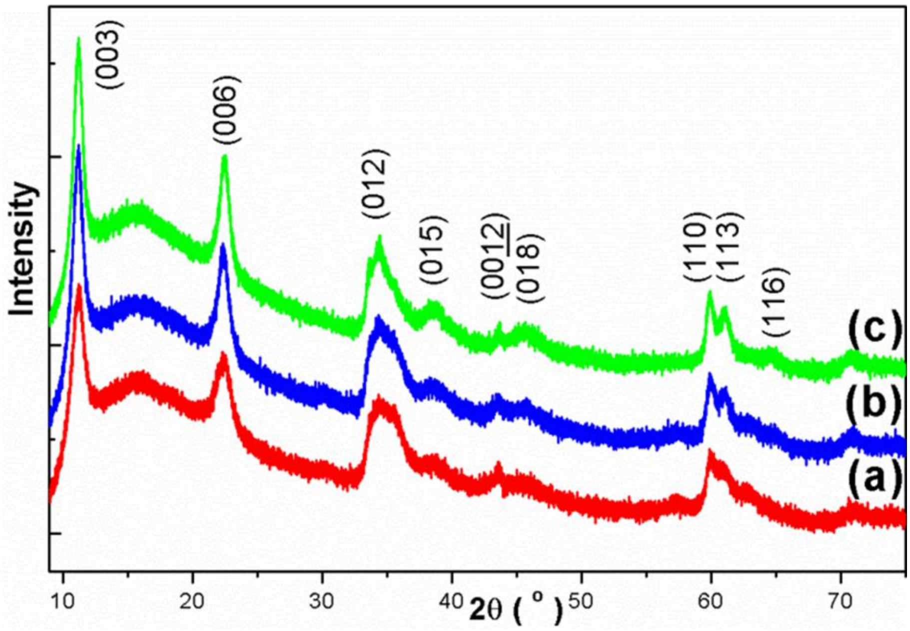

Figure 5-7: Powder XRD patterns of (a) **NiFe-DMTDAm-1**, (b) **NiFe-DMTDAm-2**, and (c) **NiFe-DMTDAm-3**.

Table 5-8: Summary of X-ray crystallographic data for **NiFe-DMTDAm-*n*** (*n* = 1 -3) samples.

Sample	Bragg Reflection 2θ (FWHM) (°)			Lattice parameters (Å)		Calculation by Scherrer Equation (nm)	
	003	006	110	*a*	*c*	*a*, *b*-plane	*c*-axis
NiFe-DMTDAm-1	11.19 (0.756)	22.46 (0.882)	59.92 (0.630)	3.09	23.74	16.16	10.10
NiFe-DMTDAm-2	11.14 (0.630)	22.37 (0.756)	59.91 (0.504)	3.09	23.83	21.84	12.13
NiFe-DMTDAm-3	11.18 (0.630)	22.47 (0.630)	59.87 (0.504)	3.09	23.74	21.83	13.35

5.2.3. Elemental analyses

The general composition of LDHs is often described as $[M^{z+}_{1-x}M'^{3+}_{x}(OH)_2]^{a+}(A^{n-})_{a/n}\cdot mH_2O$. When $z = 2$, phase pure LDHs can be obtained when x is in the range from 0.2 to 0.33. The ICP analysis data can give the ratio of M/M’, while CHN analysis results verify the interlayer molecules and water. The elemental analysis data and estimated formulas are given in **Table 5-9** and **Table 5-10**.

Table 5-9: Summary of elemental analysis data for the LDHs containing transition metals synthesised in single component microemulsions.

Sample	Observed (*calc.*) (%)				Calc. Formula
	M	M’	C	H	
CoAl-OAm-1	50.05	7.28	5.72	2.5	$[Co_{2.3}Al_{0.7}(OH)_6]Cl_{0.7}$ [a]
	(45.15)	(6.29)	(5.10)	(2.89)	
CoAl-OAm-2	43.68	7.16	6.09	2.29	$[Co_{2.2}Al_{0.8}(OH)_6]Cl_{0.8}$ [a]
	(42.63)	(7.10)	(5.97)	(3.02)	
CoAl-OAm-3	63.89	11.84	1.16	2.47	$[Co_{2.1}Al_{0.9}(OH)_6]Cl_{0.4}(OH)_{0.5}$ [a]
	(46.4)	(8.68)	(0.80)	(2.43)	
CoAl-DMTDAm-1	34.42	5.33	1.53	4.65	$[Co_{2.2}Al_{0.8}(OH)_6]Cl_{0.8}\cdot 5.4H_2O$ [b]
	(33.69)	(5.61)	(1.53)	(4.68)	
CoAl-DMTDAm-2	26.11	3.45	1.36	5.35	$[Co_{2.3}Al_{0.7}(OH)_6]Cl_{0.7}\cdot 12.6H_2O$ [b]
	(26.25)	(3.66)	(1.38)	(6.35)	
CoAl-DMTDAm-3	54.58	9.67	0.38	3.59	$[Co_{2.2}Al_{0.8}(OH)_6](OH)_{0.8}$
	(48.38	(8.05)	(0.33)	(2.62)	
NiAl-OAm-1	33.28	5.24	13.85	4.36	$[Ni_{2.2}Al_{0.8}(OH)_6]Cl_{0.8}\cdot 2.2H_2O$ [c]
	(33.33)	(5.33)	(14.07)	(5.12)	
NiAl-OAm-2	35.60	6.70	19.72	4.52	$[Ni_{2.1}Al_{0.9}(OH)_6](OH)_{0.9}$ [c]
	(35.16)	(6.93)	(19.74)	(5.39)	
NiAl-OAm-3	47.14	8.36	4.72	3.58	$[Ni_{2.2}Al_{0.8}(OH)_6](OH)_{0.8}$ [c]
	(45.11)	(8.07)	(4.39)	(3.21)	
NiAl-DMTDAm-1	43.86	7.99	5.16	3.45	$[Ni_{2.1}Al_{0.9}(OH)_6]Cl_{0.2}(OH)_{0.7}$ [d]
	(42.92)	(8.46)	(5.16)	(3.30)	
NiAl-DMTDAm-2	39.70	7.37	2.84	3.34	$[Ni_{2.1}Al_{0.9}(OH)_6](OH)_{0.9}\ 0.6H_2O$ [d]
	(39.15)	(7.71)	(2.86)	(3.12)	
NiAl-DMTDAm-3	45.80	8.41	0.22	1.15	$[Ni_{2.1}Al_{0.9}(OH)_6]Cl_{0.9}$
	(44.67)	(8.60)	(0.20)	(2.18)	
ZnAl-DMTDAm-1	56.55	14.67	3.16	1.72	$[Zn_{1.8}Al_{1.2}(OH)_6](CO_3)_{0.6}$
	(40.85)	(11.24)	(2.50)	(2.10)	
ZnAl-DMTDAm-2	65.22	18.14	1.40	1.95	$[Zn_{1.8}Al_{1.2}(OH)_6](CO_3)_{0.2}(OH)_{1.2}$
	(41.36)	(11.38)	(0.84)	(2.55)	
ZnAl-DMTDAm-3	63.08	19.97	0.61	2.86	$[Zn_{1.7}Al_{1.3}(OH)_6](CO_3)_{0.1}(OH)_{1.1}$
	(40.72)	(12.85)	(0.44)	(2.62)	
NiFe-DMTDAm-1	22.35	8.62	6.73	4.75	$[Ni_{2.1}Fe_{0.9}(OH)_6]Cl_{0.9}\cdot 9.9H_2O$ [e]
	(23.45)	(9.56)	(6.03)	(6.00)	
NiFe-DMTDAm-2	21.47	8.31	6.57	4.62	$[Ni_{2.1}Fe_{0.9}(OH)_6]Cl_{0.9}\cdot 12.3H_2O$ [e]
	(21.37)	(8.71)	(6.60)	(6.50)	
NiFe-DMTDAm-3	25.24	10.27	4.27	2.42	$[Ni_{2.1}Fe_{0.9}(OH)_6]Cl_{0.9}\cdot 8.4H_2O$ [e]
	(25.41)	(10.36)	(4.30)	(5.48)	

[a] **CoAl-OAm-*n*** (*n* = 1 - 3) contain *wt.* 6%, 7% and 1% OAm impurity, respectively.

[b] **CoAl- DMTDAm-1** and **CoAl-DMTDAm-2** contain *wt.* 2% DMTDAm impurity.

[c] **NiAl-OAm-*n*** (*n* = 1 - 3) contain *wt.* 17%, 24% and 6% OAm impurity respectively.

[d] **NiAl-DMTDAm-1** and **NiAl-DMTDAm-2** contain *wt.* 6% and 12% DMTDAm impurity, respectively.

[e] **NiFe-DMTDAm-*n*** (*n* = 1 - 3) contain *wt.* 8%, 8% and 5% OAm impurity respectively.

Table 5-10: Summary of elemental analysis data for the other LDHs synthesised in single component microemulsions.

Sample	Observed (*calc.*) (%)				Calc. Formula
	M	M'	C	H	
LiAl-DMTDAm-1	-	12.42	1.42	3.06	$[LiAl_2(OH)_6](OH) \cdot 12H_2O$ [a]
	(1.72)	(13.36)	(1.52)	(8.02)	
LiAl-DMTDAm-2	-	12.19	0.79	3.25	$[LiAl_2(OH)_6](OH) \cdot 12H_2O$ [a]
	(1.73)	(13.46)	(0.86)	(7.95)	
LiAl-DMTDAm-3	-	31.68	0.32	3.42	$[Li_{0.4}Al_2(OH)_6](OH)_{0.4}$ [a]
	(1.67)	(32.44)	(0.3)	(3.94)	
CaAl-OAm-1	18.62	9.24	1.86	2.28	$[Ca_{1.7}Al_{1.3}(OH)_6]Cl_{1.3} \cdot 5.4H_2O$ [b]
	(19.10)	(9.83)	(1.82)	(5.06)	
CaAl-OAm-2	30.43	13.56	2.07	2.35	$[Ca_{1.8}Al_{1.2}(OH)_6]Cl_{0.4}(OH)_{0.8}$ [b]
	(30.00)	(13.47)	(2.05)	(3.20)	
CaAl-DOAm-OAm-1	21.05	9.06	1.44	2.31	$[Ca_{1.8}Al_{1.2}(OH)_6]Cl_{1.2} \cdot 4.5H_2O$ [b]
	(21.44)	(39.62)	(1.50)	(4.85)	

[a] **LiAl-DMTDAm-*n*** (*n* = 1 - 3) contain *wt.* 2%, 1% and 0.5% DMTDAm impurity, respectively.

[b] **CaAl-OAm-1**, **CaAl-OAm-2** and **CaAl-DOAm-OAm-1** contain *wt.* 2%, 3% and 2% amine impurity, respectively.

Due to the absorbed amines and the error of the ICP measurement, accurate compositions are not accessible for some samples, especially those containing comparatively large amount of amines. All these samples contain trace amount of CO_3^{2-} which can be confirmed in IR spectra.

5.2.4. FT-IR spectroscopy

The FT-IR spectra of all the LDHs synthesised in single component microemulsions are shown in **Figure 5-8** to **Figure 5-13**. All the spectra contain a broad band centred at *ca.* 3400 cm^{-1}, which corresponds to a superposition of the stretching vibration of the hydroxide groups in the brucite sheets and the interlayer water molecules ($\nu_{O\text{-}H}$).[16] The three absorptions at *ca.* 3000 cm^{-1} are due to the long carbon chains in the amines. The absorptions at *ca.* 1620 cm^{-1} are assigned to be the bending vibrations of the interlayer water molecules ($\delta_{O\text{-}H}$).[17] The strong absorptions at around at *ca.* 1355 cm^{-1} indicate the existence of CO_3^{2-} ($\nu_{C\text{-}O}$), which is due to unavoidable absorption of CO_2 in the air. The absorptions below 1000 cm^{-1} can be ascribed as vibrations of metal oxygen bonds ($\nu_{M\text{-}O}$).

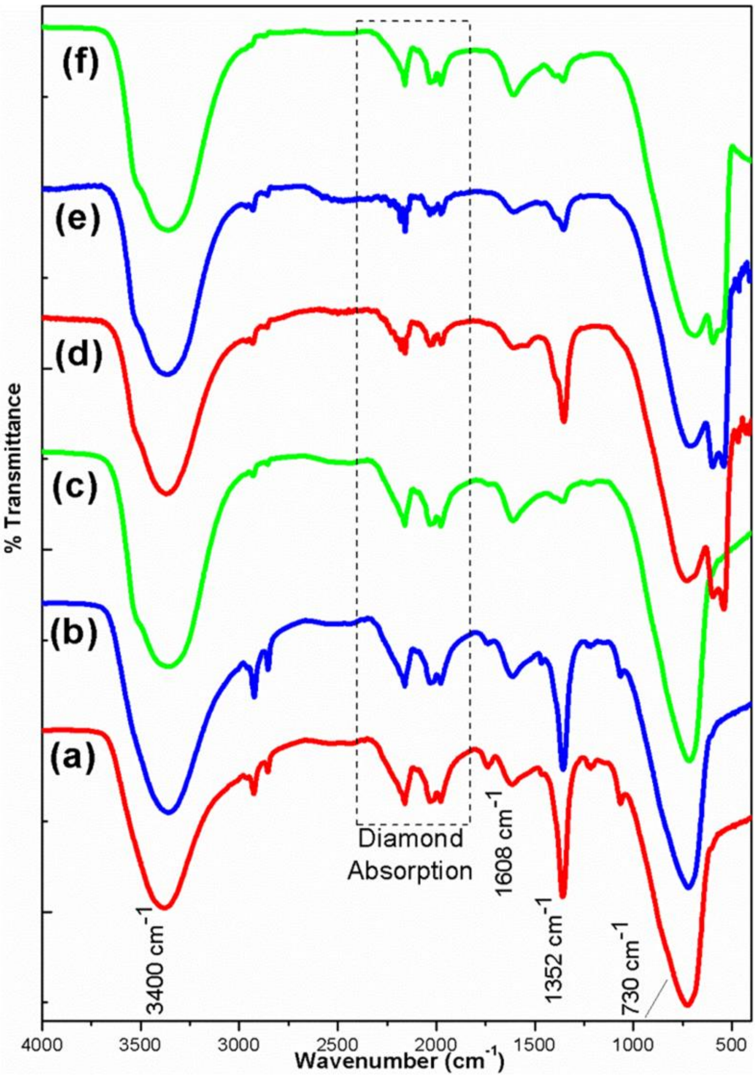

Figure 5-8: FT-IR spectra of (a) **CoAl-OAm-1**, (b) **CoAl-OAm-2**, (c) **CoAl-OAm-3**, (d) **CoAl-DMTDAm-1**, (e) **CoAl-DMTDAm-2**, and (f) **CoAl-DMTDAm-3**.

All the FT-IR spectra further verified the composition and structure of the LDH samples. It worth mentioning that in all the spectra the comparative intensities of absorption from CO_3^{2-} at 1355 cm^{-1} vary and exhibit a tendency of 1 > 2 > 3. Since

CO_3^{2-} ions were introduced by amines reacting with CO_2 in the air and form alkylammonium alkylcarbamate (AAAC) pairs, it is approximately consistent that the more amine used, the more CO_3^{2-} is contained in the final products.

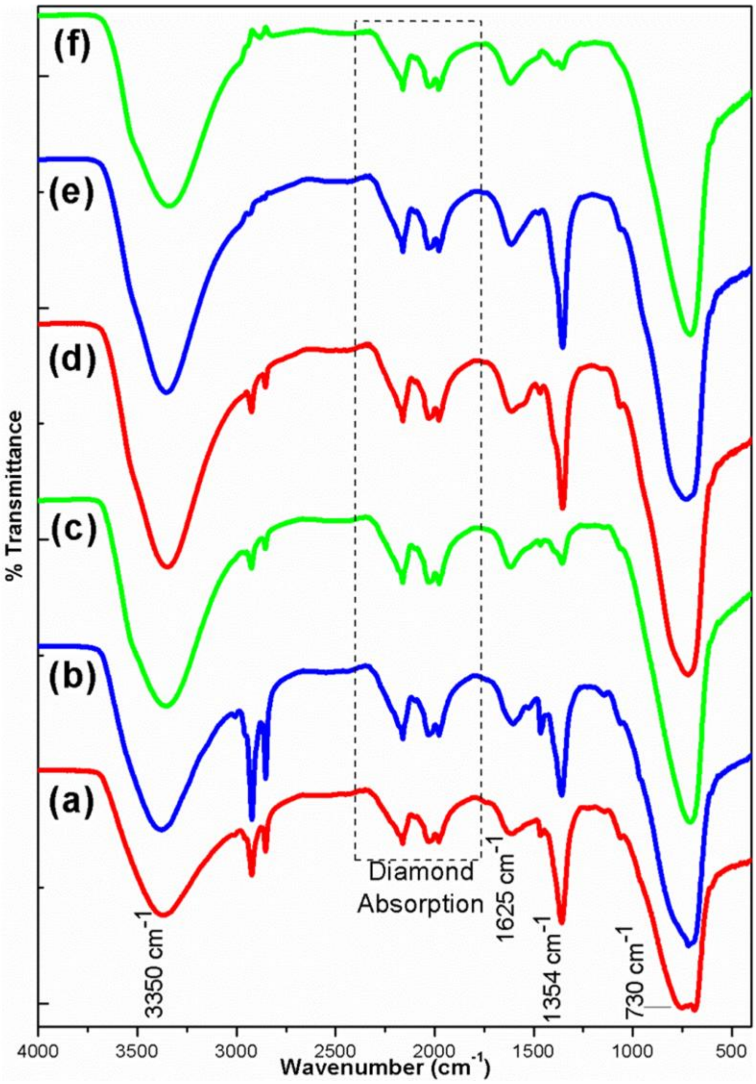

Figure 5-9: FT-IR spectra of (a) **NiAl-OAm-1**, (b) **NiAl-OAm-2**, (c) **NiAl-OAm-3**, (d) **NiAl-DMTDAm-1**, (e) **NiAl-DMTDAm-2**, and (f) **NiAl-DMTDAm-3**.

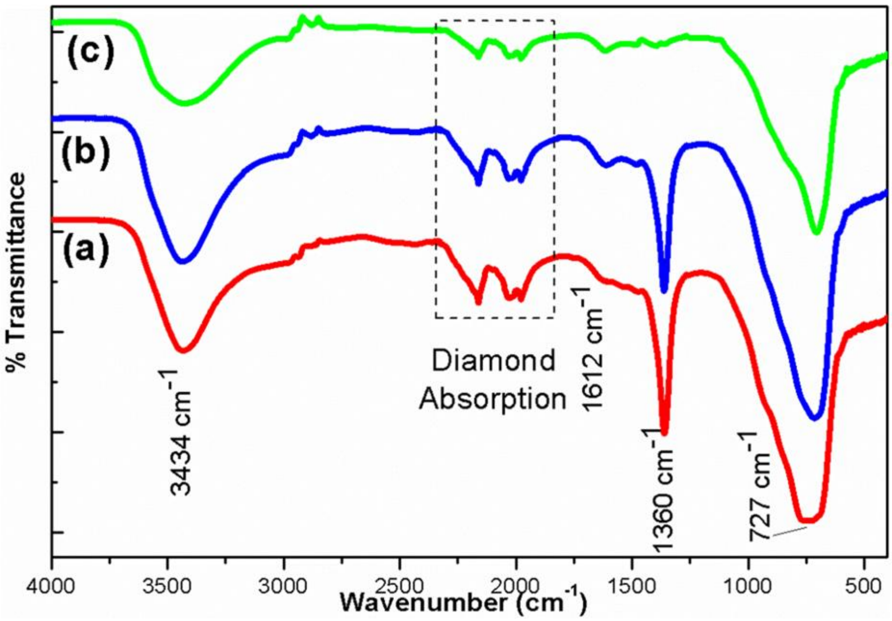

Figure 5-10: FT-IR spectra of (a) **ZnAl-DMTDAm-1**, (b) **ZnAl-DMTDAm-2**, and (c) **ZnAl-DMTDAm-3**.

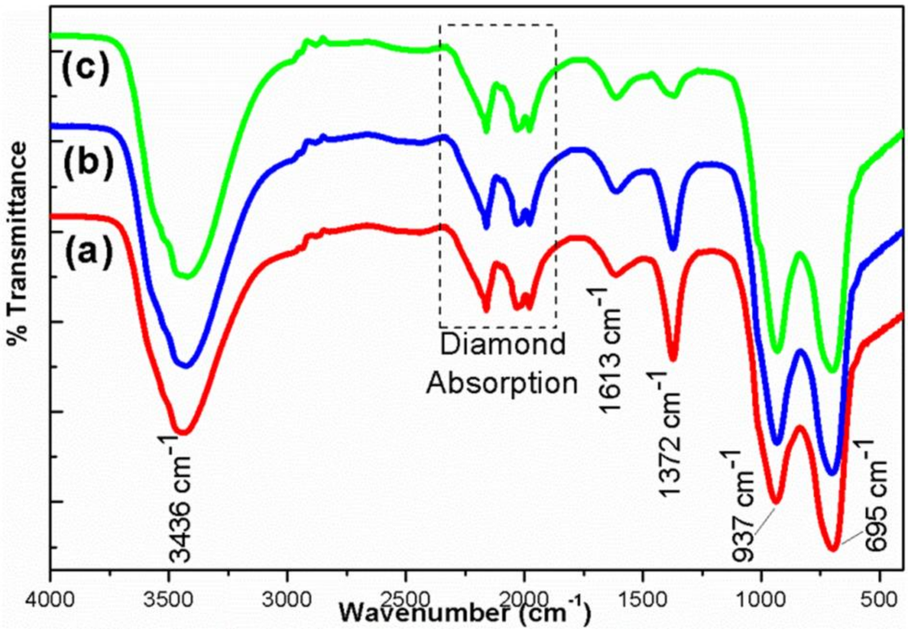

Figure 5-11: FT-IR spectra of (a) **LiAl-DMTDAm-1**, (b) **LiAl-DMTDAm-2**, and (c) **LiAl-DMTDAm-3**.

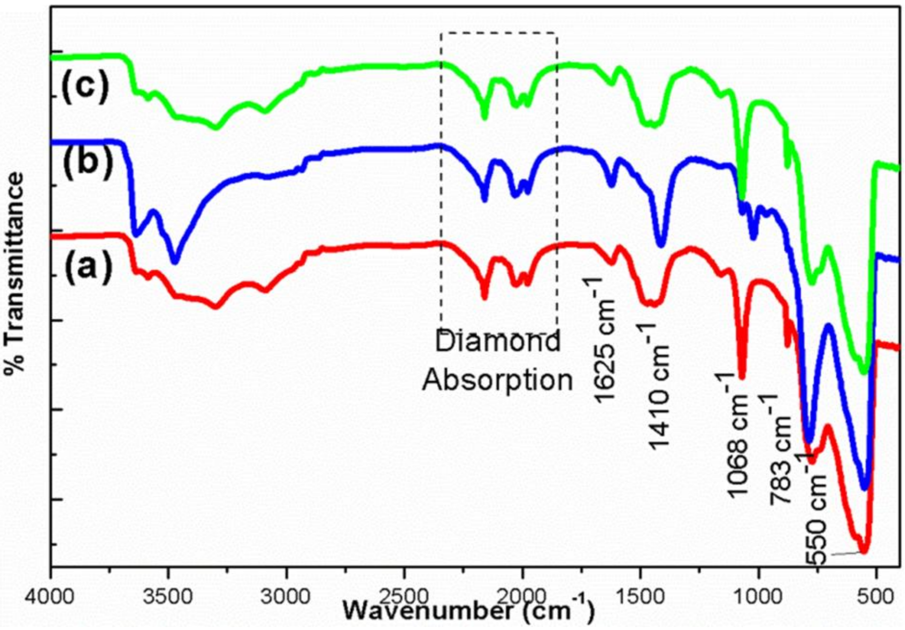

Figure 5-12: FT-IR spectra of (a) **CaAl-DOAm-1**, (b) **CaAl-DOAm-2**, and (c) **CaAl-DOAm-OAm-1**.

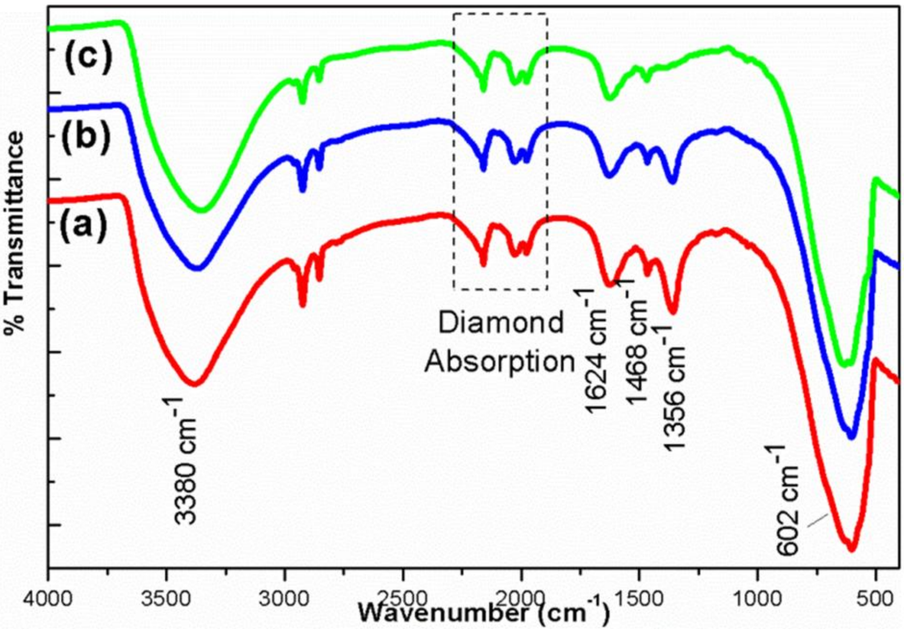

Figure 5-13: FT-IR spectra of (a) **NiFe-DMTDAm-1**, (b) **NiFe-DMTDAm-2**, and (c) **NiFe-DMTDAm-3**.

5.2.5. TEM imaging and particle size analyses

5.2.5.1. TEM images and particle size analyses of Co-Al LDHs

The TEM images and particle size analyses of **CoAl-OAm-*n*** and **CoAl-DMTDAm-*n*** (*n* = 1 - 3) are shown in **Figure 5-14** and **Figure 5-15**.

The particles of **CoAl-OAm-1** and **CoAl-OAm-2** exhibit a platelet morphology, with both thin isolated platelets and larger agglomerates being observed. The average diameters are around 65 nm. However, the particles of **CoAl-OAm-3** form well-dispersed circular platelets with an average diameter of 117 nm. The diameter is slightly larger than that estimated using the Scherrer equation. The diameters of **CoAl-OAm-*n*** (*n* = 1 - 3) fail to show direct relationship with the volume ratios of oil phase to water. Although the reasons are unclear, a highly alkaline environment may be a factor. The metal ions may fully react in the nucleation step because of the high pH, but the subsequent crystal growth step may be slower. Consequently, the controlling function of oleylamine may not be effective.

The TEM images of **CoAl-DMTDAm-*n*** (*n* = 1 - 3) particles show that they have a morphology consisting of hexagonal thin platelets with average diameters of 145, 165, and 122 nm, respectively. The diameters are in an order of **CoAl-DMTDAm-1** ≈ **CoAl-DMTDAm-3** < **CoAl-DMTDAm-2**, which agrees with that estimated by XRD patterns, though the accurate sizes are larger. Statistical analysis of the particle size distributions to a normal distribution gives the mean (μ), standard deviation (σ) and variance (σ^2) parameters (**Table 5-11**).

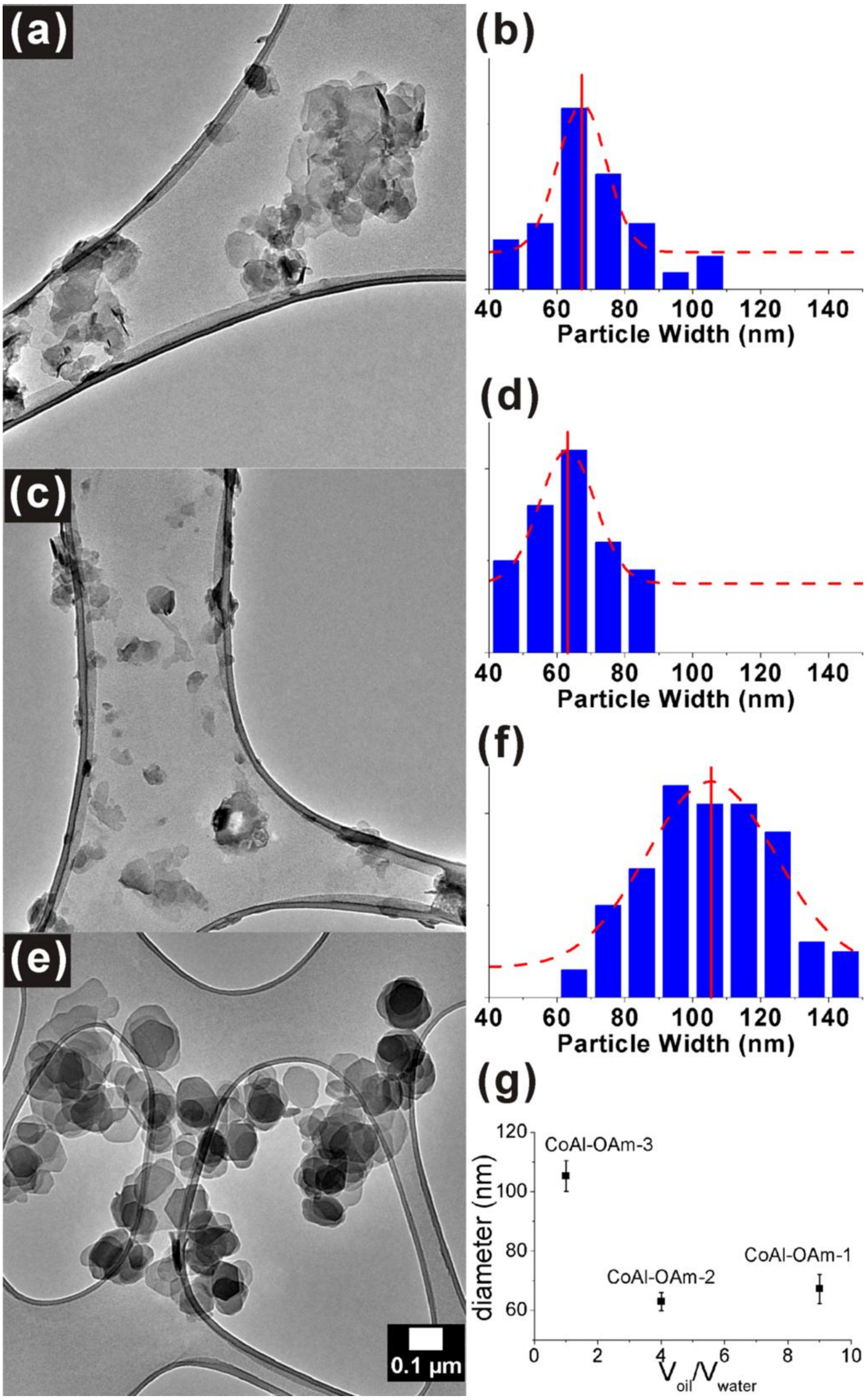

Figure 5-14: (a) TEM image and (b) particle size distribution of **CoAl-OAm-1**, (c) TEM image and (d) particle size distribution of **CoAl-OAm-2**, (e) TEM image and (f) particle size distribution of **CoAl-OAm-3**. (g) The plot of diameters of particles versus volume ratios of oil to water. The dashed lines in (b), (d) & (f) are best fit to Gaussian equation, and the error bars are the 95% confidence intervals.

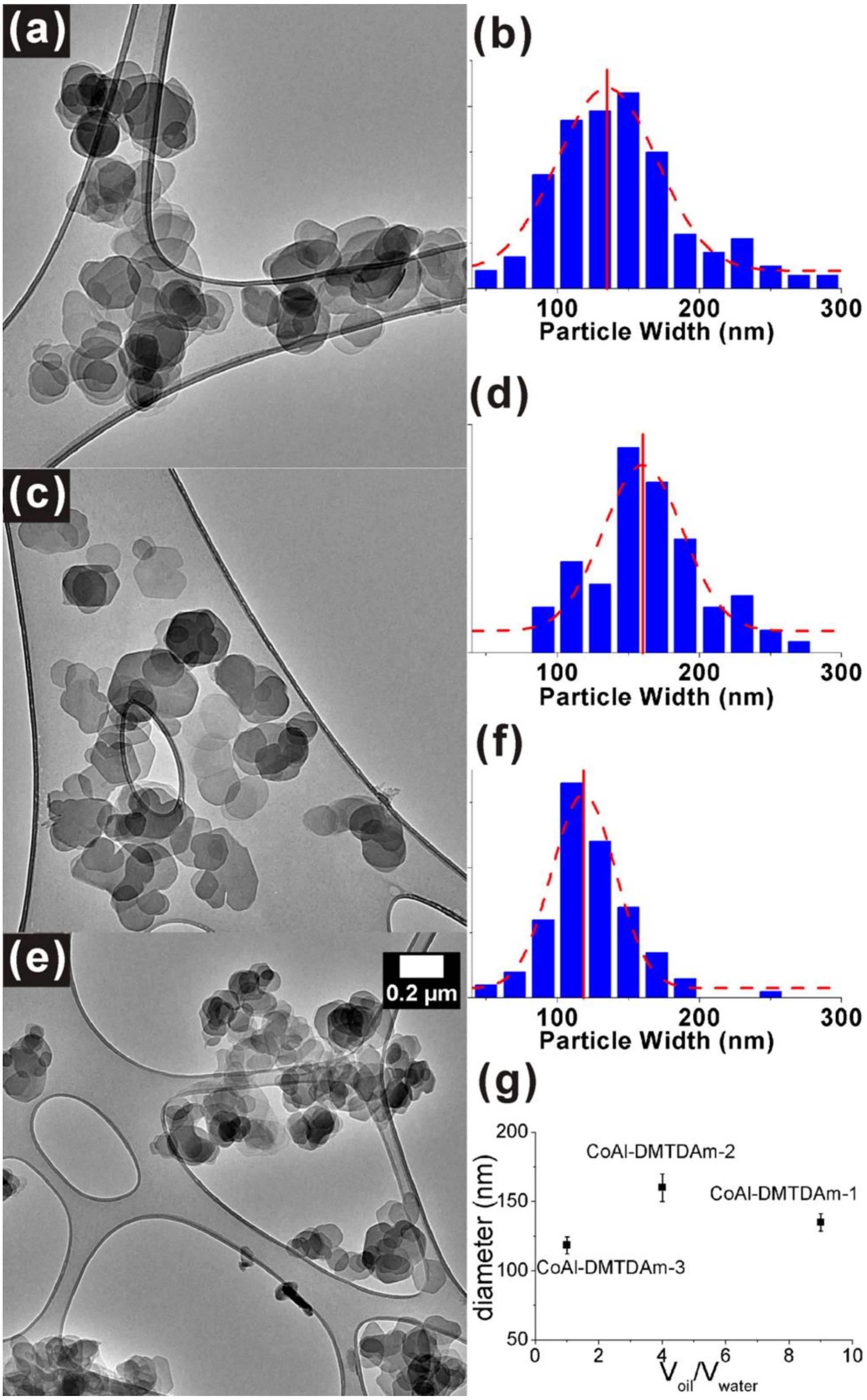

Figure 5-15: (a) TEM image and (b) particle size distribution of **CoAl-DMTDAm-1**, (c) TEM images and (d) particle size distribution of **CoAl-DMTDAm-2**, (e) TEM image and (f) particle size distribution of **CoAl-DMTDOAm-3**. (g) The plot of diameters of particles versus volume ratios of oil to water. The dashed lines in (b), (d) & (f) are best fit to Gaussian equation, and the error bars are the 95% confidence intervals.

Table 5-11: Data of statistical analysis of Co-Al LDH particle diameters.

Sample	Diameter (nm)		
	Mean (μ)	Stdev. (σ)	Var. (σ^2)
CoAl-OAm-1	68.34	14.22	202.4
CoAl-OAm-2	60.85	13.43	180.5
CoAl-OAm-3	116.8	31.95	1020
CoAl-DMTDAm-1	145.2	47.49	2256
CoAl-DMTDAm-2	164.9	43.74	1913
CoAl-DMTDAm-3	122.2	30.89	953.9

We can conclude that DMTDAm creates a better microemulsion for the synthesis of Co-Al LDHs with a more appropriate pH than OAm. Although the particle sizes do not agree with the theoretical prediction, these microemulsions can be applied for synthesising Co-Al LDH particles with diameters of between 100 to 160 nm.

5.2.5.2. TEM images and particle size analyses of Ni-Al LDHs

The TEM images and particle size analyses of **NiAl-OAm-*n*** and **NiAl-DMTDAm-*n*** (*n* = 1 - 3) are shown in **Figure 5-16** and **Figure 5-17**.

Well dispersed nanoparticles with diameters below 10 nm were observed for **NiAl-OAm-1** and **NiAl-OAm-2**. The accurate particle size distributions were not available due to lack of resolution. The particles of **NiAl-OAm-3** are well dispersed circular platelets with an average diameter of 17 nm. The diameter is similar to that estimated using the Scherrer equation. The diameters of **NiAl-OAm-*n*** (*n* = 1 - 3) fail to show a direct relationship with the volume ratios of oil phase to water but have a similar tendency as **CoAl-OAm-*n*** (*n* = 1 - 3). The reasons may be similar as well, which are that the over alkaline environment precipitates most of the metal ions, thus the controlling effect of oleylamine was weakened.

The TEM images of **NiAl-DMTDAm-*n*** (*n* = 1 - 3) particles indicate that the

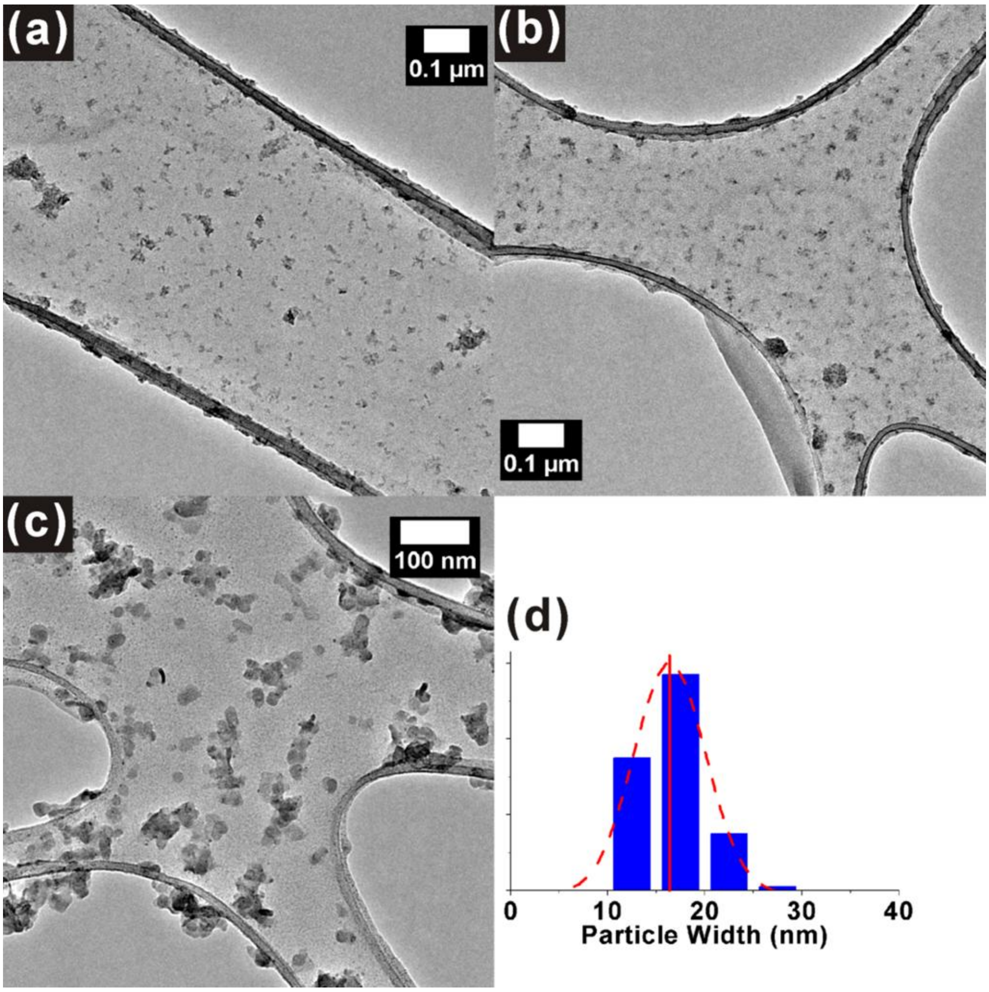

Figure 5-16: TEM images of (a) **NiAl-DMTDAm-1**, (b) **NiAl-DMTDAm-2**, (c) **NiAl-DMTDOAm-3**, and (d) particle size distribution of **NiAl-DMTDOAm-3**. The dashed line in (d) is best fit to Gaussian equation.

particles have a morphology consisting of hexagonal thin platelet with average diameters of 26, 29, and 34 nm, respectively. The diameters are slightly larger than those estimated from XRD patterns. The particle sizes are correlated to the volume ratio of oil phase to water, which verifies that the particle sizes were effectively controlled by the microemulsions in the synthesis. Statistical analysis of the particle size distributions to a normal distribution gives the mean (μ), standard deviation (σ) and variance (σ^2) parameters (**Table 5-12**).

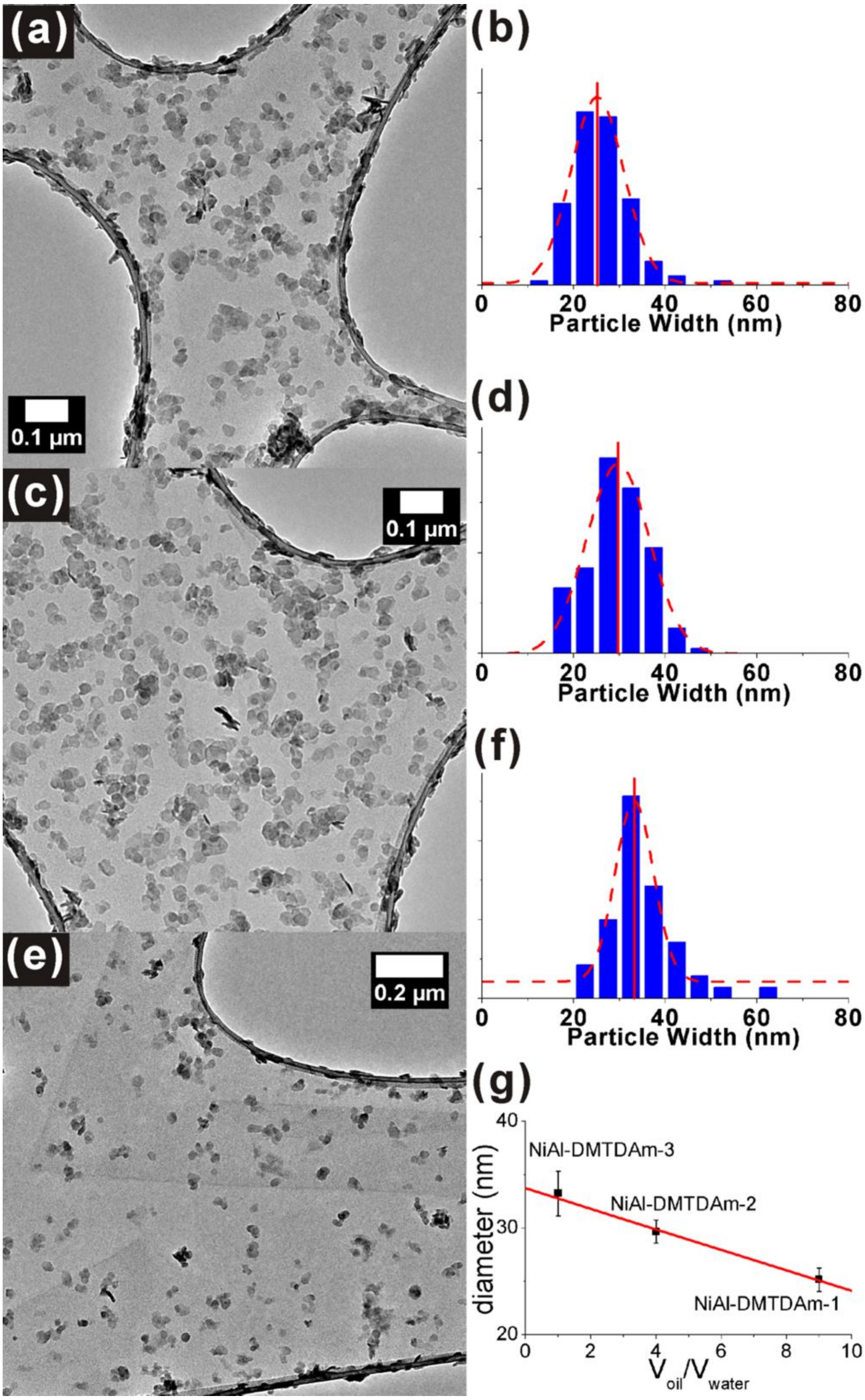

Figure 5-17: (a) TEM image and (b) particle size distribution of **NiAl-DMTDAm-1**, (c) TEM image and (d) particle size distribution of **NiAl-DMTDAm-2**, (e) TEM image and (f) particle size distribution of **NiAl-DMTDAm-3**. (g) The plot of diameters of particles versus volume ratios of oil to water. The dashed lines in (b), (d) & (f) are best fit to Gaussian equation, and the error bars are the 95% confidence intervals.

Table 5-12: Data of statistical analysis of Ni-Al LDH particle diameters.

Sample	Diameter (nm)		
	Mean (μ)	Stdev. (σ)	Var. (σ^2)
NiAl-OAm-3	17.06	3.038	9.227
NiAl-DMTDAm-1	25.54	5.976	35.71
NiAl-DMTDAm-2	29.02	6.331	40.09
NiAl-DMTDAm-3	34.23	7.337	53.84

We can conclude that DMTDAm creates better microemulsions for the syntheses of Ni-Al LDHs with more appropriate pH than OAm. The systems formed by DMTDAm can be used to synthesise Ni-Al LDH particles with diameters around 30 nm and provide accurate control on the particle sizes.

5.2.5.3. TEM images of Zn-Al LDHs

Figure 5-18 shows the TEM images of **ZnAl-DMTDAm-*n*** (*n* = 1 - 3).

The TEM images illustrate that the particles of these three Zn-Al LDH samples have crystallite morphologies consisting of thin sheets, but the sizes are random with no uniform distribution. It seems that the microemulsion systems are not able to control the particle size for Zn-Al LDHs. The reason for this is not clear.

In addition to the ZnO impurities in **ZnAl-DMTDAm-1** sample, the failure of size control suggests the microemulsion system formed by DMTDAm is not suitable for synthesising Zn-Al LDHs. Either new organic phases or new synthetic conditions need to be developed.

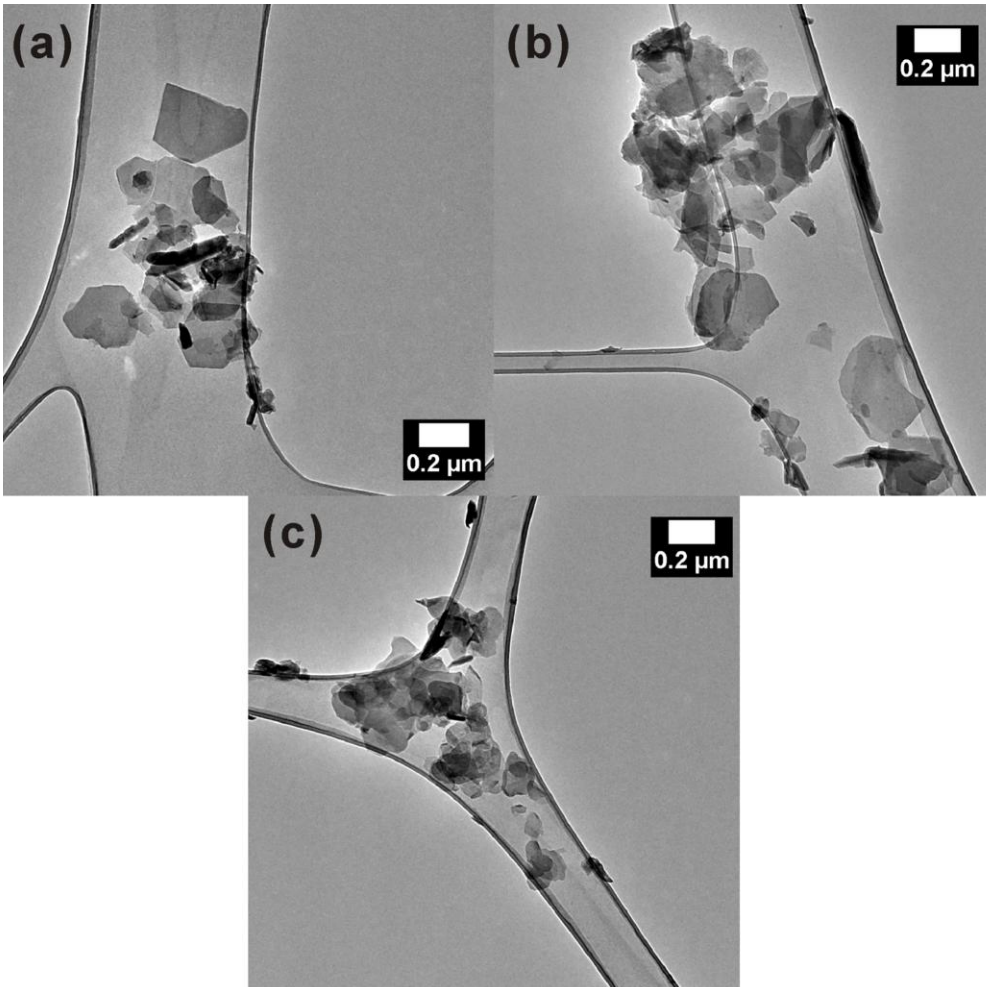

Figure 5-18: TEM images of (a) **ZnAl-DMTDAm-1**, (b) **ZnAl-DMTDAm-2**, and (c) **ZnAl-DMTDAm-3**.

5.2.5.4. TEM images and particle size analyses of Li-Al LDHs

The TEM images and particle size analyses of **LiAl-DMTDAm-*n*** (*n* = 1 - 3) are shown in **Figure 5-14**.

The particles of **LiAl-DMTDAm-*n*** (*n* = 1 - 3) exhibit a hexagonal platelet morphology with a uniform diameter of 78 nm for **LiAl-DMTDAm-1**, 109 nm for **LiAl-DMTDAm-2**, and 119 nm for **LiAl-DMTDAm-3**. The platelet sizes are significantly larger than those estimated using the Scherrer equation. The diameters of **LiAl-DMTDAm -*n*** (*n* = 1 - 3) show a direct relationship with the volume ratio of oil

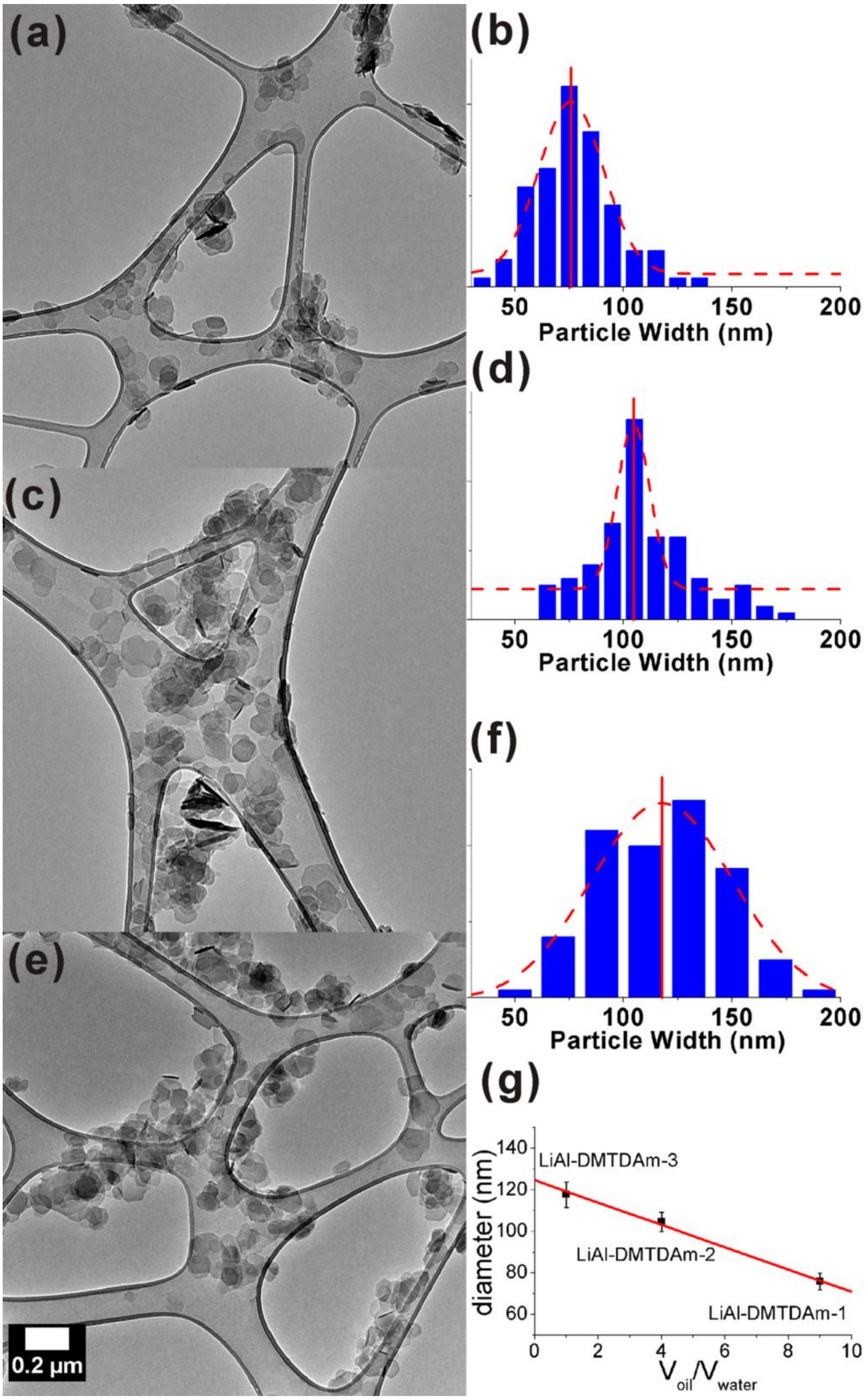

Figure 5-19: (a) TEM image and (b) particle size distribution of **LiAl-DMTDAm-1**, (c) TEM image and (d) particle size distribution of **LiAl-DMTDAm-2**, (e) TEM image and (f) particle size distribution of **LiAl-DMTDAm-3**. (g) The plot of diameters of particles versus volume ratios of oil to water. The dashed lines in (b), (d) & (f) are best fit to Gaussian equation, and the error bars are the 95% confidence intervals.

phase to water, which proves the microemulsions provide a good mean to synthesise Li-Al LDHs with controlled diameters between 70 nm and 120 nm. Statistical analysis of the particle size distributions to a normal distribution gives the mean (μ), standard deviation (σ) and variance (σ^2) parameters (**Table 5-13**).

Table 5-13: Data of statistical analysis of Li-Al LDH particle diameters.

Sample	Diameter (nm)		
	Mean (μ)	Stdev. (σ)	Var. (σ^2)
LiAl-DMTDAm-1	77.69	18.96	359.4
LiAl-DMTDAm-2	108.6	23.88	570.1
LiAl-DMTDAm-3	119.3	31.25	976.3

5.2.5.5. TEM images of Ca-Al LDHs

Figure 5-20 shows the TEM images of **CaAl-OAm-1**, **CaAl-OAm-2** and **CaAl-DOAm-OAm-1**.

The particles of **CaAl-OAm-1** exhibit unique needle morphology with lengths of *ca.* 30 nm and thickness of *ca.* 5 nm. For **CaAl-OAm-2**, besides the needle-like particles, thin platelets with a width of 30 - 50 nm can also be observed. This phenomenon may suggest the oleylamine can also have an effect on changing the surface energy thus enhancing growth along the *c*-axis. The existence of both needle and platelet crystallites with the same composition suggests there was insufficient surfactant to modify the morphology. In addition, the needle-like particles explain the comparatively larger intensity of the (110) Bragg reflection in the XRD patterns of **CaAl-OAm-1** and **CaAl-OAm-2**, since the needles will have a preferential orientation effect on the XRD.

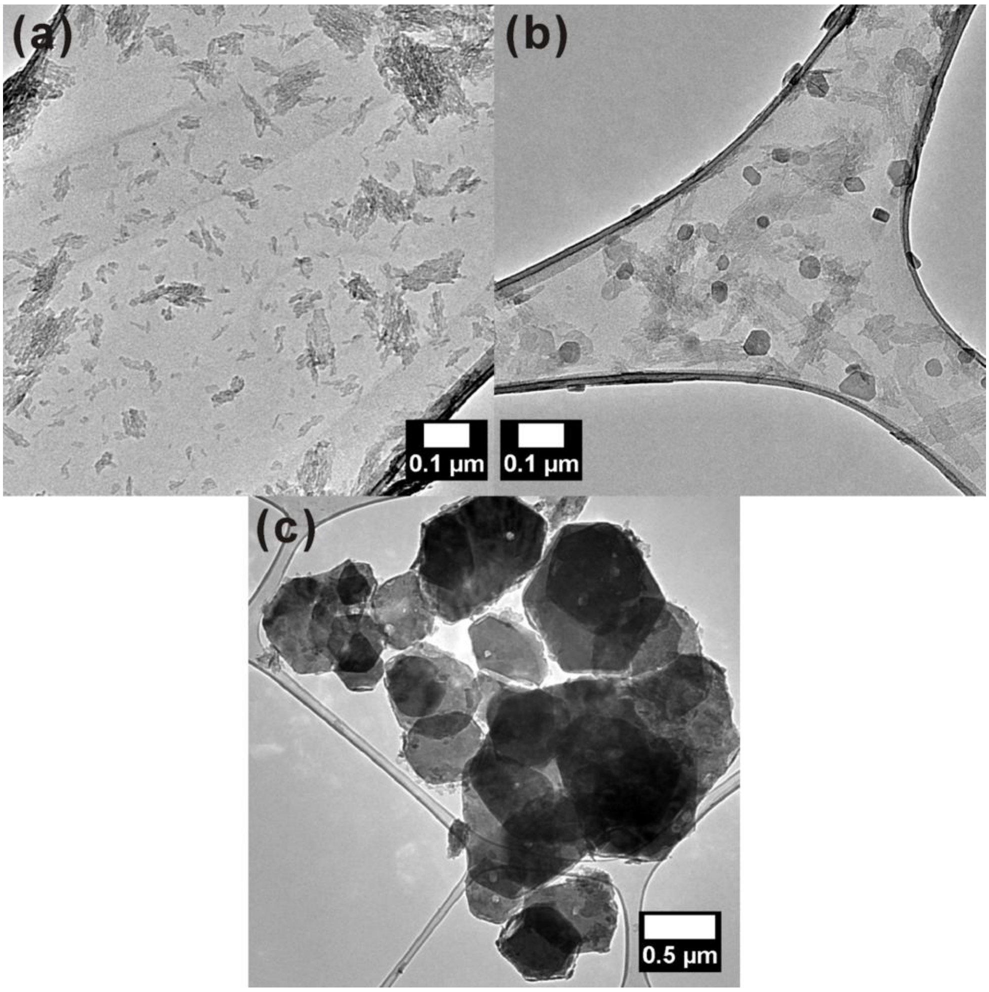

Figure 5-20: TEM images of (a) **CaAl-OAm-1**, (b) **CaAl-OAm-2**, and (c) **CaAl-DOAm-OAm-1**.

On the other hand, the particles of **CaAl-DOAm-OAm-1** are completely different from those of **CaAl-OAm-1** and **CaAl-OAm-2**. They are large hexagonal platelets with diameters from 0.5 μm to 1 μm. They are much larger than those estimated using the Scherrer equation. In addition, the platelets are significantly thicker as they show a striking contrast in the TEM image.

We can conclude that the systems using OAm are able to form needle like Ca-Al LDHs, which are a rarely seen one-dimensional nanostructure. The microemulsion created by half DOAm and half OAm has less control on the particle sizes, and is suitable for synthesising large particles over 0.5 μm in size.

5.2.5.6. TEM images and particle size analyses of Ni-Fe LDHs

Figure 5-21 shows the TEM images and particle size analyses of **NiFe-DMTDAm-*n*** (*n* = 1 - 3).

The particles of **NiFe-DMTDAm-*n*** (*n* = 1 - 3) exhibit a hexagonal platelet morphology with uniform diameters of 25 nm for **NiFe-DMTDAm-1**, 31 nm for **NiFe-DMTDAm-2**, and 35 nm for **NiFe-DMTDAm-3**. The diameters are slightly larger than those estimated using the Scherrer equation. The diameters of **NiFe-DMTDAm-*n*** (*n* = 1 - 3) show a direct relationship between the volume ratio of oil phase to water, which suggests the microemulsions formed by DMTDAm can control the particle sizes precisely in the synthesis of Ni-Fe LDHs. Statistical analysis of the particle size distribution to a normal distribution gives the mean (μ), standard deviation (σ) and variance (σ^2) parameters (**Table 5-14**).

Table 5-14: Data of statistical analysis of Ni-Fe LDH particle diameters.

Sample	Diameter (nm)		
	Mean (μ)	Stdev. (σ)	Var. (σ^2)
NiFe-DMTDAm-1	24.68	6.690	44.76
NiFe-DMTDAm-2	30.78	7.354	54.09
NiFe-DMTDAm-3	35.21	7.289	53.13

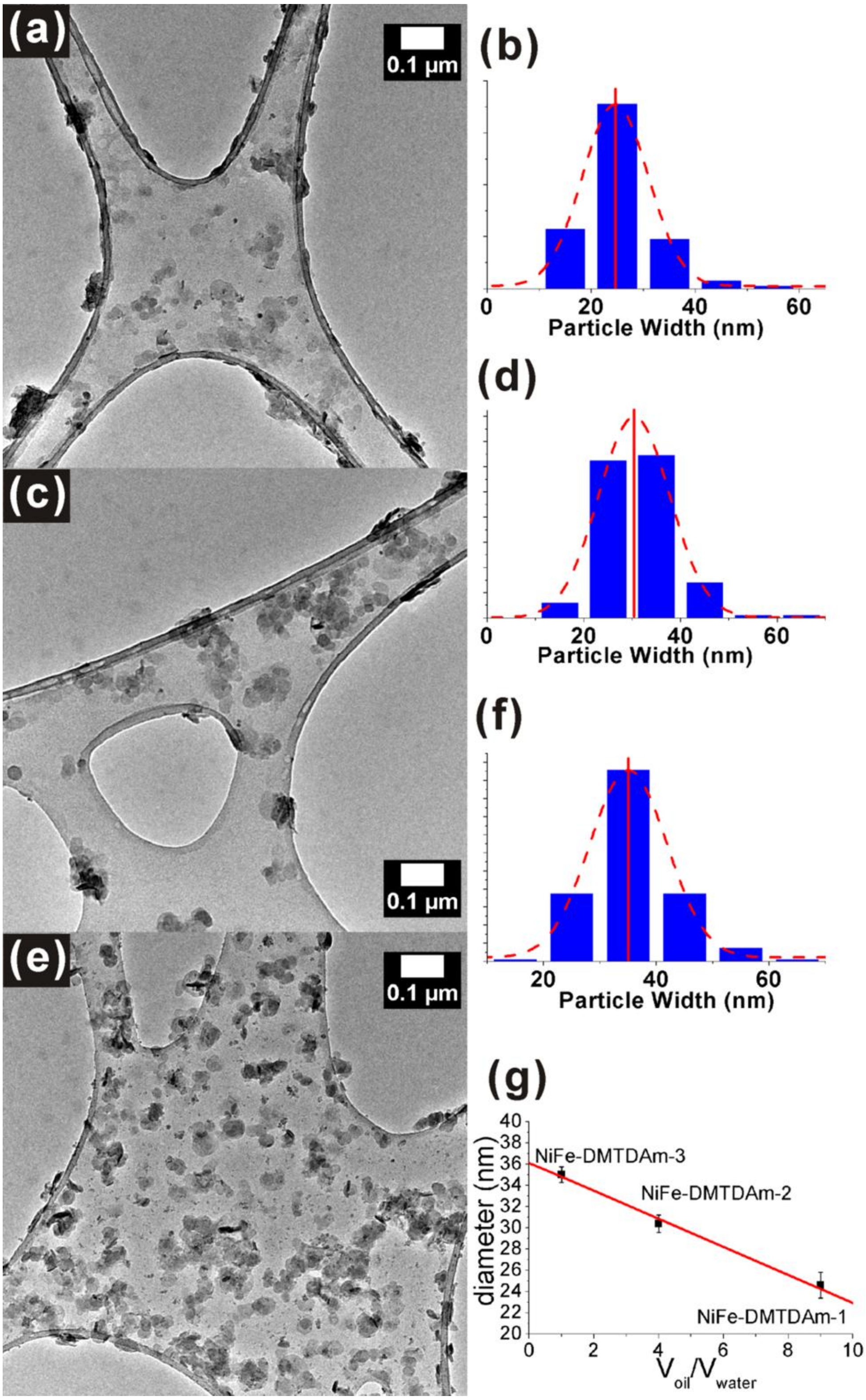

Figure 5-21: (a) TEM image and (b) particle size distribution of **NiFe-DMTDAm-1**, (c) TEM image and (d) particle size distribution of **NiFe-DMTDAm-2**, (e) TEM image and (f) particle size distribution of **NiFe-DMTDAm-3**. (g) The plot of diameters of particles versus volume ratios of oil to water. The dashed lines in (b), (d) & (f) are best fit to Gaussian equation, and the error bars are the 95% confidence intervals.

5.2.6. Magnetic properties

5.2.6.1. Magnetic properties of CoAl-OAm-*n* (*n* = 1 - 3)

The magnetic properties were investigated to compare with the Co-Al LDHs in **Chapter 3**. The molar magnetic susceptibilities of **CoAl-OAm-*n*** (*n* = 1 - 3) were measured between 2 K and 300 K. **Figure 5-22** (a), (c) & (e) shows plots of $\chi_M T$ and χ_M^{-1} *vs* T for **CoAl-OAm-*n*** (*n* = 1 - 3). The curves are similar to those of CoAl-DDS LDH samples in **Chapter 3**. Between 50 and 300 K, the materials obey the Curie-Weiss law with C = 8.85 emu K mol^{-1} (μ_{eff} = 5.57 μ_B per Co), 8.14 emu K mol^{-1} (μ_{eff} = 5.54 μ_B per Co) and 7.37 emu K mol^{-1} (μ_{eff} = 5.36 μ_B per Co) for **CoAl-OAm-*n*** (*n* = 1 - 3) respectively (**Table 5-15**). These values are also very close to the observed moment of the Co-Al LDHs in **Chapter 3**, which are larger than the expected spin-only value for octahedral Co^{2+}, d^7, (μ_{eff} = 3.87 μ_B, S = 3/2) indicating that a significant orbital contribution is involved, but are in line with other octahedral Co^{2+} containing compounds with oxide or hydroxide ligand fields. The values of the Weiss constant (θ) is 0 K, 2.99 K, and 3.77 K for **CoAl-OAm-*n*** (*n* = 1 - 3), respectively, suggesting very short range ferromagnetic interactions.

Table 5-15: Summary of the magnetic data for **CoAl-OAm-*n*** (*n* = 1 - 3).

	CoAl-OAm-1	**CoAl-OAm-2**	**CoAl-OAm-3**
$\chi_M T$ @ 300K (emu K mol^{-1})	8.64	8.57	7.55
μ_{eff} (μ_B per Co^{2+})	5.57	5.54	5.36
C (emu K mol^{-1})	8.85	8.14	7.37
θ (K)	0	2.99	3.77
TIP (emu mol^{-1})	0	0.002	0
T_{irr} (K)	3.5	3.2	3.8
T_B (K)	2.1	-	2.2

T_{irr}: temperature of the divergence of the ZFC and FC magnetic susceptibility
T_b: maximum in χ' or maximum in the ZFC magnetic susceptibility

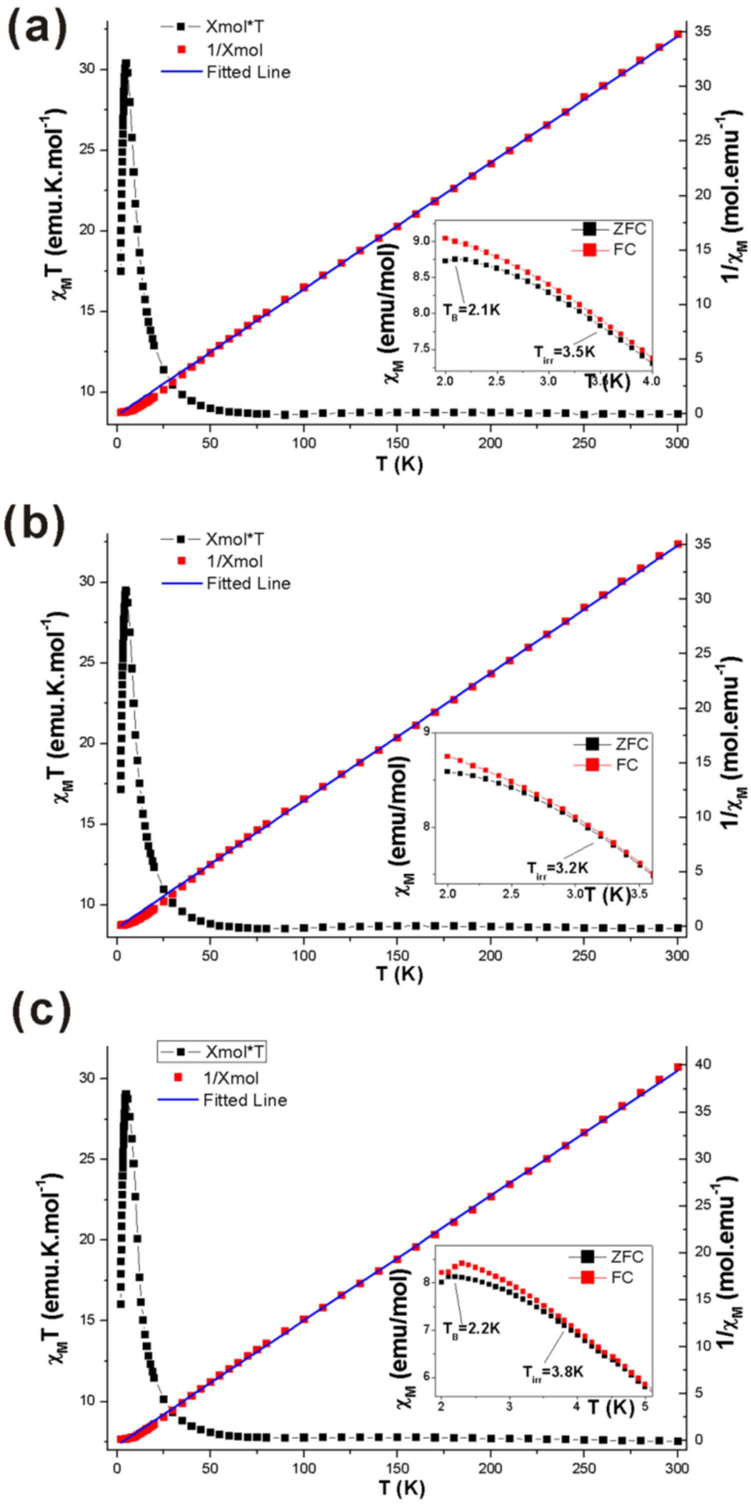

Figure 5-22: Plots of χ_MT (black squares) and χ_M^{-1} (red circles) *vs.* T between 2 to 300 K for (a) **CoAl-OAm-1**, (b) **CoAl-OAm-2**, and (c) **CoAl-OAm-3**. The solid lines are best fit to Curie-Weiss law. (Insets: Low temperature ZFC (black squares) and FC (red squares) molar magnetisation showing the bifurcation point (T$_{irr}$) and blocking temperature (T$_B$).)

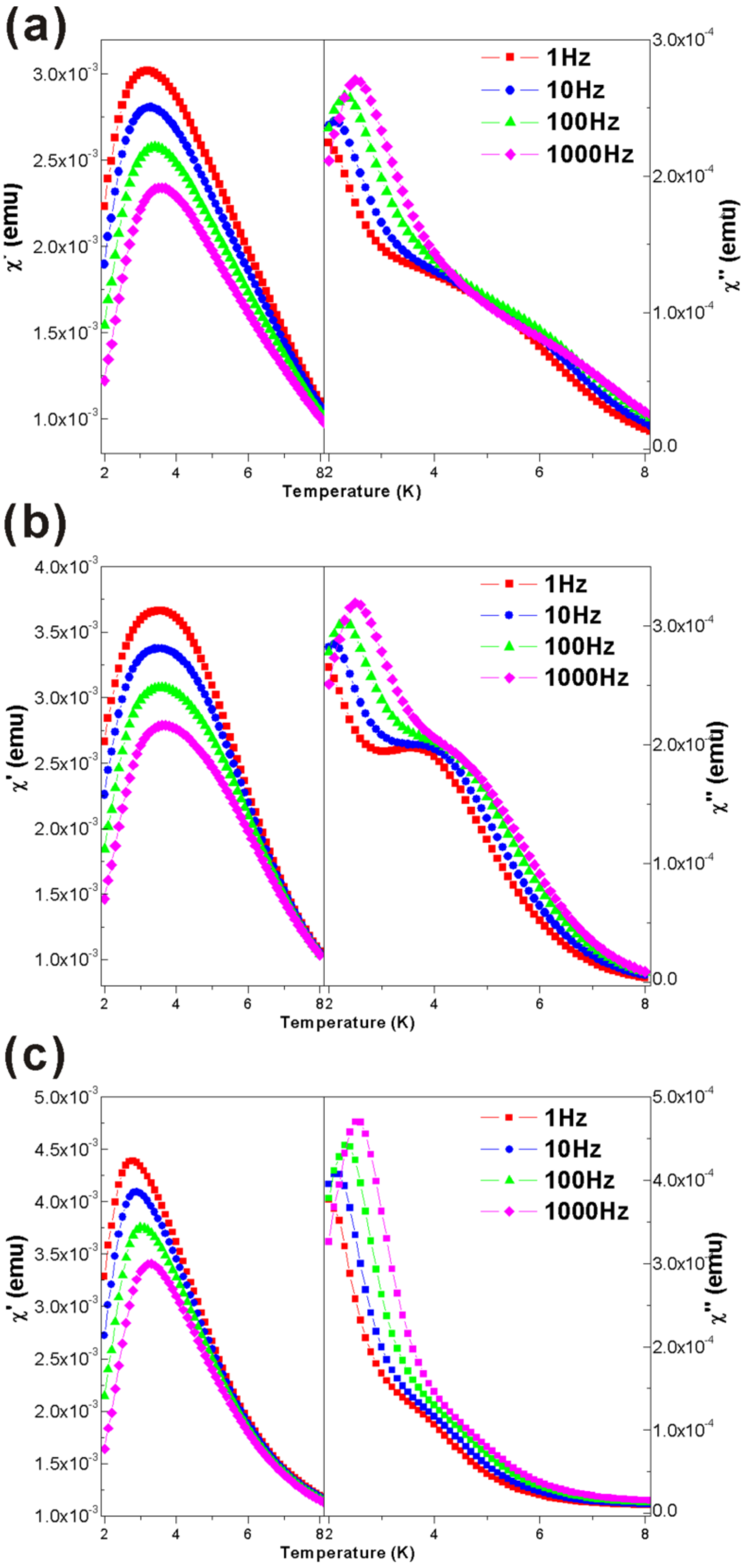

Figure 5-23: Frequency dependence of in-phase (χ') and out-of-phase (χ'') susceptibilities under an oscillating field of 5 Oe (a) **CoAl-OAm-1**, (b) **CoAl-OAm-2** and (c) **CoAl-OAm-3**.

Below 50 K, the values of $\chi_M T$ exhibit a rapid increase to a maximum at 7 K, which is ascribed to the onset of ferromagnetic ordering of the Co^{2+} spins. Bifurcations in the zero-field (ZFC) and field cooled (FC) magnetic susceptibilities below the irreversibility temperature T_{irr} are observed (**Figure 5-22** inset). At low temperatures the FC magnetisation continues increasing, while the ZFC magnetisation shows a broad maximum. However, the ZFC curves for **CoAl-OAm-2** do not reach a maximum at temperatures above 2 K, suggesting the maximum may occur below this value.

The onset of spontaneous magnetisation was confirmed by the occurrence of nonzero signals in the in-phase (χ') and out of phase (χ'') ac magnetic susceptibility (**Figure 5-22** (b) & (d) & (f)). We observe that the temperature at which the in-phase (χ') reaches a maximum slightly increases with increasing frequency, implying a slow relaxation process. The out of phase (χ'') AC magnetic susceptibilities show two peaks at *ca.* 2.2 K and 4.5 K, indicating two processes occurred. The peaks at lower temperatures are related to the appearance of intralayer spontaneous magnetisation, and therefore the high-temperature peaks must be related to interlayer processes. In the CoAl-DDS LDHs in **Chapter 3**, the interlayer separations (26 Å) are significantly larger than those of **CoAl-OAm-*n*** (*n* = 1 - 3) (7.7 Å). Consequently, the peak at higher temperature shifts to low temperature, and overlaps with the other peak.

5.2.6.2. Magnetic properties of NiFe-DMTDAm-*n* (*n* = 1 - 3)

The magnetic properties of NiFe-CO_3, NiFe-NO_3, NiFe- adipic, and NiFe- sebacic LDHs were studied by Raja *et al.*[18] and Coronado *et al.*[12, 19] For comparison, the magnetic behaviours of **NiFe-DMTDAm-*n*** (*n* = 1 - 3) samples were investigated in this chapter.

The elemental analyses indicate the molar ratio of Ni^{2+} to Fe^{3+} is 2.1/0.9 = 2.33. Due to the fact that neighbouring trications will be avoided in phase pure LDHs,[20-23] it can be considered that only Ni^{2+}-O-Ni^{2+} and Ni^{2+}-O-Fe^{3+} superexchange exists in the compounds, while the Fe^{3+}-O-Fe^{3+} superexchange is ignored. This situation promotes total ferrimagnetic coupling since the Ni^{2+}-O-Ni^{2+} interactions are ferromagnetic and Ni^{2+}-O-Fe^{3+} interactions are usually considered as antiferromagnetic.

The mass magnetic susceptibilities per gram of **NiFe-DMTDAm-*n*** (*n* = 1 - 3) were measured between 2 K and 300 K. **Figure 5-24** (a), (c) & (e) show plots of χ_g *vs* T for **NiFe-DMTDAm-*n*** (*n* = 1 - 3). Below 50 K, bifurcations in the zero-field cooling (ZFC) and field cooling (FC) magnetic susceptibilities below the irreversibility temperature T_{irr} are observed. Both T_{irr} and T_b are higher than those observed for Ni-Al LDHs in **Chapter 3**, suggesting the transitions occur at higher temperature. Above 50 K, the mass magnetic susceptibilities decrease with increasing temperature. However, the molar magnetic susceptibilities fail to obey Curie Weiss law with reasonable values for the parameters.

In order to exploit the abnormal magnetic behaviour, we measure the field dependent of the molar magnetisations from 300 K to 100 K (**Figure 5-25**). For all three samples the molar magnetisation increased quickly following the application of a small applied magnetic field suggesting a ferromagnetic response. At high applied magnetic field the molar magnetisation became linearly dependent on the applied magnetic field indicating paramagnetic behaviour. We believe the samples contain small amounts of a ferromagnetic impurity, possibly iron oxide, which is quickly saturated at low field. In the high field region, the Ni-Fe LDHs should exhibit a paramagnetic behaviour once the magnetism of the ferromagnetic impurity is fully saturated. A least squares fit of the M

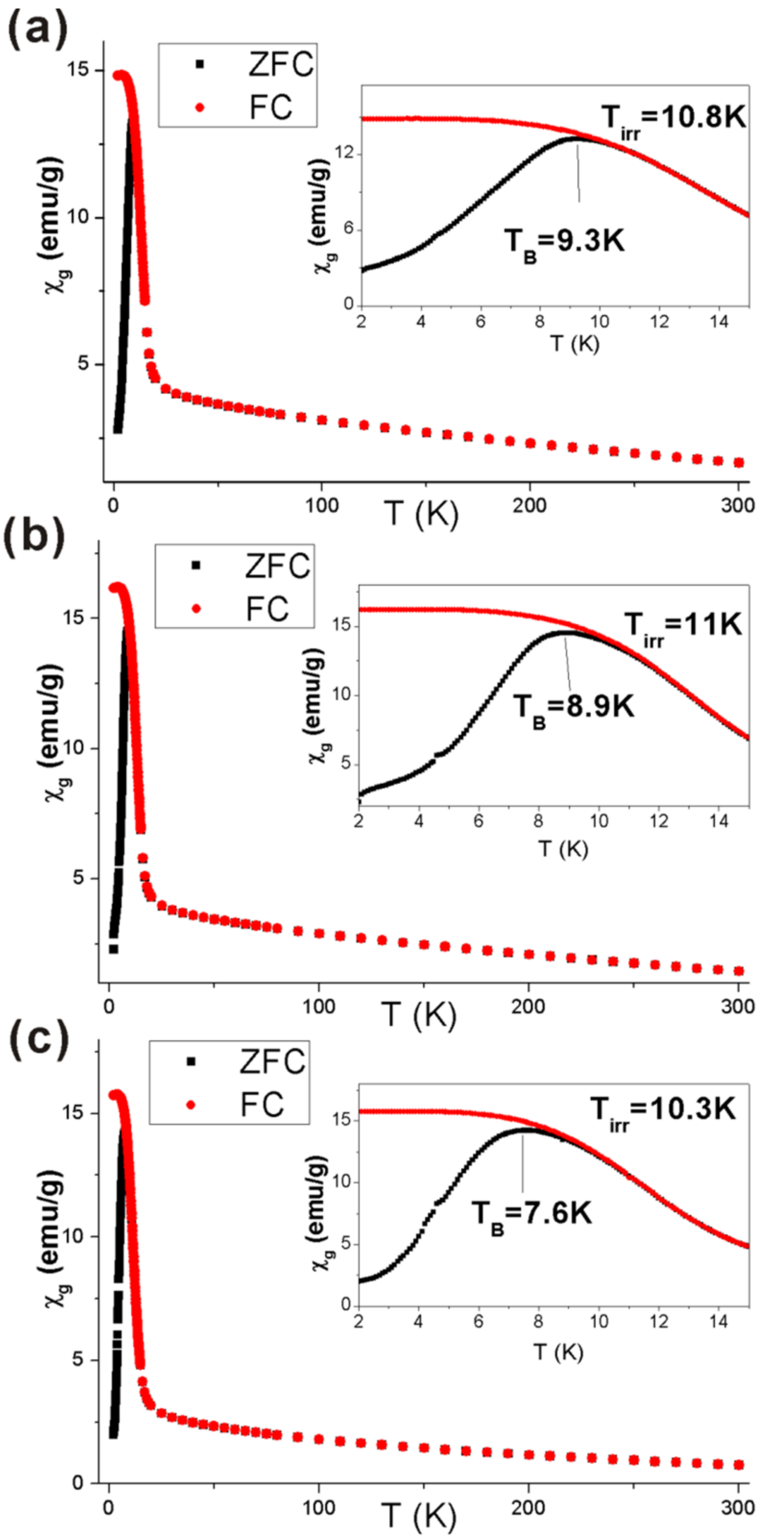

Figure 5-24: Plots of χ_g *vs.* T between 2 to 300 K for (a) **NiFe-DMTDAm-1**, (b) **NiFe-DMTDAm-2**, and (c) **NiFe-DMTDAm-3**. (Insets: Low temperature ZFC (black squares) and FC (red squares) magnetisation showing the bifurcation point (T_{irr}) and blocking temperature (T_B).)

vs. H data at high field was used to estimate the paramagnetic susceptibility for each sample. The molar magnetic susceptibilities calculated from the slopes obey the Curie Weiss law with Curie constants of 7.76 emu K mol^{-1} (μ_{eff} = 7.88 μ_B), 9.87 emu K mol^{-1} (μ_{eff} = 8.89 μ_B) and 7.24 emu K mol^{-1} (μ_{eff} = 7.61 μ_B) for **NiFe-DMTDAm-*n*** (*n* = 1 - 3), respectively (**Table 5-16**). These values are slightly higher than the expected effective magnetic moment for a compound with composition $Ni_{2.1}Fe_{0.9}$ ($\mu^2_{SO} = 2.1 \times \mu^2_{Ni} + 0.9 \times \mu^2_{Fe} = 2.1 \times 8 + 0.9 \times 35$, so $\mu_{SO} = 6.95\ \mu_B$), however the moment is very sensitive the precise metal composition. The calculated Weiss constants are –10.5 K, –14.1 K and 1.38 K, respectively. For the known NiFe-NO_3 LDH,[12] the Weiss constant is 31.99 K and decreases to negative value when the interlamellar separation increases. The authors explained this using intralayer antiferromagnetic exchange and interlayer ferromagnetic exchange. For **NiFe-DMTDAm-*n*** (*n* = 1 - 3), the metal compositions and interlayer separations are all similar, however the IR spectra indicate the CO_3^{2-} contents vary among them in the sequence of **NiFe-DMTDAm-1** ≈ **NiFe-DMTDAm-2** > **NiFe-DMTDAm-3**. One possible explanation for the Weiss constants may be the CO_3^{2-} ions provided more efficient pathways for interlayer exchange than Cl^- ions,[24] therefore the interlayer ferromagnetic exchanges cooperated with intralayer ferrimagnetic processes to promote total ferrimagnetic behaviours with negative Weiss constants. For the **NiFe-DMTDAm-3**, the IR spectrum indicates no CO_3^{2-} ions are present, resulting in much weaker Cl^- pathways.

The three samples exhibit hysteretic behaviour below 20 K (**Figure 5-26**), which suggests an ordered spin ensemble.

The onset of spontaneous magnetisation was confirmed by the occurrence of nonzero signals in the in-phase (χ’) and out of phase (χ’’) ac magnetic susceptibility

(**Figure 5-27**). The critical temperature (T_c) is *ca.* 16 K for all the samples. The temperature at which both the in-phase (χ') and out-of-phase (χ'') reaches a maximum increases with increasing frequency, implying a slow relaxation process (**Figure 5-27**). The maximum value of χ' also decreases by *ca.* one-third when using frequencies between 1 - 10^3 Hz. When sizes of magnetically ordered particles are reduced to the nanometre length scale they may become single domain particles. At finite temperature and in the absence of any magnetic field, the ferromagnetically aligned magnetic moments within these single-domain particles fluctuate between their two energetically degenerate states on a time scale, assuming a simple Arrhénius law (**Equation 3-4**, where τ is the relaxation time, τ_0 is a constant and E_a is the total magnetocrystalline anisotropy energy of the particle.).

The blocking temperature (T_B) is the temperature at which χ' and χ'' reach a maximum. It corresponds to the temperature at which $\tau = \tau_m$, the measurement time or frequency^{-1} of the measurement. A fit of ln(τ) *vs.* T_B^{-1} to **Equation 3-4** for **NiFe-DMTDAm-*n*** (*n* = 1 - 3) is shown in the **Figure 5-27** insets. The values of τ_0 and E_a/k_B for **NiFe-DMTDAm-*n*** (*n* = 1 - 3) are tabulated in **Table 5-16**. Furthermore, the frequency dependence of the maximum in χ' can be parameterised using the frequency-shift parameter, φ, according to **Equation 3-6**, which are 0.007, 0.005 and 0.011 for **NiFe-DMTDAm-*n*** (*n* = 1 - 3), respectively. A material is usually considered to be spin glass when $0.001 \leq \varphi \leq 0.1$. However, the nature of the magnetic interactions in these materials is not straightforward, which may be a combined effect of spin glass and superparamagnetism.

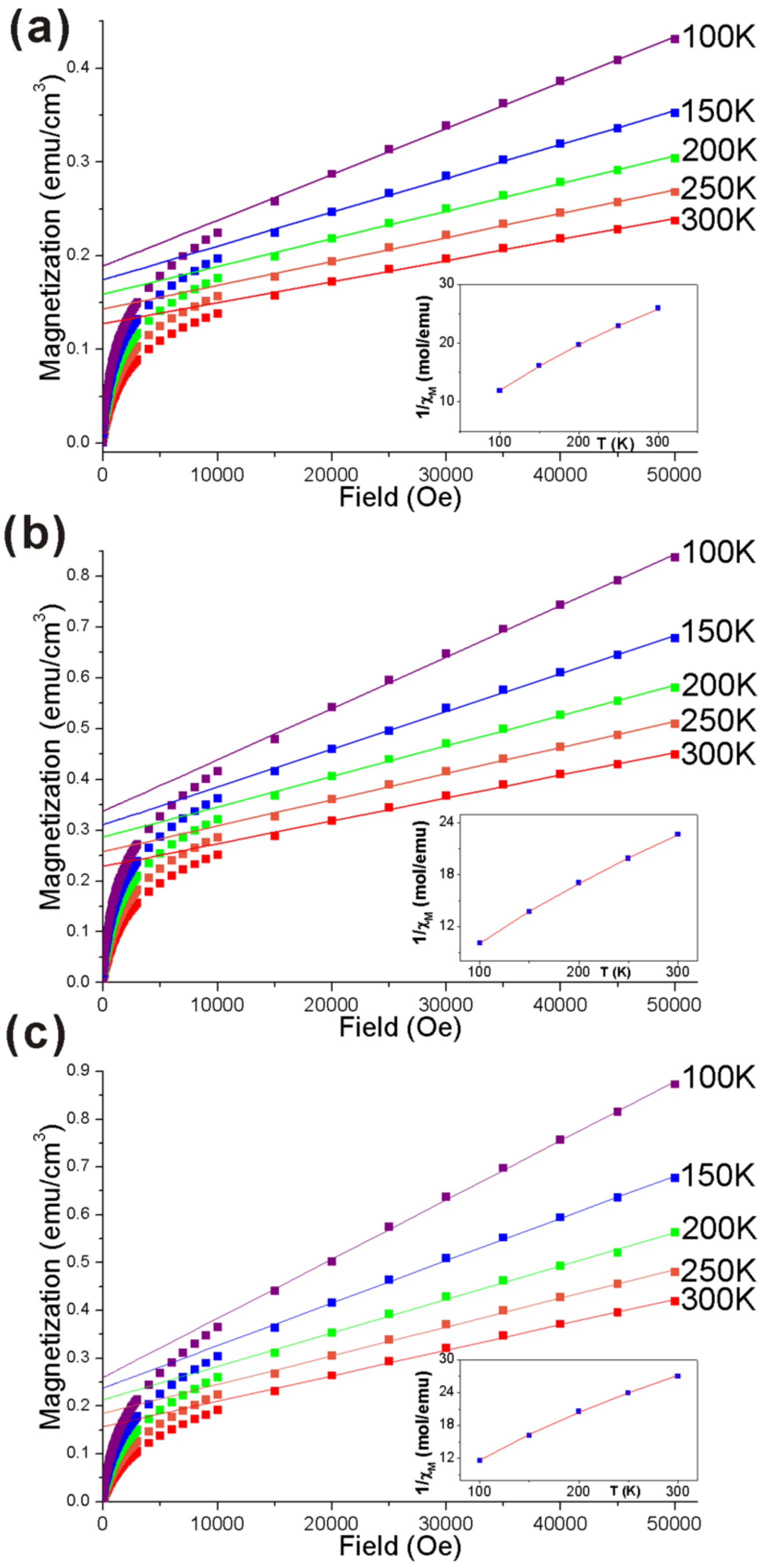

Figure 5-25: Field dependence of magnetisation of (a) **NiFe-DMTDAm-1**, (b) **NiFe-DMTDAm-2**, and (c) **NiFe-DMTDAm-3** at 100 K (red), 150 K (orange), 200 K(green), 250 K (blue) and 300 K (purple). The solid lines are best linear fit. (Insets: plots of the slopes of the fitted line verse temperature.)

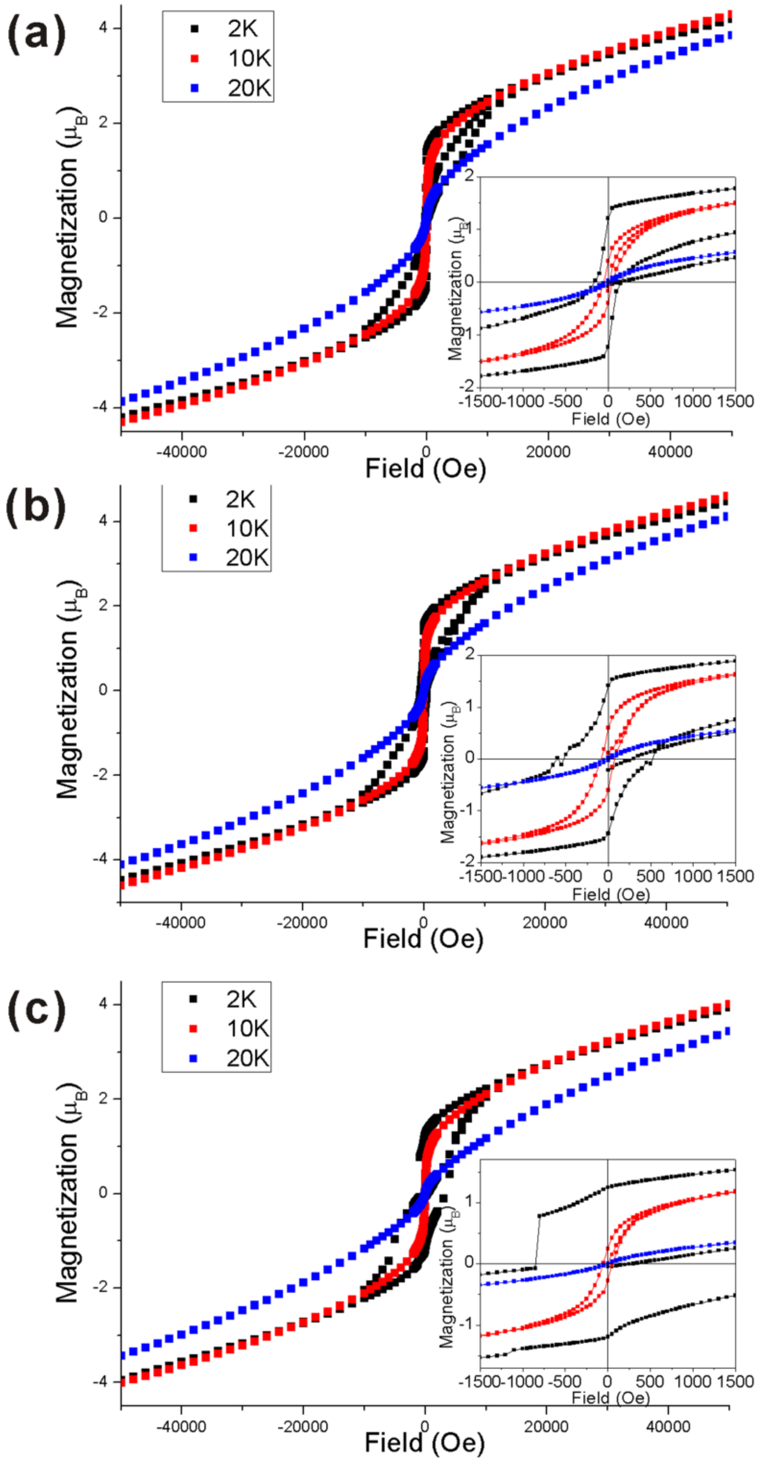

Figure 5-26: M *vs.* H at 2 K (black squares), 10 K (red) and 20 K (blue) for (a) **NiFe-DMTDAm-1**, (b) **NiFe-DMTDAm-2**, and (c) **NiFe-DMTDAm-3**. (Insets: curves at low field.)

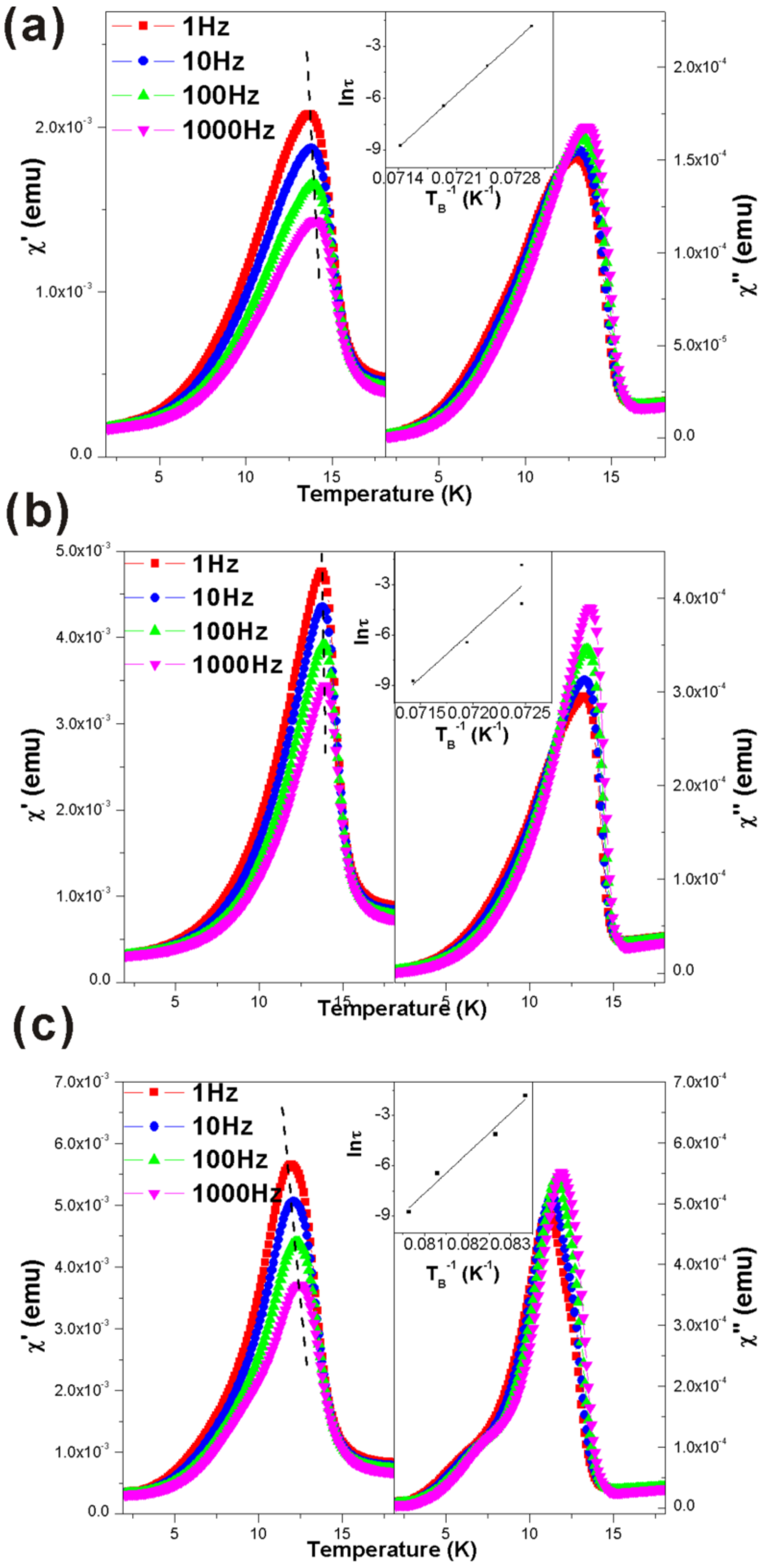

Figure 5-27: Frequency dependence of in-phase (χ’) and out-of-phase (χ’’) susceptibilities under an oscillating field of 5 Oe (a) **NiFe-DMTDAm-1**, (b) **NiFe-DMTDAm-2** and (c) **NiFe-DMTDAm-3**. (Inset: Frequency dependence of the blocking temperature T_B. Line is least squares fit to the Arrhénius law (**Equation 3-4**).)

Table 5-16: Summary of the magnetic data for **NiFe-DMTDAm-*n*** (*n* = 1 - 3).

	NiFe-DMTDAm-1	**NiFe-DMTDAm-2**	**NiFe-DMTDAm-3**
$\chi_{mol}T$ @ 300K (emu K ·mol^{-1})	25.18	29.78	25.79
μ_{eff} (μ_B)	7.88	8.89	7.61
C (emu K mol^{-1})	7.76	9.87	7.24
θ (K)	–10.54	–14.05	1.38
TIP (emu mol^{-1})	0.0137	0.0127	0.0126
T_{irr} (K)	10.8	11.0	10.3
T_B (K)	9.3	8.9	7.6
τ_0 (s)^a	1.6×10^{-141}	3.4×10^{-180}	2.0×10^{-88}
E_a/k_B (K)^a	4416	5660	2398
φ	0.007	0.005	0.011

T_{irr}: temperature of the divergence of the ZFC and FC magnetic susceptibility.
T_B: maximum in χ’ or maximum in the ZFC magnetic susceptibility.
^{a} parameters obtained by fitting of the ac magnetic susceptibility data to **Equation 3-4**.

5.3. Conclusion

Four different single component microemulsions were prepared to synthesise various LDHs. Co-Al LDHs and Ni-Al LDHs were successfully synthesised in both microemulsions formed by OAm or DMTDAm. Among them, the DMTDAm system provides accurate control of particle size for Ni-Al LDHs by adjusting the ratio of oil phase to water, while in other systems the particle sizes fail to illustrate a direct relationship to the ratio of oil phase to water. Li-Al and Ni-Fe LDHs were also successfully prepared with controlled particle sizes. Ca-Al LDHs synthesised in OAm system exhibit a unique needle-like morphology. The magnetic properties of **CoAl-OAm-*n*** and **NiFe-DMTDAm-*n*** (*n* = 1 - 3) were investigated to compare with known compounds.

5.4. References

1. Y. Zhao, F. Li, R. Zhang, D. G. Evans and X. Duan, *Chem. Mater.*, 2002, **14**, 4286-4291.
2. Z. P. Xu, G. Stevenson, C.-Q. Lu and G. Q. Lu, *J. Phys. Chem. B*, 2006, **110**, 16923-16929.
3. L. Qiu and B. Qu, *J. Colloid Interface Sci.*, 2006, **301**, 347-351.
4. B. Yu, H. Bian and J. Plank, *J. Phys. Chem. Solids*, 2010, **71**, 468-472.
5. X. Ruan, P. Sun, X. Ouyang and G. Qian, *Chin. Sci. Bull.*, 2011, **56**, 3431-3436.
6. J. Plank, Z. Dai and N. Zouaoui, *J. Phys. Chem. Solids*, 2008, **69**, 1048-1051.
7. R. Ma, J. Liang, K. Takada and T. Sasaki, *J. Am. Chem. Soc.*, 2010, **133**, 613-620.
8. R. Z. Ma, Z. P. Liu, K. Takada, N. Iyi, Y. Bando and T. Sasaki, *J. Am. Chem. Soc.*, 2007, **129**, 5257-5263.
9. M. Intissar, R. Segni, C. Payen, J.-P. Besse and F. Leroux, *J. Solid State Chem.*, 2002, **167**, 508-516.
10. H. Hansen, C. Koch and R. Taylor, *J. Solid State Chem.*, 1994, **113**, 46-53.
11. Y. F. Han, Z. H. Liu, Z. P. Yang, Z. L. Wang, X. H. Tang, T. Wang, L. H. Fan and K. Ooi, *Chem. Mater.*, 2008, **20**, 360-363.
12. E. Coronado, J. Galan-Mascaros, C. Marti-Gastaldo, A. Ribera, E. Palacios, M. Castro and R. Burriel, *Inorg. Chem.*, 2008, **47**, 9103-9110.
13. G. Abellan, E. Coronado, C. Marti-Gastaldo, E. Pinilla-Cienfuegos and A. Ribera, *J. Mater. Chem.*, 2010, **20**, 7451-7455.
14. R. A. Scherrer and S. M. Howard, *J. Med. Chem.*, 1977, **20**, 53-58.
15. Y. Q. Sun, Y. M. Zhou, Z. Q. Wang and X. Y. Ye, *Appl. Surf. Sci.*, 2009, **255**, 6372-6377.
16. W. Kagunya, R. Baddour-Hadjean, F. Kooli and W. Jones, *Chem. Phys.*, 1998, **236**, 225-234.
17. Z. P. Xu and G. Q. Lu, *Chem. Mater.*, 2005, **17**, 1055-1062.
18. T. Raja and J. Santhanalakshmi, *J. Mater. Sci. Lett.*, 1996, **15**, 718-720.
19. E. Coronado, C. Martí-Gastaldo, E. Navarro-Moratalla and A. Ribera, *Appl. Clay Sci.*, 2010, **48**, 228-234.
20. M. Bellotto, B. Rebours, O. Clause, D. Bazin and E. Elkaïm, *J. Phys. Chem.*, 1996, **100**, 8527-8534.
21. A. I. Khan and D. O'Hare, *J. Mater. Chem.*, 2002, **12**, 3191-3198.
22. M. Vucelic, W. Jones and G. D. Moggridge, *Clays Clay Miner.*, 1997, **45**, 803-813.
23. G. Bourrié, F. Trolard, P. Refait and F. Feder, *Clays Clay Miner.*, 2004, **52**, 382-394.
24. M. Bujoli-Dœuff, L. Force, V. Gadet, M. Verdaguer, K. El Malki, A. de Roy, J. P. Besse and J. P. Renard, *Mater. Res. Bull.*, 1991, **26**, 577-587.

Chapter 6

Simulation of the XRD patterns of LDHs

6.1. Introduction

Layered double hydroxides (LDHs) are a family of layered materials with the composition $[M^{z+}{}_{1-x}M^{3+}{}_{x}(OH)_2]^{a+}(X^{n-})_{a/n}\cdot mH_2O$. The most common LDHs have $z = 2$ (and so $a = x$), and known M^{2+} include Ca^{2+}, Mg^{2+}, Fe^{2+}, Mn^{2+}, Zn^{2+}, Cu^{2+}, Ni^{2+} or Co^{2+}, while known M^{3+} for these structures include Al^{3+}, Cr^{3+}, Mn^{3+}, Fe^{3+}, Ga^{3+}, Co^{3+}, Ni^{3+}, V^{3+} or Sc^{3+}. The structure of LDHs can be considered to comprise positively charged brucite-like layers of mixed metal hydroxides with charge-balancing anions and water molecules in the interlayer space.[1-3] Li-Al LDHs, where $z = 1$, are the only known examples that contain M^+ and M^{3+} cations. The structures of Li-Al LDHs are based on two polytypes of $Al(OH)_3$, gibbsite and bayerite.[4-7] Li^+ ions occupy one-third of the octahedral sites and the positive charge is neutralized by the anions located in the interlayer space.

In phase pure LDH crystals, the layer charge $x = M^{3+}/(M^{2+}+M^{3+})$ in the formula $[M^{2+}{}_{1-x}M^{3+}{}_{x}(OH)_2]^{x+}(A^{n-})_{x/n}\cdot mH_2O$ should be in the range of 0.2 to 0.33, though exceptions have been found in LDHs when $M^{3+} = Cr^{3+}$.[8] It has been shown by solid state NMR spectroscopy that in Mg-Al LDHs, the Al^{3+} ions are fully ordered in a hexagonal arrangement when $x = Al^{3+}/(Al^{3+}+Mg^{2+}) = 0.33$. When $x < 0.33$ the Al^{3+} ions are distributed without any Al-O-Al close contacts.[9]

The stacking sequences of the layers in LDHs can be classified into two main groups, those with a rhombohedral sequence (3R) and those with a hexagonal sequence (2H). If upper case symbols A, B and C represent the hydroxyl ion positions, and lower case symbols *m* and *a* represent the positions for metal ions and interlayer cations, the rhombohedral stacking sequence could be expressed as A*m*B *a* B*m*C *a* C*m*A *a* A*m*B…, while the hexagonal stacking sequence is A*m*B *a* B*m*A *a* A*m*B…(**Figure 6-1**).

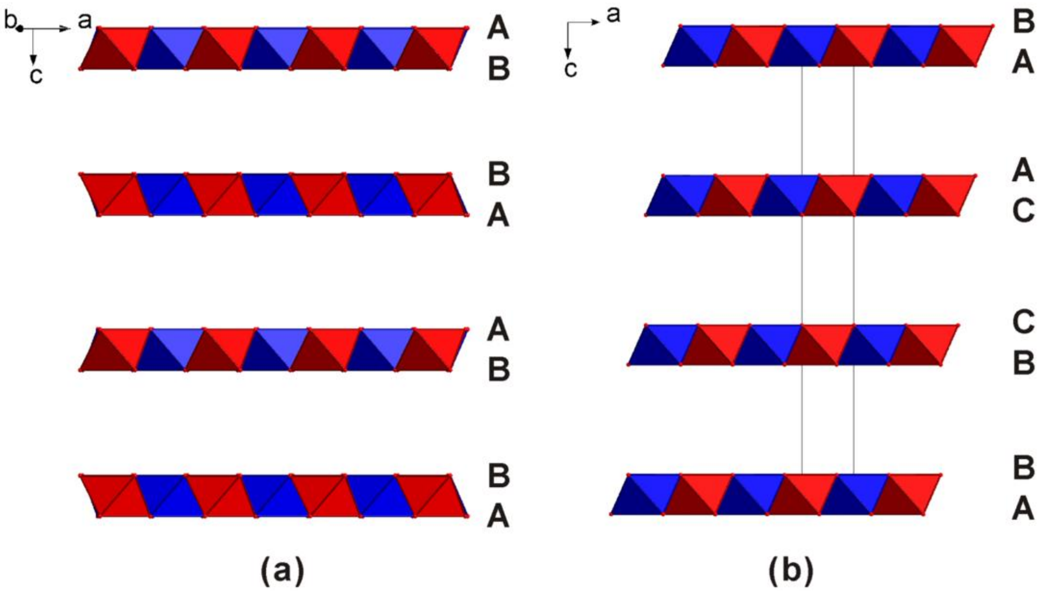

Figure 6-1: Schematic structures of Mg-Al LDHs with (a) a hexagonal sequence (Quintinite) and (b) a rhombohedral sequence (Hydrotalcite). Red octahedra are Al^{3+} centred, blue are Mg^{2+} centred.

6.1.1. Stacking disorder in LDH structures

As illustrated above, the structure of LDHs can be viewed as a stacking of brucite-like hydroxide sheets containing an intercalated layer of anions and water molecules. In principle, the brucite-like sheets can orientate in two different ways during crystallisation.[10] However, the real crystals could fall beyond these two ideal classifications. The polytypes of all possible stacking sequences have been described by Bookin and Drits (**Figure 6-2**),[11, 12] including one one-layer polytype (1H), three

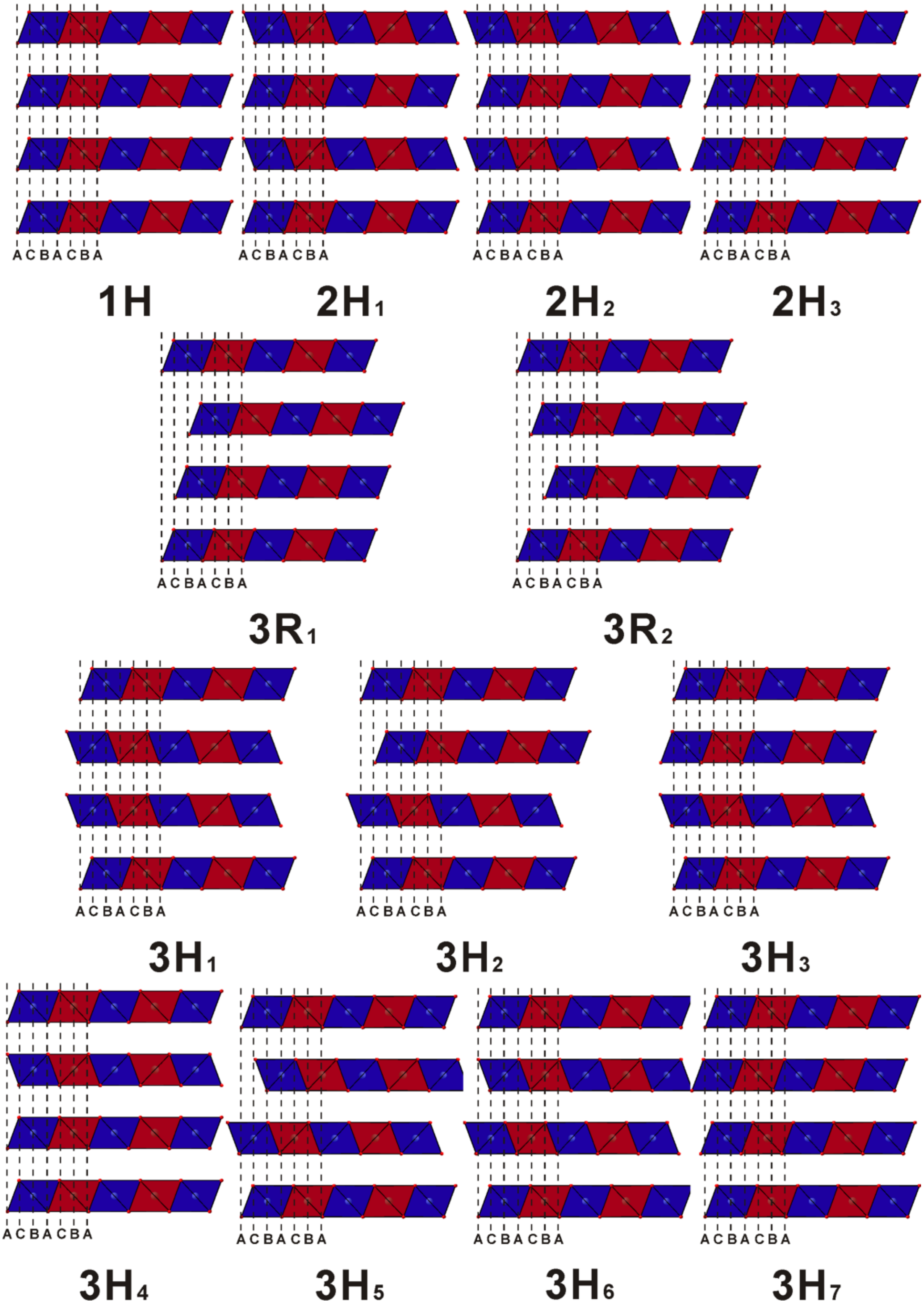

Figure 6-2: Possible polytypes of LDH crystals.

two-layer polytypes ($2H_1$, $2H_2$, $2H_3$), nine three-layer polytypes ($3R_1$, $3R_2$, $3H_1$, $3H_2$, $3H_3$, $3H_4$, $3H_5$, $3H_6$, $3H_7$), and a number of six-layer polytypes (among them, the ones with rhombohedral symmetry are $6R_1$, $6R_2$, $6R_3$, $6R_4$, $6R_5$). Besides these fairly regular arrangements, LDH materials can contain stacking faults and disorders. All of these polytypes could co-exist in crystals to form a mixture of stacking sequence.[13] Random turbostratic disorder is also widely present in crystals, especially those synthesised using co-precipitation methods.

All the different polytypes can be considered as hydroxide layers stacking one above another with different stacking vectors. In that case, the $3R_1$ sequence can be simulated by a predefined brucite-like layer (A*m*B) and a stacking vector (2/3, 1/3, 1/3), while the $2H_1$ sequence can be simulated by two predefined layers (A*m*B B*m*A) and a stacking vector (0, 0, 1/2). The turbostratic disorder can be introduced by the use of more than one stacking vector with predetermined probabilities and a stacking vector incorporating a random translation (*x*, *y*, 1/2) or (*x*, *y*, 1/3) (*x*, *y*: random).

6.1.2. DIFFaX and DIFFaX+

The program DIFFaX,[14] which is a Fortran based code, can be used to simulate powder X-ray diffraction patterns from crystals containing stacking faults. The implementation of the DIFFaX program requires the *c*-axis to be defined along the stacking direction, as well as a set of possible layer choices and the translation vectors between them. The powder XRD pattern is then simulated by integrating the diffraction intensities layer by layer. A lot of layered materials have been investigated using DIFFaX,[15-23] while layered double hydroxides (LDHs) are one of the most extensively used materials in this program.[13, 24-36]

DIFFaX+,[37] which is based on DIFFaX, allows the simultaneous refinement of both structural and microstructural parameters of a layered crystal. It can show advanced functions in simulation and refinement of inorganic crystals.[29, 35, 38-43]

6.2. Factors that influence the XRD patterns

To investigate the factors that have an influence on LDH powder XRD patterns, a hypothetical perfectly ordered crystal of Mg_2-Al LDH was chosen as an example. The Al ions are distributed so that no such ions are positioned in neighbouring octahedra. The interlayer molecules and hydrogen atoms are ignored to simplify the structure. A unit cell of a single hydroxide layer is shown in **Figure 6-3**.

The crystal parameters of Mg_2-Al LDH are defined using the values calculated in **Chapter 4**, which are $a = b = 5.290$ Å, $c = 22.810$ Å, $\alpha = \beta = 90°$ and $\gamma = 120°$ for a 3R sequence, while for 2H sequence, $c = 15.207$ Å. The symmetry of the unit cell is defined as centrosymmetric. The space group was declared unknown, which enables the DIFFaX code to evaluate the Laue symmetry. Two sets of crystal information shown in **Table 6-1** are used to describe two inverted symmetrical single layers. For 3R sequences, unit cell 3A stack along the c-axis with a stacking vector (2/3, 1/3, 1/3), while for 2H sequences, unit cells 2A and 2B stack alternately along the c-axis with a stacking vector (0, 0, 1/2).[29] The detailed input file can be found in **APPENDIX II**.

The ideal XRD pattern is produced using an ideal crystal within which atoms arrange in a regular repeating pattern over large distances (relative to the atomic size). The factors which have an effect on the PXRD pattern include the number of layers, the size of particles, the stacking faults and other defects within the crystal.

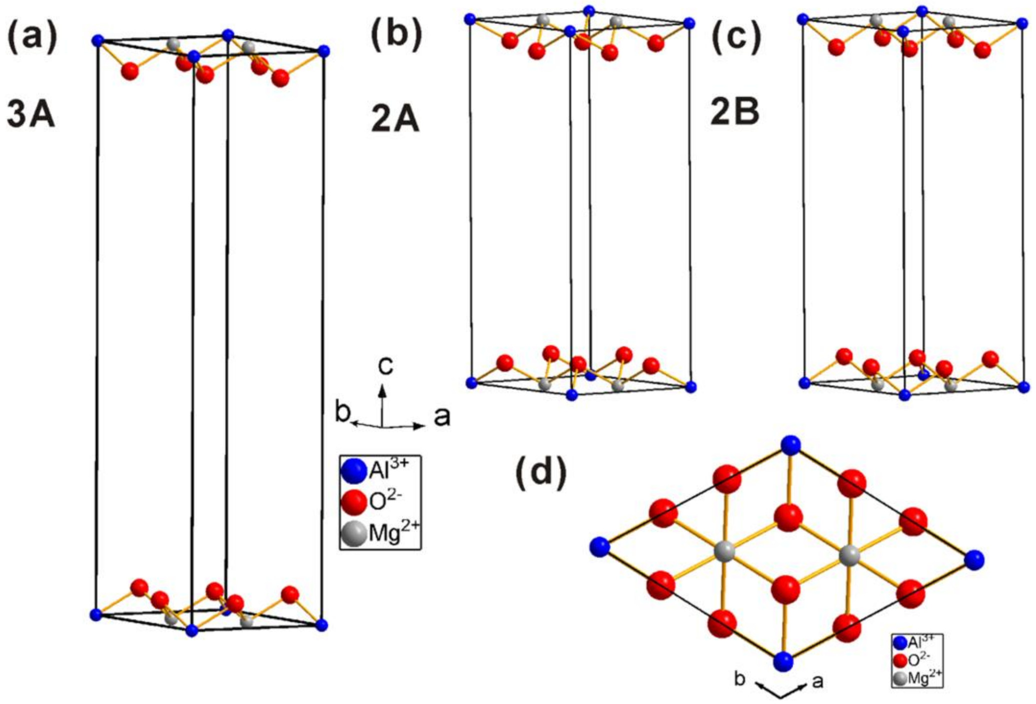

Figure 6-3: The simulated structures of Mg_2-Al LDH unit cells (a) 3A, (b) 2A, (c) 2B, and (d) top-view of the unit cells.

Table 6-1: Crystal information used for the simulation of the powder XRD pattern of Mg_2-Al LDH.

		Site	x/a	y/b	z/c	B_{iso}	Occ.
Layer 3A	Al^{3+}	1b	0	0	0	1.0	0.5
	Mg^{2+}	2i	1/3	2/3	0	1.0	1
	O^{2-}	2i	1/3	0	0.0438	1.0	1
	O^{2-}	2i	0	1/3	0.0438	1.0	1
	O^{2-}	2i	2/3	2/3	0.0438	1.0	1
Layer 2A	Al^{3+}	1b	0	0	1/2	1.0	0.5
	Mg^{2+}	2i	1/3	2/3	1/2	1.0	1
	O^{2-}	2i	1/3	0	0.0657	1.0	1
	O^{2-}	2i	0	1/3	0.0657	1.0	1
	O^{2-}	2i	2/3	2/3	0.0657	1.0	1
Layer 2B	Al^{3+}	1b	0	0	1/2	1.0	0.5
	Mg^{2+}	2i	1/3	2/3	1/2	1.0	1
	O^{2-}	2i	2/3	0	0.0657	1.0	1
	O^{2-}	2i	0	2/3	0.0657	1.0	1
	O^{2-}	2i	1/3	1/3	0.0657	1.0	1

6.2.1. Stacking disorder

The stacking sequence is one of the most important factors that influence the powder XRD patterns of crystals. Changes in stacking can transform the total crystal symmetry. For LDH crystals, the brucite-like single layer exhibits hexagonal symmetry and is centrosymmetric. We used different stacking vectors and two pre-defined single layers to construct the thirteen polytypes of LDHs. The DIFFaX program is able to output the simulated XRD patterns according to the setting values.

Polytypes 1H, $2H_1$ and $3R_1$ are the most commonly seen in minerals and lab-prepared LDHs. They have trigonal, hexagonal and rhombohedral symmetry, and belong to Laue groups of $\bar{3}m$, $6/mmm$, and $\bar{3}m$, respectively. Their simulated patterns are shown in **Figure 6-4**. Patterns for polytypes 1H and $3R_1$ are similar to each other since they have similar symmetrical elements. The unit cells of 1H, $2H_1$ and $3R_1$ contain 1, 2, and 3 layers respectively, and as a result their diffraction patterns have a series of

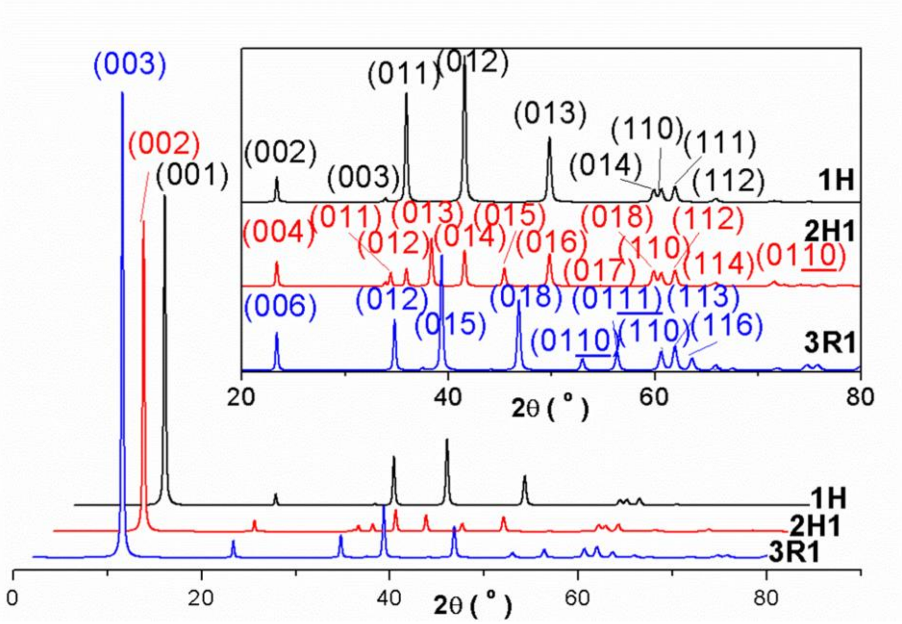

Figure 6-4: Simulated PXRD patterns of (a) 1H, (b) $2H_1$, (c) $3R_1$ polytypes of Mg_2-Al LDHs.

(00$\underline{nl}$) reflections (n = 1 for 1H, 2 for $2H_1$ and 3 for $3R_1$). In addition, a series of (01l) reflections can be observed across the range of $30 \leq 2\theta$ (°) ≤ 60. There is only (110) reflections near 60 ° in the pattern of $3R_1$ sequence, while two overlapping reflections are observed in the patterns of the 1H and $2H_1$ sequences which can be indexed to the (014) and (110) reflections for 1H and (018) and (110) reflection for $2H_1$. This phenomenon can be used as a characterisation technique to differentiate the 1H, $2H_1$ and $3R_1$ polytypes.

Patterns of the rest of the hexagonal polytypes are also simulated (**Figure 6-5**). They are generally similar when $2\theta \leq 30$ °, but the intensities of the peaks for $2H_2$ and $2H_3$ are comparatively lower than those in other sequences. In the range $2\theta \geq 30$ °, both of the positions and the intensities of the diffraction reflections vary due to different stacking sequences leading to different symmetries.

Stacking faults can be introduced to a perfectly ordered crystal using different

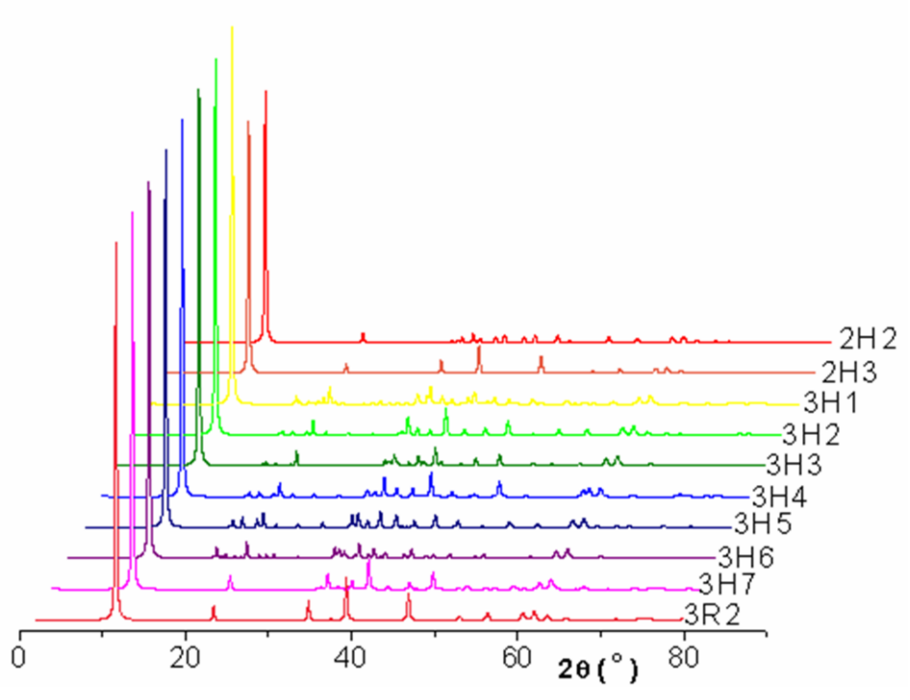

Figure 6-5: Simulated PXRD patterns of other polytypes.

stacking vectors and occurrence probabilities.[44] Crystals with such planar disorder are expected to be stable compared with the ordered crystals.[45] We created a series of mixtures of polytype $2H_1$ and $3R_1$ with the percentage of polytype $2H_1$ from 0 to 100 to investigate the influence of stacking faults on powder XRD patterns (**Figure 6-6**). The (015) reflection in $3R_1$ polytype at $2\theta = 40°$ gradually moves to $2\theta = 38°$ (where the (013) reflection appears in the $2H_1$ polytype), while the (018) reflection in the $3R_1$ polytype at $2\theta = 47°$ shifts to $2\theta = 45°$ (equivalent to the (015) reflection of the $2H_1$ polytype). New peaks emerge, which illustrate structure transformation, *e.g.* the (018) reflection in $2H_1$ polytype near $2\theta = 60°$ that does not exist in the pattern of $3R_1$ polytype gradually appear when the probability of the $2H_1$ polytype increases. Due to the incorporation of stacking faults, the symmetry of the crystal is reduced, leading to broader peaks and some new peaks.

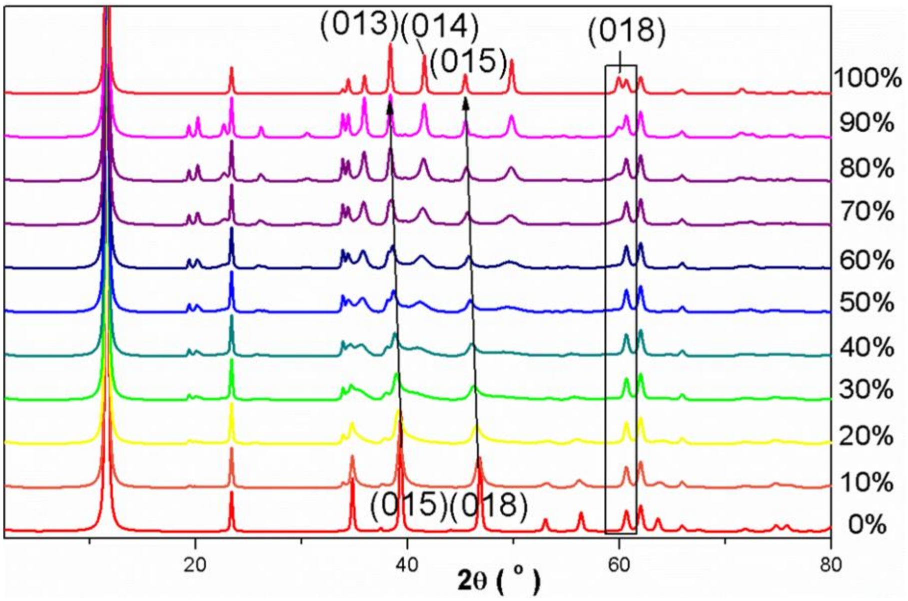

Figure 6-6: Simulated PXRD patterns of polytype $3R_1$ LDH incorporating $2H_1$ stacking faults with probabilities from 0% to 100%.

6.2.2. Turbostratic disorder

Besides the existence of regular stacking faults, turbostratic disorder is another type of disorder that appears more randomly, for instance malposition and abnormal stacking. Ignoring the disorder along the stacking axis, we could define the concept “turbostratic” using the stacking vector (*x*, *y*, 1/3) (*x*, *y*: random).[13, 26, 27, 32, 33, 46] Turbostratic disorder inevitably changes the symmetry of the crystal and results in peak broadening and displacement. By continually increasing the presence of turbostratic disorder in a crystal, the crystal would eventually become an amorphous state. **Figure 6-7** gives the simulated powder XRD patterns of an LDH with 0% to 20% turbostratic disorder. It is obvious that all the reflections where $h, k \neq 0$ are broadened and weakened, such as the (015) reflection at 2θ = 40° and the (018) reflection at 2θ = 47°. Crucially however, for the (003) reflection at 2θ = 11.5° and the (006) reflection at 2θ = 23°, the peak intensity and FWHM remain almost unchanged. This is because the *z* stacking vector is set to 1/3 while *x*, *y* are input randomly, hence the stacking turbostratic

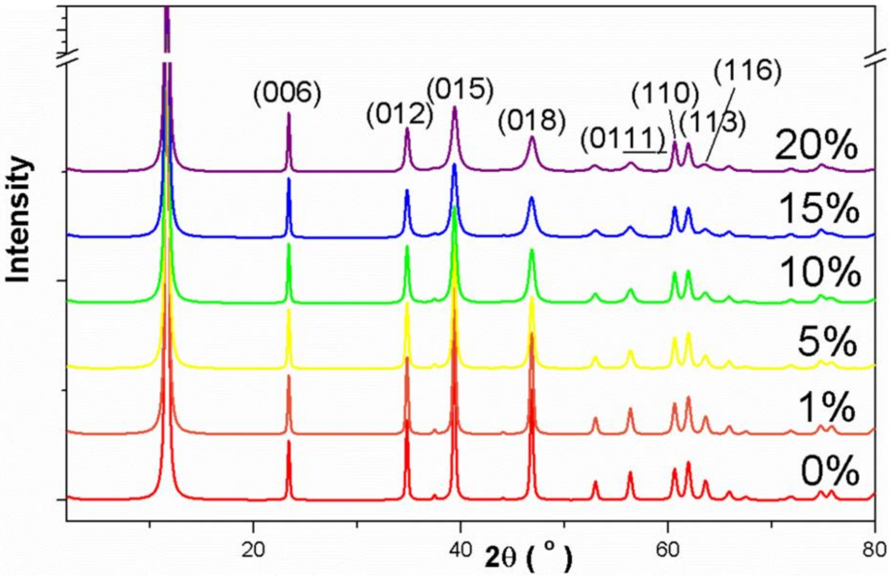

Figure 6-7: Simulated PXRD patterns of $3R_1$ LDH containing turbostratic disorder from 0% to 20%.

disorder along *c*-axis is not considered.

6.2.3. Crystallite size

Although X-ray scattering follows Bragg's law (**Equation 6-1**), reflections from experimental data do not appear as sharp lines at precise angles but as peaks that display broadening. This phenomenon is due to practical limitations on the sample and the incident light not usually being monochromatic.[47]

$$2\mathrm{dsin}\theta_B = \lambda$$

Equation 6-1

Figure 6-8 illustrates how the crystallite size affects the powder XRD scattering. An incident beam is focussed on a layered material comprising m layers. Consider the hypothetical situation where incident beam A is focused onto layer 0 of a multi-layered material at Bragg angle θ_B. Reflected beams B (from layer 0) and B' (from layer 1) can interfere constructively to produce a Bragg peak, only if the optical path difference (OPD) between B and B' is the wavelength, λ. Analogously, beam P focussed at Bragg angle $\theta_B \pm \delta\theta$ is also scattered, resulting in diffracted beam Q (form layer 0) and Q' (from layer 1). The OPD between beam Q and Q' is slightly bigger than λ, which we can define as $\lambda + \Delta$. Suppose $\Delta = \lambda/\mathrm{N}$ (N: integral), the OPD between Q and Q'' (from layer N) is λ, which means Q and Q'' can interfere to generate a Bragg peak at$\theta_B \pm \delta\theta$. Then we could deduce **Equation 6-2**, where t is the thickness along the direction perpendicular to the crystal plane (*hkl*). It is clear that the FWHM is inversely proportional to the thickness.

$$2\mathrm{Nd}\sin(\theta_B + \delta\theta) = (N+1)\lambda$$

$$\xRightarrow{when\ \delta\theta\ is\ very\ small} 2Nd(sin\theta_B + cos\theta_B \cdot \delta\theta) = (N+1)\,\lambda$$

$$\xRightarrow{2dsin\theta_B=\lambda} 2Ndcos\theta_B \cdot \delta\theta = \lambda$$

$$\therefore \mathrm{FWHM} = 2\delta\theta_{max} = \frac{\lambda}{N_{max}dcos\theta_B} = \frac{\lambda}{mdcos\theta_B} = \frac{\lambda}{tcos\theta_B}$$

Equation 6-2

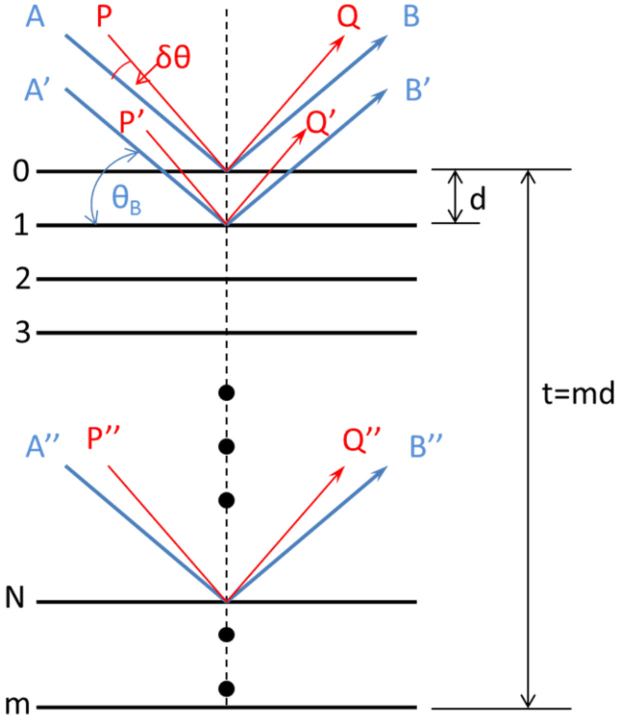

Figure 6-8: Schematic illustration of the effect of particle size on X-ray scattering.

Using DIFFaX simulation, we simplified the crystallite size effect on the powder XRD pattern to two parameters, the diameter in *a*, *b*-plane and the stacking layer number.

Figure 6-9 shows the simulated patterns for LDHs with defined crystallite width, but with the number of layers kept as infinite. It can be concluded that besides all the

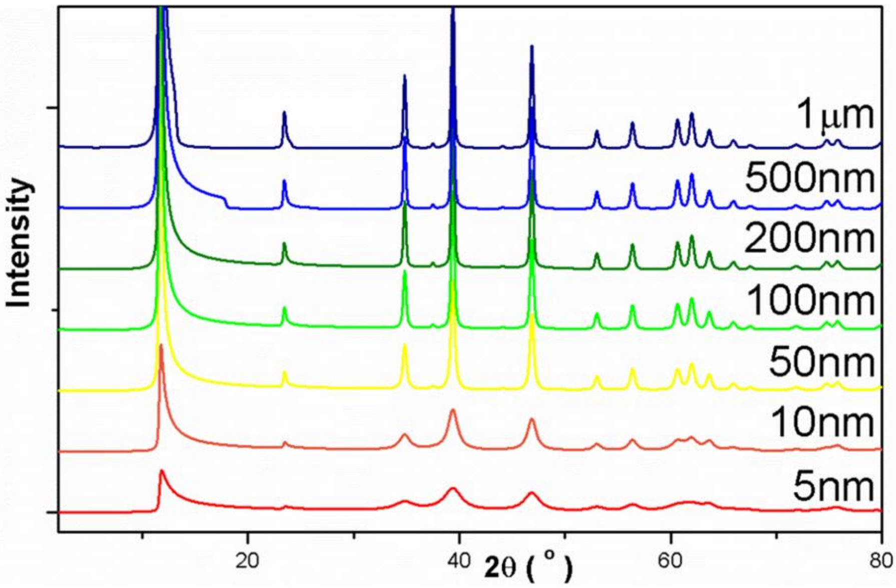

Figure 6-9: Simulated PXRD patterns of LDH particles with width from 5 nm to 1 μm.

reflections being broader and weaker, the width of the (003) reflection clearly increases as the diameter decreases. In addition, the (003) reflection becomes asymmetrical, which could be caused by a lack of long-range order.

Figure 6-10 and **Figure 6-11** illustrates the influence of the number of stacking layers on PXRD patterns, while keeping the width of the *a*, *b*-plane infinite. It is clear that all the peaks are broader and weaker when the number of stacking layers decreases. Several new peaks appear in the low angle region, which may be due to the lowered symmetry. The (002) reflection in the $2H_1$ sequence and the (003) reflection in the $3R_1$ sequence at 2θ = 11.64 °, both shift to lower angle when the stacking number is below 10. This is typical for nanoparticles when the number of repetitive units in crystal is too small to be considered as long-range order relative to the atomic size. A plot of the FWHM of (002) reflection in $2H_1$ sequence versus layer numbers are shown in **Figure 6-10** inset. It shows an exponential relationship between these two factors.

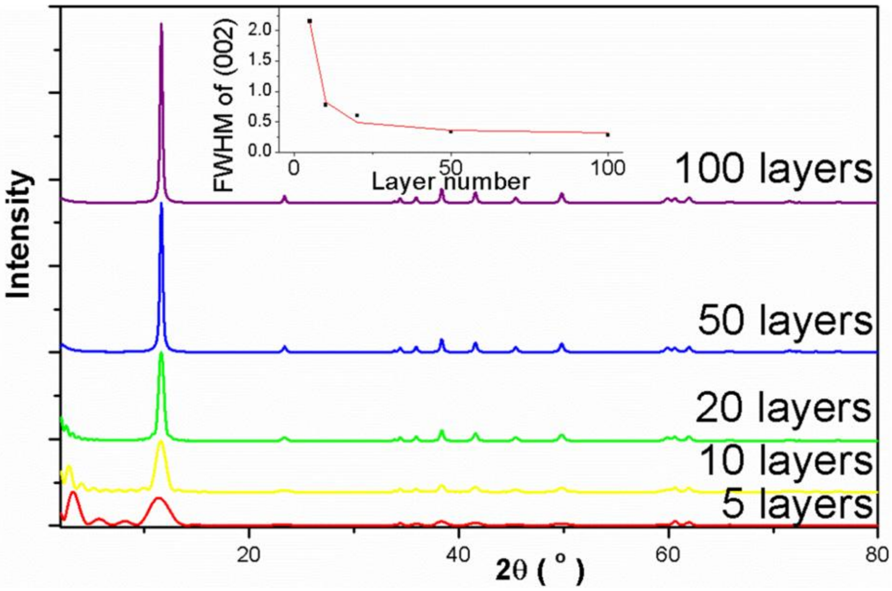

Figure 6-10: Simulated PXRD patterns of $2H_1$ LDH with layer number from 5 to 100. (Inset: FWHM of (002) reflection *vs*. the layer number. Solid curve is fitted to y = exp(a+b/(x+c)).)

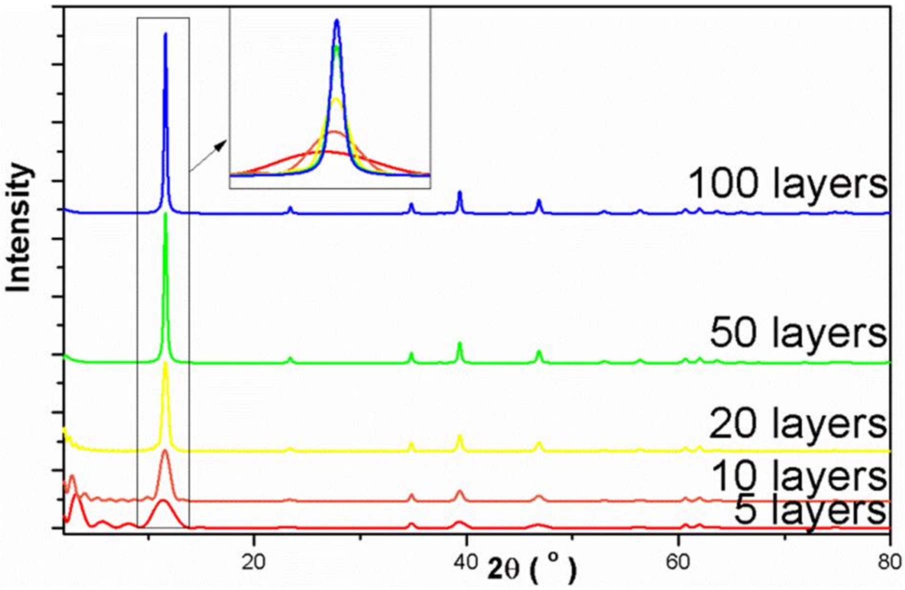

Figure 6-11: Simulated PXRD patterns of $3R_1$ LDH with layer number from 5 to 100. (Inset: zoom-in image of the lower angle region.)

6.3. Simulations of the XRD patterns of the samples described in Chapter 4

The samples in **Chapter 4**, **MgAl-OAm-*n*** (*n* = 1 - 3), are Mg-Al LDH nanoplatelets with intercalated Cl^- ions, water molecules and trace CO_3^{2-} ions (**Section**

4.2.2.). A standard model was constructed to simulate the XRD patterns of **MgAl-OAm-*n*** (*n* = 1 - 3). Mg^{2+} and Al^{3+} are considered randomly distributed in the hydroxide layers with an occupancy obtained from elemental analysis. CO_3^{2-} ions were ignored since their small amount has limited influence on the XRD patterns. Cl^- ions and H_2O molecules take up (x, y, 1/2) positions in 3R symmetry as calculated using GSAS.[48]

For the crystal with $3R_1$ sequence, a corresponding monoclinic cell (**Figure 6-12**) was defined by transforming the crystal axis using **Equation 6-3**. The coordinates of the atoms can be calculated using the inverse of matrix P's transpose, $(P^T)^{-1}$.

$$\begin{pmatrix} \overrightarrow{a_m} \\ \overrightarrow{b_m} \\ \overrightarrow{c_m} \end{pmatrix} = \begin{pmatrix} -2 & -1 & 0 \\ 0 & 1 & 0 \\ 2/3 & 1/3 & 1/3 \end{pmatrix} \begin{pmatrix} \overrightarrow{a_r} \\ \overrightarrow{b_r} \\ \overrightarrow{c_r} \end{pmatrix} = P \begin{pmatrix} \overrightarrow{a_r} \\ \overrightarrow{b_r} \\ \overrightarrow{c_r} \end{pmatrix}$$

$$\begin{pmatrix} x_m \\ y_m \\ z_m \end{pmatrix} = (P^T)^{-1} \begin{pmatrix} x_r \\ y_r \\ z_r \end{pmatrix} = \begin{pmatrix} -1/2 & 0 & 1 \\ -1/2 & 1 & 0 \\ 0 & 0 & 3 \end{pmatrix} \begin{pmatrix} x_r \\ y_r \\ z_r \end{pmatrix}$$

Equation 6-3

The cell with the $2H_1$ sequence was transformed to an orthorhombic cell with a

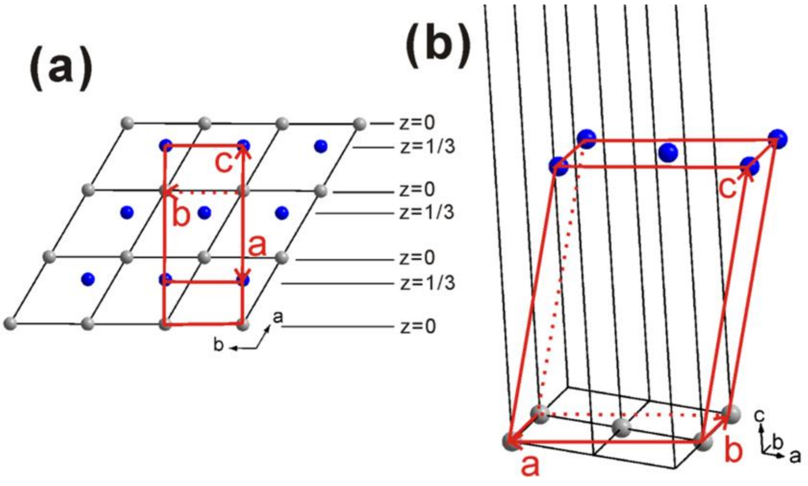

Figure 6-12: The monoclinic cell is transformed from the original rhombohedral cell.

similar a, b-plane to the $3R_1$ sequence by calculating $\overrightarrow{a_o} = 2\overrightarrow{a_h} + \overrightarrow{b_h}$ and $\overrightarrow{b_o} = \overrightarrow{b_h}$. The c-axis direction was left unchanged ($\overrightarrow{c_o} = \frac{2}{3}\overrightarrow{c_h}$) due to the $2H_1$ polytype containing two unique layers.

The unit cells for both $3R_1$ sequence and $2H_1$ sequence were filled up with Mg^{2+}, Al^{3+}, O^{2-} and Cl^{-} ions, which are shown in **Figure 6-13** and **Figure 6-14**. The coordinates of the atoms are given in **Table 6-2**.

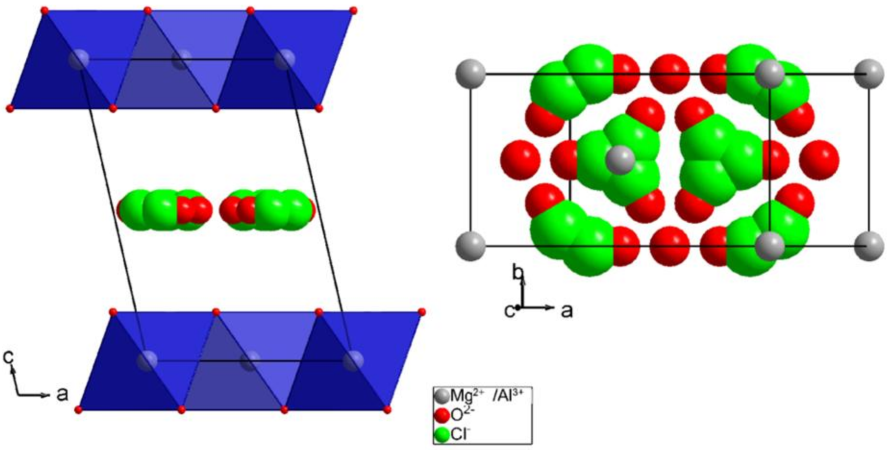

Figure 6-13: The monoclinic unit cell of Mg-Al LDH with $3R_1$ sequence. (left: view along the b-axis, right: view perpendicular to the a, b-plane.)

The background was subtracted from the original XRD patterns, which were then analysed using GSAS to obtain the accurate cell parameters and the atom positions. The refined values were then used for simulations in DIFFaX+. The transition vectors are (0, 0, 1).

Figure 6-15 shows the simulated XRD patterns of **MgAl-OAm-*n*** (n = 1 - 3). The estimated crystallite diameters of a, b-plane are 56.6, 51.8 and 127.3 nm for **MgAl-OAm-*n*** (n = 1 - 3), respectively. Although the values are slightly off the actual

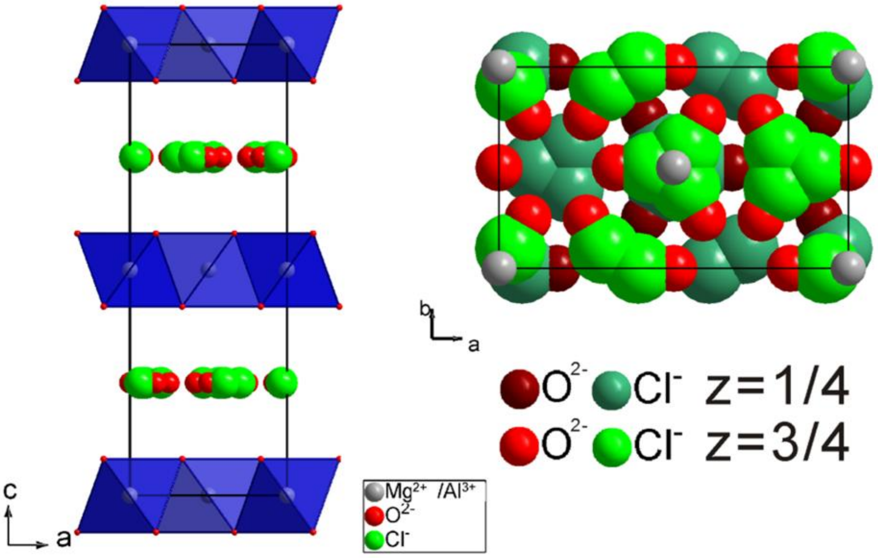

Figure 6-14: The orthorhombic unit cell of Mg-Al LDH with $2H_1$ sequence. (left: view along the *b*-axis, right: view along the *c*-axis.)

Table 6-2: Crystal information of the unit cells created for simulating XRD patterns.

$3R_1$	Crystal system		monoclinic	*a* =5.2875Å *b* =3.0453Å *c* =7.9349Å β = 102.8 °				
	Space group		C 1 2/m 1	composition		$Mg_{4/3}Al_{2/3}O_4Cl_{0.14}O_{1.04}$		
	Atoms		Site	*x/a*	*y/b*	*z/c*	B_{iso}	Occ.
	Al^{3+}	1	2/m	0	0	0	1.0	1/3
	Mg^{2+}	2	2/m	0	0	0	1.0	2/3
	O^{2-}	3	m	0.3874	0	0.1622	1.0	1
	O^{2-}	4	1	–1/12	1/4	1/2	1.0	0.087
	O^{2-}	5	m	–1/3	0	1/2	1.0	0.087
	Cl^-	6	m	–0.2681	1/2	1/2	1.0	0.012
	Cl^-	7	1	–0.1340	0.0979	1/2	1.0	0.012
$2H_1$	Crystal system		monoclinic	*a* =5.2875Å *b* =3.0453Å *c* =15.206Å β = 90 °				
	Space group		C 1 2/m 1	composition		$Mg_{8/3}Al_{4/3}O_8Cl_{0.28}O_{2.08}$		
	Atoms		Site	*x/a*	*y/b*	*z/c*	B_{iso}	Occ.
	Al^{3+}	1	2/m	0	0	0	1.0	1/3
	Al^{3+}	2	2/m	0	0	1/2	1.0	1/3
	Mg^{2+}	3	2/m	0	0	0	1.0	2/3
	Mg^{2+}	4	2/m	0	0	1/2	1.0	2/3
	O^{2-}	5	m	5/6	1/2	0.0811	1.0	1
	O^{2-}	6	m	5/6	1/2	0.4189	1.0	1
	O^{2-}	7	m	0	1/2	1/4	1.0	0.087
	O^{2-}	8	1	–1/12	1/4	1/4	1.0	0.087
	O^{2-}	9	m	–1/3	1/2	1/4	1.0	0.087
	O^{2-}	10	1	–1/4	1/4	1/4	1.0	0.087
	Cl^-	11	1	–0.0326	0.0979	1/4	1.0	0.012
	Cl^-	12	1	–0.3007	0.0979	1/4	1.0	0.012
	Cl^-	13	m	–0.3986	0	1/4	1.0	0.012
	Cl^-	14	m	–0.4347	1/2	1/4	1.0	0.012

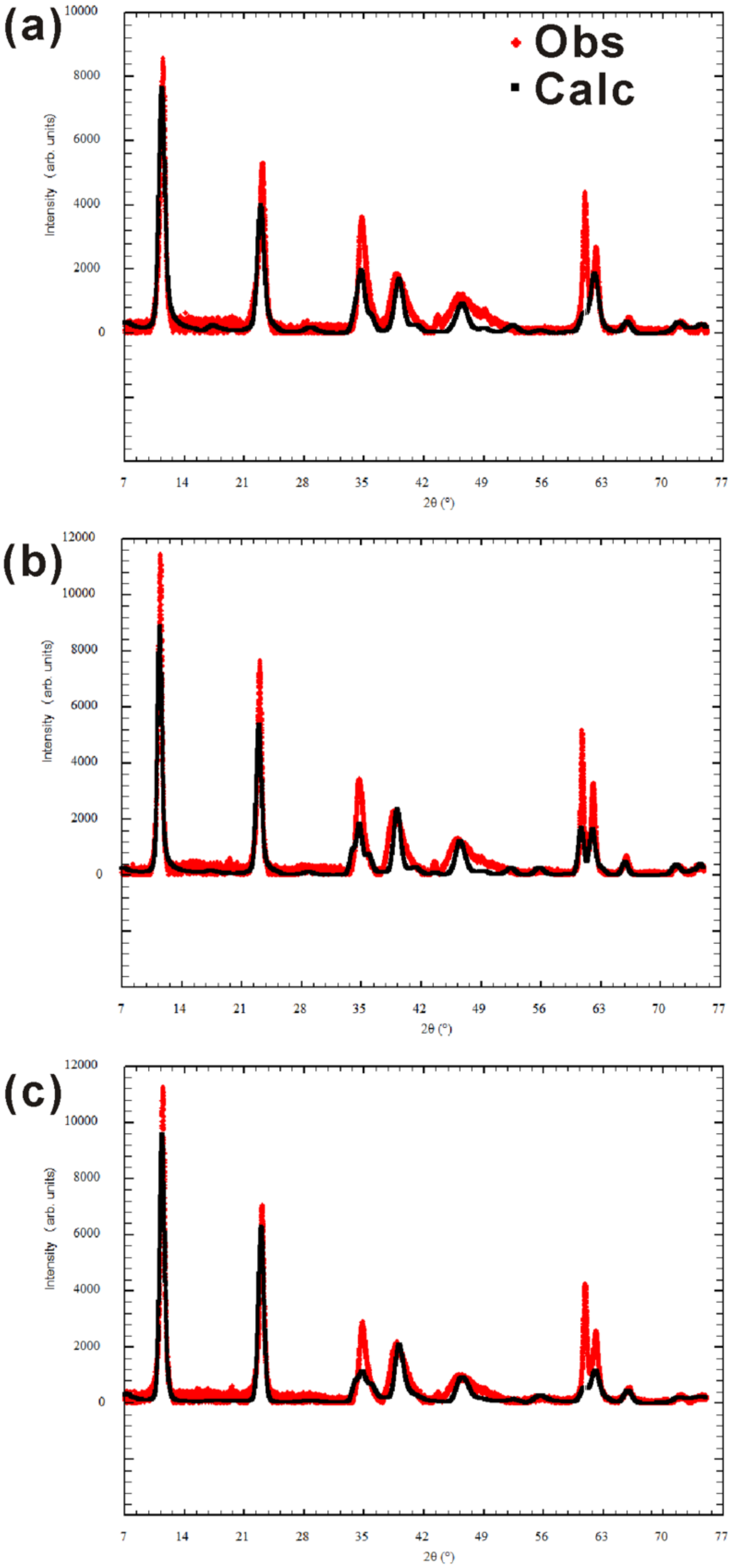

Figure 6-15: Simulated (black) and observed (red) XRD patterns of (a) **MgAl-OAm-1**, (b) **MgAl-OAm-2**, and (c) **MgAl-OAm-3**.

sizes obtained from the TEM images (**Section 4.2.5.**), they give a good estimate of the crystallite sizes. The crystal structures of **MgAl-OAm-*n*** (*n* = 1 - 3) are found to be based on $3R_1$ polytype incorporated with 11%, 6% and 19% of $2H_1$ stacking faults, respectively. The detailed results are listed in **APPENDIX III**.

6.4. Conclusion

In this chapter, factors that may influence powder XRD pattern, including stacking disorder, crystallite size and layer number were investigated using the DIFFaX program to compute the powder XRD patterns. A simulation of the real XRD patterns using DIFFaX+ provides an estimate of the size and disorder in the crystallite.

6.5. References

1. L. Pesic, S. Salipurovic, V. Markovic, D. Vucelic, W. Kagunya and W. Jones, *J. Mater. Chem.*, 1992, **2**, 1069-1073.
2. A. I. Khan and D. O'Hare, *J. Mater. Chem.*, 2002, **12**, 3191-3198.
3. P. S. Braterman, Z. P. Xu and F. Yarberry, in *Handbook of layered materials*, Marcel Dekker, New York, Editon edn., 2004, pp. 373-474.
4. R. Rothbauer, F. Zigan and H. O'Daniel, *Zeitschrift fuer Kristallographie, Kristallgeometrie, Kristallphysik, Kristallchemie*, 1967, **125**, 317-331.
5. H. D. Megaw, *Zeitschrift fuer Kristallographie, Kristallgeometrie, Kristallphysik, Kristallchemie*, 1934, **87**, 185-204.
6. A. V. Besserguenev, A. M. Fogg, R. J. Francis, S. J. Price, D. O'Hare, V. P. Isupov and B. P. Tolochko, *Chem. Mater.*, 1997, **9**, 241-247.
7. A. Fogg, A. Freij and G. Parkinson, *Chem. Mater.*, 2002, **14**, 232-234.
8. N. Gutmann and B. Müller, *J. Solid State Chem.*, 1996, **122**, 214-220.
9. P. J. Sideris, U. G. Nielsen, Z. Gan and C. P. Grey, *Science*, 2008, **321**, 113-117.
10. H. F. W. Taylor, *Mineralogical Magazine*, 1973, **39**, 377-389.
11. A. S. Bookin and V. A. Drits, *Clays Clay Miner.*, 1993, **41**, 551-557.
12. A. S. Bookin, V. I. Cherkashin and V. A. Drits, *Clays Clay Miner.*, 1993, **41**, 558-564.
13. A. Radha, P. Kamath and C. Shivakumara, *Acta Crystallogr. Sect. B: Struct. Sci.*, 2007, 243-250.
14. M. M. J. Treacy, M. W. Deem and J. M. Newsam, *DIFFaX v1.813*, NEC Research Institute, Princeton, New Jersey, 2010.
15. V. Todorova, A. Leineweber, L. Kienle, V. Duppel and M. Jansen, *J. Solid State Chem.*, 2011, **184**, 1112-1119.
16. R. T.N, *Inorg. Chem. Commun.*, 2009, **12**, 832-834.

17. S. Martin, C. Ullrich, D. Simek, U. Martin and D. Rafaja, *J. Appl. Crystallogr.*, 2011, **44**, 779-787.
18. Z. Lu and J. R. Dahn, *Chem. Mater.*, 2001, **13**, 2078-2083.
19. F. Kiefer, A. J. Karttunen, M. Döblinger and T. F. Fässler, *Chem. Mater.*, 2011, **23**, 4578-4586.
20. H. Gies, U. Müller, B. Yilmaz, T. Tatsumi, B. Xie, F.-S. Xiao, X. Bao, W. Zhang and D. D. Vos, *Chem. Mater.*, 2011, **23**, 2545-2554.
21. R. Gautier, N. Audebrand, E. Furet, R. g. Gautier and E. L. Fur, *Inorg. Chem.*, 2011, **50**, 4378-4383.
22. M. Casas-Cabanas, J. Rodríguez-Carvajal, J. Canales-Vázquez, Y. Laligant, P. Lacorre and M. R. Palacín, *J. Power Sources*, 2007, **174**, 414-420.
23. A. W. Burton, S. I. Zones, T. Rea and I. Y. Chan, *Microporous Mesoporous Mater.*, 2010, **132**, 54-59.
24. G. S. Thomas, M. Rajamathi and P. V. Kamath, *Clays Clay Miner.*, 2004, **52**, 693-699.
25. M. Bellotto, B. Rebours, O. Clause, D. Bazin and E. Elkaïm, *J. Phys. Chem.*, 1996, **100**, 8527-8534.
26. G. S. Thomas, A. V. Radha, P. V. Kamath and S. Kannan, *J. Phys. Chem. B*, 2006, **110**, 12365-12371.
27. G. S. Thomas, P. V. Kamath and S. Kannan, *J. Phys. Chem. C*, 2007, **111**, 18980-18984.
28. R. Thimmasandra Narayan, *J. Solid State Chem.*, 2010, **183**, 1433-1436.
29. T. N. Ramesh, C. Shivakumara and P. V. Kamath, *Acta Crystallogr. Sect. B*, 2006, **62**, 530-536.
30. T. N. Ramesh and P. V. Kamath, *Mater. Res. Bull.*, 2008, **43**, 2827-2832.
31. T. N. Ramesh and P. V. Kamath, *Mater. Res. Bull.*, 2008, **43**, 3227-3233.
32. M. Rajamathi, P. V. Kamath and R. Seshadri, *Mater. Res. Bull.*, 2000, **35**, 271-278.
33. A. V. Radha, P. Vishnu Kamath and G. N. Subbanna, *Mater. Res. Bull.*, 2003, **38**, 731-740.
34. A. V. Radha, C. Shivakumara and P. V. Kamath, *Clays Clay Miner.*, 2005, **53**, 520-527.
35. S. V. Prasanna, P. V. Kamath and C. Shivakumara, *Mater. Res. Bull.*, 2007, **42**, 1028-1039.
36. S. Britto, G. S. Thomas, P. V. Kamath and S. Kannan, *J. Phys. Chem. C*, 2008, **112**, 9510-9515.
37. M. Leoni, A. F. Gualtieri and N. Roveri, *J. Appl. Crystallogr.*, 2004, **37**, 166-173.
38. A. Arguelles, M. Leoni, J. A. Blanco and C. Marcos, *Z Kristallogr*, 2009, 429-434.
39. A. Arguelles, M. Leoni, J. A. Blanco and C. Marcos, *Am. Mineral.*, 2010, **95**, 126-134.
40. R. Gautier, N. Audebrand, E. Furet, R. Gautier and E. Le Fur, *Inorg. Chem.*, 2011, **50**, 4378-4383.
41. R. E. Johnsen and P. Norby, *J. Phys. Chem. C*, 2009, **113**, 19061-19066.
42. A. Leineweber and M. Leoni, *Z Kristallogr*, 2009, 423-428.
43. M. Leoni, A. F. Gualtieri and N. Roveri, *J. Appl. Crystallogr.*, 2004, **37**, 166-173.
44. R. Prasad and O. N. Srivastava, *J. Appl. Crystallogr.*, 1971, **4**, 516-521.
45. A. R. Verma and P. Krishna, *Polymorphism and polytypism in crystals*, Wiley, 1966.
46. B. E. Warren and P. Bodenstein, *Acta Crystallogr.*, 1966, **20**, 602-605.
47. Y. Qian, *An introduction to crystal chemistry*, USTC press, Hefei, 1999.

48. A. C. Larson and R. B. Von Dreele, *General Structure Analysis System (GSAS)*, Los Alamos National Laboratory Report LAUR 86-748, 2004.

Chapter 7 Conclusion

In the preceding chapters, LDH nanoparticles were synthesised under control using different directing templates. Rigid templates for simple intercalation reactions have the advantages of flexibility and morphology consistency. Soft templates are more applicable for particle size control, since they provide kinetic control on the crystal growth.

To obtain nanoparticles with desired morphology, a hard rod-like template is used. In **Chapter 2**, rod-like gibbsite nanoparticles were first synthesised. Upon further topotactic intercalation, lithium aluminium LDH nanorods were successfully synthesised. They kept the hexagonal prismatic morphology after the ions diffuse into the crystal.

Reverse micelles formed by surfactants are soft templates, which can offer good control on the particle size by spatially confining the crystal growth within the micelles. Reverse microemulsion systems were studied in **Chapter 3**, **Chapter 4** and **Chapter 5**. Traditional ternary systems were first extended to Co-Al and Ni-Al LDHs. Homogeneous co-precipitations within the micelles was carried out to enhance crystallinity and control particle size. LDH nanoplatelets with adjustable size ranging from 30 nm to 150 nm were obtained.

A novel single component microemulsion was developed based on the ternary microemulsion, in which amines perform multiple functions as oil phase, base and surfactant. To tune the pH of the systems, different amines were selected in order to provide a suitable environment with the correct pH for the precipitation of different LDHs. Oleylamine (OAm), dioctylamine (DOAm) and N,N-dimethyltetradecylamine (DMTDAm) were used, and the systems formed by them provide good size control on Mg-Al, Ni-Al, Li-Al and Co-Fe LDH nanoplatelets. In addition, Ca-Al LDHs synthesised in the OAm system exhibit a unique needle-like morphology, which suggests that the amines may have morphology modifying effect on the nanoparticles besides size control.

The properties of LDH nanoparticles vary when the morphology and particle size are changed. In **Chapter 2**, the Li-Al LDH nanorods retained the ability of ion-exchange, but exhibit preferential orientation effect in their XRD patterns. This is due to a rod-like sample adopting an orientation in which the cylinder axis is perpendicular to the diffraction plane.

In **Chapter 3** and **Chapter 5**, the magnetic properties of Co-Al, Ni-Al and Ni-Fe LDHs were studied, and were found to be size dependent. In Co-Al and Ni-Al LDHs, there is only one spin carrier and the interaction between the spins is ferromagnetic superexchange. The long range dipole-dipole interactions between layers enable the development of a 3D ordered state. The nanoparticles exhibit superparamagnetic behaviour since the nanoparticles contain only a single domain, which is quite different from the bulk sample. Ni-Fe LDHs display ferromagnetic interlayer and ferrimagnetic intralayer exchange. The interlayer carbonate ions may affect the magnetic properties by providing a more efficient magnetic exchange pathway. However, the nature of the magnetic interactions in these materials is not straightforward. It is thought to be a combination of spin glass behaviour and superparamagnetism.

A systematic study of the XRD patterns of LDH crystals with the stacking faults and disorder was described in **Chapter 6**. By simulating powder XRD patterns using the DIFFaX program, factors that may influence powder XRD pattern, including stacking disorder, crystallite size and layer number were investigated.

In conclusion, novel synthetic methods of LDHs were developed which enable precise control on morphology and particle size of LDH nanoparticles. The properties of these materials were studied, especially the size effect.

Chapter 8 Experiment Details

8.1. Analytical techniques

8.1.1. pH measurement

The pH values of the reverse microemulsions were measured by Hanna HI 83141 portable PH/mV/ ℃ meter.

8.1.2. X-Ray diffraction (XRD)

Powder X-ray diffraction (XRD) patterns were recorded on a PANalytical X'Pert Pro instrument in reflection mode with Cu Kα radiation. The accelerating voltage was set at 40 kV with 40 mA current. If the amount of the sample is insufficient to fill the sample holder, Bragg reflections due to the sample holder are observed at *ca.* $2\theta = 43.4°$ and 50.4 °((111) and (200) reflections for Ni, JCPDS PDF 00-001-1258).

The calculations of particle size were carried out using Scherrer equation (**Equation 8-1**). The instrumental broadening was determined by a standard pattern of calcined Al_2O_3 (**Figure 8-1**) recorded under the same conditions and program. The FWHM values of the peaks in the standard pattern at 25.62 °, 35.20 ° and 57.54 ° are 0.203 °, 0.226 ° and 0.285 °.

$$\mathrm{t} = \frac{0.89\lambda}{cos\theta\sqrt{B_{obs}^2 - B_{std}^2}}$$

Equation 8-1

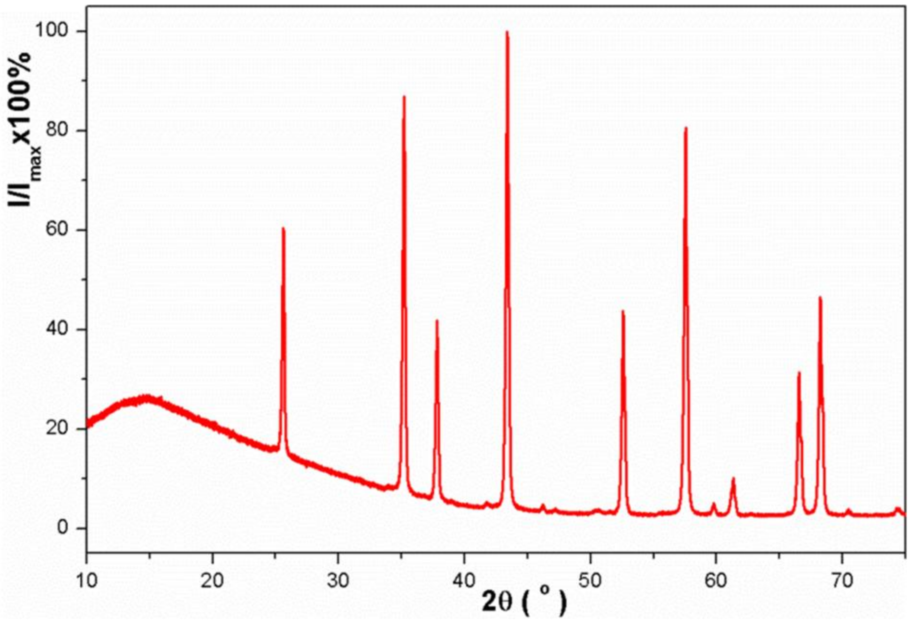

Figure 8-1: XRD pattern of calcined Al_2O_3 used as the standard pattern for particle size calculation.

8.1.3. Elemental analysis

Metals were analysed using inductively coupled plasma optical emission spectroscopy (ICP-OES) at the Chemistry Department, University of Manchester and the School of Human Sciences, London Metropolitan University. C and H contents were determined using the quantitative combustion technique at the School of Human Sciences, London Metropolitan University.

8.1.4. Fourier-transform infrared spectroscopy (FT-IR)

All the IR spectra were recorded on a Bio-Rad FTS 6000 FTIR Spectrometer equipped with a DuraSamplIR II diamond accessory in attenuated total reflectance (ATR) mode in the range of 400 - 4000 cm^{-1}; 100 scans at 4 cm^{-1} resolution were collected. The strong absorbance in the range 2500 - 1667 cm^{-1} is from the DuraSamplIR II diamond surface.

8.1.5. UV-Vis spectroscopy

All the UV-Vis diffuse reflectance spectra were performed on a Lambda 750S UV-Vis spectrometer between 8000 and 25000 cm^{-1}. The samples were first compressed into pellets with KBr.

8.1.6. Transmission electron microscopy (TEM)

Nanoplatelet TEM samples were dispersed in ethanol with sonication and then cast onto lacey carbon film. TEM was performed on JEOL 4000HR microscope with an accelerating voltage of 400 kV, or JEOL 2000/JEOL2100 microscope with an accelerating voltage of 200 kV.

8.1.7. Scanning electron microscopy (SEM)

Sample was spread on carbon tape adhered to an SEM stage and coated with Pt using sputter deposition. SEM was performed on a JEOL JSM-840A scanning microscope with an accelerating voltage of 20 kV.

8.1.8. Atomic force microscopy (AFM)

Approximately 15 mg of sample was suspended in 200 ml ethanol with sonication and deposited onto freshly cleaved highly oriented pyrolytic graphite (HOPG, 10 × 10 × 2 mm, Agar) by spin-coating (1000 rpm, 30 s). AFM imaging was performed in tapping made using a Nanoscope Multimode system (Digital Instruments, Santa Barbara, USA) with a Nanoscope IIIa controller and a “J” scanner having a lateral range of approximately 100 μm and a vertical range of 6 μm. The imaging was completed at room temperature and 30 - 50% relative humidity, with a silicon tip NST-NCHFR (Nascatec GmbH). Calibration of the AFM was accomplished by scanning a 10 μm pitch 200 nm 3D reference from Digital instruments.

8.1.9. Dynamic light scattering measurements

Dynamic light scattering measurements were performed on a Malvern Zetasizer Nano ZS instrument. 1 - 2 mg of powder samples were suspended in ethanol or methanol with sonication.

8.1.10. Magnetic measurements

Solid state magnetic measurements were performed on a Quantum Design MPSM-5 SQUID magnetometer. Powered samples of *ca.* 40 mg mass were weighed accurately and loaded into gelatine capsules. The DC data were collected with an applied field of 1000 Oe (0.1 T) between 2 K and 300K. The field dependence of the magnetism was determined as a function of field between –5 and 5 T at different temperatures from 2 K and 300 K. The AC data were collected with an applied alternating field of 5 Oe (5×10^{-3} T) at different frequencies from 1 Hz to 1000 Hz.

8.2. Experimental details for Chapter 2

8.2.1. Synthesis of Gibbsite precursor

The gibbsite nanorods precursor **(pre-Gibbsite)** was prepared following the previously reported synthesis by Y. Liu *et al.*[1] Typically, $AlCl_3 \cdot 6H_2O$ 1.207 g (Aldrich, 99%) and NaOH 0.8 g (Fisher Scientific, 98.69%) were dissolved in 18 ml deionized water to form a transparent $NaAlO_2$ solution (solution A). 1.565 g of cetyl trimethylammonium bromide (CTAB; Sigma-Aldrich, ≥ 99%) was dissolved in 18 ml ethanol under 30 ℃ to form solution B. Then solution B was added dropwise into solution A under magnetic stirring. After further stirring for 1 hour, the mixture was transferred into a 40 ml Teflon lined stainless autoclave and kept under 120 ℃ for 12 hours. The solid product was collected by centrifugation, washed three times with distilled water and ethanol and dried in air.

8.2.2. Synthesis of LiAl-X-rod LDH (X= Cl^-, Br^-, NO_3^-)

About 0.2 g as-prepared **pre-Gibbsite** sample were dispersed in saturated solutions of LiX (X=Cl, Br, NO_3; LiCl: Aldrich, 98%; LiBr: Aldrich, 99%+; $LiNO_3$: Aldrich, 99.99%) under N_2 gas protection. After stirring for half hour, the mixture was transferred into a 30 ml Teflon lined stainless autoclave and kept for 15 hours under 120 ℃. The products were collected by centrifugation, washed three times with distilled water and ethanol and dried in air.

8.2.3. Ion-exchange of LiAl-Cl-rod LDH

LiAl-Cyclamate was synthesised following the method similar to that reported by Markland *et al.*[2] Approximately 0.2 g of the **LiAl-Cl-rod** LDH was added to an aqueous solution (15 ml) containing 5 g sodium cyclamate (99%, Fluka). The solution was stirred vigorously at 80 ℃ for 16 h, then the product was collected by centrifugation, washed three times with distilled water and ethanol and dried in air.

8.2.4. Synthesis of standard LiAl-LDH

LiAl-Cl-std LDH was synthesised using the conventional method described by A. V. Besserguenev.[3] 1 g gibbsite was dispersed in a 100 ml aqueous solution containing a 4-fold molar excess of lithium salts (LiCl, LiBr or $LiNO_3$). The suspensions were kept with vigorous stirring at 90 ℃ for 6 h.

8.3. Experimental details for Chapter 3

8.3.1. Synthesis of CoAl-RM*n* (*n* = 1 - 3)

Different particle sized **CoAl-RM*n*** (*n* = 1 - 3) samples were prepared using three types of reverse microemulsion systems, with water contents ω = 12, 24 and 48 respectively. To prepare these reverse microemulsion systems, sodium dodecyl sulphate (2.88 g for **CoAl-RM1**, 1.44 g for **CoAl-RM2**, 0.72 g for **CoAl-RM3**; Sigma-Aldrich, approx. 95%), isooctane (100 ml; Sigma-Aldrich, ≥ 99%) and deionized water (2.2 ml) were mixed in a flask with magnetic stirring, and 1-butanol (*appx.* 3 ml; Sigma-Aldrich, 99.4%) was added dropwise until the reverse microemulsions were stable and transparent. $CoCl_2 \cdot 6H_2O$ (0.628 g; Sigma-Aldrich, 99%) and $AlCl_3 \cdot 6H_2O$ (0.319 g; BDH, 99%) were then added into the microemulsion and stirred until everything had dissolved. Finally, urea (0.555 g; Fluka, ≥ 90%) was added into the mixture and the reaction solution heated at 90 ℃ for 4 days with refluxing and magnetic stirring. A pink precipitate formed which was collected by filtration, washed with distilled water and acetone, and air dried at room temperature.

8.3.2. Conventional synthesis of CoAl-Bulk

A conventional **CoAl-Bulk** LDH was prepared as reported by Liu *et al.*[4] $CoCl_2$ $6H_2O$, $AlCl_3$ $6H_2O$ and urea were added into 1 L deionized water to give a final concentrations of 10, 5, and 35 mM, respectively. The mixture was refluxed at 97 ℃ for 2 days. The solid product, $Co_2Al(OH)_6(CO_3)_{0.5}$ yH_2O, was washed by three times with water and then collected by filtration. 1 g of this product was dispersed in 1 L water with 1 M NaCl and 3.3 mM HCl under a flow of N_2 gas to give $Co_2Al(OH)_6Cl$ yH_2O. The as-prepared $Co_2Al(OH)_6Cl$ and sodium dodecyl sulphate were dispersed in deionized water with concentrations of 3 and 50 mM and refluxed for 12 hours to form $Co_{1.89}Al(OH)_6(DDS)_{0.8}\cdot 4.3H_2O$.

8.3.3. Synthesis of NiAl-RM*n* (*n* = 1 - 3)

NiAl- RM*n* (*n* = 1 -3) samples were prepared in identical microemulsion systems as **CoAl-RM*n*** (*n* = 1 -3) with water to surfactant ratio of ω = 12, 24 and 48, respectively. The synthesis processes were similar as well. Sodium dodecyl sulphate (2.88 g for NiAl-RM1, 1.44 g for NiAl-RM2, 0.72 g for NiAl-RM3; Sigma-Aldrich, *approx.* 95%), isooctane (100 ml; Sigma-Aldrich, ≥ 99%) and deionized water (2.2 ml) were mixed in a flask with magnetic stirring, and 1-butanol (*approx.* 3 ml; Sigma-Aldrich, 99.4 %) was added dropwise until the reverse microemulsions were stable and transparent. $Ni(NO_3)_2\cdot 6H_2O$ (1.535 g; AnalaR, 98%) and $Al(NO_3)_3\cdot 9H_2O$ (0.99 g; Fluka, 98%) were then added into the microemulsion and stirred until no solids left. Finally, hexamethylenetetramine (HMT; 2.5 g; Riedel-de Haën, ≥ 99%) was added into the mixture and the reaction solution heated at 90 °C for 4 days with refluxing and magnetic stirring. A green precipitate formed which was collected by filtration, washed with distilled water and acetone, and air dried at 80 °C.

8.4. Experimental details for Chapter 4

8.4.1. Synthesis of MgAl-OAm-*n* (*n* = 1 - 3)

MgAl-OAm-*n* (*n* = 1 - 3) nanoplatelets were prepared in single component microemulsions. A typical synthesis process is as follows: Solution A was prepared by dissolving $MgCl_2\cdot 6H_2O$ (Sigma-Aldrich, 99%) and $AlCl_3\cdot 6H_2O$ (BDH, 99%) in deionized water with the concentrations of 1.5 M and 0.75 M for Mg^{2+} and Al^{3+} ions respectively. Oleylamine (Sigma-Aldrich, 70%) and assistant surfactant 1-butanol (5 ml; Sigma-Aldrich, 99.4 %) were mixed under magnetic stirring with N_2 purging. Then, solution A was added dropwise. The total volume of solution A and oleylamine was kept 10 ml, while the volume ratio of oleylamine/solution A was controlled as 9 for **MgAl-OAm-1**, 4 for **MgAl-OAm-2**, and 1 for **MgAl-OAm-3**. After further stirring for 10 minutes, the mixture was heated at 120 ℃ for 24 hours in a Teflon lined stainless steel autoclave. The products were collected by centrifugation, washed three times with H_2O : EtOH = 1 : 1, and dried at 80 ℃.

8.4.2. Synthesis of MgAl-OAm-1-*n*h (*n* = 1, 3, and 5)

MgAl-OAm-1-*n*h (*n* = 1, 3, and 5) was prepare using the same chemicals and stoichiometric ratio, but was kept heating for 1, 3, and 5 hours respectively. The samples were collected by centrifugation, washed, dried, and named as **MgAl-OAm-1-1h**, **MgAl-OAm-1-3h**, and **MgAl-OAm-1-5h**.

8.5. Experimental details for Chapter 5

8.5.1. Synthesis of CoAl-OAm-*n* and CoAl-DMTDAm-*n* (*n* = 1 - 3)

CoAl-OAm-*n* (*n* = 1 - 3) nanoplatelets were prepared in single component microemulsions. A typical synthesis process is as follows: Solution A was prepared by dissolving $CoCl_2\ 6H_2O$ (Sigma-Aldrich, 99%) and $AlCl_3\ 6H_2O$ (BDH, 99%) in deionized water with the concentrations of 1.5 M and 0.75 M for Co^{2+} and Al^{3+} ions respectively. Oleylamine (Sigma-Aldrich, 70%) and assistant surfactant 1-butanol (5 ml; Sigma-Aldrich, 99.4 %) were mixed under magnetic stirring with N_2 purging. Then, solution A was added dropwise. The total volume of solution A and oleylamine was kept

10 ml, while the volume ratio of oleylamine/solution A was controlled as 9 for **CoAl-OAm-1**, 4 for **CoAl-OAm-2**, and 1 for **CoAl-OAm-3**. After further stirring for 10 minutes, the mixture was heated at 120 ℃ for 24 hours in a Teflon lined stainless steel autoclave. The products were collected by centrifugation, washed three times with H_2O : EtOH = 1 : 1, and dried at 80 ℃.

CoAl-DMTDAm-*n* (*n* = 1 - 3) nanoplatelets were prepared in the same process with N,N-dimethyltetradecylamine (Sigma-Aldrich, 98%) substituting oleylamine.

8.5.2. Synthesis of NiAl-OAm-*n* and NiAl-DMTDAm-*n* (*n* = 1 - 3)

NiAl-OAm-*n* (*n* = 1 - 3) nanoplatelets were prepared in single component microemulsions. A typical synthesis process is as follows: Solution B was prepared by dissolving $NiCl_2$ $6H_2O$ (Sigma-Aldrich, 99%) and $AlCl_3$ $6H_2O$ (BDH, 99%) in deionized water with the concentrations of 1.5 M and 0.75 M for Ni^{2+} and Al^{3+} ions respectively. Oleylamine (Sigma-Aldrich, 70%) and assistant surfactant 1-butanol (5 ml; Sigma-Aldrich, 99.4 %) were mixed under magnetic stirring with N_2 purging. Then, solution A was added dropwise. The total volume of solution B and oleylamine was kept 10 ml, while the volume ratio of oleylamine/solution B was controlled as 9 for **NiAl-OAm-1**, 4 for **NiAl-OAm-2**, and 1 for **NiAl-OAm-3**. After further stirring for 10 minutes, the mixture was heated at 120 ℃ for 24 hours in a Teflon lined stainless steel autoclave. The products were collected by centrifugation, washed three times with H_2O : EtOH = 1 : 1, and dried at 80 ℃.

NiAl-DMTDAm-*n* (*n* = 1 - 3) nanoplatelets were prepared in the same process with N,N-dimethyltetradecylamine (Sigma-Aldrich, 98%) substituting oleylamine.

8.5.3. Synthesis of ZnAl-DMTDAm-*n* (*n* = 1 - 3)

ZnAl-DMTDAm-*n* (*n* = 1 - 3) nanoplatelets were prepared in single component microemulsions. A typical synthesis process is as follows: Solution C was prepared by dissolving $ZnCl_2$ (Sigma-Aldrich, ≥98%) and $AlCl_3$ $6H_2O$ (BDH, 99%) in deionized water with the concentrations of 1.5 M and 0.75 M for Zn^{2+} and Al^{3+} ions respectively. N,N-dimethyltetradecylamine (Sigma-Aldrich, 98%) and assistant surfactant 1-butanol (5 ml; Sigma-Aldrich, 99.4 %) were mixed under magnetic stirring with N_2 purging. Then, solution A was added dropwise. The total volume of solution C and oleylamine was kept 10 ml, while the volume ratio of oleylamine/solution C was controlled as 9 for **ZnAl-DMTDAm-1**, 4 for **ZnAl-DMTDAm-2**, and 1 for **ZnAl-DMTDAm-3**. After further stirring for 10 minutes, the mixture was heated at 60 ℃ for 24 hours in a Teflon lined stainless steel autoclave. The products were collected by centrifugation, washed three times with H_2O : EtOH = 1 : 1, and dried at 60 ℃.

8.5.4. Synthesis of LiAl-DMTDAm-*n* (*n* = 1 - 3)

LiAl-DMTDAm-*n* (*n* = 1 - 3) nanoplatelets were prepared in single component microemulsions. A typical synthesis process is as follows: Solution D was prepared by dissolving LiCl (Sigma-Aldrich, ≥99%) and $AlCl_3$ $6H_2O$ (BDH, 99%) in deionized water with the concentrations of 1.5 M and 0.75 M for Li^+ and Al^{3+} ions respectively. N,N-dimethyltetradecylamine (Sigma-Aldrich, 98%) and assistant surfactant 1-butanol (5 ml; Sigma-Aldrich, 99.4 %) were mixed under magnetic stirring with N_2 purging. Then, solution A was added dropwise. The total volume of solution D and oleylamine was kept 10 ml, while the volume ratio of oleylamine/solution D was controlled as 9 for **LiAl-DMTDAm-1**, 4 for **LiAl-DMTDAm-2**, and 1 for **LiAl-DMTDAm-3**. After further stirring for 10 minutes, the mixture was heated at 120 ℃ for 24 hours in a Teflon lined stainless steel autoclave. The products were collected by centrifugation, washed three times with H_2O : EtOH = 1 : 1, and dried at 80 ℃.

8.5.5. Synthesis of CaAl-DOAm-*n*, CaAl-OAm-*n* and CaAl-DOAm-OAm-*n* (*n* = 1 - 3)

CaAl-OAm-*n* (*n* = 1 - 3) nanoplatelets were prepared in single component microemulsions. A typical synthesis process is as follows: Solution E was prepared by dissolving $CaCl_2$ (Sigma-Aldrich, ≥93%) and $AlCl_3 \cdot 6H_2O$ (BDH, 99%) in deionized water with the concentrations of 1.5 M and 0.75 M for Ca^{2+} and Al^{3+} ions respectively. N,N-dimethyltetradecylamine (Sigma-Aldrich, 98%) and assistant surfactant 1-butanol (5 ml; Sigma-Aldrich, 99.4 %) were mixed under magnetic stirring with N_2 purging. Then, solution A was added dropwise. The total volume of solution E and oleylamine was kept 10 ml, while the volume ratio of oleylamine/solution E was controlled as 9 for **CaAl-OAm-1**, 4 for **CaAl-OAm-2**, and 1 for **CaAl-OAm-3**. After further stirring for 10 minutes, the mixture was heated at 120 ℃ for 24 hours in a Teflon lined stainless steel autoclave. The products were collected by centrifugation, washed three times with H_2O : EtOH = 1 : 1, and dried at 80 ℃.

CaAl-DOAm-*n* (*n* = 1 - 3) nanoplatelets were prepared in the same process with dioctylamine (Sigma-Aldrich, ≥ 95%) substituting oleylamine.

CaAl-DOAm-OAm-*n* (*n* = 1 - 3) nanoplatelets were prepared in the same process with a mixture of equal DOAm and OAm substituting oleylamine.

8.5.6. Synthesis of NiFe-DMTDAm-*n* (*n* = 1 - 3)

NiFe-DMTDAm-*n* (*n* = 1 - 3) nanoplatelets were prepared in single component microemulsions. A typical synthesis process is as follows: Solution F was prepared by dissolving $NiCl_2 \cdot 6H_2O$ (BDH, 97%) and $FeCl_3$ (BDH, 98%) in deionized water with the concentrations of 1.5 M and 0.75 M for Ni^{2+} and Fe^{3+} ions respectively. N,N-dimethyltetradecylamine (Sigma-Aldrich, 98%) and assistant surfactant 1-butanol (5 ml; Sigma-Aldrich, 99.4 %) were mixed under magnetic stirring with N_2 purging. Then, solution A was added dropwise. The total volume of solution F and oleylamine was kept 10ml, while the volume ratio of oleylamine/solution F was controlled as 9 for **NiFe-DMTDAm-1**, 4 for **NiFe-DMTDAm-2**, and 1 for **NiFe-DMTDAm-3**. After further stirring for 10 minutes, the mixture was heated at 120 ℃ for 24 hours in a Teflon lined stainless steel autoclave. The products were collected by centrifugation, washed three times with H_2O : EtOH = 1 : 1, and dried at 80 ℃.

8.6. Reference

1. Y. Liu, D. Ma, R. A. Blackley, W. Z. Zhou, X. W. Han and X. H. Bao, *J. Phys. Chem. C*, 2008, **112**, 4124-4128.
2. C. Markland, G. R. Williams and D. O'Hare, *J. Mater. Chem.*, 2011, **21**, 17896-17903.
3. A. V. Besserguenev, A. M. Fogg, R. J. Francis, S. J. Price, D. O'Hare, V. P. Isupov and B. P. Tolochko, *Chem. Mater.*, 1997, **9**, 241-247.
4. Z. Liu, R. Ma, M. Osada, N. Iyi, Y. Ebina, K. Takada and T. Sasaki, *J. Am. Chem. Soc.*, 2006, **128**, 4872-4880.

Appendix I

Refinement against XRD data using GSAS in Chapter 2

Table I-1: Summary of the Crystallographic Data for **LiAl-Cl-rod**, **LiAl-Cl-std** and **LiAl-Br-rod**.

	LiAl-Cl-rod	**LiAl-Cl-std**	**LiAl-Br-rod**
emprical formula	$LiAl_2(OH)_6Cl$	$LiAl_2(OH)_6Cl \cdot H_2O$	$LiAl_2(OH)_6Br$
cystal system	hexagonal	hexagonal	hexagonal
a, Å	5.0877(5)	5.0578(9)	5.0992(8)
c, Å	15.3178(9)	15.2992(7)	15.2092(4)
V, Å^3	343.3848(3)	339.9534(8)	342.4962(8)
space group	P $6_3/mcm$	P $6_3/m$	P$6_3/mcm$
laue group	$6/mmm$	$6/m$	$6/mmm$
radiation	X ray, Cu α	X ray, Cu α	X ray, Cu α
λ, Å	1.5405(7)	1.5405(9)	1.5405(9)
zero point	–41.9389(0)	–1.7127(9)	–36.2596(0)
scale	9.0694	687.66	29.180
MD Preferential Orientation,R_0	4.0267(8)	1.1078(6)	1.6864(1)
χ^2	1.389	5.933	4.283
R_{wp}, %	20.49	10.88	3.32
R_p, %	15.54	7.65	2.07

Table I-2: Fractional Atomic Coordinates and Occupancies for **LiAl-Cl-rod**.

atoms	oxidation	x	y	z	Occupacy	Uiso
Al	+3	1/3	2/3	0	0.709477	0.060337
O	–2	0.659781	0.659781	0.532444	0.895847	0.087212
Li	+1	0	0	0	1.012601	0.206381
Cl	–1	0	0	1/4	1.763638	0.575068

Table I-3: Other refined parameters for **LiAl-Cl-rod**.

Background fitting parameters	6	0.337550E+02 0.657415E+01	–0.160948E+02 0.165421E+01	0.175637E+02 0.139851E+01	
GU	0.203920E+03	GV	–0.123240E+02	GW	–0.205323E+01
LX	0.481762E+01	LY	0.366828E+01	Asym	–0.321497E+00
GP	0.186852E+00	stec	0.270316E+01	ptec	0.385335E+01
sfec	0.000000E+00				
L11	0.227487E–02	L22	0.568591E+00	L33	0.528481E–04
L12	–0.305231E+00	L13	0.162888E+00	L23	–0.976458E–01

Table I-4: Fractional Atomic Coordinates and Occupancies for **LiAl-Cl-std**.

atoms	oxidation	x	y	z	occupacy	U_{iso}
Al	+3	1/3	2/3	–0.009987	0.490443	0.033378
O1	–2	0.660794	0.650406	0.558807	0.881471	0.173531
Li	+1	0	0	0	0.683691	–0.089372
Cl1	–1	–0.017538	0.370323	1/4	0.085096	0.081692
Cl2	–1	0.146271	0.592686	1/4	0.037626	–0.052140
Cl3	–1	0.842604	0.301850	1/4	0.068423	0.142130
Cl4	–1	0.255065	0.300178	1/4	0.080315	0.090465
Cl5	–1	0.139439	0.092866	1/4	0.023180	0.511128
O2	–2	0.620317	0.199991	1/4	0.076300	0.029601
O3	–2	0.287908	0.436440	1/4	0.077863	–0.053159
O4	–2	0.628960	0.221917	1/4	–0.023128	0.731724
O5	–2	0.055029	0.070533	1/4	0.054343	–0.037601
O6	–2	–0.027068	–0.480782	1/4	0.058103	–0.060433

Table I-5: Other refined parameters for **LiAl-Cl-std**.

Background fitting parameters	6	0.443864E+03 –0.631500E+02	–0.451418E+03 0.229782E+02	0.160505E+03 –0.271883E+02	
GU	0.365085E+03	GV	–0.457599E+02	GW	0.282703E+01
LX	0.372305E+01	LY	0.144214E+02	Asym	0.327290E+01
GP	0.000000E+00	stec	0.228784E+02	ptec	–0.159885E+01
sfec	0.000000E+00				
L11	0.220237E+01	L22	0.586278E–01	L33	0.591971E–04
L12	–0.121225E+01	L13	–0.225862E+00	L23	0.416851E+00

Table I-6: Fractional Atomic Coordinates and Occupancies for **LiAl-Br-rod**.

atoms	oxidation	x	y	z	Occupacy	Uiso
Al	+3	1/3	2/3	0	1.146017	0.093546
O	–2	0.620606	0.620606	0.521268	0.537766	0.071873
Li	+1	0	0	0	0.504038	0.140422
Br	–1	0	0	1/4	0.435581	0.022085

Table I-7: Other refined parameters for **LiAl-Br-std**.

GU	0.000000E+00	GV	0.000000E+00	GW	0.812566E+02
GP	0.000000E+00	LX	0.000000E+00	ptec	0.000000E+00
trns	0.636480E+00	shift	0.474910E+00	sfec	0.000000E+00

Appendix II

Input data file for simulating PXRD patterns using DIFFaX

Data File II-1: Standard input data file for DIFFaX.[1]

{user input data file -- in Backus-Naur form}
{comments are in curly braces, blank lines are allowed}
{The pipe symbol | implies that one of a series of arguments must be chosen}
{arguments in parentheses () are optional}
{Header for radiation data}
INSTRUMENTAL
{radiation type}
X-RAY | NEUTRON | ELECTRON
{wavelength in Å }
λ
{Instrumental broadening type}
NONE
| GAUSSIAN␣half-width | u␣ v␣w␣(TRIM)
| LORENTZIAN␣half-width | u␣v␣w␣(TRIM)
| PSEUDO-VOIGT␣u␣v␣w␣¾␣(TRIM)
{Header for structure data}
STRUCTURAL
{cell dimensions, in Å and °}
a␣b␣c␣γ
{diffraction point group symmetry}
–1 | 2/M(1) | 2/M(2) | MMM | –3 | –3M | 4/M | 4/MMM | 6/M | 6/MMM | AXIAL | UNKNOWN (% tolerance)
{total number of layer types}
n
{in-plane layer widths in Å (optional)}
('width along *a*'␣'width along b') | ('average diameter') | (INFINITE)
{New layer definition}
LAYER␣1
{Layer structure symmetry}
NONE | CENTROSYMMETRIC
{Atom data record}
name␣#␣x_{rel}␣y_{rel}␣z_{rel}␣'isotropic Debye-Waller factor B_{iso}' ␣occupancy
…
{New layer definition}
LAYER␣number | LAYER␣number='a previous layer number'
{If this is not equivalent to a prior layer, then enter ...}
{Layer structure symmetry}

NONE | CENTROSYMMETRIC
{Atom data record}
name␣#␣x_{rel}␣y_{rel}␣z_{rel}␣'isotropic Debye-Waller factor Biso' ␣occupancy
…
{Header for stacking description}
STACKING
{How to treat layer sequencing}
EXPLICIT | RECURSIVE
{If EXPLICIT}
{either, an explicit sequence}
lay#␣lay#␣lay#␣lay#␣lay#␣lay#␣lay#␣lay#␣lay#␣lay#␣lay#␣lay#␣lay#␣lay#␣lay#␣lay#...
{or, generate sequence}
RANDOM 'number of layers in crystal'
{If RECURSIVE}
{number of layers in crystal}
'number of layers' | INFINITE
{Header for stacking parameters}
TRANSITIONS
{stacking probability, stacking vector (optional anisotropic stacking uncertainty factor)}
α_{11}␣R^{x}_{11}␣R^{y}_{11}␣R^{z}_{11} (C_{11}^{11}␣C_{11}^{22}␣C_{11}^{33}␣C_{11}^{12}␣C_{11}^{13}␣C_{11}^{23})
α_{12}␣R^{x}_{12}␣R^{y}_{12}␣R^{z}_{12} (C_{12}^{11}␣C_{12}^{22}␣C_{12}^{33}␣C_{12}^{12}␣C_{12}^{13}␣C_{12}^{23})
…
α_{1n}␣R^{x}_{1n}␣R^{y}_{1n}␣R^{z}_{1n} (C_{1n}^{11}␣C_{1n}^{22}␣C_{1n}^{33}␣C_{1n}^{12} ␣C_{1n}^{13}␣C_{1n}^{23})
α_{21}␣R^{x}_{21}␣R^{y}_{21}␣R^{z}_{21} (C_{21}^{11}␣C_{21}^{22}␣C_{21}^{33}␣C_{21}^{12}␣C_{21}^{13}␣C_{21}^{23})
α_{22}␣R^{x}_{22}␣R^{y}_{22}␣R^{z}_{22} (C_{22}^{11}␣C_{22}^{22}␣C_{22}^{33}␣C_{22}^{12}␣C_{22}^{13}␣C_{22}^{23})
...
α_{2n}␣R^{x}_{2n}␣R^{y}_{2n}␣R^{z}_{2n} (C_{2n}^{11}␣C_{2n}^{22}␣C_{2n}^{33}␣C_{2n}^{12}␣ C_{2n}^{13}␣C_{2n}^{23})
…
α_{n1}␣R^{x}_{n1}␣R^{y}_{n1}␣R^{z}_{n1} (C_{n1}^{11}␣C_{n1}^{22}␣C_{n1}^{33}␣C_{n1}^{12}␣C_{n1}^{13}␣C_{n1}^{23})
α_{n2}␣R^{x}_{n2}␣R^{y}_{n2}␣R^{z}_{n2} (C_{n2}^{11}␣C_{n2}^{22}␣C_{n2}^{33}␣C_{n2}^{12}␣C_{n2}^{13}␣C_{n2}^{23})
...
α_{nn}␣R^{x}_{nn}␣R^{y}_{nn}␣R^{z}_{nn} (C_{nn}^{11}␣C_{nn}^{22}␣C_{nn}^{33}␣C_{nn}^{12}␣C_{nn}^{13}␣C_{nn}^{23})

Data File II-2: Input data file for Mg_2-Al LDH with $2H_1$ polytype

```
{date file for Mg2Al-LDH with 2H1 polytype : ACCAAC}
{no stacking faults, infinite particle}
INSTRUMENTAL {Header for instrumental section}
X-RAY {Simulate X-ray diffraction}
1.5418 {X-ray wavelength}
PSEUDO-VOIGT␣0.89␣–0.32␣0.08␣0.6␣trim {Instrumental broadening}
STRUCTURAL {Header for structural section}
5.2897␣5.2897␣15.2066␣120.0 {unit cell coordinates}
UNKNOWN {defined as unknown, will be given by code}
2 {2 layer types: brucite layer, plus its mirror}
INFINITE {infinite layer width}
LAYER 1 {brucite, centrosymmetric}
CENTROSYMMETRIC
Al3+␣1␣0␣0␣0␣1.0␣0.5
Mg2+␣2␣ 1/3␣2/3␣0␣1.0␣1.0
O␣2–␣3␣2/3␣0␣0.06565␣1.0␣1.0
O␣2–␣4␣0␣2/3␣0.06565␣1.0␣1.0
O␣2–␣5␣1/3␣1/3␣0.06565␣1.0␣1.0
{the centrosymmetric atoms does not need to be declared}
LAYER 2 {mirror image of layer 1}
CENTROSYMMETRIC
Al3+␣1␣0␣0␣0␣1.0␣0.5
Mg2+␣2␣ 1/3␣2/3␣0␣1.0␣1.0
O␣2–␣3␣1/3␣0␣0.06565␣1.0␣1.0
O␣2–␣4␣0␣1/3␣0.06565␣1.0␣1.0
O␣2–␣5␣2/3␣2/3␣0.06565␣1.0␣1.0
{the centrosymmetric atoms does not need to be declared}
STACKING {Header for stacking description}
RECURSIVE {Statistical ensemble}
INFINITE {Infinite number of layers}
TRANSITIONS {Header for transitions}
{Transitions from layer 1}
0.0␣0␣0␣0.5 {layer 1 to layer 1, 0% chance}
1.0␣0␣0␣0.5 {layer 1 to layer 2, 100% chance}
{Transitions from layer 2}
1.0␣0␣0␣0.5 {layer 2 to layer 1, 100% chance}
0.0␣0␣0␣0.5 {layer 2 to layer 2, 0% chance}
```

Data File II-3: Input date file for Mg_2-Al LDH with 1H polytype [i]

```
{date file for Mg2Al-LDH with 1H polytype : ACACAC}
{no stacking faults, infinite particle}
…
LAYER 2=1{same as layer 1}
STACKING
…
```

Data File II-4: Input date file for Mg_2-Al LDH with $2H_2$ polytype [i]

```
{date file for Mg2Al-LDH with 2H2 polytype : ACABACAB}
{no stacking faults, infinite particle}
…
{Transitions from layer 1}
0.0␣0␣0␣1.0 {layer 1 to layer 1, 0% chance}
1.0␣0␣1/3␣1.0 {layer 1 to layer 2, 100% chance}
{Transitions from layer 2}
1.0␣1/3␣0␣1.0 {layer 2 to layer 1, 100% chance}
0.0␣0␣0␣1.0 {layer 2 to layer 2, 0% chance}
```

Data File II-5: Input date file for Mg_2-Al LDH with $2H_3$ polytype [i]

```
{date file for Mg2Al-LDH with 2H3 polytype : ACBAACBA}
{no stacking faults, infinite particle}
…
LAYER 2=1{same as layer 1}
STACKING
…
{Transitions from layer 1}
0.0␣0␣0␣1.0 {layer 1 to layer 1, 0% chance}
1.0␣0␣1/3␣1.0 {layer 1 to layer 2, 100% chance}
{Transitions from layer 2}
1.0␣1/3␣0␣1.0 {layer 2 to layer 1, 100% chance}
0.0␣0␣0␣1.0 {layer 2 to layer 2, 0% chance}
```

Data File II-6: Input date file for Mg_2-Al LDH with $3R_1$ polytype

```
{date file for Mg2Al-LDH with 3H1 polytype : ACCBBA}
{no stacking faults, infinite particle}
INSTRUMENTAL {Header for instrumental section}
X-RAY {Simulate X-ray diffraction}
1.5418 {X-ray wavelength}
PSEUDO-VOIGT␣0.89␣–0.32␣0.08␣0.6␣trim {Instrumental broadening}
STRUCTURAL {Header for structural section}
5.2897␣5.2897␣22.8099␣120.0 {unit cell coordinates}
UNKNOWN {defined as unknown, will be given by code}
2 {2 layer types: brucite layer, plus its mirror}
INFINITE {infinite layer width}
LAYER 1 {brucite, centrosymmetric}
CENTROSYMMETRIC
Al3+␣1␣0␣0␣0␣1.0␣0.5
Mg2+␣2␣ 1/3␣2/3␣0␣1.0␣1.0
O␣2–␣3␣2/3␣0␣0.04377␣1.0␣1.0
O␣2–␣4␣0␣2/3␣0.04377␣1.0␣1.0
O␣2–␣5␣1/3␣1/3␣0.04377␣1.0␣1.0
{the centrosymmetric atoms does not need to be declared}
LAYER 2 = 1 {a new layer as same as layer 1}
LAYER 3 = 1 {a new layer as same as layer 1}
{the centrosymmetric atoms does not need to be declared}
STACKING {Header for stacking description}
RECURSIVE {Statistical ensemble}
INFINITE {Infinite number of layers}
TRANSITIONS {Header for transitions}
{Transitions from layer 1}
0.0␣1/3␣0␣1/3 {layer 1 to layer 1, 0% chance}
1.0␣1/3␣0␣1/3 {layer 1 to layer 2, 100% chance}
0.0␣1/3␣0␣1/3 {layer 1 to layer 3, 0% chance}
{Transitions from layer 2}
0.0␣1/3␣0␣1/3 {layer 2 to layer 1, 0% chance}
0.0␣1/3␣0␣1/3 {layer 2 to layer 2, 0% chance}
1.0␣1/3␣0␣1/3 {layer 2 to layer 3, 100% chance}
{Transitions from layer 3}
1.0␣1/3␣0␣1/3 {layer 3 to layer 1, 100% chance}
0.0␣1/3␣0␣1/3 {layer 3 to layer 2, 0% chance}
0.0␣1/3␣0␣1/3 {layer 3 to layer 3, 0% chance}
```

Data File II-7: Input date file for Mg_2-Al LDH with $3H_1$ polytype [ii]

```
{date file for Mg2Al-LDH with 3H1 polytype : ACABABAC}
{no stacking faults, infinite particle}
…
LAYER 2 {brucite, centrosymmetric}
CENTROSYMMETRIC
Al3+␣1␣0␣0␣0␣1.0␣0.5
Mg2+␣2␣ 1/3␣2/3␣0␣1.0␣1.0
O␣2–␣3␣1/3␣0␣0.04377␣1.0␣1.0
O␣2–␣4␣0␣1/3␣0.04377␣1.0␣1.0
O␣2–␣5␣2/3␣2/3␣0.04377␣1.0␣1.0
LAYER 3=2{a new layer as same as layer 2}
STACKING
…
{Transitions from layer 1}
0.0␣0␣0␣1/3 {layer 1 to layer 1, 0% chance}
1.0␣0␣1/3␣1/3 {layer 1 to layer 2, 100% chance}
0.0␣0␣0␣1/3 {layer 1 to layer 3, 0% chance}
{Transitions from layer 2}
0.0␣0␣0␣1/3 {layer 2 to layer 1, 0% chance}
0.0␣0␣0␣1/3 {layer 2 to layer 2, 0% chance}
1.0␣0␣0␣1/3 {layer 2 to layer 3, 100% chance}
{Transitions from layer 3}
1.0␣1/3␣0␣1/3 {layer 3 to layer 1, 100% chance}
0.0␣0␣0␣1/3 {layer 3 to layer 2, 0% chance}
0.0␣0␣0␣1/3 {layer 3 to layer 3, 0% chance}
```

Data File II-8: Input date file for Mg_2-Al LDH with $3H_2$ polytype [ii]

```
{date file for Mg2Al-LDH with 3H2 polytype : ACABCBAC}
{no stacking faults, infinite particle}
…
LAYER 2 {brucite, centrosymmetric}
CENTROSYMMETRIC
Al3+␣1␣0␣0␣0␣1.0␣0.5
Mg2+␣2␣ 1/3␣2/3␣0␣1.0␣1.0
O␣2–␣3␣1/3␣0␣0.04377␣1.0␣1.0
O␣2–␣4␣0␣1/3␣0.04377␣1.0␣1.0
O␣2–␣5␣2/3␣2/3␣0.04377␣1.0␣1.0
LAYER 3=1{a new layer as same as layer 1}
STACKING
…
```

```
{Transitions from layer 1}
0.0␣0␣0␣1/3 {layer 1 to layer 1, 0% chance}
1.0␣0␣1/3␣1/3 {layer 1 to layer 2, 100% chance}
0.0␣0␣0␣1/3 {layer 1 to layer 3, 0% chance}
{Transitions from layer 2}
0.0␣0␣0␣1/3 {layer 2 to layer 1, 0% chance}
0.0␣0␣0␣1/3 {layer 2 to layer 2, 0% chance}
1.0␣0␣1/3␣1/3 {layer 2 to layer 3, 100% chance}
{Transitions from layer 3}
1.0␣0␣1/3␣1/3 {layer 3 to layer 1, 100% chance}
0.0␣0␣0␣1/3 {layer 3 to layer 2, 0% chance}
0.0␣0␣0␣1/3 {layer 3 to layer 3, 0% chance}
```

Data File II-9: Input date file for Mg$_2$-Al LDH with 3H$_3$ polytype [ii]

```
{date file for Mg2Al-LDH with 3H3 polytype : ACABBAAC}
{no stacking faults, infinite particle}
…
LAYER 2 {brucite, centrosymmetric}
CENTROSYMMETRIC
Al3+␣1␣0␣0␣0␣1.0␣0.5
Mg2+␣2␣ 1/3␣2/3␣0␣1.0␣1.0
O␣2–␣3␣1/3␣0␣0.04377␣1.0␣1.0
O␣2–␣4␣0␣1/3␣0.04377␣1.0␣1.0
O␣2–␣5␣2/3␣2/3␣0.04377␣1.0␣1.0
LAYER 3=1{a new layer as same as layer 1}
STACKING
…
{Transitions from layer 1}
0.0␣0␣0␣1/3 {layer 1 to layer 1, 0% chance}
1.0␣0␣1/3␣1/3 {layer 1 to layer 2, 100% chance}
0.0␣0␣0␣1/3 {layer 1 to layer 3, 0% chance}
{Transitions from layer 2}
0.0␣0␣0␣1/3 {layer 2 to layer 1, 0% chance}
0.0␣0␣0␣1/3 {layer 2 to layer 2, 0% chance}
1.0␣0␣0␣1/3 {layer 2 to layer 3, 100% chance}
{Transitions from layer 3}
1.0␣1/3␣0␣1/3 {layer 3 to layer 1, 100% chance}
0.0␣0␣0␣1/3 {layer 3 to layer 2, 0% chance}
0.0␣0␣0␣1/3 {layer 3 to layer 3, 0% chance}
```

Data File II-10: Input date file for Mg_2-Al LDH with $3H_4$ polytype [ii]

```
{date file for Mg2Al-LDH with 3H4 polytype : ACACCAAC}
{no stacking faults, infinite particle}
…
LAYER 2 {brucite, centrosymmetric}
CENTROSYMMETRIC
Al3+␣1␣0␣0␣0␣1.0␣0.5
Mg2+␣2␣ 1/3␣2/3␣0␣1.0␣1.0
O␣2–␣3␣1/3␣0␣0.04377␣1.0␣1.0
O␣2–␣4␣0␣1/3␣0.04377␣1.0␣1.0
O␣2–␣5␣2/3␣2/3␣0.04377␣1.0␣1.0
LAYER 3=1{a new layer as same as layer 1}
STACKING
…
{Transitions from layer 1}
0.0␣0␣0␣1/3 {layer 1 to layer 1, 0% chance}
0.0␣0␣0␣1/3 {layer 1 to layer 2, 0% chance}
1.0␣0␣0␣1/3 {layer 1 to layer 3, 100% chance}
{Transitions from layer 2}
1.0␣0␣0␣1/3 {layer 2 to layer 1, 100% chance}
0.0␣0␣0␣1/3 {layer 2 to layer 2, 0% chance}
0.0␣0␣0␣1/3 {layer 2 to layer 3, 0% chance}
{Transitions from layer 3}
0.0␣0␣0␣1/3 {layer 3 to layer 1, 0% chance}
1.0␣0␣0␣1/3 {layer 3 to layer 2, 100% chance}
0.0␣0␣0␣1/3 {layer 3 to layer 3, 0% chance}
```

Data File II-11: Input date file for Mg_2-Al LDH with $3H_5$ polytype [ii]

```
{date file for Mg2Al-LDH with 3H5 polytype : ACABBCAC}
{no stacking faults, infinite particle}
…
LAYER 2 {brucite, centrosymmetric}
CENTROSYMMETRIC
Al3+␣1␣0␣0␣0␣1.0␣0.5
Mg2+␣2␣ 1/3␣2/3␣0␣1.0␣1.0
O␣2–␣3␣1/3␣0␣0.04377␣1.0␣1.0
O␣2–␣4␣0␣1/3␣0.04377␣1.0␣1.0
O␣2–␣5␣2/3␣2/3␣0.04377␣1.0␣1.0
LAYER 3=2{a new layer as same as layer 2}
STACKING
```

```
…
{Transitions from layer 1}
0.0␣0␣0␣1/3 {layer 1 to layer 1, 0% chance}
1.0␣0␣1/3␣1/3 {layer 1 to layer 2, 100% chance}
0.0␣0␣0␣1/3 {layer 1 to layer 3, 0% chance}
{Transitions from layer 2}
0.0␣0␣0␣1/3 {layer 2 to layer 1, 0% chance}
0.0␣0␣0␣1/3 {layer 2 to layer 2, 0% chance}
1.0␣0␣1/3␣1/3 {layer 2 to layer 3, 100% chance}
{Transitions from layer 3}
1.0␣0␣1/3␣1/3 {layer 3 to layer 1, 100% chance}
0.0␣0␣0␣1/3 {layer 3 to layer 2, 0% chance}
0.0␣0␣0␣1/3 {layer 3 to layer 3, 0% chance}
```

Data File II-12: Input date file for Mg_2-Al LDH with $3H_6$ polytype [ii]

```
{date file for Mg2Al-LDH with 3H6 polytype : ACABCAAC}
{no stacking faults, infinite particle}
…
LAYER 2 {brucite, centrosymmetric}
CENTROSYMMETRIC
Al3+␣1␣0␣0␣0␣1.0␣0.5
Mg2+␣2␣ 1/3␣2/3␣0␣1.0␣1.0
O␣2–␣3␣1/3␣0␣0.04377␣1.0␣1.0
O␣2–␣4␣0␣1/3␣0.04377␣1.0␣1.0
O␣2–␣5␣2/3␣2/3␣0.04377␣1.0␣1.0
LAYER 3=2{a new layer as same as layer 2}
STACKING
…
{Transitions from layer 1}
0.0␣0␣0␣1/3 {layer 1 to layer 1, 0% chance}
1.0␣0␣1/3␣1/3 {layer 1 to layer 2, 100% chance}
0.0␣0␣0␣1/3 {layer 1 to layer 3, 0% chance}
{Transitions from layer 2}
0.0␣0␣0␣1/3 {layer 2 to layer 1, 0% chance}
0.0␣0␣0␣1/3 {layer 2 to layer 2, 0% chance}
1.0␣1/3␣0␣1/3 {layer 2 to layer 3, 100% chance}
{Transitions from layer 3}
1.0␣0␣0␣1/3 {layer 3 to layer 1, 100% chance}
0.0␣0␣0␣1/3 {layer 3 to layer 2, 0% chance}
0.0␣0␣0␣1/3 {layer 3 to layer 3, 0% chance}
```

Data File II-13: Input date file for Mg2Al-LDH with 3H_7 polytype [ii]

```
{date file for Mg2Al-LDH with 3H7 polytype : ACACBAAC}
{no stacking faults, infinite particle}
…
LAYER 2=1{same as layer 1}
LAYER 3=1{same as layer 1}
STACKING
…
{Transitions from layer 1}
0.0␣0␣0␣1/3 {layer 1 to layer 1, 0% chance}
1.0␣0␣0␣1/3 {layer 1 to layer 2, 100% chance}
0.0␣0␣0␣1/3 {layer 1 to layer 3, 0% chance}
{Transitions from layer 2}
0.0␣0␣0␣1/3 {layer 2 to layer 1, 0% chance}
0.0␣0␣0␣1/3 {layer 2 to layer 2, 0% chance}
1.0␣0␣1/3␣1/3 {layer 2 to layer 3, 100% chance}
{Transitions from layer 3}
1.0␣1/3␣0␣1/3 {layer 3 to layer 1, 100% chance}
0.0␣0␣0␣1/3 {layer 3 to layer 2, 0% chance}
0.0␣0␣0␣1/3 {layer 3 to layer 3, 0% chance}
```

Data File II-14: Input date file for Mg_2-Al LDH with 3R_1 polytype incorporated with 10% 2H_1 stacking faults.[iii]

```
{date file for Mg2Al-LDH with 3R1 polytype : ACCBBAC}
{10% 2H1 stacking faults, infinite particle}
INSTRUMENTAL {Header for instrumental section}
X-RAY {Simulate X-ray diffraction}
1.5418 {X-ray wavelength}
PSEUDO-VOIGT␣0.89␣–0.32␣0.08␣0.6␣trim {Instrumental broadening}
STRUCTURAL {Header for structural section}
5.2897␣5.2897␣22.8099␣120.0 {unit cell coordinates}
UNKNOWN {defined as unknown, will be given by code}
2 {2 layer types: brucite layer, plus its mirror}
INFINITE {infinite layer width}
LAYER 1 {brucite, centrosymmetric}
CENTROSYMMETRIC
Al3+␣1␣0␣0␣0␣1.0␣0.5
Mg2+␣2␣ 1/3␣2/3␣0␣1.0␣1.0
O␣2–␣3␣2/3␣0␣0.04377␣1.0␣1.0
O␣2–␣4␣0␣2/3␣0.04377␣1.0␣1.0
O␣2–␣5␣1/3␣1/3␣0.04377␣1.0␣1.0
{the centrosymmetric atoms does not need to be declared}
LAYER 2 {brucite, centrosymmetric}
CENTROSYMMETRIC
Al3+␣1␣0␣0␣0␣1.0␣0.5
Mg2+␣2␣ 1/3␣2/3␣0␣1.0␣1.0
```

```
O␣2–␣3␣1/3␣0␣0.04377␣1.0␣1.0
O␣2–␣4␣0␣1/3␣0.04377␣1.0␣1.0
O␣2–␣5␣2/3␣2/3␣0.04377␣1.0␣1.0
LAYER 3 = 1 {a new layer as same as layer 1}
{the centrosymmetric atoms does not need to be declared}
STACKING {Header for stacking description}
RECURSIVE {Statistical ensemble}
INFINITE {Infinite number of layers}
TRANSITIONS {Header for transitions}
{Transitions from layer 1}
0.0␣1/3␣0␣1/3 {layer 1 to layer 1, 0% chance}
0.1␣0␣0␣1/3 {layer 1 to layer 2, 10% chance}
0.9␣1/3␣0␣1/3 {layer 1 to layer 3, 90% chance}
{Transitions from layer 2}
0.5␣0␣0␣1/3 {layer 2 to layer 1, 50% chance}
0.0␣0␣0␣1/3 {layer 2 to layer 2, 0% chance}
0.5␣0␣0␣1/3 {layer 2 to layer 3, 50% chance}
{Transitions from layer 3}
0.9␣1/3␣0␣1/3 {layer 3 to layer 1, 90% chance}
0.1␣0␣0␣1/3 {layer 3 to layer 2, 10% chance}
0.0␣1/3␣0␣1/3 {layer 3 to layer 3, 0% chance}
```

Data File II-15: Input date file for Mg$_2$-Al LDH with 3R$_1$ polytype and 5 nm particle diameter.[iv]

```
{date file for Mg2Al-LDH with 3R1 polytype : ACCBBAAC}
{no stacking faults, particles with 5nm diameters}
…
50 {average diameter in Å}
LAYER 1
…
LAYER 2=1{same as layer 1}
```

Data File II-16: Input date file for Mg$_2$-Al LDH with 3R$_1$ polytype and 5 stacking layers.[v]

```
{date file for Mg2Al-LDH with 3R1 polytype : ACCBBAAC}
{no stacking faults, stacking number 5}
…
STACKING
RECURSIVE
5 {number of layers in crystal}
…
```

Data File II-17: Input date file for Mg$_2$-Al LDH with 3R$_1$ polytype and 5% turbostratic disorder.[vi]

```
{date file for Mg2Al-LDH with 3R1 polytype : ACCBBAAC}
{5% turbostratic disorder, infinite particle}
…
TRANSITIONS
{Transitions from layer 1}
0.005␣x␣y␣1/3 {layer 1 to layer 1, 0.5% chance}[vii]
0.99␣1/3␣0␣1/3 {layer 1 to layer 2, 99% chance}
0.005␣x␣y␣1/3 {layer 1 to layer 3, 0.5% chance}
{Transitions from layer 2}
0.005␣x␣y␣1/3 {layer 2 to layer 1, 0.5% chance}
0.005␣x␣y␣1/3 {layer 2 to layer 2, 0.5% chance}
0.95␣1/3␣0␣1/3 {layer 2 to layer 3, 99% chance}
{Transitions from layer 3}
0.99␣1/3␣0␣1/3 {layer 3 to layer 1, 99% chance}
0.005␣x␣y␣1/3 {layer 3 to layer 2, 0.05% chance}
0.005␣x␣y␣1/3 {layer 3 to layer 3, 0.05% chance}
```

References

1. M. M. J. Treacy, M. W. Deem and J. M. Newsam, *DIFFaX v1.813*, 1.813 edn., NEC Research Institute, Princeton, New Jersey, 2010.

---

[i] In these data files, lines as same as in **Data File II-2** were omitted.

[ii] In these data files, lines as same as in **Data File II-6** were omitted.

[iii] The rest input data files for 20%-90% stacking faults can be deducted on the analogy of this file for 10% stacking faults.

[iv] The rest input data files for 10nm - 1µm particle diameters can be deducted on the analogy of this file for 5nm particle diameter.

[v] The rest input data files for 10 - 100 stacking layers can be deducted on the analogy of this file for 5 stacking layers.

[vi] The rest input data files for 10% - 20% turbostracity can be deducted on the analogy of this file for 5% turbostracity.

[vii] *x*, *y* here are random numbers between 0 and 1.

Appendix III

Simulated XRD data file using DIFFaX+ in Chapter 6

Table III-1: Obtained crystal data by simulating XRD pattern for **MgAl-OAm-1**.

Crystallite size		
Crystallite size	Diameter (nm)	56.6
	Layer number	14

$3R_1$	Crystal system		monoclinic	a =5.2821Å b =3.0496Å c =7.9418Å β = 102.81 °				
	Atoms		Site	*x/a*	*y/b*	*z/c*	B_{iso}	Occ.
	Al^{3+}	1	2/m	0	0	0	1.0	0.29
	Mg^{2+}	2	2/m	0	0	0	1.0	0.71
	O^{2-}	3	m	0.3963	0	0.1490	1.0	1
	O^{2-}	4	1	–1/12	1/2	1/2	1.0	0.161
	O^{2-}	5	m	–1/3	0	1/2	1.0	0.161
	Cl^{-}	6	m	–0.2681	1/2	1/2	1.0	0.012
	Cl^{-}	7	1	–0.1340	0.0979	1/2	1.0	0.012
$2H_1$	Crystal system		monoclinic	a =5.2821Å b =3.0496Å c =15.488Å β = 90 °				
	Atoms		Site	*x/a*	*y/b*	*z/c*	B_{iso}	Occ.
	Al^{3+}	1	2/m	0	0	0	1.0	0.29
	Al^{3+}	2	2/m	0	0	1/2	1.0	0.29
	Mg^{2+}	3	2/m	0	0	0	1.0	0.71
	Mg^{2+}	4	2/m	0	0	1/2	1.0	0.71
	O^{2-}	5	m	5/6	1/2	0.0435	1.0	1
	O^{2-}	6	m	5/6	1/2	1/2	1.0	1
	O^{2-}	7	m	0	1/2	1/4	1.0	0.161
	O^{2-}	8	1	–1/12	1/4	1/4	1.0	0.161
	O^{2-}	9	m	–1/3	1/2	1/4	1.0	0.161
	O^{2-}	10	1	–1/4	1/4	1/4	1.0	0.161
	Cl^{-}	11	1	–0.0326	0.0979	1/4	1.0	0.012
	Cl^{-}	12	1	–0.3007	0.0979	1/4	1.0	0.012
	Cl^{-}	13	m	–0.3986	0	1/4	1.0	0.012
	Cl^{-}	14	m	–0.4347	1/2	1/4	1.0	0.012

	Probability (%)	Layer	Vector		
Transition	88.81	$3R_1$ - $3R_1$	0	0	1
	11.19	$3R_1$ - $2H_1$	0	0	1
	44.39	$2H_1$ - $3R_1$	0	0	1
	55.61	$2H_1$ - $2H_1$	0	0	1

Table III-2: Obtained crystal data by simulating XRD pattern for **MgAl-OAm-2**.

Crystallite size	Diameter (nm)				51.8			
	Layer number				20			
$3R_1$	Crystal system		monoclinic	*a* =5.2809Å *b* =3.0489Å *c* =7.9128Å β = 102.85 °				
	Atoms		Site	*x/a*	*y/b*	*z/c*	B_{iso}	Occ.
	Al^{3+}	1	2/m	0	0	0	1.0	0.33
	Mg^{2+}	2	2/m	0	0	0	1.0	0.67
	O^{2-}	3	m	0.3481	0	0.1392	1.0	1
	O^{2-}	4	1	–1/12	1/4	1/2	1.0	0.143
	O^{2-}	5	m	–1/3	0	1/2	1.0	0.143
	Cl^{-}	6	m	–0.2681	1/2	1/2	1.0	0.043
	Cl^{-}	7	1	–0.1340	0.0979	1/2	1.0	0.043
$2H_1$	Crystal system		monoclinic	*a* =5.2875Å *b* =3.0453Å *c* =15.206Å β = 90 °				
	Atoms		Site	*x/a*	*y/b*	*z/c*	B_{iso}	Occ.
	Al^{3+}	1	2/m	0	0	0	1.0	0.33
	Al^{3+}	2	2/m	0	0	1/2	1.0	0.33
	Mg^{2+}	3	2/m	0	0	0	1.0	0.67
	Mg^{2+}	4	2/m	0	0	1/2	1.0	0.67
	O^{2-}	5	m	5/6	1/2	0.0280	1.0	1
	O^{2-}	6	m	5/6	1/2	1/2	1.0	1
	O^{2-}	7	m	0	1/2	1/4	1.0	0.143
	O^{2-}	8	1	–1/12	1/4	1/4	1.0	0.143
	O^{2-}	9	m	–1/3	1/2	1/4	1.0	0.143
	O^{2-}	10	1	–1/4	1/4	1/4	1.0	0.143
	Cl^{-}	11	1	–0.0326	0.0979	1/4	1.0	0.043
	Cl^{-}	12	1	–0.3007	0.0979	1/4	1.0	0.043
	Cl^{-}	13	m	–0.3986	0	1/4	1.0	0.043
	Cl^{-}	14	m	–0.4347	1/2	1/4	1.0	0.043
Transition	Probability (%)		Layer	Vector				
	93.80		$3R_1$ - $3R_1$	0	0	1		
	6.20		$3R_1$ - $2H_1$	0	0	1		
	24.05		$2H_1$ - $3R_1$	0	0	1		
	75.95		$2H_1$ - $2H_1$	0	0	1		

Table III-3: Obtained crystal data by simulating XRD pattern for **MgAl-OAm-3**.

Crystallite size		
Crystallite size	Diameter (nm)	127.3
	Layer number	35

	Crystal system		monoclinic	*a* =5.2767Å *b* =3.0465Å *c* =7.9204Å β =102.83 °				
	Atoms		Site	*x/a*	*y/b*	*z/c*	B_{iso}	Occ.
$3R_1$	Al^{3+}	1	2/m	0	0	0	1.0	0.3
	Mg^{2+}	2	2/m	0	0	0	1.0	0.7
	O^{2-}	3	m	0.3863	0	0.1353	1.0	1
	O^{2-}	4	1	–1/12	1/4	1/2	1.0	0.104
	O^{2-}	5	m	–1/3	0	1/2	1.0	0.104
	Cl^{-}	6	m	–0.2681	1/2	1/2	1.0	0.059
	Cl^{-}	7	1	–0.1340	0.0979	1/2	1.0	0.059

	Crystal system		monoclinic	*a* =5.2767Å *b* =3.0465Å *c* =15.445Å β = 90 °				
	Atoms		Site	*x/a*	*y/b*	*z/c*	B_{iso}	Occ.
$2H_1$	Al^{3+}	1	2/m	0	0	0	1.0	0.3
	Al^{3+}	2	2/m	0	0	1/2	1.0	0.3
	Mg^{2+}	3	2/m	0	0	0	1.0	0.7
	Mg^{2+}	4	2/m	0	0	1/2	1.0	0.7
	O^{2-}	5	m	5/6	1/2	0.0446	1.0	1
	O^{2-}	6	m	5/6	1/2	1/2	1.0	1
	O^{2-}	7	m	0	1/2	1/4	1.0	0.104
	O^{2-}	8	1	–1/12	1/4	1/4	1.0	0.104
	O^{2-}	9	m	–1/3	1/2	1/4	1.0	0.104
	O^{2-}	10	1	–1/4	1/4	1/4	1.0	0.104
	Cl^{-}	11	1	–0.0326	0.0979	1/4	1.0	0.059
	Cl^{-}	12	1	–0.3007	0.0979	1/4	1.0	0.059
	Cl^{-}	13	m	–0.3986	0	1/4	1.0	0.059
	Cl^{-}	14	m	–0.4347	1/2	1/4	1.0	0.059

	Probability (%)	Layer	Vector		
Transition	80.77	$3R_1$ - $3R_1$	0	0	1
	19.23	$3R_1$ - $2H_1$	0	0	1
	65.28	$2H_1$ - $3R_1$	0	0	1
	34.72	$2H_1$ - $2H_1$	0	0	1